

University of Southampton Research Repository ePrints Soton

Copyright © and Moral Rights for this thesis are retained by the author and/or other copyright owners. A copy can be downloaded for personal non-commercial research or study, without prior permission or charge. This thesis cannot be reproduced or quoted extensively from without first obtaining permission in writing from the copyright holder/s. The content must not be changed in any way or sold commercially in any format or medium without the formal permission of the copyright holders.

When referring to this work, full bibliographic details including the author, title, awarding institution and date of the thesis must be given e.g.

AUTHOR (year of submission) "Full thesis title", University of Southampton, name of the University School or Department, PhD Thesis, pagination

UNIVERSITY OF SOUTHAMPTON

FACULTY OF ENGINEERING AND THE ENVIRONMENT

INSTITUTE OF SOUND AND VIBRATION RESEARCH

**HYBRID ACTIVE-PASSIVE CONSTRAINED LAYER DAMPING TREATMENTS IN
BEAMS, PLATES AND SHELLS**

by

BYUNGJUN KOH

Thesis for the degree of Doctor of Philosophy

June 2016

UNIVERSITY OF SOUTHAMPTON

ABSTRACT

FACULTY OF ENGINEERING AND THE ENVIRONMENT

Institute of Sound and Vibration Research

Doctor of Philosophy

HYBRID ACTIVE-PASSIVE CONSTRAINED LAYER DAMPING TREATMENTS IN BEAMS, PLATES AND SHELLS

by Byungjun Koh

The basic concept of Hybrid Active-Passive Constrained Layer Damping (HAPCLD) treatment was proposed by introducing active control to the concept of passive constrained layer damping configuration in the 1990s to compensate for weak points in active and passive controls by using their respective merits for more robust and stable control. Since then, combinations of various configurations and applicable control strategies have been proposed and studied in many engineering areas. However, there is still a need for a new modelling method to more easily establish models of HAPCLD treatment and its validation through control analysis and experiment with various structures from beams to curved plates.

In this thesis, velocity feedback control strategy was applied to cantilever beams with four different configurations of HAPCLD treatment to check their applicability. Moreover, the application was expanded to flat and curved plates. Control results with each configuration for flat and curved plates were analysed by using self-established MATLAB codes based on the Finite Element Method (FEM) with the basic concept of a layer-wise approach for coupling each layer of structures and deriving Equivalent Single Layer (ESL) models. This new numerical modelling method was established by introducing coupling matrices based on a layer-wise approach to combine individual FE mass and stiffness matrices of each layer into one ESL model for a whole structure. Furthermore, these numerical models were supported by experiments in a lab. All measured data was compared with simulation results and they were confirmed in good agreement in general. In addition to this, the relation between mode shapes and control by piezoelectric patches occupying a broader area than an ideal actuator was studied to find the conditions for more stable control of flat and curved plates.

In conclusion, as discussed for active control with beams, AC/PSOLD treatment, which consists of a piezoelectric actuator directly attached to a base structure and a stand-off layer with a viscoelastic core and elastic constraining patch laminated on the piezoelectric actuator, was clarified to give the most efficient and robust active control results for plates regardless of the cur-

vature of all HAPCLD treatments dealt within this thesis as well. AC/PSOLD treatment could give similar reductions with smaller control gain in simulation. And, larger reductions were obtained with measured transfer functions in experiments than other configurations.

Contents

ABSTRACT	i
Contents	i
List of Tables	vii
List of figures	ix
List of Accompanying Materials	xxv
DECLARATION OF AUTHORSHIP.....	xxvii
Acknowledgements.....	xxix
Definitions and Abbreviations	xxxi
1 INTRODUCTION.....	1
1.1 Background and motivations.....	1
1.2 Objectives of the thesis.....	4
1.3 Contributions of the thesis	6
1.4 Structure of the thesis.....	8
2 LITERATURE REVIEW.....	11
2.1 Passive and active controls with constrained layer damping treatment.....	11
2.2 Modelling method for constrained layer damping treatment	21
2.2.1 FE modelling method for beams with constrained layer damping treatment.....	21
2.2.2 FE modelling method for plates with constrained layer damping treatment.....	22
2.2.3 Other modelling methods for constrained layer damping treatment	25
2.3 State of the art for FE modelling of laminated structures	26
3 FE MODELLING OF BEAMS WITH HAPCLD TREATMENTS.....	29
3.1 Overview of beams with HAPCLD treatment	29
3.2 FE model for an elastic beam	30
3.2.1 Definition of a beam's deformation.....	30
3.2.2 FE formulation of an elastic beam	31
3.3 FE model for a piezoelectric beam.....	35
3.3.1 The constitutive equations of piezoelectric material of a 1D element	35
3.3.2 FE formulation of a piezoelectric beam.....	37

3.4	FE model for a laminated beam with one viscoelastic layer	41
3.4.1	GHM method for viscoelastic material.....	41
3.4.2	Basic assumptions for a viscoelastic layer constrained between two elastic beams	43
3.4.3	FE formulation of a viscoelastic layer constrained between two elastic beams	45
3.4.4	Coupling method for a laminated beam.....	47
3.5	FE model for a beam with HAPCLD treatment	50
3.6	Calculation of FRF using FE beam models	54
3.7	Summary and conclusions	55
4	PARAMETER ESTIMATION OF FE BEAM MODELS THROUGH EXPERIMENT	57
4.1	Model update and parameter estimation by impact hammer test of beams.....	57
4.1.1	Elastic beam model	57
4.1.2	Elastic beam with a layered patch with a PZT and viscoelastic material model.....	61
4.2	Transfer function measurement of beams with hybrid control patches	64
4.2.1	Measurement of transfer functions of hybrid system	65
4.2.2	Result comparison of FE models with measured transfer functions	69
4.3	Summary and conclusion	71
5	VELOCITY FEEDBACK HYBRID ACTIVE-PASSIVE CONTROL OF BEAMS.....	73
5.1	Velocity feedback controller design for beams	73
5.2	Experimental controller design of a beam with HAPCLD treatment	74
5.2.1	Determination of control gain margins	74
5.2.2	Study of a realisation method for an ideal low-pass filter by means of an all-pass filter or phase compensator	79
5.2.3	Optimal control gains with the proposed ideal filter	82
5.3	Summary and conclusions	87
6	FE MODELLING OF FLAT PLATES.....	89
6.1	Overview of flat plates with HAPCLD treatments	89
6.2	FE model of an elastic plate.....	90
6.2.1	Basic assumption of a Kirchhoff plate.....	90
6.2.2	FE formulation for an elastic Kirchhoff plate	91
6.3	FE model for a piezoelectric plate.....	93

6.3.1	The constitutive equations of piezoelectric material for a 2D element	93
6.3.2	FE formulation for a piezoelectric Kirchhoff plate	94
6.4	FE model for a laminated plate with one viscoelastic layer	98
6.4.1	Basic assumptions for a viscoelastic layer constrained between two elastic plates	99
6.4.2	FE formulation of a viscoelastic layer constrained between two elastic plates	100
6.4.3	Coupling method for a laminated plate	102
6.5	FE model for a plate with HAPCLD treatment	104
6.6	Validation of FE flat plate models	108
6.7	Summary and conclusions	110
7	FE MODELLING OF CURVED PLATES	113
7.1	FE modelling of a slightly curved plate	114
7.1.1	Basic assumption for a slightly curved plate	114
7.1.2	Coordinate transfer and FE modelling	116
7.1.3	Comparison with approximated theoretical results	119
7.2	Experimental investigation of FE curved plate models	121
7.2.1	Impact hammer test with curved plates	121
7.2.2	Effect of curvature on mode shapes and resonance frequencies with FE plate models	123
7.3	Summary and conclusions	127
8	HYBRID ACTIVE-PASSIVE CONTROL OF PLATES	129
8.1	Numerical study of control applied to FE plate models	129
8.1.1	Control results for flat plates	130
8.1.2	Control results for singly curved plates	133
8.1.3	Summary of control simulation of a plate with HAPCLD treatments	139
8.2	Study of plate vibration control with measured FRFs and results comparison	143
8.2.1	Experimental results from impact hammer test	144
8.2.2	Experiment set-up, measurement procedure and FRF measurement results	146
8.2.3	Active control based on experimental data	149
8.3	Summary and conclusions	153
9	CONCLUSIONS AND SUGGESTIONS FOR FUTURE WORK	155
9.1	Summary	155
9.2	Conclusions	156
9.3	Suggestions for future work	158

APPENDIX A FINITE ELEMENT MODELLING METHOD.....	161
A.1 Shape functions and the Jacobian matrix of a 1-D element	161
A.2 Assembly of global matrices of a 1-D element	163
A.3 Shape functions and the Jacobian matrix of a 2-D element	165
A.4 Composition of global matrices of a 2-D element	167
APPENDIX B ANALYTICAL MODELS OF BEAMS.....	171
B.1 Exact solution of a Euler beam.....	171
B.2 Modal analysis of a Euler beam	173
B.3 Transfer matrix method for analysis of a Euler beam	174
APPENDIX C BASIC STUDY OF ACTIVE CONTROL.....	175
C.1 Effect of active control on an SDOF system	175
C.2 Optimisation of velocity feedback control.....	176
C.2.1 Effect of collocation on active control for a 2 DOF system.....	177
C.2.2 Effect of collocation on active control of a beam.....	180
C.2.3 Determination of optimal control gains	183
C.2.4 Phase plots for Figure 5.13, 5.14, 5.15 and 5.16.....	188
APPENDIX D EQUATIONS OF MOTION FOR PLATES WITH HAPCLD	
TREATMENTS.....	191
D.1 APCLD treatment.....	191
D.2 AC/PCLD treatment.....	196
D.3 AC/PSOLD treatment.....	199
APPENDIX E RESULTS OF SIMULATION AND MEASUREMENT FOR	
CHAPTER 8.....	203
E.1 Simulation result for determination of optimal control gain and mobility reduction with flat plates.....	203
E.1.1 APCLD treatment	203
E.1.2 AC/PCLD treatment.....	204
E.1.3 AC/PSOLD treatment.....	204
E.2 Simulation result for determination of optimal control gain and mobility reduction with curved plates	205
E.1.1 APCLD treatment	205
E.1.2 AC/PCLD treatment.....	207
E.1.3 AC/PSOLD treatment.....	208
E.3 FRFs of curved plated with HAPCLD treatments in impact hammer test	210
E.4 Nyquist plot for a measured closed-loop and control simulation results for curved plates	210

E.4.1 APCLD treatment	211
E.4.2 AC/PCLD treatment	212
E.4.3 AC/PSOLD treatment	213
List of References	215

List of Tables

Table 4.1 Resonance frequency comparison between beam theory and FE beam models	58
Table 4.2 Material properties and sensitivity of a free-free beam	60
Table 4.3 Parameters used for the GHM method [11].....	62
Table 4.4 Material properties of a free-free beam with PZT and a viscoelastic layered patch	64
Table 5.1 G_{3dB} for each configuration according to the application of a low-pass filter	79
Table 5.2 Change of peak values in the case of active control using ACLD treatment in beams.....	83
Table 5.3 Change of peak values in the case of active control using APCLD treatment in a beam.....	85
Table 5.4 Change of peak values in the case of active control using AC/PCLD treatment in a beam.....	86
Table 5.5 Change of peak values in the case of active control using AC/PSOLD treatment in a beam.....	86
Table 6.1 Resonance frequency comparison between beam theory and FE plate models	109
Table 7.1 Fundamental frequency comparison of flat and curved plates	120
Table 8.1 Passive and active loss factors for a flat plate with ACLD treatment	131
Table 8.2 Passive and active loss factors for a flat plate with APCLD treatment	132
Table 8.3 Passive and active loss factors for a flat plate with AC/PCLD treatment.....	133
Table 8.4 Passive and active loss factors for a flat plate with AC/PSOLD treatment.....	133

Table 8.5 Changes in control gain and maximum absorbed power for all cases according to the change in curvature.....	139
Table 8.6 Active control result summary in each case	141
Table 8.7 Sign of mode shapes around the centre point for each mode	143
Table 8.8 Passive modal loss factors up to the 5th peak in each case	145
Table 8.9 Changes in peak values in the case of active control using ACLD treatment in a plate structure	151
Table 8.10 Changes in peak values in the case of active control using APCLD treatment in a plate structure	152
Table 8.11 Changes in peak values in the case of active control using AC/PCLD treatment in a plate structure	152
Table 8.12 Changes in peak values in the case of active control using AC/PSOLD treatment in a plate structure	152
Table 8.13 Changes in peak values in the case of active control using inverse AC/PCLD treatment in a plate structure	152
Table A.1 Integration points and weight coefficients for the Gauss integration formula	164
Table C.1 Optimised control gains for collocated cases	186

List of figures












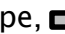

Figure 1.1 (a) Concepts of PULD;  : elastic beam and patch and  : viscoelastic layer and (b) Bending of motion in PULD	2
Figure 1.2 (a) Concepts of PCLD;  : elastic beam and patch and  : viscoelastic layer and (b) Bending of motion in PCLD	3
Figure 1.3 Examples of PCLD treatment application in industry [www.dae-hyup.com/en_product_02_18.html].....	3
Figure 1.4 Concepts of control methods (a) Passive control (b) Active control..	3
Figure 2.1 The changes of shear modulus and loss factor versus temperature at 100 Hz of epoxy adhesive ('3M' 9323), typical damping material ('Dyad' 606) and silicone elastomer ('Silastic' J) [9].....	12
Figure 2.2 Schematic drawing of the ACLD treatment by Baz and Ro [9];  : elastic beam,  : viscoelastic layer and  : piezoelectric patch	13
Figure 2.3 Finite element model of a plate treated with ACLD treatment by Baz and Ro [15];  : elastic plate,  : viscoelastic layer and  : piezoelectric patch.....	14
Figure 2.4 Schematic diagram of the shell (pipe)/ACLD treatment system by Ray et al. [16];  : elastic pipe,  : viscoelastic layer and  : piezoelectric patch.....	14
Figure 2.5 Schematic representation of a lamina of vertically reinforced 1-3 piezoelectric composite material and the cross-sections of a representative volume element (RVE) of the composite by Ray and Pradhan (a) Lamina of 1-3 Piezoelectric composite and (b) Cross-Sections of an RVE of the 1-3 piezoelectric composite in xz and xy planes [17].....	15
Figure 2.6 (a) Schematic representation of an acoustic cavity with a flexible wall of laminated plate integrated with a patch of ACLD treatment and (b) the dynamics of ACLD treatment [18].....	15








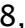
Figure 2.7 Four configurations of HAPCLD treatment [3]; ACLD: Active Constrained Layer Damping, APCLD: Active Passive Constrained Layer Damping, AC/PCLD: Active Control/Passive Constrained Layer Damping and AC/PSOLD: Active Control/Passive Stand-Off Layer Damping	17
Figure 2.8 Concept of Enhanced ACLD treatment;  : elastic beam, patch and edge element,  : viscoelastic layer and  : piezoelectric patch	19
Figure 2.9 A cantilever sandwich beam with viscoelastic core and collocated piezoelectric sensor/actuator [53]	20
Figure 3.1 Configuration of a beam with (a) ACLD treatment, (b) APCLD treatment, (c) AC/PCLD treatment and (d) AC/PSOLD treatment;  : elastic beam (Layer 3) and patch (Layer c),  : viscoelastic layer (Layer 2) and  : piezoelectric patch (Layer 1)	29
Figure 3.2 Deformation of a Euler beam bending under small deflection.....	30
Figure 3.3 Cross-section change of a Euler beam under deformation	30
Figure 3.4 Poisson contraction of cross section in beams	31
Figure 3.5 Classic viscoelastic element: (a) Maxwell material and (b) Kelvin material	41
Figure 3.6 Shear deformation of viscoelastic materials.....	42
Figure 3.7 GHM model for viscoelastic material	42
Figure 3.8 Shear modulus and Loss factor of viscoelastic material:  Shear modulus;  Loss factor for $G^\infty = 0.1633$ MPa, $a_1 = 4.8278$, $a_2 = 14.548$, $a_3 = 40.043$, $\hat{z}_1 = 22.013$, $\hat{z}_2 = 3.1275$, $\hat{z}_3 = 0.6165$, $\hat{w}_1 = 22.013$, $\hat{w}_2 = 3.1275$ and $\hat{w}_3 = 0.6165$	43
Figure 3.9 Geometric concept of a viscoelastic layer constrained between two elastic beams	44
Figure 3.10 Basic concept of layer-wise approach model for a sandwich beam with a viscoelastic core.....	48







Figure 3.11 Configuration of a beam with ACLD treatment;  : elastic beam,  : viscoelastic layer and  : piezoelectric patch	50
Figure 3.12 Configuration of a beam with (a) APCLD treatment, (b) AC/PCLD treatment and (c) AC/PSOLD treatment;  : elastic beam and patch,  : viscoelastic layer and  : piezoelectric patch	52
Figure 4.1 Setup of impact hammer test for an aluminium beam	58
Figure 4.2 Input accelerance of a free-free beam (a) Magnitude and (b) Phase: ---- FEM (MATLAB); -- Analytical (modal analysis); — Experiment; - - - FEM (Patran/Nastran)	59
Figure 4.3 Setup of impact hammer test for an aluminium beam with PZT and viscoelastic layered patch.....	61
Figure 4.4 Input accelerance of a free-free beam with PZT and viscoelastic layered patch (a) Magnitude, (b) Phase and (c) Coherence of measured data: ---- FEM; — Experiment	62
Figure 4.5 Voltage of a free-free beam with PZT and viscoelastic layered patch (a) Magnitude, (b) Phase and (c) Coherence of measured data: ---- FEM; — Experiment	63
Figure 4.6 Dynamics of PZT patch with different boundary conditions; (a) free, (b) simply supported and (c) clamped.....	63
Figure 4.7 (a) Base aluminium cantilever beam for beam control experiment and (b) modal loss factors in each case	65
Figure 4.8 Block diagram of the system for a general case.....	66
Figure 4.9 Schematic diagram of a control system set-up for beams.....	66
Figure 4.10 Experiment set-up for measurement of FRFs of velocity per unit volt with electric pseudo-random excitation; (a) real system and (b) schematic diagram.....	67
Figure 4.11 Experimental set up for measurement of mobilities with shaker excitation; (a) real system and (b) schematic diagram	68


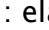









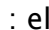

Figure 4.12 (a) FRFs of velocity per unit volt at point P_1 (H_s^v) and (b) phases of velocity per unit volt at point P_1 for a beam with ACLD treatment when an electrical signal is applied to a PZT patch; — FE model and - - - measured data	69
Figure 4.13 (a) Mobility at point P_1 (H_{se}^f) and (b) phases of Mobility at point P_1 for a beam with ACLD treatment when pseudo-random force is applied; — FE model and - - - measured data	70
Figure 4.14 (a) FRFs of velocity per unit volt with the effect of a low-pass filter at point P_1 (H_s^v) and (b) phases of velocity per unit volt with the effect of a low-pass filter at point P_1 for a beam with ACLD treatment when an electrical signal is applied to a PZT patch; — FE model and - - - measured data	70
Figure 4.15 (a) Mobility with the effect of a low-pass filter at point P_1 (H_{se}^f) and (b) phases of Mobility with the effect of a low-pass filter at point P_1 for a beam with ACLD treatment when a pseudo-random force is applied; — FE model and - - - measured data	70
Figure 5.1 Beam with ACLD treatment for experiment;  : elastic beam,  : viscoelastic layer and  : piezoelectric patch	74
Figure 5.2 Beam with APCLD treatment for experiment;  : elastic beam,  : viscoelastic layer and  : piezoelectric patch	75
Figure 5.3 Beam with AC/PCLD treatment for experiment;  : elastic beam,  : viscoelastic layer and  : piezoelectric patch	75
Figure 5.4 Beam with AC/PSOLD treatment for experiment;  : elastic beam,  : viscoelastic layer and  : piezoelectric patch	75
Figure 5.5 The Nyquist plots for the open loop of beam structures without a KEMO low-pass filter: (a) ACLD treatment, (b) APCLD treatment, (c) AC/PCLD treatment and (d) AC/PSOLD treatment	76
Figure 5.6 The Nyquist plots for the open loop of beam structures with a KEMO low-pass filter (Cut-off frequency: 300 Hz): (a) ACLD treatment, (b) APCLD treatment, (c) AC/PCLD treatment and (d) AC/PSOLD treatment	77

Figure 5.7 An ideal low-pass filter with 300 Hz cut-off frequency: (a) Frequency response and (b) Phase response	78
Figure 5.8 The Nyquist plots for the open loop of beam structures with an ideal low-pass filter (Cut-off frequency: 300 Hz): (a) ACLD treatment, (b) APCLD treatment, (c) AC/PCLD treatment and (d) AC/PSOLD treatment.....	78
Figure 5.9 Frequency response of an all-pass filter from [http://www.uaudio.com/blog/allpass-filters] (a) Magnitude Response and (b) Phase	80
Figure 5.10 Phase shift minimisation method in real-time active control using a combination of a band-pass filter and an all-pass filter.....	81
Figure 5.11 Control results for ACLD treatment on a beam with (a) No filter ($G_{3dB} = 14.09$), (b) a KEMO low-pass filter ($G_{3dB} = 261.97$) and (c) a proposed ideal filter ($G_{3dB} = 825.10$); — No control; - - with control	82
Figure 5.12 Phases for ACLD treatment on a beam with (a) No filter ($G_{3dB} = 14.09$), (b) a KEMO low-pass filter ($G_{3dB} = 261.97$) and (c) a proposed ideal filter ($G_{3dB} = 825.10$); — No control; - - with control.....	82
Figure 5.13 Control results for APCLD treatment on a beam with (a) No filter ($G_{3dB} = 24.58$), (b) a KEMO low-pass filter ($G_{3dB} = 167.61$) and (c) a proposed ideal filter ($G_{3dB} = 1240$); — No control; - - with control	83
Figure 5.14 Control results for AC/PCLD treatment on a beam with (a) No filter ($G_{3dB} = 8.42$), (b) a KEMO low-pass filter ($G_{3dB} = 61.79$) and (c) a proposed ideal filter ($G_{3dB} = 8.42$); — No control; - - with control	84
Figure 5.15 Control results for AC/PSOLD treatment on a beam with (a) No filter ($G_{3dB} = 4.79$), (b) a KEMO low-pass filter ($G_{3dB} = 69.77$) and (c) a proposed ideal filter ($G_{3dB} = 1302$); — No control; - - with control	84
Figure 5.16 Control simulation results with a proposed ideal filter and G_{3dB} for (a) ACLD, (b) APCLD, (c) AC/PCLD and (d) AC/PSOLD treatments ...	85
Figure 6.1 Configuration of a plate with (a) ACLD treatment, (b) APCLD treatment, (c) AC/PCLD treatment and (d) AC/PSOLD treatment;  :	









elastic plate and patch,  : viscoelastic layer and  : piezoelectric patch	90
Figure 6.2 (a) The coordinate system of a plate (b) Deflection of plate in the x direction (c) Deflection of a plate in the y direction.....	90
Figure 6.3 Geometric concept of a viscoelastic layer constrained between two elastic plates (a) in the x-axis and (b) y-axis.....	99
Figure 6.4 Basic concept of a layer-wise approach model for a sandwich plate with a viscoelastic core on the y-axis.....	103
Figure 6.5 Configuration of a plate with ACLD treatment;  : elastic plate,  : viscoelastic layer and  : piezoelectric patch	105
Figure 6.6 Configuration of a plate with (a) APCLD treatment, (b) AC/PCLD treatment and (c) AC/PSOLD treatment;  : elastic plate,  : viscoelastic layer and  : piezoelectric patch	108
Figure 6.7 Input accelerance for a free narrow plate using 2-D FEM (a) Magnitude and (b) Phase: ---- FEM (MATLAB); -- Analytic (modal analysis); — Experiment; - - - FEM (Patran/Nastran)	109
Figure 6.8 Input accelerance for a free narrow plate with PZT and a viscoelastic layered patch using 2-D FEM (a) Magnitude and (b) Phase: ---- FEM; — Experiment.....	109
Figure 6.9 Voltage of a free narrow plate with PZT and a viscoelastic layered patch using 2-D FEM (a) Magnitude and (b) Phase: ---- FEM; — Experiment	110
Figure 7.1 Examples of curved plate application in machinery (a) airplane [http://hendrynoya.wordpress.com/2011/04/17/aircraft-load-part-i/], (b) car [http://www.boronextrication.com/2011/08/02/2012-audi-a6-body-structure/] and (c) ship [http://navyadministration.tpub.com/12966/css/12966_302.htm]	113
Figure 7.2 Change of coordinates for a slightly curved plate from an FE element	114
Figure 7.3 Basic concept of a slightly curved plate	115

Figure 7.4 FE model of a slightly curved plate; (a) the relationship between the global coordinates and the local coordinates in a slightly curved plate and (b) rotation of an FE element along the curvature.....	118
Figure 7.5 Change of fundamental frequency according to the increase of maximum rise at the centre: — Warburton's theory; -.- FEM (Matlab, 8X8); ----- FEM (Matlab, 12X12)	120
Figure 7.6 Change of resonance frequency according to the increase of maximum rise at the centre; (a) second resonance frequency and (b) third resonance frequency: — Warburton's theory; -.- FEM (Matlab, 8X8); ----- FEM (Matlab, 12X12).....	121
Figure 7.7 Impact hammer test for a singly curved plate.....	122
Figure 7.8 Result comparison for an impact hammer test between an FE plate model and a real curved plate (a) point mobility and (b) phase: — FEM (MATLAB); -.- Experiment	122
Figure 7.9 Mode shapes for a free-free flat plate for out-of-plane motion (a) 1st mode (1, 1) at 49.4305 Hz, (b) 2nd mode (2, 0) at 71.4336 Hz, (c) 3rd mode (0, 2) at 92.3491 Hz, (d) 4th mode (2, 1) at 126.20 Hz, (e) 5th mode (1, 2) at 130.82 Hz, (f) 6th mode (3, 0) at 217.67 Hz, (g) 7th mode (2, 2) at 235.54 Hz, (h) 8th mode (0, 3) at 239.55 Hz and (i) 9th mode (3, 1) at 253.51 Hz.....	123
Figure 7.10 Mode shapes for a free-free curved plate with the maximum rise of 10 mm for out-of-plane motion (a) 1st mode at 52.08 Hz, (b) 2nd mode at 85.08 Hz, (c) 3rd mode at 130.71 Hz, (d) 4th mode at 156.43 Hz, (e) 5th mode at 178.84 Hz, (f) 6th mode at 223.47 Hz, (g) 7th mode at 262.84 Hz, (h) 8th mode at 298.48 Hz and (i) 9th mode at 327.21 Hz.....	124
Figure 7.11 Mode shapes for a free-free curved plate with the maximum rise of 20 mm for out-of-plane motion (a) 1st mode at 59.08 Hz, (b) 2nd mode at 102.75 Hz, (c) 3rd mode at 142.46 Hz, (d) 4th mode at 207.35 Hz, (e) 5th mode at 218.61 Hz, (f) 6th mode at 239.75 Hz, (g) 7th mode at 278.27 Hz, (h) 8th mode at 393.98 Hz and (i) 9th mode at 400.74 Hz.....	124








Figure 7.12 The MAC result between a flat plate and (a) a curved plate with 10 mm rise and (b) a curved plate with 20 mm rise	125
Figure 7.13 The relationship between related modes of plates; Top: a flat plate, Middle: a singly curved plate with a 1cm rise and Bottom: a singly curved plate with 2cm rise (— with ACLD treatment & no active control, --- with ACLD treatment & active control using control gain $\beta_{min,KE}$)	126
Figure 7.14 The relation between associated modes of plates with mode shapes for (a) 2nd mode, (b) 3rd mode and (c) 7th mode of a flat plate	127
Figure 8.1 Configuration of a plate with (1) ACLD treatment, (2) APCLD treatment, (3) AC/PCLD treatment and (4) AC/PSOLD treatment;  : elastic plate,  : viscoelastic layer and  : piezoelectric patch	130
Figure 8.2 The kinetic energy and absorbed power for a flat plate with ACLD treatment with control gains: (a) Change of the kinetic energy of a plate and (b) Change of absorbed power by an actuator	131
Figure 8.3 Control result for a flat plate with ACLD treatment (a) Magnitude and phase of point mobility; — no control; --- with control and (b) the Nyquist plot for a closed loop with the optimised control gain of 1667.5;  circle with negative effect on active control	131
Figure 8.4 The kinetic energy and absorbed power for a singly curved plate with a maximum rise of 10 mm with ACLD treatment with control gains: (a) Change of the kinetic energy of a plate and (b) Change of absorbed power by an actuator	134
Figure 8.5 The kinetic energy and absorbed power for a singly curved plate with a maximum rise of 20 mm with ACLD treatment with control gains: (a) Change of the kinetic energy of a plate and (b) Change of absorbed power by an actuator	134
Figure 8.6 Control result for a singly curved plate with a maximum rise of 10 mm with ACLD treatment (a) Magnitude and phase of point mobility; — no control; --- with control and (b) the Nyquist plot for closed loop with the optimised control gain of 1795.5	135

Figure 8.7 Control result for a singly curved plate with a maximum rise of 20 mm with ACLD treatment (a) Magnitude and phase of point mobility; — no control; --- with control and (b) the Nyquist plot for a closed loop with the optimised control gain of 1687.3.....	135
Figure 8.8 The change rate for mode shapes in a plate according to curvature for (a) 2nd peak, (b) 3rd peak and (c) 7th peak.....	136
Figure 8.9 The change of control gains according to the curvature (ACLD) ..	140
Figure 8.10 The changes of mobility in each case for (a) flat plates, (b) singly curved plates with 10mm rise and (c) singly curved plates with 20mm rise; — ACLD, - - - APCLD, - . - AC/PCLD and ----- AC/PSOLD	140
Figure 8.11 The changes of normalised mobility by control gain in each case for (a) flat plates, (b) singly curved plates with 10mm rise and (c) singly curved plates with 20mm rise; — ACLD, - - - APCLD, - . - AC/PCLD and ----- AC/PSOLD	140
Figure 8.12 Configuration of a plate with inverse AC/PCLD treatment;  : elastic plate and patch,  : viscoelastic layer and  : piezoelectric patch.....	145
Figure 8.13 Basic connection between accelerometer and electrical cables (a) attachment of accelerometer, (b) connection of electrical cables for ACLD, APCLD and AC/PSOLD treatments and (c) connection of electrical cables for AC/PCLD treatment	146
Figure 8.14 Shaker attachment for mechanical pseudo-random excitation for (a) ACLD, APCLD and AC/PSOLD treatments and (b) AC/PCLD treatment	147
Figure 8.15 Input signal connection for (a) pseudo-random PZT excitation with electrical signal and (b) pseudo-random mechanical excitation by a shaker	147
Figure 8.16 Schematic diagram of free-free curved plate control	147
Figure 8.17 (a) FRFs at the centre with a pseudo-random moment by a PZT actuator and (b) phases of FRFs at the centre with a pseudo-random moment by a PZT actuator; — without filter; - - - with a low-pass	

filter with a cut-off frequency of 500 Hz (ACLD treatment on a curved plate)	148
Figure 8.18 (a) FRF at the centre with a pseudo-random force by a shaker and (b) phase of FRF at the centre with a pseudo-random force by a shaker (ACLD treatment on a curved plate).....	149
Figure 8.19 (a) Nyquist plot for a closed loop without filter and (b) controlled result without filter (ACLD treatment).....	149
Figure 8.20 (a) Nyquist plot for a closed loop with a low-pass filter with a cut-off frequency of 500 Hz and (b) controlled result with a low-pass filter with a cut-off frequency of 500 Hz (ACLD treatment).....	150
Figure 8.21 (a) Nyquist plot for a closed loop with an ideal low-pass filter with a cut-off frequency of 500 Hz and (b) controlled result with an ideal low-pass filter with a cut-off frequency of 500 Hz (ACLD treatment).....	150
Figure A.1 FE beam element	161
Figure A.2 Geometry of a single axial element	162
Figure A.3 Geometry of a single bending element.....	162
Figure A.4 Example of basic global matrix structure	164
Figure A.5 2-D FE element	165
Figure A.6 Geometry of a single plate element.....	167
Figure A.7 Integration points and weight coefficients for 9-point Gauss integration for a 2-D element	170
Figure B.1 Forces and moments acting on a Euler beam element	171
Figure B.2 Stress distribution in a bent beam.....	172
Figure C.1 Change of receptances of a system under control (a) Displacement control, (b) Velocity control and (c) Acceleration control; — No control; - - - $\alpha, \beta, \gamma = 1$; - · - $\alpha, \beta, \gamma = 10$; - - - $\alpha, \beta, \gamma = 100$ [Label in x-axis: Frequency ratio (ω/ω_n), Label in y-axis: Receptance (dB ref. 1 N/m)]	176

Figure C.2 General 2-DOF system	177
Figure C.3 (a) Normalised displacement at mass m_1 for Case 1 (b) Normalised displacement at mass m_2 for Case 1; — No control; — $\beta = 1$; — $\beta = 150$; — $\beta = 300$	179
Figure C.4 (a) Normalised displacement at mass m_1 for Case 2 (b) Normalised displacement at mass m_2 for Case 2; — No control; — $\beta = 1$; — $\beta = 150$; — $\beta = 300$	179
Figure C.5 (a) Normalised displacement at mass m_1 for Case 3 (b) Normalised displacement at mass m_2 for Case 3; — No control; — $\beta = 1$; — $\beta = 150$; — $\beta = 300$	179
Figure C.6 (a) Normalised displacement at mass m_1 for Case 4 (b) Normalised displacement at mass m_2 for Case 4; — No control; — $\beta = 1$; — $\beta = 150$; — $\beta = 300$	180
Figure C.7 Control case for 4-element FE cantilever beam mode (a) Case 1 (Collocated), (b) Case 2 (Non-collocated), (c) Case 3 (Non-collocated) and (d) Case 4 (Collocated)	181
Figure C.8 (a) Displacement at the centre for Case 1 (b) Displacement at the tip for Case 1; — No control; — $\beta = 1$; — $\beta = 10$; — $\beta = 100$	182
Figure C.9 (a) Displacement at the centre for Case 2 (b) Displacement at the tip for Case 2; — No control; — $\beta = 1$; — $\beta = 10$; — $\beta = 100$	182
Figure C.10 (a) Displacement at the centre for Case 3 (b) Displacement at the tip for Case 3; — No control; — $\beta = 1$; — $\beta = 10$; — $\beta = 100$.	182
Figure C.11 (a) Displacement at the centre for Case 4 (b) Displacement at the tip for Case 4; — No control; — $\beta = 1$; — $\beta = 10$; — $\beta = 100$.	183
Figure C.12 Nyquist plots for an open loop for (a) Case 1, (b) Case 2, (c) Case 3 and (d) Case 4 with $\beta = 1$ up to 1 kHz	184
Figure C.13 (a) Displacement at the centre for Case 2 (b) Displacement at the tip for Case 2; — No control; — $\beta_{3dB} = 0.061$	185


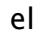

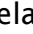

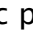



Figure C.14 (a) Displacement at the centre for Case 3 (b) Displacement at the tip for Case 3; — No control; - - $\beta_{3dB} = 0.061$	185
Figure C.15 Changes in kinetic energy of the whole structure for (a) Case 1 and (b) Case 4, and changes of absorbed power by an actuator for (c) Case 1 and (d) Case 4.....	186
Figure C.16 (a) Displacement at the centre for Case 1 (b) Displacement at the tip for Case 1; — No control; - - $\beta_{max. AP} = 59$	187
Figure C.17 (a) Displacement at the centre for Case 4 (b) Displacement at the tip for Case 4; — No control; - - $\beta_{min. KE} = 4.9$	188
Figure C.18 Phases for APCLD treatment on a beam with (a) No filter ($G_{3dB} = 24.58$), (b) a KEMO low-pass filter ($G_{3dB} = 167.61$) and (c) a proposed ideal filter ($G_{3dB} = 1240$); — No control; - - with control	188
Figure C.19 Phases for AC/PCLD treatment on a beam with (a) No filter ($G_{3dB} = 8.42$), (b) a KEMO low-pass filter ($G_{3dB} = 61.79$) and (c) a proposed ideal filter ($G_{3dB} = 8.42$); — No control; - - with control	188
Figure C.20 Phases results for AC/PSOLD treatment on a beam with (a) No filter ($G_{3dB} = 4.79$), (b) a KEMO low-pass filter ($G_{3dB} = 69.77$) and (c) a proposed ideal filter ($G_{3dB} = 1302$); — No control; - - with control.....	189
Figure C.21 Phase simulation results with a proposed ideal filter and G_{3dB} for (a) ACLD, (b) APCLD, (c) AC/PCLD and (d) AC/PSOLD treatments	189
Figure D.1 Configuration of a plate with APCLD treatment;  : elastic plate,  : viscoelastic layer and  : piezoelectric patch	191
Figure D.2 Configuration of a plate with AC/PCLD treatment;  : elastic plate,  : viscoelastic layer and  : piezoelectric patch	196
Figure D.3 Configuration of a plate with AC/PSOLD treatment;  : elastic plate,  : viscoelastic layer and  : piezoelectric patch	199
Figure E.1 The kinetic energy and absorbed power for a flat plate with APCLD treatment with control gains: (a) Change of the kinetic energy of a plate and (b) Change of absorbed power by an actuator	203

Figure E.2 Control result for a flat plate with APCLD treatment (a) Magnitude and phase of point mobility; — no control; --- with control and (b) the Nyquist plot for a closed loop with the optimised control gain of 814.7	203
Figure E.3 The kinetic energy and absorbed power for a flat plate with AC/PCLD treatment with control gains: (a) Change in the kinetic energy of a plate and (b) Change of absorbed power by an actuator	204
Figure E.4 Control result for a flat plate with AC/PCLD treatment (a) Magnitude and phase of point mobility; — no control; --- with control and (b) the Nyquist plot for a closed loop with the optimised control gain of 192.7	204
Figure E.5 The kinetic energy and absorbed power for a flat plate with AC/PSOLD treatment with control gains: (a) Change in the kinetic energy of a plate and (b) Change in the absorbed power by an actuator	204
Figure E.6 Control result for a flat plate with AC/PSOLD treatment (a) Magnitude and phase of point mobility; — no control; --- with control and (b) the Nyquist plot for a closed loop with the optimised control gain of 196.8	205
Figure E.7 The kinetic energy and absorbed power for a singly curved plate with a maximum rise of 10 mm with APCLD treatment with control gains: (a) Change of the kinetic energy of a plate and (b) Change of absorbed power by an actuator	205
Figure E.8 Control result for a singly curved plate with a maximum rise of 10 mm with APCLD treatment (a) Magnitude and phase of point mobility; — no control; --- with control and (b) the Nyquist plot for a closed loop with the optimised control gain of 670.9; ○ circle with negative effect on active control	206
Figure E.9 The kinetic energy and absorbed power for a singly curved plate with a maximum rise of 20 mm with APCLD treatment with control gains: (a) Change of the kinetic energy of a plate and (b) Change of absorbed power by an actuator	206

Figure E.10 Control result for a singly curved plate with a maximum rise of 20 mm with APCLD treatment (a) Magnitude and phase of point mobility; — no control; --- with control and (b) the Nyquist plot for a closed loop with the optimised control gain of 720.7	206
Figure E.11 The kinetic energy and absorbed power for a singly curved plate with a maximum rise of 10 mm with AC/PCLD treatment with control gains: (a) Change in the kinetic energy of a plate and (b) Change in absorbed power by an actuator.....	207
Figure E.12 Control gains for an unstable result obtained from kinetic energy and absorbed power for a singly curved plate with a maximum rise of 10 mm with AC/PCLD treatment with the change in control gain: (a) Change in the kinetic energy of a plate and (b) Change in absorbed power by an actuator	207
Figure E.13 Control result for a singly curved plate with a maximum rise of 10 mm with AC/PCLD treatment (a) Magnitude and phase of point mobility; — no control; --- with control and (b) the Nyquist plot for a closed loop with the optimised control gain of 41.7; ○ circle with negative effect on active control.....	207
Figure E.14 The kinetic energy and absorbed power for a singly curved plate with a maximum rise of 20 mm with AC/PCLD treatment with control gains: (a) Change in the kinetic energy of a plate and (b) Change in absorbed power by an actuator.....	208
Figure E.15 Control result for a singly curved plate with a maximum rise of 20 mm with AC/PCLD treatment (a) Magnitude and phase of point mobility; — no control; --- with control and (b) the Nyquist plot for a closed loop with the optimised control gain of 137.4	208
Figure E.16 The kinetic energy and absorbed power for a singly curved plate with a maximum rise of 10 mm with AC/PSOLD treatment with control gains: (a) Change in the kinetic energy of a plate and (b) Change in absorbed power by an actuator.....	208
Figure E.17 Control result for a singly curved plate with a maximum rise of 10 mm with AC/PSOLD treatment (a) Magnitude and phase of point	

mobility; — no control; --- with control and (b) the Nyquist plot for a closed loop with the optimised control gain of 161.2	209
Figure E.18 The kinetic energy and absorbed power for a singly curved plate with a maximum rise of 20 mm with AC/PSOLD treatment with control gains: (a) Change in the kinetic energy of a plate and (b) Change in absorbed power by an actuator	209
Figure E.19 Control result for a singly curved plate with a maximum rise of 20 mm with AC/PSOLD treatment (a) Magnitude and phase of point mobility; — no control; --- with control and (b) the Nyquist plot for a closed loop with the optimised control gain of 151.7	209
Figure E.20 FRFs of curved plated with HAPCLD treatments in impact hammer test; — without damping treatment; --- with damping treatment (a) ACLD treatment, (b) APCLD treatment, (c) AC/PCLD treatment, (d) AC/PSOLD treatment and (e) inverse AC/PCLD treatment	210
Figure E.21 (a) Nyquist plot for a closed loop without a filter and (b) controlled result without a filter (APCLD treatment, $G_{3dB} = 382.3789$)	211
Figure E.22 (a) Nyquist plot for a closed loop with a low-pass filter with a cut-off frequency of 500 Hz and (b) controlled result with a low-pass filter with a cut-off frequency of 500 Hz (APCLD treatment, $G_{3dB} = 22.2564$)	211
Figure E.23 (a) Nyquist plot for a closed loop with an ideal low-pass filter with a cut-off frequency of 500 Hz and (b) controlled result with an ideal low-pass filter with a cut-off frequency of 500 Hz (APCLD treatment, $G_{3dB} = 943.4783$)	211
Figure E.24 (a) Nyquist plot for a closed loop without a filter and (b) controlled result without a filter (AC/PCLD treatment, $G_{3dB} = 218.8235$)	212
Figure E.25 (a) Nyquist plot for a closed loop with a low-pass filter with a cut-off frequency of 500 Hz and (b) controlled result with a low-pass filter with a cut-off frequency of 500 Hz (AC/PCLD treatment, $G_{3dB} = 4,4233$)	212

Figure E.26 (a) Nyquist plot for a closed loop with an ideal low-pass filter with a cut-off frequency of 500 Hz and (b) controlled result with an ideal low-pass filter with a cut-off frequency of 500 Hz (AC/PCLD treatment, $G_{3dB} = 206.6667$).....	212
Figure E.27 (a) Nyquist plot for a closed loop without a filter and (b) controlled result without a filter (AC/PSOLD treatment, $G_{3dB} = 175.4717$).....	213
Figure E.28 (a) Nyquist plot for a closed loop with a low-pass filter with a cut-off frequency of 500 Hz and (b) controlled result with a low-pass filter with a cut-off frequency of 500 Hz (AC/PSOLD treatment, $G_{3dB} = 5.3278$).....	213
Figure E.29 (a) Nyquist plot for a closed loop with an ideal low-pass filter with a cut-off frequency of 500 Hz and (b) controlled result with an ideal low-pass filter with a cut-off frequency of 500 Hz (AC/PSOLD treatment, $G_{3dB} = 160.7407$).....	213

List of Accompanying Materials

DECLARATION OF AUTHORSHIP

I, Byungjun Koh

declare that the thesis entitled

HYBRID ACTIVE-PASSIVE CONSTRAINED LAYER DAMPING TREATMENTS IN BEAMS, PLATES AND SHELLS

and the work presented in the thesis are both my own, and have been generated by me as the result of my own original research. I confirm that:

- this work was done wholly or mainly while in candidature for a research degree at this University;
- where any part of this thesis has previously been submitted for a degree or any other qualification at this University or any other institution, this has been clearly stated;
- where I have consulted the published work of others, this is always clearly attributed;
- where I have quoted from the work of others, the source is always given. With the exception of such quotations, this thesis is entirely my own work;
- I have acknowledged all main sources of help;
- where the thesis is based on work done by myself jointly with others, I have made clear exactly what was done by others and what I have contributed myself;
- parts of this work have been published as:
B. Koh, E. Rustighi, B. Mace and M. Amabili, Numerical and experimental assessment of hybrid active-passive damping treatments, The proceedings of ISMA2012 (2012), Katholieke Universiteit Leuven, Belgium

Signed:

Date:.....

Acknowledgements

Most of all, I would like to dedicate this thesis to my father, the greatest supporter of my research career. My inherent thirst for life-lasting learning something new is inherited from you, and your words about self-development in your life have encouraged me not to settle for the present. I strongly hope that this thesis can be the touchstone for my stepping forward to our aim of life and console you as a small reward for your invaluable sacrifice.

Moreover, I would like to send deep appreciation to my family; mother, elder sisters, brothers-in-law, nieces and nephews, for your belief and support on what I have done. Without them, I could not reach this moment at all. I want to ask your changeless minds toward me for the rest of my life.

I also want to send my gratefulness and respect to my supervisors; Dr. Emiliano Rustighi, Prof. Brian Mace, Dr. Tim Waters and Prof. Mike Brennan, for your endless patience and effort in spite of my immaturity in research. I have learnt so much from your enthusiasm and attitude for research and study.

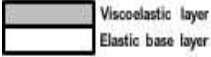
I would like to thank my invaluable friends I had met during my study in Southampton. Our relation and sharing time made my memory in Southampton brilliant and unforgettable. And, I could learn many things from my experiences with you. All DG family of mine, you will be missed and I am keen to meet you sooner or later as honourable ISVR alumni. All members of the Korean Southampton Society, you also will be appreciated for your care and help. Without you, my life in Southampton might have been as dry as in a desert. And, other friends I have met and shared our time with in the UK, you will be remembered in mind with great thankfulness for your allowance for our friendship. And, all my friends in South Korea, thank you for your time and support you have shown when we met in South Korea during my annual breaks for refreshment. Especially, my soul mate, as you described (laugh), although there have been many things happened between us so far, I wish that our relation will be helpful for each other's development and achievement later on as it has been and we agreed.

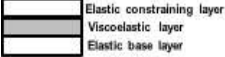
Finally, thank God. I finally did it with your blessing.

Definitions and Abbreviations

PC: Passive Control

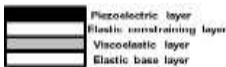
AC: Active Control

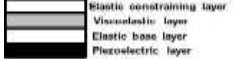
PULD: Passive Unconstrained Layer Damping 

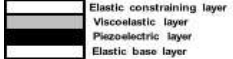
PCLD: Passive Constrained Layer Damping 

HAPCLD: Hybrid Active-Passive Constrained Layer Damping

ACLD: Active Constrained Layer Damping 

APCLD: Active Passive Constrained Layer Damping 

AC/PCLD: Active Control/Passive Constrained Layer Damping 

AC/PSOLD: Active Control/Passive Stand-Off Layer Damping 

LQR: Linear Quadratic Regulator

GHM Method: Golla-Hughes-McTavish Method

ADF Model: Anelastic Displacement Fields Model

LQG: Linear-Quadratic Gaussian

FE: Finite Element

DOF: Degree Of Freedom

HSDT: Higher-order Shear Deformation Theory

FSDT: First-order Shear Deformation Theory

ESL: Equivalent Single Layer

FRF: Frequency Response Function

FFT: Fast Fourier Transform

IFFT: Inverse Fast Fourier Transform

MAC: Modal Assurance Criterion

1 INTRODUCTION

1.1 Background and motivations

In order to reduce the vibration of mechanical structures effectively, Passive Control (PC) has been used traditionally. For example, in the case of PC by structural modification, equivalent mass or stiffness of a whole structure can be changed by adding extra masses to the original structures for mass modification, and springs or stiffeners for stiffness modification respectively. However, although this kind of structural modification can have an effect at a specific target frequency as well as other frequencies in the aspect of modal mass and stiffness, the most dominant effect is expected at the target frequency. This method is usually applied to the system under the excitation at one specific frequency, which matches natural frequencies of the system in each degree of freedom. The resultant natural frequency of the structure is moved away from the primary exciting frequency of the vibration sources (such as engines, motors and so forth). However, when there are other excitation components at different frequencies which can match adjusted resonance frequencies of the system, the structural modification can cause a resonance problem at other frequencies. Therefore, the structural modification with extra mass and stiffness as an example of PC is effective for a system with vibration sources of single operation frequency. As an example, this structural modification is used as a primary measure to void the resonance of main equipment with normal operation frequencies of main engine and propulsive blades. After checking the resonance frequencies of local areas including equipment, foundation and supporting structure, structural modification is performed to move overlapped resonance frequency to 10% higher than operating frequencies. In order to control vibration caused by broadband or variable frequency sources with this kind of method, the same number of structural modification methods as the one for target frequencies should be applied. Moreover, since resonance peaks remain sharp although shifted, shifted resonance frequencies can cause resonance problems with other operation frequencies as mentioned above.

The addition of more damping is another PC technique, which allows vibration reduction by reduction of the resonance peaks. Additional damping is effective and preferable especially in the high frequency range, where overall average vibration energy distribution is important rather than concentrated energy at each mode. While the increase of mass or stiffness results in the change of resonance frequency to avoid the coincidence between the resonance frequency of a system and the exciting frequency of the disturbance, the increase in damping results in the reduction of modal peaks in vibration. Therefore, the addition of more damping is preferred in vibration control with broadband excitation mainly applied in frequency range where initial

1. INTRODUCTION

damping, mainly structural damping, is relatively smaller than added damping [1]. However, in order to achieve enough reduction with adding damping, when viscoelastic materials are used for this purpose, a treated structure has a tendency to have greater energy dissipation in a higher frequency range than in a lower frequency range due to the dynamic characteristics of structure. Since a certain ratio of energy dissipation by damping occurs in one cycle of motion and the total amount of vibration reduction increases through the repetition of this cycle, more damping leading the increase of mass for larger reduction in one cycle of motion is mandatory in lower frequency range. As an example of this approach, a Passive Unconstrained Layer Damping (PULD) treatment consists of a viscoelastic layer attached to a base structure without any kind of constraining layer on it, as shown in Figure 1.1 (a). Despite this, a substantial increase in weight is needed to achieve significant vibration reduction, which affects general motion of structures, especially in the low frequency range.

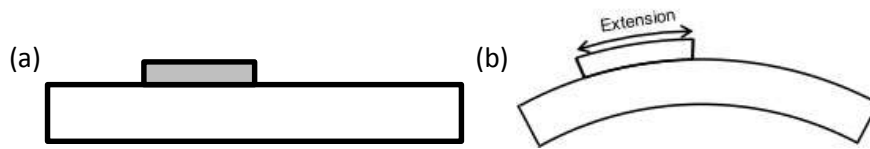




Figure 1.1 (a) Concepts of PULD;  : elastic beam and patch and  : viscoelastic layer and (b) Bending of motion in PULD

Passive Constrained Layer Damping (PCLD) treatment consists of a viscoelastic layer between two elastic constraining layers, one of which is a base structure [2], as shown in Figure 1.2. (a). This was introduced to maximise the effects of the viscoelastic layer in increasing the damping and stiffness of the structures limiting weight addition at the same time [3, 4]. Since the bending stiffness of a structure increases according to the distances of face layers from the neutral axis or plane of the whole structure, a structure with a constraining layer has increased bending stiffness according to the increasing distance of a constraining layer from the neutral axis of a base structure. Weight increase by adding the constraining layer within PULD treatment is smaller than weight increase by the thickness increase of the original base structure despite the same increase in bending stiffness. In addition, PCLD treatment can give more damping than a simple application of PULD treatment. Energy is dissipated only by extensional motion in an unconstrained viscoelastic material attached to a base structure in PULD treatment as described in Figure 1.1 (b). On the other hand, energy is dissipated by extensional motion as well as shear deformation of viscoelastic material, which is caused by an elastic constraining layer attached to viscoelastic material and leading the increase of viscous friction in viscoelastic layer, in PCLD treatment [1, 5]. Moreover, since the increase of damping in PULD treatment is caused by larger extension of viscoelastic layer, viscoelastic layer should locate as far from the neutral axis of structure, which is considered as the reference line for axial (beams) or in-plane (plates) exten-

1. INTRODUCTION

sion in bending, as possible to obtain more damping [1]. Otherwise, since transverse shear stress, which is the greatest at the neutral axis and zero at the outer surface, is used in PCLD treatment to increase damping, it can give enough damping with thin structure or even inside structure [1]. This PCLD treatment easily can be found in various industrial areas, e.g. shipbuilding industry as sound and vibration reduction measures for floors as given in Figure 1.3.

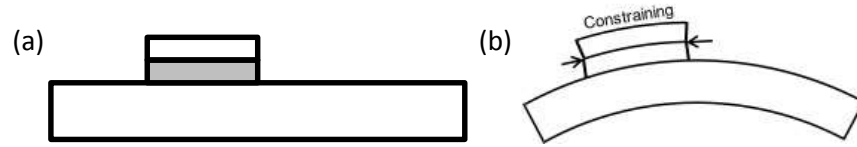



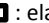
Figure 1.2 (a) Concepts of PCLD;  : elastic beam and patch and  : viscoelastic layer and (b) Bending of motion in PCLD



Figure 1.3 Examples of PCLD treatment application in industry [www.dae-hyup.com/en_product_02_18.html]

All passive controls have some disadvantages such as a significant increase in weight for large vibration reduction in the low frequency range. Therefore, Active Control (AC) was introduced from the need for a lighter but still efficient method for vibration reduction in the low frequency range [3, 4]. Brief concepts of PC and AC are shown in Figure 1.4. Figure 1.4 (b) explains the control concept of the feedback control as an example of AC. As shown in Figure 1.4 (b), control force/moment is applied to the system to reduce the motion, i.e. vibration according to the reference signal, which is determined by measurement of displacement, velocity or acceleration, in AC. The effect of each measured signal in AC was studied in Appendix C.

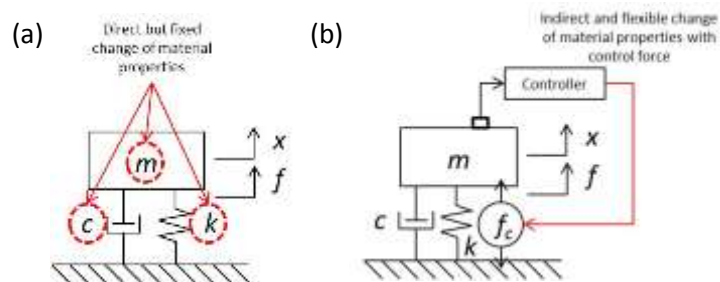


Figure 1.4 Concepts of control methods (a) Passive control (b) Active control

1. INTRODUCTION

Therefore, for PC and PCLD treatment, since vibration reduction completely relies on the changes of equivalent material properties in a system due to the application of treatment as described in Figure 1.4 (a), the response of treated structures cannot easily be adjusted in operation according to users' requirements. On the other hand, if AC is in use, target frequencies and target modes can be changed according to requirements and situations by changing the set-up of the controller. Moreover, an improvement of control performance can be achieved by the change of control gain without the increase of weight in AC.

However, there are also limits related to the application of AC for vibration reduction. Most of all, the application of AC is mainly limited to a low frequency range, where the distinction between each mode is clear. This condition is necessary for a more effective and efficient control in terms of control effort. Due to this, high frequency components contained in a real-time signal are generally truncated for better control performance. This kind of signal process results in instability problems, so called higher frequency spill-over effects, which are liable to degrade (control spill-over: actuators give undesirable effects on uncontrolled modes) or even destabilise (observation spill-over: sensors detect the deflection of uncontrolled modes) the response of the closed-loop system, especially when active feedback control is implemented [6, 7].

In order to achieve a more efficient and better control system, the hybrid active-passive constrained layer damping (HAPCLD) treatment has been introduced by combining the advantages of AC and PCLD treatment, which showed better control performance than a conventional PC. The objective of this configuration is to obtain better control performance in broadband frequency range by adding control performance of AC in a low frequency range to control performance of PC in a high frequency range. Generally, a piezoelectric actuator replaces the elastic constraining layer of PCLD treatment for AC as the simplest configuration of HAPCLD treatment, called Active Constrained Layer Damping (ACL D) treatment. Some researchers included a piezoelectric sensor in its configuration for the collocation of the sensor and actuator.

1.2 Objectives of the thesis

HAPCLD treatments can be categorised into four types according to the type of layers and lamination order used in the configurations: (1) ACLD treatment, (2) Active Passive Constrained Layer Damping (APCLD) treatment, (3) Active Control/Passive Constrained Layer Damping (AC/PCLD) treatment and (4) Active Control/Passive Stand-Off Layer Damping (AC/PSOLD) treatment respectively [3]. For a detailed description of the configuration and literature review, please refer to Figure 2.9 in Section 2.1. Although another configuration called

Enhanced ACLD treatment was given in [3], this can be categorised as a kind of ACLD treatment and will not be considered in this thesis. The main reason for exclusion of Enhanced ACLD treatment is based on the related literature review and will be explained in Chapter 2.

The review and assessment of four different types of HAPCLD treatment on beams were conducted in [3]. However, a parameter study related to the thickness of viscoelastic layers and the length of HAPCLD treatment was performed only for beams with numerical analysis using FE models. A need for experimental assessment remains.

The applicability of the four types of HAPCLD treatment to more complex structures such as flat and curved plates still has to be studied. Moreover, the assessment results for beams in [3] should be checked for applicability to flat and curved plates as well. Therefore, four types of HAPCLD treatment need to be applied to flat and curved plates to check if the same result for beams can be obtained for flat and curved plates as well. In vibration control for flat and curved plates, additional in-plane, bending and twisting motions related to the y-axis have to be considered.

In the aspect of numerical modelling, there are many studies on laminated structures with PCLD or ACLD treatments (see Chapter 2 for a detailed literature review). However, individual equations of motions for displacement terms in each layer have been used in these studies. With this kind of approach, if more complex configurations than PCLD and ACLD treatments are used, their applicability is not guaranteed. Therefore, based on previous studies for viscoelastic materials and laminated structures with viscoelastic layers, some new coupling methods to combine each layer as one equivalent structure could be studied, which can guarantee applicability of coupling theory.

The aims of this thesis are to further the numerical modelling of smart viscoelastic layered structures and increase understanding of applicability of HAPCLD treatments to beams, flat and curved plates.

When considering the remaining research topics mentioned above, objectives of the thesis can be established.

1. To examine the previous results of assessment and conclusions about various HAPCLD treatments obtained only through simulation with a cantilever beam by a control algorithm called LQR through simulations as well as experiments using real cantilever beams with four different HAPCLD treatments. Different variables such as dimensions of structures and treatments, control algorithm, etc. are used in this study to check the versatility of configurations of HAPCLD treatment with different control circumstances.

1. INTRODUCTION

2. To derive Equivalent FE models used for active control by newly established coupling methods from a layer-wise approach. In this modelling, analysis of motion for 1-D laminated structures with viscoelastic and piezoelectric layers will be included. Moreover, active control including optimal and stable controller design using the kinetic energy of a whole structure, the absorbed power by controllers and the Nyquist plot for a controller's open-loop will be studied for active control.
3. To develop FE modelling and analysis for 2-D laminated structures, i.e. flat and curved plates. Although modelling and analysis can be conducted by using commercial numerical analysis programs such as ANSYS, PATRAN/NASTRAN and so on, better understanding of motions of structures, the mutual relationship between local degree-of-freedom of each layer and dynamic characteristics of viscoelastic materials in time or frequency domain is expected by studying related theories, establishing numerical models and analysing motions of structure with or without active control. In order to derive FE dynamic stiffness matrices for each layer of configurations, understanding about equations of motions of structures should precede. In addition to this, behavioural characteristics of a viscoelastic layer constrained between two elastic layers and mutual relationships between each layer should be understood. The establishment of numerical FE models including piezoelectric and viscoelastic layers, which can be used more easily for laminated structures, will be an aim. Instead of deriving individual equations of motion for a whole structure according to the change of configurations, general equations of motion for each layer will be derived considering their material properties. They will be combined as an equation of motion for the equivalent structure by introducing a coupling matrix.
4. To ascertain whether the same conclusions on beam control with four different HAPCLD treatments can be obtained for flat and curved plates. Simulations using newly established numerical models and experiments with five curved plates with different configurations of HAPCLD treatments will be developed.

1.3 Contributions of the thesis

According to the objectives of the thesis explained in the previous section, the following contributions of the thesis were achieved.

1. A new numerical modelling method was established by introducing coupling matrices based on a layer-wise theory to combine the separate FE mass and stiffness matrices of

each layer. In this modelling, individual mass and stiffness matrices of base, viscoelastic, piezoelectric and elastic constraining layers were composed without deriving equations of motion for the whole structure considering mutual motions of neutral axes in each layer. Coupling matrices were derived instead by considering mutual motions between neutral axes in each layer. After stacking individual mass and stiffness matrices of each layer according to the order of lamination, coupling matrices and their transverse matrices were multiplied to laminated mass and stiffness matrices to derive equivalent mass and stiffness matrices for the whole structure. This modelling method is more useful for expanding the application to more complex configurations relatively easily than other previous methods. This modelling method was validated by experiments using real structures.

2. Effectiveness of HAPCLD treatments in differently laminated configurations was verified with a velocity feedback control algorithm on a beam through simulation and experiment. In [2], Trindade and Benjeddou made a choice for a specific system configuration and a control algorithm, LQR, for ease of comparison. Therefore, their conclusion should be validated to be applicable to different cases to show the versatility of the HAPCLD treatments used in [2]. Moreover, since the conclusion was obtained only with simulation based on a parameter study, it needed to be validated through related experiments.
3. More complex configurations of HAPCLD treatments than ACLD treatment including constraining elastic, piezoelectric and viscoelastic layers were applied for the first time to flat and curved plates. Although ACLD treatment has been used for active control of flat plates, curved plates or shells including radiated noise control in the inner cavity of structures, the application of more complex configurations had not yet been found, in spite of their better vibration reduction performance. As a conclusion to simulation with established FE models using a new numerical modelling method and experiment, AC/PSOLD treatment can provide the largest reduction of local vibration of all cases. Furthermore, active control with this configuration is stable and more robust in various cases than ACLD treatment, which was studied to provide more stable control results than conventional AC especially in a high frequency range according to previous studies.
4. An improved method of stability in active control was proposed considering the phase shift by filters such as low-pass filters. When any kind of filter is used to limit the frequency range of an input signal, phase shift occurs in the filtered signal. Due to this phase shift, there is a possibility that the input signal for a controller becomes unstable, though it was in a stable region before filtering. Therefore, the method for compensating the effect of phase shift in real-time active control in a broadband frequency range was discussed. Additionally, for more stable active control, the relationship between the stability of active

1. INTRODUCTION

control and mode shapes of structures was studied. When shakers are used as actuators in active control, stable active control can be guaranteed with collocated sensors and actuators according to the location, the relation between input and target signals and so forth. However, if piezoelectric actuators are used, since they usually occupy broader space than shakers, they apply a distributed control force or moment along edges. Since these forces and moments have bilateral symmetry, the relationship between the dynamics of a PZT actuator and mode shapes of a base structure can have a greater influence on active control. Thus, the symmetry of moment generated by a rectangular piezoelectric actuator should be considered in relation to the change of mode shapes around the location of the actuator to guarantee stable control.

1.4 Structure of the thesis

Chapter 2 presents the literature review results relating to the main research topics of the thesis. The chapter is divided into three sections. The first section is about the active control methods using constrained layer damping treatments, mainly ACLD treatment, and a study of their configurations. Another is related to the numerical modelling method, mainly the Finite Element Method (FEM), for beams and plates (flat and curved plates). The other relates to recently published research results of FE modelling for laminated structures. According to the summary and review of previous research, research direction will be given.

Chapter 3 focuses on the establishment of 1-D numerical modelling for laminated beams using the FE method. FE mass and stiffness matrices for elastic base beams, viscoelastic, piezoelectric and elastic constraining layers are derived. Elastic base beams, piezoelectric and elastic constraining layers are assumed as Euler beams, while the viscoelastic layer is assumed to be a Timoshenko beam considering first-order shear deformation using the GHM method. According to the mutual relationships of displacements for each layer, coupling matrices are derived for different configurations of HAPCLD treatment based on a layer-wise theory. In this procedure, FE modelling for laminated beams, which is mentioned as the first contribution, is used.

Chapter 4 is related to the validation of FE 1-D models established in Chapter 3 with experimental measurement results. At first, an untreated beam and a beam with PCLD treatment were validated by comparison with impact hammer test results. After that, beams for experiments were fabricated with four different HAPCLD treatments. Using these four beams, measurements of FRFs in two cases of pseudo-random moment excitation with PZT actuators and pseudo-random force excitation with shakers were conducted. By comparison with simulation results

and measured data, the validation of established FE 1-D models was performed. Through this validation, the usability of established FE beam models in Chapter 3 and the first contribution related to beams are confirmed.

Chapter 5 discusses active control with HAPCLD treatments of beams based on simulation and measured data obtained in the previous chapters. The effects of phase shift on active control by a low-pass filter used to limit the range of control frequency up to 3rd mode as done in [3] are discussed, and the compensation method of the phase shift is studied by introducing extra filters. Finally, control results in [3] are assessed with active control results with the proposed filtering method. With these analyses and experiments, the second and forth contributions related to a stability improvement method for active control using a filter for this thesis mentioned in the previous section are achieved. For the second contribution, simple velocity feedback control is used instead of LQR.

Chapter 6 focuses on the establishment of 2-D numerical modelling for laminated flat plates using an FE method to expand the application of HAPCLD treatments discussed in the previous chapters. As was done for 1-D structures in Chapter 3, mass and stiffness matrices for each layer are derived individually, and converted into an equivalent mass and stiffness matrices by multiplying coupling matrices. Base plates, piezoelectric and elastic constraining layers are assumed to be Kirchhoff plates ignoring shear deformations, while viscoelastic layers are assumed to be Mindlin plates considering first-order shear deformation using the GHM method. Simulation results using established FE flat plate models will be validated by experimental results.

Chapter 7 consists of FE modelling and its validation for laminated curved plates, which is mentioned as the first contribution, and study of curvature's contribution on mode shapes. Based on coordinate transfer between a flat and curved plate, FE flat plate models can be changed to FE curved plate models. Using FE flat and curved plate models, the change of mode shapes due to the curvature will be studied.

Chapter 8 is related to the validation of 2-D FE models established in Chapter 6 and 7 and analysis of active control with HAPCLD treatments of flat and curved plates using the numerical models and measured data considering mode shapes of structures. Simulation results for active control are analysed based on the changes of mode shapes, and the effects of the changes of mode shapes on active control are discussed. With the filtering method proposed in Chapter 5, active control results, using measured FRFs of curved plates with various HAPCLD treatments, are compared, and final conclusions are derived. In this chapter, the third contribution is achieved and the forth contributions related to the relationship between active control and mode shapes are studied.

1. INTRODUCTION

Chapter 9 includes the summary and conclusions of the results of study conducted in the thesis. Moreover, future works are proposed for further study.

2 LITERATURE REVIEW

In this chapter, previous studies which have been conducted into active and passive controls using constrained layer damping treatments, and related numerical modelling will be reviewed. Firstly, previous studies about passive and active controls using constrained layer damping treatments will be reviewed. As a result of review, successive studies by one researcher have a tendency to add more variables to their research models with the same configuration. The review of numerical modelling methods related to constrained layer damping treatments will follow. This review will include viscoelastic material modelling methods, and the literature review of state-of-the-art FE formulation of laminated structures, mainly focusing on recently published journal papers, will follow.

2.1 Passive and active controls with constrained layer damping treatment

Conventional AC, which mainly is conducted at distinctive modes in low frequency range, can have limits in control performance as mentioned in Section 1.1 due to instability caused by the spill-over effect with the truncation of high frequency components for the efficiency of control. Various control methods have been proposed to obtain better and more robust controls. The method most obviously related to this work, the combination of PCLD treatment and AC was firstly proposed by Plump and Hubbard in 1986 and named ACLD treatment [4]. Plump and Hubbard replaced the cover layer of PCLD treatment with a piezoelectric material which acts as an actuator in AC. Therefore, this configuration has advantages for both AC and PCLD treatment at the same time and a more efficient control can be achieved. PCLD treatment has a limited efficient range of application which depends on frequency and temperature. Sufficient vibration reduction due to the increase of damping caused by the frequency response of viscoelastic materials is mainly guaranteed in a mid (transition region) and high frequency range. On the other hand, AC has a poor performance at high frequencies, where no individual mode dominates response of system, and good performance in low frequency range, where responses of system are dominated by individual modes on resonance frequencies [8]. High frequency components are truncated in AC to increase efficiency of control. Therefore, Plump and Hubbard proposed to combine AC and PCLD treatments for more efficient control results in the low frequency range as well as in the high frequency range. Low frequency components are controlled by a PZT actuator, and mid and high frequency components are reduced by passive damping of

2. LITERATURE REVIEW

a constrained viscoelastic layer.

ACLD treatment gained widespread recognition through the publications by Baz in the early 1990s [4]. He proposed an optimum design for its control [9]. In the paper, the obtained results emphasize the potential of the optimally designed ACLD treatment as an effective means for providing broadband attenuation capabilities over a wide range of operating temperatures as compared to PCLD treatments. Since the mechanical properties of viscoelastic material can vary from the rubbery (soft) region to the glassy (stiff) region and vice versa according to the change of temperature and frequency [10], control effect of PCLD treatments can be affected by it. However, the ACLD treatment proposed in [9] showed better control results than PCLD treatment in spite of the change of mechanical properties in viscoelastic materials. When considering the change of real viscoelastic material properties at a fixed frequency given in Figure 2.1 [9], the performance of ACLD can be less affected by the change of temperature due to the heat generated by a piezoelectric actuator with the proper selection of viscoelastic material. Based on this reason, the most of studies regarding HAPCLD treatment using piezoelectric materials as an actuator and viscoelastic layers as additional damping have not considered the change of mechanical properties in viscoelastic layers significantly. Even in experiment to extract the parameters for viscoelastic material models, those at a specific temperature were extracted from measured data [11].

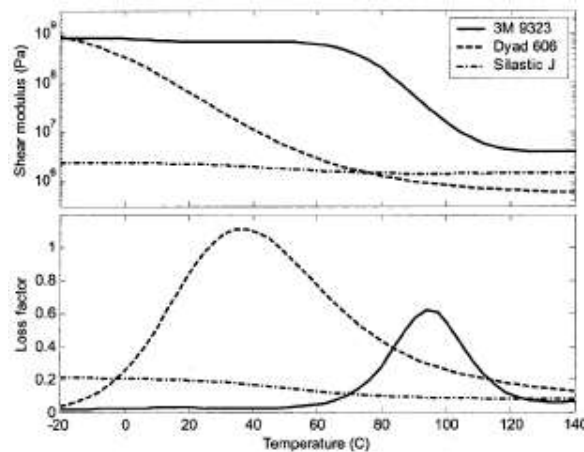


Figure 2.1 The changes of shear modulus and loss factor versus temperature at 100 Hz of epoxy adhesive ('3M' 9323), typical damping material ('Dyad' 606) and silicone elastomer ('Silastic' J) [9]

He used the model described in Figure 2.2. Piezoelectric patches were used as an actuator as well as a sensor, located in the same position. By using this kind of configuration, some possible problems in active control such as duality (mismatch between error signal and control force, e.g. displacement and moment) and collocation (mismatch of location between disturbance, error signal measurement and control points) could be avoided. Moreover, Baz used a similar configuration of ACLD treatment to the one in Figure 2.2 for boundary control of a cantilever beam [12, 13]. He extended the length of ACLD treatment including the piezoelectric sensor to the

length of the base beam to cover the whole beam with ACLD treatment, and he derived the equation for an equivalent beam with the assumption treating a piezoelectric sensor and a base beam as one structure. This resembles the same configuration as the sandwich beam with a viscoelastic core given in [2], to compare compliances of PCLD and ACLD treatments. However, in this case, there is a limit in that the length of the sensor and base beam should be same.

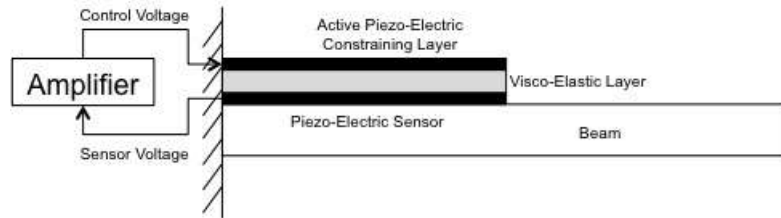





Figure 2.2 Schematic drawing of the ACLD treatment by Baz and Ro [9];  : elastic beam,  : viscoelastic layer and  : piezoelectric patch

The application of ACLD treatment was expanded to different types of structure such as rotating beams [14], plates [15] and thin cylindrical shells [16] (See figure 2.3 and 2.4). In [14], the study for rotating beams demonstrated the applicability of ACLD treatment to vibration control of helicopter rotor blades. (This work was funded by the US Army Research Office (Grant number DAAH-04-93-G-0202) [14].) Configuration of ACLD treatment was the same as in Figure 2.2, and the blade deflection due to rotation, which is dominant at an operation frequency, was used as an input signal for the controller. Furthermore, studies related to flat plates in [15] and thin cylindrical shells in [16] showed the possibility of ACLD treatment application to more complex structures than beams such as flat and curved plates. In [15], applied ACLD treatments are attached on both sides of the plate forming a symmetric configuration for the neutral plane of the base plate, as shown in Figure 2.3, with the same length of plate, but different width to control the free-end deflection of a cantilever structure at the centre line. Moreover, a polyvinylidene fluoride (PVDF), which is generally used in the form of film rather than a solid type, is used as a piezoelectric actuator [15]. This inspired the use of various piezoelectric materials as actuators for HAPCLD treatment, although it remains uncertain if a PVDF film can give a large constraining PCLD treatment effect as a conventional solid type piezoelectric actuator. In [16], two ACLD treatments with no piezoelectric sensors are attached inside a pipe as shown in Figure 2.4. Using this configuration, vibrations at the first two modes of shell were controlled comparing control results with PCLD treatment. As mentioned in [16], this study was implemented as a basic study for radiated noise control in the inner cavity of a shell, which was related to Ray's later studies.

2. LITERATURE REVIEW

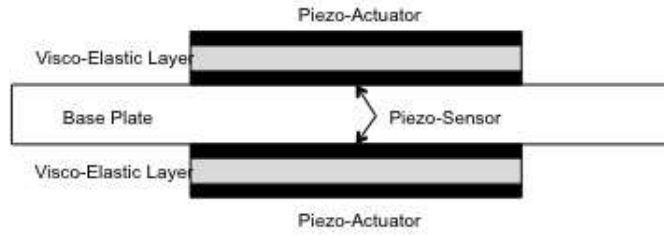





Figure 2.3 Finite element model of a plate treated with ACLD treatment by Baz and Ro [15];  : elastic plate,  : viscoelastic layer and  : piezoelectric patch

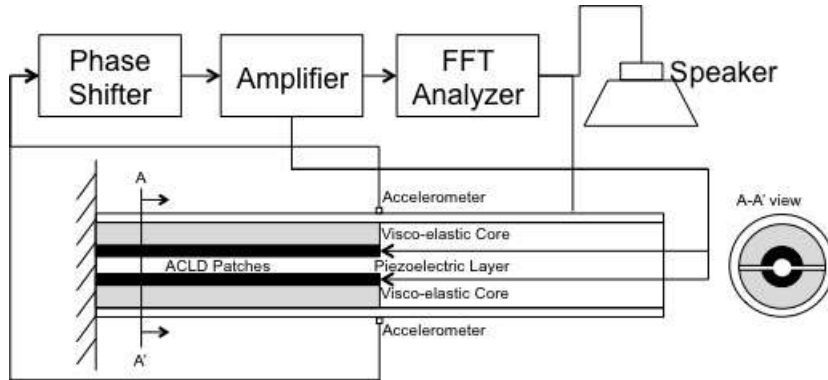





Figure 2.4 Schematic diagram of the shell (pipe)/ACLD treatment system by Ray et al. [16];  : elastic pipe,  : viscoelastic layer and  : piezoelectric patch

Except [16], ACLD treatments used in Baz's studies include piezoelectric sensors in the configuration instead of accelerometers for collocation between locations of sensors and actuator, and avoidance of the duality problems. Duality can be caused by the mismatch between the control force and error signal. For example, if moment (control force) is applied to a system to control out-of-plane deflection (error signal), unstable control results may be obtained due to the mismatch between them. Since out-of-plane deflection is caused by force in out-of-plane direction, negative force in out-of-plane direction should be applied as control force to reduce the out-of-plane deflection.

Following the study with a conventional solid piezoelectric actuator [16], Ray introduced a different configuration for ACLD treatment, i.e. vertically reinforced piezoelectric composites with piezoelectric fibres in an epoxy matrix as shown in Figure 2.5 [17]. According to [17], this kind of configuration has larger applicability to structures than the one with conventional piezoelectric materials. Due to the flexibility of shape, this configuration is applied to pipe structures to control vibration of structures for reduction of radiated sound into water. This kind of configuration, using coefficients of piezoelectric materials in 33-direction as a form of fibre moulded in epoxy material, had been used for distributed sensors and actuators. Coefficients of piezoelectric materials in 33-direction are generally ignored in conventional configurations due to their small contribution on control, rather than coefficients in 31-direction, which are generally used in con-

ventional configurations. Ray expanded the application of the configuration to distributed sensors and actuators as smart structures with ACLD treatment instead of conventional ACLD treatment using monolithic piezoelectric material.

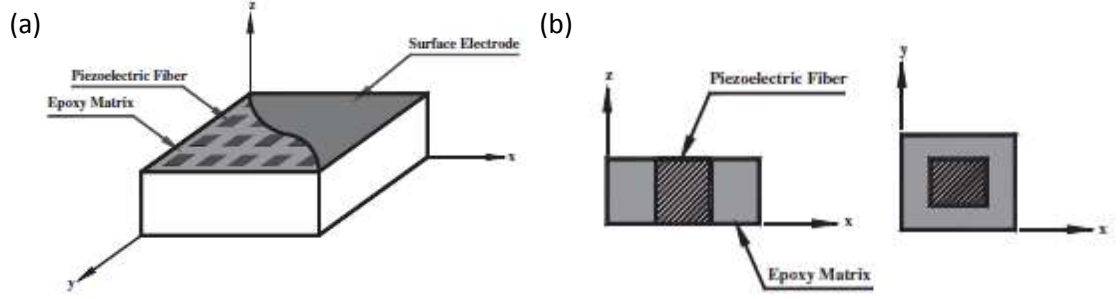


Figure 2.5 Schematic representation of a lamina of vertically reinforced 1–3 piezoelectric composite material and the cross-sections of a representative volume element (RVE) of the composite by Ray and Pradhan (a) Lamina of 1-3 Piezoelectric composite and (b) Cross-Sections of an RVE of the 1-3 piezoelectric composite in xz and xy planes [17]

As was done for a conventional piezoelectric patch by Baz, the application of this configuration of ACLD treatment is expanded to plates [18]. In [18], the performance of vertically reinforced 1-3 piezoelectric fibre-reinforced composite (PFRC) layers of the patches has been investigated for active control of sound radiated from thin symmetric and antisymmetric cross-ply and antisymmetric angle-ply laminated composite plates into the acoustic cavity with the test box as shown in Figure 2.6 (a). The dynamics of ACLD treatment used in [18] can be found in Figure 2.6 (b). Since the fundamental mode of the acoustic cavity is related to the fundamental mode of wall, the changes in central displacement and Sound Pressure Level at one point of the cavity were studied at the fundamental frequency only.

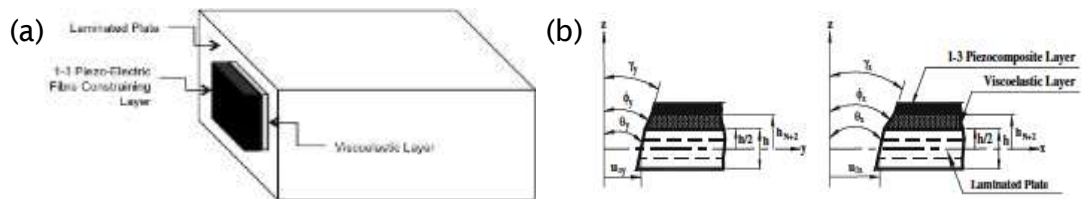


Figure 2.6 (a) Schematic representation of an acoustic cavity with a flexible wall of laminated plate integrated with a patch of ACLD treatment and (b) the dynamics of ACLD treatment [18]

Considering that thin cylindrical shells are usually used as a major building block for many critical structures such as cabins of aircrafts, hulls of submarines and bodies of rockets and missiles rather than flat plates, the vibro-acoustic study in [18] was expanded to cylindrical shells [19, 20, 21]. The study in [19] is an expanded version of the study in [18] for a cylindrical shell, one end of which is clamped to a wall. Two ACLD treatments were attached on the outer surface of a shell and radiated noise in the cavity was controlled at the first two modes with vibra-

2. LITERATURE REVIEW

tion control. In addition to the study result in [19], in order to keep the angle of piezoelectric fibres in ACLD treatment perpendicular to the surface of the shell, piezoelectric fibres were obliquely arranged considering the curvature of the shell [20]. The result in [20] was adapted in [21] with the application to cross-ply and angle-ply laminated composite shells. This study was performed for nonlinear vibration of cylindrical shells [22] and a specific shell structure such as a carbon nanotube [23]. And, since carbon nanotubes were considered to be beams in [23], their structural characteristics were investigated to derive FE formulations for equivalent cantilever beams.

As reviewed above, active control with constrained layer damping treatment has been implemented from beams to flat and curved plates, and it has been done for linear and nonlinear vibrations. These studies have shown a tendency to consider more variables (DOFs) and nonlinear terms than previous studies. However, they have used the same configurations that were established in the early stage of their study. Therefore, space to improve configurations for better control performance still remains.

A brief history relating to the effect of HAPCLD treatment configurations on beams is explained in [3] and each configuration used in previous studies was categorised as is given in Figure 2.7. It focuses mainly on the improvement of configurations for constrained layer damping treatments with a PZT actuator and a viscoelastic layer to obtain better passive and active control results. Configuration improvement has been proposed by additionally introducing an elastic constraining layer and changing the lamination order of each layer as shown in Figure 2.7.

The first six implementations of Figure 2.7, i.e. from (a) to (f) can be categorised as ACLD treatment, which is the standard configuration for hybrid damping treatments [24-36]. In the case of (a), optical sensors are used instead of piezoelectric sensors to eliminate the structural modification caused by piezoelectric sensors. The use of optical sensors, since they are usually used for measurement of velocity or acceleration, can cause duality problems, which can cause instability of active control. In other cases, where piezoelectric sensors are used, the possibility of duality problems is minimised. However, the addition of piezoelectric sensors leads to possible changes in the dynamic characteristics of whole structures and HAPCLD treatments. Agnes and Napoliano [29], Huang et al. [30] and Yelling and Shen [31] proposed a piezoelectric patch to use a sensor and an actuator simultaneously to minimise this problem, but this method requires a complicated signal processing design in the controller.

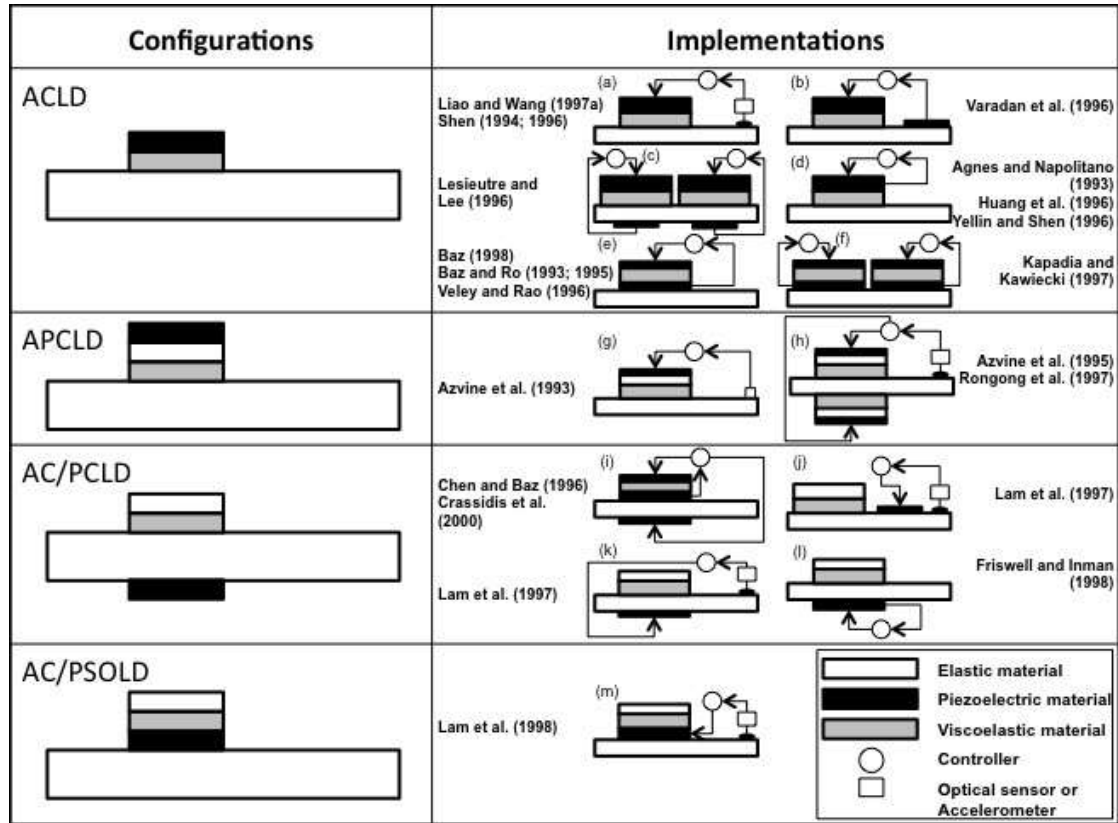


Figure 2.7 Four configurations of HAPCLD treatment [3]; ACLD: Active Constrained Layer Damping, APCLD: Active Passive Constrained Layer Damping, AC/PCLD: Active Control/Passive Constrained Layer Damping and AC/PSOLD: Active Control/Passive Stand-Off Layer Damping

On the other hand, the next two implementations in (g) and (h) are categorised as APCLD treatment, which is a configuration where piezoelectric actuators are attached to PCLD treatments [37, 38, 39]. Since this has an additional elastic constraining layer, increase of stiffness can be expected. Moreover, as PCLD treatment can maintain its original configuration during active control, passive damping of configurations can remain constant during active control. From the configuration of APCLD treatment, although the motions of piezoelectric actuators are limited by elastic constraining layers, better control results are obtained by APCLD treatment than ACLD treatment in the assessment of [3] and the studies in this thesis. This is because the increase of damping and stiffness results in an increase in control gain as clarified in this thesis. Moreover, the sizes of piezoelectric actuators are not to be the same for PCLD treatment and can be determined according to requirements. Piezoelectric actuators in ACLD treatment should have the same sizes of viscoelastic layers.

In the last two groups, piezoelectric actuators are directly attached to base structures different from other configurations mentioned above. Four implementations in the 3rd group are categorised as AC/PCLD treatment [40-43] and the last implementation is categorised as AC/PSOLD treatment [44]. AC/PCLD and AC/PSOLD treatments can deliver control force and moment

2. LITERATURE REVIEW

from a piezoelectric actuator to a base structure without any energy loss inside a viscoelastic layer. The difference between these two configurations is the location of piezoelectric actuators. For AC/PSOLD treatment, a piezoelectric actuator located between a base structure and a viscoelastic layer act as a spacer layer forming a Stand-Off layer. This Stand-Off layer acts as a strain magnifier that amplifies the shear strain in the viscoelastic layer by virtue of increasing the distance between the viscoelastic layer and the neutral axis of the base structure [45]. According to the assessment in [3], AC/PSOLD treatment can give the best control results for four types of HAPCLD treatment.




In addition to the literature review based on the categorization of HAPCLD treatments focusing on configuration improvement, further consideration of the relevant literature regarding beam vibration control using HAPCLD treatments in different viewpoints has been undertaken as follows.

Firstly, control result comparison between continuous and segmented treatments was conducted. Segmented treatments can have advantages in the reduction of added weight with treatments and locally controlled vibration considering modes of structures. Lesieutre and Lee [28] showed that segmented ACLD treatments can give more robust control results than continuous treatment when a whole cantilever beam is covered by ACLD treatments. Because of phasing associated with mode shapes, control using a single continuous ACL can be destabilizing. A segmented ACL is more robust than a continuous treatment, in that the damping of modes at least up to the number of independent patches is increased by control action. However, this configuration requires a more complicated signal processing design of controller to provide correct input signals to each segment. Li et al. [46] confirmed that the result of [28] is applicable to partially covered ACLD treatment for beams as well. Li et al. [46] showed that the application of two ACLD treatments in different positions required a smaller control gain for sufficient vibration reduction than the application of one ACLD treatment with the same total covering area through numerical simulation. Trindade [47] applied segmented piezoelectric actuators to configurations categorised in [3], while having an extra elastic spacer (stand-off) layer for larger passive damping, to improve control effectiveness for beams. After the selection of configuration, optimization of active-passive damping treatments was implemented [47], but the effect of configuration change from [3] on control results was not mentioned. Studies categorised in this section were based on studies relating to the active control performance of ACLD treatment. Similar research has not been carried out for more complex configurations such as APCLD, AC/PCLD and AC/PSOLD treatments, which should be based on individual research results for each configuration.

There are also some studies treating the effect of a viscoelastic material layer on active control with HAPCLD treatments. Balamurgan and Narayanan [48] studied the effects of the viscoelas-

tic layer thickness and material properties on the vibration control performance in ACLD treatment with linear quadratic regulator (LQR) for optimal control and the Golla-Hughes-McTavish (GHM) method for viscoelastic material modelling as well as doing a control result comparison between pure AC, PCLD and ACLD treatments. Trindade et al. [49] compared the Anelastic Displacement Fields (ADF) model, the GHM model and a modal strain energy (MSE) based iterative model for viscoelastic material modelling. After applying a modal reduction technique to each model to reduce the size of the numerical models, viscoelastic material models were used for a cantilever beam with ACLD treatments. The parameter study of the viscoelastic layer in HAPCLD treatments relating to the effect on passive and active control was implemented in [3] as well. The parameter study regarding the viscoelastic layer has already been conducted with APCLD, AC/PCLD and AC/PSOLD treatments. Although it is not written in this thesis, two different models of viscoelastic materials, i.e. the ADF and GHM models, were used for comparison during the study. Since the obtained results using two models did not show significant differences, the GHM model, which has been used recently more than the ADF model, was selected as a main model for viscoelastic material.



Figure 2.8 Concept of Enhanced ACLD treatment;  : elastic beam, patch and edge element,  : viscoelastic layer and  : piezoelectric patch

In order to improve control efficiency, structural adjustment of ACLD treatment has been proposed. Enhanced ACLD treatment with elastic edge elements, the configuration of which is described in Figure 2.8, was introduced to reduce energy dissipation in viscoelastic materials and maximise control force/moment transfer from piezoelectric actuators to base structures by Liao and Wang [50]. The applied boundary elements were modelled as springs connecting the piezoelectric layer and base beam. By providing the connecting path between the piezoelectric actuator and base beam, dissipated active control energy in the viscoelastic layer can be minimised and the active control energy transmission from the actuator to the base beam can be maximised. The optimal thickness of viscoelastic layer can be found through parameter study with varying the thickness of the layer. The change of passive and active loss factor of each case can be compared and time response of a structure also can be compared. The introduction of AC/PCLD and AC/PSOLD treatments explained above related to Figure 2.7 has the same purpose as this, i.e. the maximisation of active control energy transmission from the actuator to base structure. Moreover, Badre-Alam et al. [51] developed this kind of enhanced ACLD treatment for aero-mechanical stability augmentation in helicopter flex beams, which connect the rotor and heli-

2. LITERATURE REVIEW

copter blade and have a symmetric configuration. Design optimization was also implemented.

Finally, beams with different structural composition have been targets for the application of constrained layer damping treatment.

Sun and Tong [52] studied the control performance of partially debonded ACLD treatment on beams. Their study concluded that edge debonding can lead to a reduction in both passive and active damping, and hybrid damping, which can be expressed as the sum of passive and active damping and may be more sensitive to the debonding of the damping layer than the passive damping. This research can explain poorer control results than expected due to the poor construction of real constrained layer damping treatment. Thus, it can be used to explain the reason for poor control performance expected in experiments, and does not seem appropriate as an individual research topic in this thesis.

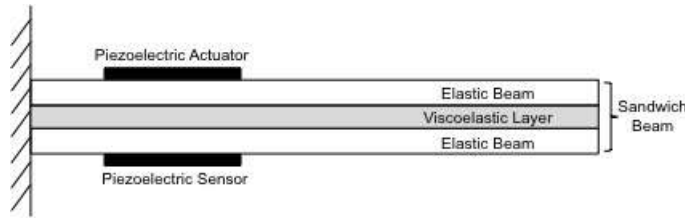


Figure 2.9 A cantilever sandwich beam with viscoelastic core and collocated piezoelectric sensor/actuator [53]

Trindade et al. [53] applied collocated piezoelectric treatments to a sandwich cantilever beam instead of the study of conventional configuration of hybrid damping treatments as shown in Figure 2.9. In this study, a sandwich beam with a viscoelastic layer, as explained in [3], was used as a base structure. On two opposite sides of the base beam, the piezoelectric sensor and actuator were located at the collocated position. This kind of configuration can be treated as a variation of APCLD treatment, especially model (g) in Figure 2.7. Following the study in [53], Trindade [54] also tried new configurations based on the configuration given in [53] by changing the location of the piezoelectric actuator to the viscoelastic core. Due to the patches attached on the surface of the base structure, the increase in maximum thickness of the whole structure has been an issue for the application of constrained layer damping treatments. This approach is understood as a trial to minimise the increase in thickness whilst maintaining passive and active control efficiency. This approach is understood to maximise the increase of passive damping and shear deformation in the base structure with the change of configuration to a sandwich beam as proposed in [2]. However, since the change of base beam structure is unavoidable in this approach, it will not be considered in this thesis.

As reviewed in this section, the application of a more complex configuration for HAPCLD treatments such as APCLD, AC/PCLD and AC/PSOLD treatments for 2-D structures, i.e. flat

and curved plates have not yet been studied. In order to deal with various research topics about HAPCLD treatment mentioned in this section with these kinds of more complex configurations, their active control performance for flat and curved plates should be studied first. This is first inspiration for the research in this thesis.

2.2 Modelling method for constrained layer damping

treatment

As reviewed in the previous section, numerical, especially the Finite Element Method (FEM), and analytic models have been used in control performance analysis and parameter studies for various constrained layer damping treatments [15, 18, 19, 46]. General FE formulation procedure and equations of motion (analytic models) for PCLD treatments (See figure 1.2) and sandwich structures are well known as the Mead-Markus model for beams [2] and the Kantrovich-Krylov method for plates. In these models, individual in-plane displacements for a constraining layer and base structure (for PCLD treatment) or cover layers (for sandwich structures) are introduced. Detailed explanation of these methods is given in Chapters 3 and 6. Many researchers have derived equations of motion for their proposed configurations and used these numerical analysis methods to validate their usefulness. This section will be divided into three subsections; the first section is related to the FE formulation for 1-D structures, i.e. beams, and the second one is for 2-D structures, i.e. flat and curved plates. The final section relates to other modelling methods than the numerical method such as the derivation of an equivalent SDOF system, the Lagrangian formulation of system and spectral element modelling.

2.2.1 FE modelling method for beams with constrained layer damping

treatment

There have been some attempts to establish a new FE formulation for constrained layer damping treatments having more complex configurations, i.e. arbitrarily laminated beams. Vasques et al. [55] established FE models for arbitrary active constrained layer damping treatments from analytic models considering the first-order shear deformations in each layer. Since the first-order shear deformation is considered (Timoshenko beam approximation), it is possible to predict the motion of a constrained layer damping treatment more accurately in a higher frequency

2. LITERATURE REVIEW

range. Trindade et al. [56] proposed FE modelling formulation for a sandwich beam with a viscoelastic core (the ADF model) and arbitrarily laminated face layers including a modal reduction. The assumption for each layer is the same as the one in this thesis; an elastic and piezoelectric layer is assumed to be a Euler beam (shear deformation is negligible), and a viscoelastic layer is assumed to be a Timoshenko beam (the first order of shear deformation is considered). The more DOFs are considered in FE formulation, the more precise simulation of motions can be obtained, especially in a high frequency range. However, in terms of efficiency, the number of nodal DOFs at each node in FE models should be determined considering variables such as frequency range and number of elements used in analysis as well. In this thesis, since active control is mainly conducted for the first two or three modes, i.e. a relatively low frequency range, the assumption that the elastic and piezoelectric layers are assumed as a Euler beam (no shear deformation), and the viscoelastic layer is assumed as a Timoshenko beam, which has pure shear deformation, will be proper to obtain as precise results as practically possible. Moreover, a simpler FE formulation for arbitrarily laminated plates seems to be required than derivation of equations of motion for each layer as was done in [55].

Some researchers have shown an interest in reducing beam model order for more efficient control simulation. Shi et al. [57] proposed a new model reduction procedure for FE beam models with ACLD treatments. An iterative dynamic condensation was performed in the physical space, and Guyan condensation was taken as an initial iteration approximation. This resulted in a reduced order system of suitable size, though still unobservable and uncontrollable. A robust model reduction method was employed in the state space afterwards. Through this procedure, it was possible to overcome vibration control problems due to model size and lack of controllability and observability in [57]. Moreover, Shi et al. [58] conducted vibration control for the first three modes of beams with ACLD treatment with a linear-quadratic Gaussian (LQG) method based on the final reduced order model prior to [57]. Moreover, as reviewed in the previous section, Trindade et al. [49] applied a modal reduction method to viscoelastic models to reduce the size of the constrained layer damping treatment models. In this thesis, mode reduction was used to a proper level compared with experimental data during modal analysis as a manner of model reduction.

2.2.2 FE modelling method for plates with constrained layer damping treatment

The application of viscoelastic and piezoelectric materials was expanded from 1-D structures

to 2-D structures [15, 116], i.e. more complex and general structures. There have been two approaches. One is the application of smart treatment including a piezoelectric sensor and actuator to sandwich plates with a viscoelastic core, i.e. AC is applied to plates with PCLD treatment. The other is the application of ACLD treatments to untreated flat plates.

As in the former case, Araujo et al. [59] attached a piezoelectric sensor and actuator to a sandwich plate with a viscoelastic core and conducted analysis by considering a higher order shear deformation theory (HSDT) to represent the displacement field of the viscoelastic core and a first order shear deformation theory (FSDT) for the displacement field of the adjacent laminated anisotropic face layers and exterior piezoelectric layers. Calculated resonance frequencies from an established model are more similar to those obtained by ABAQUS than shell elements due to more DOFs involved in calculation. However, although the increase of damping by active control was given for the first five modes, a large reduction was not found in the frequency response. Prior to [59], Moita et al. [60] established an FE formulation for sandwich plates with a piezoelectric sensor and actuator, but numerical analyses were performed only as beams. In this model, the classical plate theory, i.e. the Kirchhoff plate theory was applied for elastic and piezoelectric plates and the Reddy's third-order shear deformation theory was applied to a viscoelastic plate. However, since the change of base plate from an untreated flat plate to a sandwich plate is not to be considered in this thesis, this kind of research remains a possible research topic for the future.

As in the latter case, Chantalakhana and Stanway [61] applied ACLD treatments to a clamped-clamped plate considering the mode shapes of the plate. As results of active control, large reductions of mobility for the 1st and 2nd modes were obtained. They obtained better results with multi-channel control using more than one actuator with one control loop. Kim et al. [62] detailed a 3-D FE model of plates with piezoelectric patches using 20-node solid elements, which has no approximation to piezoelectric devices and includes closed loop modelling for plates. Moreover, flat plates were also modelled with 9-node shell elements, and 13-node transition elements were introduced for transition parts between plates and ACLD treatment [62]. However, when considering results in comparison with experimental results, although this model gave results which had good agreement with experimental ones, the efficiency of simulation remains in doubt compared with the case for 2-D FE model analysis. Varadan et al. [27] expanded the FE modelling method developed in [62] to ACLD treatment. Enhanced boundaries in the form of box or bench as proposed in [50] for beams were added as a part of a parameter study for ACLD treatment. However, in contrast to the result of [50] mentioned in Section 2.1, which said that the ACLD treatment with edge elements showed better control results than conventional ACLD treatment, conventional ACLD treatment, which has no edge element and is categorised as a sandwich type in [50], gave the largest reduction of all the considered cases in [62]. This

2. LITERATURE REVIEW

contrasting result requires further study for clarification, and the study for additional edge elements has been excluded from the study in this thesis. Baz and Ro's study [15] and Ray and Faye's study [18] can be categorised in this research area as reviewed in the previous section. In FE formulation, mutual relationships between displacements in each layer were reflected in the shape functions of each layer [15, 16]. However, as mentioned above, different shape functions for each layer should be derived according to the change of configuration in this kind of FE formulation. In [16], since the first order shear deformation theory was used for each layer, different rotations were considered for elastic, viscoelastic and piezoelectric plates. In much other research, shear deformation was not considered in elastic and piezoelectric layers in spite of simulation results in good agreement with experimental results. Therefore, Ray and Faye's approach can result in the increase in size of FE matrices rather than the increase in accuracy of control results using an FE model. In this thesis, in spite of various FE plate modelling methods reviewed above, the same assumption related to shear deformation for each layer as for beams; that is, the assumption that elastic and piezoelectric layers are assumed to behave as a Kirchhoff plate, and that a viscoelastic layer is assumed to behave as a Mindlin-Reissner plate with the first-order shear deformation, was used considering the efficiency of simulation. Moreover, the same FE formulation for arbitrarily laminated flat plates as for laminated beams will also be introduced for more convenient FE formulation.

Furthermore, the application study of viscoelastic materials and smart treatments using piezoelectric materials has been expanded to more complex and general structures than flat plates, i.e. curved plates. Similar to flat plates, there have been two ways to study this. One is the application of smart treatment including a piezoelectric sensor and actuator to sandwich shells with a viscoelastic core. The other is the application of hybrid damping treatments to shells without any additional viscoelastic materials.

As in the former case, Boudaoud et al. [63] established an accurate shell FE formulation to model composite shell structures with embedded viscoelastic and piezoelectric layers and an integrated active damping control mechanism. As has been done in this thesis, the Kirchhoff plate theory was used for elastic and piezoelectric shells (shear deformation was ignored) and the first order shear deformation theory (the Mindlin-Reissner plate theory) was used for a viscoelastic shell. Used shell elements were triangular in shape. Used configuration is limited to a sandwich plate (or shell) with a viscoelastic core and cover layers used as a piezoelectric sensor and actuator. This model can be said to be an expanded model of the FE model established in [59].

As in the latter case, Kumar and Singh [64] demonstrated the utility of the technique for selecting the locations of the ACLD treatments to achieve the desired damping characteristics over a

broad frequency range. However, in this study, the used piezoelectric sensor was of the same size as the one for the actuator. In order to control selected modes, the shape of the actuator, which covered a relatively broad part of system, was decided. When considering the results of the study by Lesieutre and Lee [28], segmented ACLD treatment is expected to give a better and more robust control result than the continuous one used in [64]. The study of Ray et al. [16], Ray and Reddy's study [19], Ray and Pradhan's study [20, 21], Sarangi and Ray's study [22] and Ray and Batra's study [23] can be categorised in this research area as well, although they did not use a conventional ACLD treatment configuration as reviewed in the previous section.

Basically, since curved plates are a more general form of flat plates, the same review can be applied to curved plates as well. Sandwich structures with a viscoelastic core will not be considered in this thesis, and the same assumption related to shear deformation will be applied.

2.2.3 Other modelling methods for constrained layer damping treatment

Various modelling methods for ACLD treatment instead of the FE method have been studied to achieve lighter modelling methods than numerical modelling as well.

Illaire et al. [65] proposed a phenomenological model of active constrained layers using the lumped parameter model instead of the FE method. This phenomenological model can be beneficial in saving time and resources for analysis, but different models should be derived for different structures and configurations for constrained layer damping treatment.

Fung et al. [66] derived the Lagrangian formulation of a rotating beam with ACLD treatment in a time domain analysis. In [66], the effects of control gains, shear modulus and loss factor of the viscoelastic materials on the dynamic response are also investigated.

Lee and Kim [67] established spectral element modelling for beams with active constrained layer damping instead of FE modelling. According to [67], the spectral ACLD beam element model was found to provide very reliable results when compared with the conventional FE model. As reviewed here, since analytic models are derived from the equations of motion for ACLD treatment, different equations should be derived for different configurations.

As mentioned above, in order to use this kind of formulation, different equations of motions should be derived for different configurations. Thus, it is too hard for it to be applied to arbitrarily laminated structures. Since this formulation is very useful for validation of a relatively simple configuration such as ACLD treatment, the simulation results of ACLD treatment with an established FE beam model have been compared with the results of the phenomenological mod-

2. LITERATURE REVIEW

el of Illaire, et al. [65] and it is confirmed that they are in good agreement during the study by way of validation. (Results are not included in the thesis.)

2.3 State of the art for FE modelling of laminated structures

In addition to the literature review for the modelling method for constrained layer damping treatment in Section 2.2, state-of-the-art FE modelling for laminated structures will be discussed in this section based on recently published papers.

According to the literature review, a layer-wise approach and the Zigzag theory, the key idea of which is to add a piecewise-linear, zigzag-shaped (i.e., C_z^0 -continuous) contribution to a globally linear or cubic through-the-thickness distribution of the in-plane displacements [68], are being used to analyse the shear stress distribution in thickness-through direction. Cerracchio et al. [69] employed the inverse Finite Element Method (iFEM) and the Refined Zigzag Theory (RZT) for displacement and stress monitoring of sandwich plates. In the RZT, zigzag strain terms, which are equivalent to shear strain terms in other papers, were introduced in addition to in-plane and bending strain terms. The analysis results using this method were compared and gave the same results as analytic ones by NASTRAN. Vidal et al. [70] employed a piecewise fourth-order Lagrange polynomial of z to deduce the number of unknowns from a classical layer-wise approach for FE modelling of free edge effect. Stress distribution through the thickness of composite plates was studied to prevent the failure due to delamination of composite laminated plates. Plagianakos and Papadopoulos [71] also studied a thickness-through stress distribution in composite sandwich shells and electric voltages generated by piezoelectric transducers attached to the shells. Versino et al. [72] investigated deflections and thickness-through stress distribution in laminated shells by using a layer-wise approach. In this study, discontinuous Galerkin fluxes were used to enforce interlaminar continuity conditions in perfectly bonded laminates. The simulation results were compared with those of various models for laminated structures. Tian et al. [73] employed a layer-wise approach for stress analysis around cutouts in laminated composite structures. They introduced traction-free surfaces for the reduction of the number of unknowns around cutouts and stress distributions through thickness were discussed. Zhou et al. [74] also used a layer-wise approach for the motion analysis of microoperation systems which consist of piezoelectric cantilevers. In analyses, the distribution of thickness-through stress was investigated. Yuan et al. [75] investigated deformation and stress changes in the i -th element of sandwich plates by using a layer-wise approach.

A layer-wise approach has been used for static and vibration analysis as well. Yazdani and Ribeiro [76] used a layer-wise approach for analysis of the linear modes of vibration of Variable Stiffness Composite Laminate plates as well. In this paper, a p -version FE formulation, which is related to the employment of a piecewise fourth-order Lagrange polynomial of z in Vidal's study [70], was introduced. Natural frequencies obtained with this formulation were compared with results by ABAQUS and layer-wise B-spline FE models. This layer-wise B-spline FE formulation was used by Phung-Van et al. [77], Zuo et al. [78] and Thai et al. [79] as well. Phung-Van et al. [77] used the model for vibration control in composite structures covered by a piezoelectric sensor and actuator. Zuo et al. [78] adopted a B-spline wavelet to investigate static and free vibration of laminated composite plates. Thai et al. [79] employed non-uniform rational B-spline (NURBS) basis functions in FE formulation. Xu et al. [80] used a layer-wise approach and genetic algorithm to calculate first modal loss factors of structures with a viscoelastic material layer and optimise the layer position of it in the laminated layer. Thakur and Ray [81] studied stress distribution through thickness in deep laminated doubly curved shells by using a layer-wise approach. Although a different lamination method was used, the same modelling method for curved shells was employed as used in Section 7.1 of this thesis.

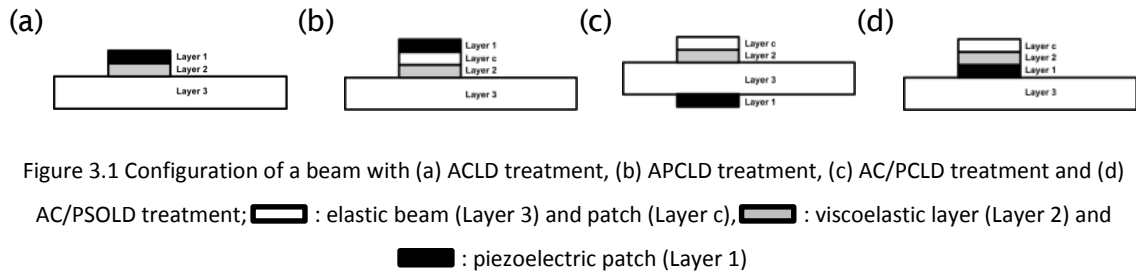
Another modelling method for laminated structures is the equivalent single layer (ESL) theory. With this theory, although stress distribution through thickness of structures cannot be analysed as is done with a layer-wise approach, analysis load with established FE models can be reduced due to a decrease in the number of variables, i.e. smaller size of FE matrices. In order to overcome disadvantages for each theory, Band and Desai [82] used ESL and layer-wise FE models in one structure simultaneously. The ESL FE model was used for a global part of the host structure, and the layer-wise FE model was used for the part of interest. Between two FE models, transition elements were introduced to match variables in each model by restraint. The introduction of transition elements between 2-D and 3-D elements was used by Kim et al. [62] and Varadan et al. [27] as well. But, the use of layer-wise FE models is not necessary in the case of vibration analysis which does not require the analysis of stress distribution through thickness. Carpentieri et al. [83] introduced coupling matrices to derive ESL FE models from local displacement terms based on a layer-wise approach. This approach is similar to the FE modelling method proposed in this thesis. However, while the former was applied to laminated composite curved beams in [83], the latter was used for straight beams, flat plates and curved plates in the thesis.

3 FE MODELLING OF BEAMS WITH HAPCLD TREATMENTS

In this chapter, Finite Element (FE) modelling of layered composite beams will be discussed. Since elastic and piezoelectric layers are assumed to be thin compared with their length and under small deflection, the Euler beam theory can be utilised for them. In the Euler beam theory, the cross-section of a beam remains perpendicular to the neutral axis of deflection. Therefore, no shear deformation exists in the cross-section of the elastic and piezoelectric layers. On the other hand, in the Timoshenko beam theory, shear deformation is considered. Since viscoelastic layers are under pure shear deformation in bending motion, the Timoshenko beam theory would be used for the viscoelastic layer. Therefore, firstly, FE modelling of an elastic beam will be explained. Next, the description of a piezoelectric beam will follow based again on the Euler beam theory, and the constitutive equations of piezoelectric material will be given to explain its electro-mechanical characteristics. FE modelling of the viscoelastic layer will be then studied using the Timoshenko beam theory and the GHM (Golla-Hughes-McTavish) method to describe the shear deformation in the viscoelastic material. Finally, a coupling method based on the layer-wise approach will be used to generate equivalent FE models of the composite layered beams.

3.1 Overview of beams with HAPCLD treatment

The final objective of FE modelling for beams with HAPCLD treatments is to establish FE models for beams described in Figure 1.2. In summary, all configurations of the structures of concern in this thesis are given in Figure 3.1. All configurations consist of the combination of elastic base beam, viscoelastic layer, elastic constraining layer and piezoelectric layer. In order to establish full FE models, FE models of each layer are derived from equations of motions in each layer. After this, final FE models of each configuration will be established considering the mutual relationships between motions of each layer.



3. FE MODELLING OF BEAMS WITH HAPCLD TREATMENTS

3.2 FE model for an elastic beam

Here an isotropic elastic beam with a constant cross section is considered. Material properties and mechanical characteristics of the beam are constant along the whole structure. The Beam's deflection and the establishment of FE global mass and stiffness matrices, based on the Euler beam theory, are briefly explained here.

3.2.1 Definition of a beam's deformation

When transverse loads are applied to a beam [84], the line of length dx in the beam, which is located along the x -axis in undeformed state, i.e. meaning the neutral axis of the beam, bends into a curve whose position relative to the original location is denoted as $w(x)$ as shown in Figure 3.2. For small deformations, an element dx in the undeformed geometry is assumed to remain at coordinate x , but it translates in the z direction by an amount $w(x)$ and rotates in the xz plane by an amount given by the slope $\frac{dw}{dx}$ of the deflection curve at coordinate x . The basic

assumption of a Euler beam is that cross sections such as ab in Figure 3.3, which are originally normal to the centreline of a beam in the undeformed state, still remain plane and normal to the centreline like the line after deformation $a'b'$ in Figure 3.3. Furthermore, in the planes of these cross sections, it is assumed that there is no stretching or shortening whatsoever; that is, they are assumed to act like rigid surfaces.

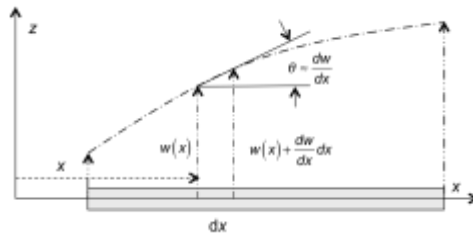


Figure 3.2 Deformation of a Euler beam bending under small deflection

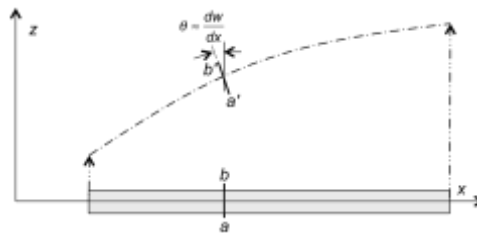


Figure 3.3 Cross-section change of a Euler beam under deformation

3. FE MODELLING OF BEAMS WITH HAPCLD TREATMENTS

The axial displacement in the x -direction $u(x, z)$ at an arbitrary point with a distance z from the centreline in a beam is influenced by the slope, i.e., the rotation angle $\theta \approx dw/dx$, as

$$u(x, z) = u(x, 0) - z \frac{dw(x, z)}{dx} = u(x) - z \frac{dw(x, z)}{dx}. \quad (3.1)$$

Since the height of beam is very small compared with the length and it is under small deflection, the neutral axis in y -direction can be assumed to remain at the same position before deflection even with the Poisson contraction as describe in Figure 3.4 [85]. Therefore, the displacement in the y -direction $v(x, z)$ can be represented by the one at the neutral axis $v(x, 0)$.

$$v(x, z) = v(x, 0) = 0. \quad (3.2)$$

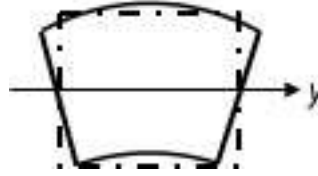


Figure 3.4 Poisson contraction of cross section in beams

Since the beam displacement in the z -direction, i.e. the transverse displacement, is the same through the thickness of the beam, it is equal to the value at the centreline so that

$$w(x, z) = w(x, 0) = w(x). \quad (3.3)$$

Therefore, eq. (3.1) can be rewritten as

$$u(x, z) = u(x) - z \frac{dw(x)}{dx} \approx u(x) - z\theta(x). \quad (3.4)$$

Eqs. (3.2), (3.3) and (3.4) describe the motion of any beam's section in the y , z and x -direction respectively.

3.2.2 FE formulation of an elastic beam

Considering eqs. (3.2), (3.3) and (3.4), the potential energy of a Euler beam element of length $2a$, width b , height h , a constant cross section, and uniform and constant material properties, that is constant Young's modulus E and density ρ , can be expressed in terms of strain and stress generated inside the beam during deformation as

3. FE MODELLING OF BEAMS WITH HAPCLD TREATMENTS

$$U_e = \frac{1}{2} \iiint_{V_e} \tau_{ij} \varepsilon_{ij} dV,$$

where $\tau_{ij} = E\varepsilon_{ij}$ for isotropic materials and $\varepsilon_{ij} = \frac{1}{2} \left(\frac{du_i}{dx_j} + \frac{du_j}{dx_i} \right)$ are the stress and strain respectively, u_i and x_i are the displacements and variables in the i -axis ($i = x, y$ and z). V_e denotes the volume of each element.

Since a beam with a constant cross section is considered here, triple integration for element volume can be simplified considering the Cartesian coordinate as

$$U_e = \frac{1}{2} b \int_{-a-h/2}^a \int_{-h/2}^{h/2} \tau_{xx} \varepsilon_{xx} dz dx.$$

From the definition of strain and stress,

$$U_e = \frac{1}{2} \int_{-a-h/2}^a \int_{-h/2}^{h/2} bE \left(\frac{du(x, z)}{dx} \right)^2 dz dx.$$

By applying eq. (3.4) for the axial displacement $u(x, z)$,

$$U_e = \frac{1}{2} \int_{-a}^a EA \left(\frac{du(x)}{dx} \right)^2 + EI \left(\frac{d^2 w(x)}{dx^2} \right)^2 dx, \quad (3.5)$$

where $A = bh$ denotes the cross sectional area and I is the moment of area ($I = bh^3/12$ for a rectangular cross section as in the example).

Similarly, the kinetic energy of a Euler beam element can be derived as

$$T_e = \frac{1}{2} \int_{-a}^a \left(\rho A \dot{u}(x)^2 + \rho A \dot{w}(x)^2 \right) dx. \quad (3.6)$$

In the case of kinetic energy, the $z\dot{\theta}(x)$ term is simplified during the integration along the thickness of a plate from $-h/2$ to $h/2$ as is done in eq. (3.5) for the potential energy of a beam. Also the $\left(z\dot{\theta}(x) \right)^2$ term which is always positive, since the thickness of a Euler beam is relatively small compared with the length, is very small and can be neglected.

In order to derive element mass and stiffness matrices from eqs. (3.5) and (3.6), the shape functions \mathbf{H} and the Jacobian matrix \mathbf{J} are used. Details of the shape functions and the Jacobi-

3. FE MODELLING OF BEAMS WITH HAPCLD TREATMENTS

an matrix can be found in Appendix A.1. Firstly, by applying the Jacobian matrix, the coordinate systems of these two equations, eq. (3.5) and (3.6), can be matched from xz -space, the original space, to ξz -space, the FE element space. As described in Figure A.2 of Appendix A.1 for straight beam elements, $\pm a$ and each point between these two end points of actual elements in xz -space are matched to ± 1 and each related point between these two end points of FE elements in ξz -space respectively. With this coordinate matching method, eqs. (3.5) and (3.6) can be re-written as

$$U_e = \frac{1}{2} \int_{-1}^1 \left(EA \frac{1}{J^2} \left(\frac{\partial u(\xi)}{\partial \xi} \right)^2 + EI \frac{1}{J^4} \left(\frac{\partial^2 w(\xi)}{\partial \xi^2} \right)^2 \right) J d\xi \quad \text{and}$$

$$T_e = \frac{1}{2} \int_{-1}^1 \left(\rho A \dot{u}(\xi)^2 + \rho A \dot{w}(\xi)^2 \right) J d\xi \quad (3.7)$$

with the Jacobian term J for straight beam elements which is derived from eq. (A.5) in Appendix A.1.

Secondly, using the shape functions for axial and transverse displacements, the axial and transverse displacement and derivative terms in eq. (3.7) can be expressed respectively as

$$\dot{u}(\xi)^2 = \dot{\mathbf{u}}_e^T \mathbf{H}_u^T(\xi) \mathbf{H}_u(\xi) \dot{\mathbf{u}}_e \quad \text{and} \quad \dot{w}(\xi)^2 = \dot{\mathbf{w}}_e^T \mathbf{H}_w^T(\xi) \mathbf{H}_w(\xi) \dot{\mathbf{w}}_e,$$

$$\frac{\partial u(\xi)}{\partial \xi} = \left(\frac{\partial \mathbf{H}_u(\xi)}{\partial \xi} \right) \mathbf{u}_e = \mathbf{H}'_u(\xi) \mathbf{u}_e \quad \text{and} \quad \frac{\partial^2 w(\xi)}{\partial \xi^2} = \left(\frac{\partial^2 \mathbf{H}_w(\xi)}{\partial \xi^2} \right) \mathbf{w}_e = \mathbf{H}''_w(\xi) \mathbf{w}_e,$$

where the axial nodal displacement vector of element \mathbf{u}_e and the linear shape function matrix for axial displacement \mathbf{H}_u are defined in eqs. (A.1) and (A.2) of Appendix A.1, and the transverse nodal displacement vector of element \mathbf{w}_e and the Hermite cubic shape function matrix for transverse displacement \mathbf{H}_w are defined in eqs. (A.3) and (A.4) of Appendix A.1.

In order to understand the Jacobian and shape functions better, description of FE element geometry in Figures A.1, A.2 and A.3 of Appendix A can be referred to. Figure A.1 describes a basic FE beam element lying on the ξ -axis, which is the FE element space, with the definition of nodal DOFs at each node of the element. Figures A.2 and A.3 show the geometry of a single axial and bending element and how the element length ratio, $1/a$, between $2a$ of real elements and 2 of FE elements, that is, the Jacobian of the 1-D element, is determined.

3. FE MODELLING OF BEAMS WITH HAPCLD TREATMENTS

Thus, the kinetic and potential energy equations of a Euler beam element in eqs. (3.5) and (3.6) can be expressed in terms of a transformed coordinate system of ξ -space. Using the above equations of shape functions for axial and transverse displacements, element mass and stiffness matrices can be derived from these changed kinetic and potential energy equations as

$$\begin{aligned}
 T_e &= \frac{1}{2} \dot{\mathbf{u}}_e^T J \int_{-1}^1 \rho A \mathbf{H}_u^T(\xi) \mathbf{H}_u(\xi) d\xi \dot{\mathbf{u}}_e + \frac{1}{2} \dot{\mathbf{w}}_e^T J \int_{-1}^1 \rho A \mathbf{H}_w^T(\xi) \mathbf{H}_w(\xi) d\xi \dot{\mathbf{w}}_e \\
 &= \frac{1}{2} \dot{\mathbf{u}}_e^T \mathbf{m}_{u_e} \dot{\mathbf{u}}_e + \frac{1}{2} \dot{\mathbf{w}}_e^T \mathbf{m}_{w_e} \dot{\mathbf{w}}_e \\
 &= \frac{1}{2} \dot{\mathbf{q}}_e^T \mathbf{m}_e \dot{\mathbf{q}}_e
 \end{aligned} \tag{3.8}$$

and

$$\begin{aligned}
 U_e &= \frac{1}{2} \mathbf{u}_e^T \frac{1}{J} \int_{-1}^1 EA \mathbf{H}_u'^T(\xi) \mathbf{H}_u'(\xi) d\xi \mathbf{u}_e + \frac{1}{2} \mathbf{w}_e^T \frac{1}{J^3} \int_{-1}^1 EI \mathbf{H}_w''^T(\xi) \mathbf{H}_w''(\xi) d\xi \mathbf{w}_e \\
 &= \frac{1}{2} \mathbf{u}_e^T \mathbf{k}_{u_e} \mathbf{u}_e + \frac{1}{2} \mathbf{w}_e^T \mathbf{k}_{w_e} \mathbf{w}_e \\
 &= \frac{1}{2} \mathbf{q}_e^T \mathbf{k}_e \mathbf{q}_e,
 \end{aligned} \tag{3.9}$$

where $\dot{\mathbf{q}}_e = \left\{ \begin{matrix} \dot{\mathbf{u}}_e & \dot{\mathbf{w}}_e & \dot{\boldsymbol{\theta}}_e \end{matrix} \right\}^T$ and $\mathbf{q}_e = \left\{ \begin{matrix} \mathbf{u}_e & \mathbf{w}_e & \boldsymbol{\theta}_e \end{matrix} \right\}^T$ are local nodal velocity and displacement vectors of each element respectively, and $\mathbf{m}_e = \begin{bmatrix} \mathbf{m}_{u_e} & \mathbf{0} & \mathbf{0} \\ \mathbf{0} & \mathbf{m}_{w_e} & \mathbf{m}_{w_e} \\ \mathbf{0} & \mathbf{m}_{w_e} & \mathbf{m}_{w_e} \end{bmatrix}$ and

$$\mathbf{k}_e = \begin{bmatrix} \mathbf{k}_{u_e} & \mathbf{0} & \mathbf{0} \\ \mathbf{0} & \mathbf{k}_{w_e} & \mathbf{k}_{w_e} \\ \mathbf{0} & \mathbf{k}_{w_e} & \mathbf{k}_{w_e} \end{bmatrix} \text{ are FE mass and stiffness matrices of each element respectively.}$$

Therefore, by composing the global mass and stiffness matrices, as explained in Appendix A.2, using mass and stiffness matrices of a beam element in eqs. (3.8) and (3.9), the equation of motion for an unconstrained beam comprising n elements can be obtained as

$$\mathbf{M} \ddot{\mathbf{q}} + \mathbf{K} \mathbf{q} = \mathbf{f}, \tag{3.10}$$

where \mathbf{M} and \mathbf{K} are the global mass matrix and stiffness matrix respectively. In the stiffness matrix, the structural damping of the system is considered by using a complex Young's modulus

3. FE MODELLING OF BEAMS WITH HAPCLD TREATMENTS

$E(1 + i\eta)$ where η is the loss factor in scalar form [86]. \mathbf{q} is a vector of nodal DOFs of the whole structure, which can be written as

$$\mathbf{q} = \left\{ u_1 \quad \cdots \quad u_{n+1} \quad w_1 \quad \theta_1 \quad \cdots \quad w_{n+1} \quad \theta_{n+1} \right\}^T, \quad (3.11)$$

and \mathbf{f} is an external exciting force vector, which is defined as

$$\mathbf{f} = \left\{ f_{x1} \quad \cdots \quad f_{x(n+1)} \quad f_{z1} \quad M_1 \quad \cdots \quad f_{z(n+1)} \quad M_{n+1} \right\}^T, \quad (3.12)$$

where f_{xi} , f_{zi} and M_i are the force in the x -axis, the force in the z -axis and the moment respectively.

In this section, FE mass and stiffness matrices of an elastic beam structure have been derived from kinetic and potential energy equations using the Euler beam theory. In the next section, the electromechanical effect of piezoelectric materials when the piezoelectric layer is under deformation will be studied in an analogous way.

3.3 FE model for a piezoelectric beam

In this section, an isotropic piezoelectric beam with a constant cross section is considered as an elastic beam was presented in Section 3.2. Since this piezoelectric beam is assumed to behave as a Euler beam, the kinetic energy related to the motion of the beam is the same as one for an elastic beam in eq. (3.6). However, since a piezoelectric material exhibits an electro-mechanical effect which causes conversion between mechanical deformation and electricity generation, that is the piezoelectric effect, it should be considered during the derivation of the stiffness matrix.

3.3.1 The constitutive equations of piezoelectric material of a 1D element

Since a piezoelectric beam is assumed as a Euler beam, the definition of displacement and geometry of deformation is the same as described in Figures 3.2 and 3.3. The energy conservation equation of a piezoelectric beam element can be expressed as

$$T - U + W_e = \text{const.}, \quad (3.13)$$

3. FE MODELLING OF BEAMS WITH HAPCLD TREATMENTS

where T , U and W_e are the kinetic, potential and electrical energy term of a piezoelectric material respectively [87]. Some potential energy generated by an exciting force is transformed into electrical energy by piezoelectric effect. This electro-mechanical phenomenon can decrease the mechanical stiffness of the structure. The mechanical and piezoelectric material properties of a piezoelectric beam can be represented by the following constitutive equations [88]

$$\begin{Bmatrix} \mathbf{t} \\ \mathbf{D} \end{Bmatrix} = \begin{bmatrix} \mathbf{c}^E & -\mathbf{e}^T \\ \mathbf{e} & \mathbf{d} \end{bmatrix} \begin{Bmatrix} \mathbf{S} \\ \mathbf{E} \end{Bmatrix}$$

or, in full expression

$$\begin{Bmatrix} t_{xx} \\ t_{yy} \\ t_{zz} \\ t_{yz} \\ t_{zx} \\ t_{xy} \end{Bmatrix} = \begin{bmatrix} c_{11} & c_{12} & c_{13} & 0 & 0 & 0 \\ c_{12} & c_{22} & c_{23} & 0 & 0 & 0 \\ c_{13} & c_{23} & c_{33} & 0 & 0 & 0 \\ 0 & 0 & 0 & c_{44} & 0 & 0 \\ 0 & 0 & 0 & 0 & c_{55} & 0 \\ 0 & 0 & 0 & 0 & 0 & c_{66} \end{bmatrix} \begin{Bmatrix} e_{xx} \\ e_{yy} \\ e_{zz} \\ e_{yz} \\ e_{zx} \\ e_{xy} \end{Bmatrix} - \begin{bmatrix} 0 & 0 & e_{31} \\ 0 & 0 & e_{32} \\ 0 & 0 & e_{33} \\ 0 & e_{24} & 0 \\ e_{15} & 0 & 0 \\ 0 & 0 & 0 \end{bmatrix} \begin{Bmatrix} E_x \\ E_y \\ E_z \end{Bmatrix},$$

$$\begin{Bmatrix} D_x \\ D_y \\ D_z \end{Bmatrix} = \begin{bmatrix} 0 & 0 & 0 & 0 & e_{15} & 0 \\ 0 & 0 & 0 & e_{24} & 0 & 0 \\ e_{31} & e_{32} & e_{33} & 0 & 0 & 0 \end{bmatrix} \begin{Bmatrix} e_{xx} \\ e_{yy} \\ e_{zz} \\ e_{yz} \\ e_{zx} \\ e_{xy} \end{Bmatrix} + \begin{bmatrix} dc_{11} & 0 & 0 \\ 0 & dc_{22} & 0 \\ 0 & 0 & dc_{33} \end{bmatrix} \begin{Bmatrix} E_x \\ E_y \\ E_z \end{Bmatrix}, \quad (3.14)$$

where \mathbf{t} is the stress vector, \mathbf{S} the strain vector, \mathbf{c}^E the elastic modulus matrix, \mathbf{e} the piezoelectric stress constant matrix, \mathbf{E} the vector of electrical difference between electrodes, \mathbf{D} the electric displacement vector and \mathbf{d} the dielectric constant matrix of a piezoelectric material.

In a beam which has displacement terms given in eq. (3.2), (3.3) and (3.4) in Section 3.2.1, the neutral axis in y -direction can remain on y -axis after deformation as show in Figure 3.4 and all related strain components are also null, then

$$\varepsilon_{yy} = \varepsilon_{yz} = \varepsilon_{xy} = 0. \quad (3.15)$$

Moreover, assuming $\tau_{zz} \approx 0$ in one-dimensional space where there is no structural deformation in the z -direction, the resulting kinematic assumptions yield

$$\varepsilon_{zz} = \frac{1}{c_{33}}(e_{33}E_z - c_{13}\varepsilon_{xx}). \quad (3.16)$$

Thus, by substituting eqs. (3.15) and (3.16) into eq. (3.14), the constitutive equations of a beam-shaped piezoelectric layer can be reduced to

$$\begin{aligned} \begin{Bmatrix} t_{xx} \\ t_{zx} \end{Bmatrix} &= \begin{bmatrix} c_{11}^* & 0 \\ 0 & c_{55} \end{bmatrix} \begin{Bmatrix} e_{xx} \\ e_{zx} \end{Bmatrix} - \begin{bmatrix} 0 & e_{31}^* \\ e_{15} & 0 \end{bmatrix} \begin{Bmatrix} E_x \\ E_z \end{Bmatrix}, \\ \begin{Bmatrix} D_x \\ D_z \end{Bmatrix} &= \begin{bmatrix} 0 & e_{15} \\ e_{31}^* & 0 \end{bmatrix} \begin{Bmatrix} e_{xx} \\ e_{zx} \end{Bmatrix} + \begin{bmatrix} dc_{11} & 0 \\ 0 & dc_{33}^* \end{bmatrix} \begin{Bmatrix} E_x \\ E_z \end{Bmatrix}. \end{aligned} \quad (3.17)$$

where $c_{11}^* = c_{11} - c_{13}^2/c_{33}$, $e_{31}^* = e_{31} - e_{33}c_{13}/c_{33}$, $\varepsilon_{33}^* = \varepsilon_{33} + e_{33}^2/c_{33}$ and c_{11} is the Young's modulus of the material, c_{55} is the shear modulus, e_{31} and e_{15} are the piezoelectric stress constants, dc_{11} and dc_{33}^* are the dielectric constants, τ_{xx} is the extensional stress, τ_{zx} is the shear stress, D_x is the axial electric displacement and D_z is the transverse electric displacement.

3.3.2 FE formulation of a piezoelectric beam

The kinetic energy of a piezoelectric beam is the same as that of an elastic Euler beam expressed in eqs. (3.6) and (3.8) in the Section 3.2.2. However, since electrical displacement relates to strain terms, the potential energy of a PZT beam element with a length of $2a$ should be expressed from eq. (3.17) as

$$\begin{aligned} U_e &= \frac{1}{2} \int_{V_e} \mathbf{S}^T \mathbf{t} dV \\ &= \frac{1}{2} \int_{V_e} (\varepsilon_{xx} \tau_{xx} + \varepsilon_{zx} \tau_{zx}) dV \\ &= \frac{1}{2} \int_{V_e} (\varepsilon_{xx} c_{11}^* \varepsilon_{xx} + \varepsilon_{zx} c_{55} \varepsilon_{zx} - \varepsilon_{xx} e_{31}^* E_z - \varepsilon_{zx} e_{15} E_x) dV. \end{aligned} \quad (3.18)$$

Adopting the Euler beam approximation, every shear strain term between longitudinal direction and transverse direction is neglected, i.e. $\varepsilon_{zx} = 0$. Moreover, if the thickness of this layer is h_p , the electric difference terms E_x and E_z between upper and lower surfaces in the case of flat-

3. FE MODELLING OF BEAMS WITH HAPCLD TREATMENTS

plate-shaped structures with d_{31} mode polarisation (piezoelectric layer polarised in thickness direction) can be expressed as [88, 89]

$$E_x = -\frac{e_{15}}{e_{11}}(w - q) = 0, \quad E_z = -\frac{\phi}{h_p}, \quad (3.19)$$

and, by assuming that the electric potential is constant over the plane of element with equally covering electrodes on top and bottom surfaces respectively, eq. (3.18) can be rewritten as [87]

$$U_e = \frac{1}{2} \int_{V_e} (\epsilon_{xx} c_{11}^* \epsilon_{xx} - \epsilon_{xx} e_{31}^* E_z) dV. \quad (3.20)$$

By using the definition of displacement of a Euler beam derived in eq. (3.4) and the definition of strain in eq. (3.5) in Section 3.2.2, eq. (3.20) can be expressed in terms of displacement as

$$U_e = \frac{1}{2} \int_{V_e} \left(c_{11}^* \left(\frac{\partial u}{\partial x} \right)^2 - 2c_{11}^* \left(\frac{\partial u}{\partial x} \right) z \left(\frac{\partial^2 w}{\partial x^2} \right) + c_{11}^* z^2 \left(\frac{\partial^2 w}{\partial x^2} \right)^2 - \left(\frac{\partial u}{\partial x} \right) e_{31}^* E_z + z \left(\frac{\partial^2 w}{\partial x^2} \right) e_{31}^* E_z \right) dV.$$

Integrating the 2nd and 5th terms over the z -axis becomes zero, and leaves

$$U_e = \frac{1}{2} \int_{-a}^a \left(c_{11}^* A \left(\frac{\partial u}{\partial x} \right)^2 + c_{11}^* I \left(\frac{\partial^2 w}{\partial x^2} \right)^2 - \int_{-h_p/2}^{h_p/2} \left(\frac{\partial u}{\partial x} \right) e_{31}^* b E_z dz \right) dx.$$

Using the definition of E_z from eq. (3.19) and integrating over the z -axis give

$$U_e = \frac{1}{2} \int_{-a}^a \left(c_{11}^* A \left(\frac{\partial u}{\partial x} \right)^2 + c_{11}^* I \left(\frac{\partial^2 w}{\partial x^2} \right)^2 + \left(\frac{\partial u}{\partial x} \right) \frac{e_{31}^*}{h_p} A \phi_e \right) dx.$$

In terms of the elemental local coordinate ξ considering the Jacobian matrix between the xz -plane and ξz -plane, the potential energy becomes

$$U_e = \frac{1}{2} \int_{-1}^1 \left(c_{11}^* A \frac{1}{J^2} \left(\frac{\partial u}{\partial \xi} \right)^2 + c_{11}^* I \frac{1}{J^4} \left(\frac{\partial^2 w}{\partial \xi^2} \right)^2 + \frac{1}{J} \left(\frac{\partial u}{\partial \xi} \right) \frac{e_{31}^*}{h_p} A \phi_e \right) J d\xi. \quad (3.21)$$

With the shape functions for axial and transverse displacements, the nodal axial and transverse displacement vectors of element and constant electric potential difference ϕ_e along the beam length, eq. (3.21), can be changed into an approximate FE form as

3. FE MODELLING OF BEAMS WITH HAPCLD TREATMENTS

$$\begin{aligned}
 U_e &= \frac{1}{2} \mathbf{u}_e^T \frac{1}{J} \int_{-1}^1 c_{11}^* A \mathbf{H}_u'^T(\xi) \mathbf{H}_u'(\xi) d\xi \mathbf{u}_e + \frac{1}{2} \mathbf{w}_e^T \frac{1}{J^3} \int_{-1}^1 c_{11}^* A \mathbf{H}_w'^T(\xi) \mathbf{H}_w''(\xi) d\xi \mathbf{w}_e \\
 &\quad + \frac{1}{2} \mathbf{u}_e^T \int_{-1}^1 \frac{e_{31}^*}{h_p} A \mathbf{H}_u'^T(\xi) d\xi \phi_e \\
 &= \frac{1}{2} \mathbf{u}_e^T \mathbf{k}_{u_e} \mathbf{u}_e + \frac{1}{2} \mathbf{w}_e^T \mathbf{k}_{w_e} \mathbf{w}_e + \frac{1}{2} \mathbf{u}_e^T \mathbf{k}_{u\phi_e} \phi_e.
 \end{aligned} \tag{3.22}$$

Furthermore, the electrical energy can be defined as [88]

$$W_e = \frac{1}{2} \int_{V_e} \left(E_z e_{31}^* \varepsilon_{xx} + E_z e_{15} \varepsilon_{zx} + E_x d c_{11} E_x + E_z d c_{33}^* E_z \right) dV.$$

Since $\varepsilon_{zx} = 0$, substituting the strain terms from eq. (3.5) into the above equation gives

$$W_e = \frac{1}{2} \int_{V_e} \left(E_z e_{31}^* \left(\frac{\partial u}{\partial x} \right) - E_z e_{31}^* z \left(\frac{\partial^2 w}{\partial x^2} \right) + E_x d c_{11} E_x + E_z d c_{33}^* E_z \right) dV.$$

Integrating over the z -axis and considering eq. (3.15) give

$$W_e = \frac{1}{2} \int_{-a}^a \left(-f_e \frac{e_{31}^*}{h_p} A \left(\frac{\partial u}{\partial x} \right) + \frac{d c_{33}^*}{h_p^2} A f_e^2 \right) dx.$$

In terms of the elemental local coordinate ξ , utilising the Jacobian matrix between the xz -plane and ξz -plane,

$$W_e = \frac{1}{2} \int_{-1}^1 \left(-f_e \frac{e_{31}^*}{h_p} A \frac{1}{J} \left(\frac{\partial u}{\partial \xi} \right) + \frac{d c_{33}^*}{h_p^2} A f_e^2 \right) J d\xi. \tag{3.23}$$

Using the same process as for eq. (3.22), eq. (3.23) can be rewritten in the form of a discrete FE equation as

$$\begin{aligned}
 W_e &= \frac{1}{2} \phi_e \int_{-1}^1 -\frac{e_{31}^*}{h_p} A \mathbf{H}_u'(\xi) d\xi \mathbf{u}_e + \frac{1}{2} 2J \frac{d c_{33}^*}{h_p^2} A \phi_e^2 \\
 &= -\frac{1}{2} \phi_e \mathbf{k}_{\phi u_e} \mathbf{u}_e + \frac{1}{2} \phi_e k_{\phi\phi_e} \phi_e.
 \end{aligned} \tag{3.24}$$

3. FE MODELLING OF BEAMS WITH HAPCLD TREATMENTS

Therefore, from eqs. (3.22) and (3.24), the total stiffness matrix of a piezoelectric beam element can be obtained by $U - W_e$. Finally, the FE equation of a piezoelectric Euler beam motion using global mass and stiffness matrices can be derived as

$$\begin{bmatrix} \mathbf{m}_u & \mathbf{0} & \mathbf{0} \\ \mathbf{0} & \mathbf{m}_w & \mathbf{0} \\ \mathbf{0} & \mathbf{0} & \mathbf{0} \end{bmatrix} \ddot{\mathbf{q}} + \begin{bmatrix} \mathbf{k}_u & \mathbf{0} & \mathbf{k}_{u\phi} \\ \mathbf{0} & \mathbf{k}_w & \mathbf{0} \\ \mathbf{k}_{\phi u} & \mathbf{0} & -k_{\phi\phi} \end{bmatrix} \mathbf{q} = \mathbf{f}, \quad (3.25)$$

where global mass and stiffness matrices for axial and transverse displacements \mathbf{m}_u , \mathbf{m}_w , \mathbf{k}_u and \mathbf{k}_w can be derived from matrices for each element \mathbf{m}_{u_e} , \mathbf{m}_{w_e} , \mathbf{k}_{u_e} and \mathbf{k}_{w_e} given in eqs. (3.8) and (3.9) considering the changes of material properties and DOF, and the nodal DOF vector of the whole structure including axial and transverse displacements of structure and electric potential ϕ generated by piezoelectric material is

$$\mathbf{q} = \{\mathbf{u} \quad \mathbf{w} \quad \phi\}^T, \quad (3.26)$$

where the axial displacement vector $\mathbf{u} = \left\{ u_1 \quad \cdots \quad u_{n+1} \right\}$ and transverse displacement vector $\mathbf{w} = \left\{ w_1 \quad \theta_1 \quad \cdots \quad w_{n+1} \quad \theta_{n+1} \right\}$,

and external exciting force and charge vector is

$$\mathbf{f} = \{\mathbf{f}_x \quad \mathbf{f}_z \quad Q\}^T, \quad (3.27)$$

where the exciting force vector in the x -direction $\mathbf{f}_x = \left\{ f_{x1} \quad \cdots \quad f_{x(n+1)} \right\}$, exciting force

vector in the z -direction $\mathbf{f}_z = \left\{ f_{z1} \quad M_1 \quad \cdots \quad f_{z(n+1)} \quad M_{n+1} \right\}$ and electrical charge Q means electrical charge.

In this section, FE mass and stiffness matrices of a piezoelectric beam structure are derived from kinetic and potential energy equations using the assumption of the Euler beam theory and constitutive equations of piezoelectric materials. In the next section, a method to consider shear deformation of viscoelastic materials will be studied based on the Timoshenko beam theory when it is in the form of a viscoelastic layer in a sandwich structure.

3.4 FE model for a laminated beam with one viscoelastic layer

In this section, FE modelling of a viscoelastic layer constrained between two elastic beams will be studied by introducing the Timoshenko beam theory and the GHM method. This layer is modelled as a Timoshenko beam model so as to consider the shear deformation. Moreover, a viscoelastic model, which can describe the change of elastic properties with temperature and frequency, is introduced. Thus, the shear modulus proposed by the GHM method is used. The case in which the viscoelastic layer is constrained between two elastic beams, which are assumed to act as Euler beams, will be considered here for simplicity. In this thesis, all the configurations of HAPCLD treatments have the viscoelastic layer always constrained between two elastic layers. In fact, as seen in the previous section, the piezoelectric layer can be assumed to be elastic.

3.4.1 GHM method for viscoelastic material

In order to understand the dynamic response of viscoelastic materials, the study of viscoelastic models is required. Classic viscoelastic models have been used a combination of the basic elements given in Figure 3.5 to explain the dynamic response of viscoelastic materials [90]. Material properties of each model can be adjusted to match the dynamic response of viscoelastic materials.

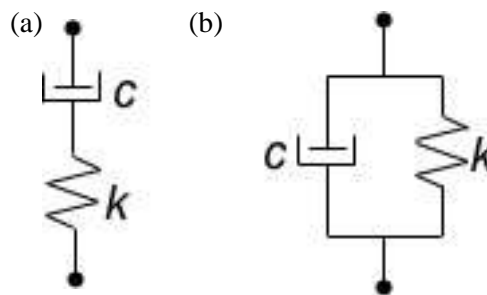


Figure 3.5 Classic viscoelastic element: (a) Maxwell material and (b) Kelvin material

Even if viscoelastic materials are only under shear deformation as in the case of constraining layer damping, these elemental viscoelastic models can be used. The relation between shear stiffness and shear modulus can be explained by eq. (3.28) for the structure under deformation shown in Figure 3.6.

3. FE MODELLING OF BEAMS WITH HAPCLD TREATMENTS

$$G = \frac{t_{xz}}{g_{xz}} = \frac{F/A}{\Delta w/l} = \frac{Fl}{A\Delta w} = k \frac{l}{A} \Rightarrow k = \frac{GA}{l}, \quad (3.28)$$

where G is shear modulus, t_{xz} and g_{xz} denote shear stress and shear strain respectively. F , A , Δw and l mean applied force, cross-sectional area, transverse displacement and initial length of viscoelastic material respectively.

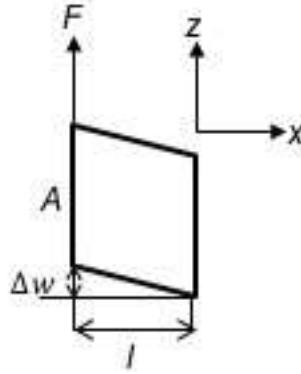


Figure 3.6 Shear deformation of viscoelastic materials

Among various viscoelastic models, the GHM method proposed by McTavish and Hughes [91] has been widely used for FE modelling of viscoelastic materials. In the GHM method, the viscoelastic model is defined by the combination of basic elements as shown in Figure 3.7. Going from the dynamic stiffness to the shear modulus gives eq. 3.29 [91].

$$G^*(f) = G^\infty \left[1 + \sum_n a_n \frac{s^2 + 2\hat{Z}_n \hat{W}_n s}{s^2 + 2\hat{Z}_n \hat{W}_n s + \hat{W}_n^2} \right], \quad (3.29)$$

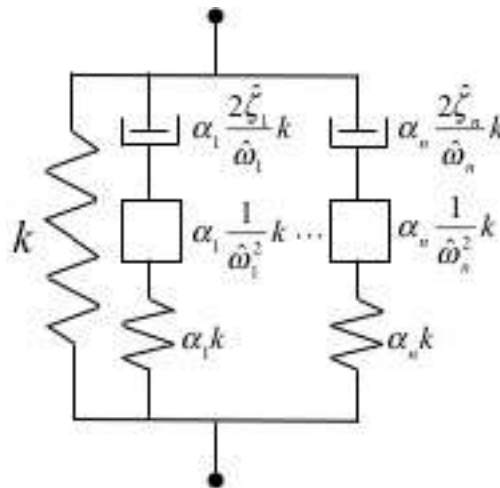


Figure 3.7 GHM model for viscoelastic material

3. FE MODELLING OF BEAMS WITH HAPCLD TREATMENTS

where f is the frequency in Hz, $s = i\omega = i2\pi f$. G^∞ is the asymptotic value of shear modulus of the viscoelastic layer after step change in strain. All the variables α_k , $\hat{\zeta}_k$ and $\hat{\omega}_k$ in eq. (3.29) which govern the shape of the modulus function over the complex plane can be obtained by a curve fitting from measured data as has been done in [11]. The real part of $G^*(f)$ represents the frequency-dependent shear modulus and the ratio of imaginary values of $G^*(f)$ over real values of $G^*(f)$ represents the frequency-dependent shear modulus loss factor. Figure 3.8 shows that such a model captures the change of the shear modulus and loss factor according to the change of frequency with the GHM model with three mini-oscillators. The same viscoelastic material given in [91] was used in this thesis for simulations and experiments using real structures. Detailed values for each variable are given in the figure and Table 4.2 in Section 4.1.2.

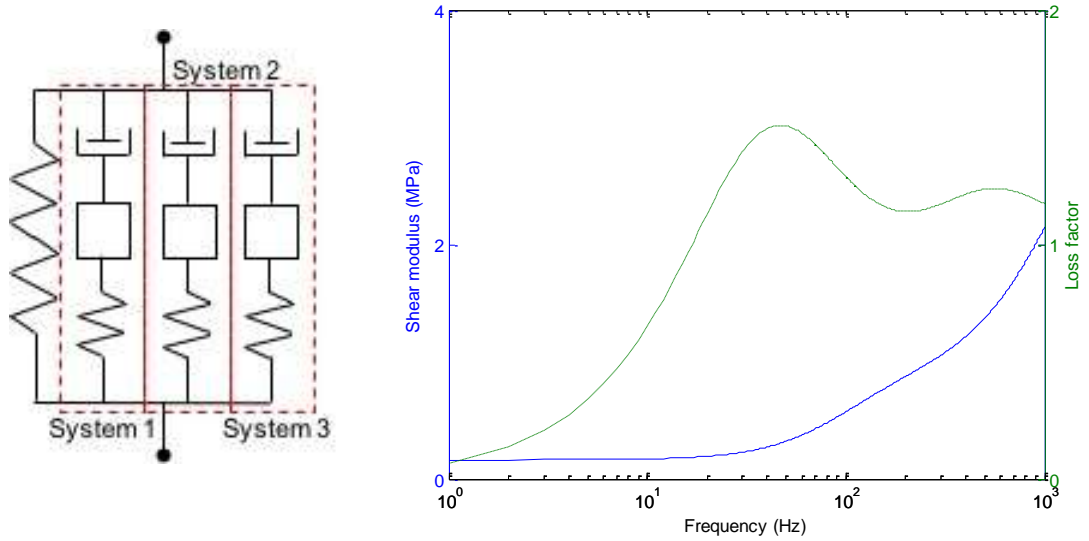


Figure 3.8 Shear modulus and Loss factor of viscoelastic material: — Shear modulus; - - - Loss factor for $G^\infty = 0.1633$ MPa, $a_1 = 4.8278$, $a_2 = 14.548$, $a_3 = 40.043$, $\hat{z}_1 = 22.013$, $\hat{z}_2 = 3.1275$, $\hat{z}_3 = 0.6165$, $\hat{w}_1 = 22.013$, $\hat{w}_2 = 3.1275$ and $\hat{w}_3 = 0.6165$

3.4.2 Basic assumptions for a viscoelastic layer constrained between two elastic beams

As shown in Figure 3.1, all viscoelastic layers are constrained between two layers which are elastic or piezoelectric. Since the deformation of viscoelastic layer is different in PULD and HAPCLD treatments as explained in Section 1.1, only viscoelastic layers constrained between two layers will be studied in this section.

3. FE MODELLING OF BEAMS WITH HAPCLD TREATMENTS

If a viscoelastic layer constrained between two elastic beams, as shown in Figure 3.9, is subject to a bending motion in z -direction, axial displacements u_i and transverse displacements w_i of each layer can be defined along the neutral axes of each layer. In Figure 3.9, subscripts 1, 2 and 3 denote cover beam, viscoelastic layer and base beam respectively. Each layer has a thickness of h_i and density ρ_i . Cover and base beams have Young's modulus E_1 and E_3 , and the viscoelastic layer has a shear modulus G^* , which will be defined by the GHM method. Finally, the cover and base beams are assumed to have the same rotation θ . For this structure, the following two basic assumptions are proposed [2]:

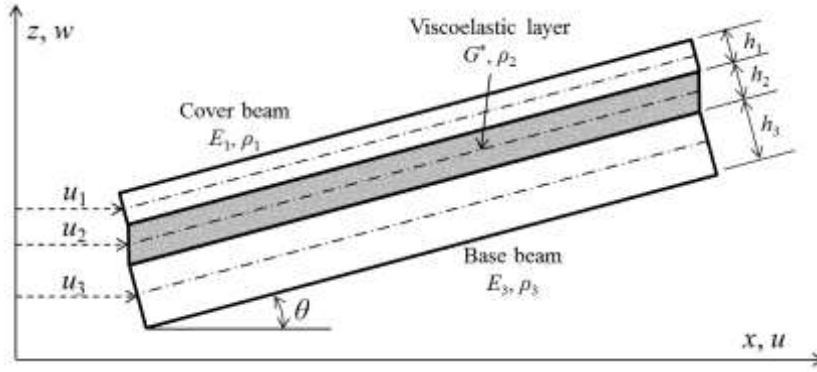


Figure 3.9 Geometric concept of a viscoelastic layer constrained between two elastic beams

(1) Shear strains in the base and cover beams are negligible: $\frac{\partial u_1}{\partial z} \approx 0$ and $\frac{\partial u_3}{\partial z} \approx 0$, and longitudinal direct strain in the viscoelastic layer is negligible: $\frac{\partial u_2}{\partial x} \approx 0$.

(2) Transverse direct strains in the viscoelastic layer, base and cover beams are also neglected, so the transverse displacements w of all points on the same cross-section of all layers before deformation are equal: $w_1 = w_2 = w_3$.

According to these basic assumptions, the shear strain and stress on the centreline line of a viscoelastic layer can be defined respectively considering eq. (3.1) as

$$\gamma = \frac{\partial w(x)}{\partial x} + \frac{\partial u_2(x, 0)}{\partial z} = \frac{\partial w(x)}{\partial x} + \frac{\partial u_2(x)}{\partial z} \quad (3.30)$$

and

$$\tau = G^* \int_{-b/2}^{b/2} \int_{-h_2/2}^{h_2/2} \gamma dz dy = G^* A \left(\frac{\partial w(x)}{\partial x} + \frac{\partial u_2(x)}{\partial z} \right), \quad (3.31)$$

where G^* is the complex shear modulus of the viscoelastic layer.

3.4.3 FE formulation of a viscoelastic layer constrained between two elastic beams

The kinetic energy of a beam element for viscoelastic layer constrained between two elastic beams with a length of $2a$ shown in Figure 3.5 can be defined as

$$T_e = \frac{1}{2} \int_{-a}^a (\rho_2 A_2 \dot{u}_2^2 + \rho_2 A_2 \dot{w}_2^2) dx.$$

By transferring the coordinate from the xz -plane to the ξz -plane with the Jacobian term,

$$T_e = \frac{1}{2} \int_{-1}^1 (\rho_2 A_2 \dot{u}_2^2 + \rho_2 A_2 \dot{w}_2^2) J d\xi. \quad (3.32)$$

If the process for finite element discretisation from the continuous structure equation done in Section 3.2.2 is applied again here, eq. (3.32) can be rewritten as

$$\begin{aligned} T_e &= \frac{1}{2} \dot{\mathbf{u}}_e^T \mathbf{m}_{u_e} \dot{\mathbf{u}}_e + \frac{1}{2} \dot{\mathbf{w}}_e^T \mathbf{m}_{w_e} \dot{\mathbf{w}}_e \\ &= \frac{1}{2} \dot{\mathbf{q}}_e^T \mathbf{m}_e \dot{\mathbf{q}}_e, \end{aligned} \quad (3.33)$$

where $\dot{\mathbf{q}}_e = \left\{ \begin{matrix} \dot{\mathbf{u}}_e & \dot{\mathbf{w}}_e & \dot{\boldsymbol{\theta}}_e & \frac{\partial \dot{\mathbf{u}}_e}{\partial z} \end{matrix} \right\}^T$ are changes in the nodal DOF vector of each FE ele-

ment and $\mathbf{m}_e = \begin{bmatrix} \mathbf{m}_{u_e} & \mathbf{0} & \mathbf{0} & \mathbf{0} \\ \mathbf{0} & \mathbf{m}_{w_e} & \mathbf{m}_{w_e} & \mathbf{0} \\ \mathbf{0} & \mathbf{m}_{w_e} & \mathbf{m}_{w_e} & \mathbf{0} \\ \mathbf{0} & \mathbf{0} & \mathbf{0} & \mathbf{0} \end{bmatrix}$ is the mass matrix of each FE element.

Furthermore, when considering only shear deformation exists in the viscoelastic layer, the potential energy of the same beam can be expressed as

3. FE MODELLING OF BEAMS WITH HAPCLD TREATMENTS

$$U_e = \frac{1}{2} \int_{-a}^a G^* A_2 \gamma^2 dx.$$

From the definition of shear stress in the viscoelastic layer eq. (3.31),

$$\begin{aligned} U_e &= \frac{1}{2} \int_{-a}^a \left(G^* A_2 \left(\frac{\partial w}{\partial x} + \frac{\partial u_2}{\partial z} \right)^2 \right) dx \\ &= \frac{1}{2} \int_{-1}^1 \left(G^* A_2 \left(\frac{1}{J^2} \left(\frac{\partial w}{\partial \chi} \right)^2 \frac{1}{J} \frac{\partial w}{\partial \chi} \frac{\partial u_2}{\partial z} + \left(\frac{\partial u_2}{\partial z} \right)^2 \right) \right) J d\chi. \end{aligned} \quad (3.34)$$

Thus, eq. (3.34) can be expressed by using the shape functions of a beam element as [92]

$$\begin{aligned} U_e &= \frac{1}{2} \mathbf{w}_e^T \frac{1}{J} \int_{-1}^1 G^* A_2 \mathbf{H}_w'^T(\chi) \mathbf{H}_w'(\chi) d\chi \mathbf{w}_e + \frac{1}{2} \mathbf{w}_e^T \int_{-1}^1 G^* A_2 \mathbf{H}_w'^T(\chi) \mathbf{H}_u(\chi) d\chi \left(\frac{\partial \mathbf{u}_e}{\partial z} \right) \\ &\quad + \frac{1}{2} \left(\frac{\partial \mathbf{u}_e}{\partial z} \right)^T \int_{-1}^1 G^* A_2 \mathbf{H}_u^T(\chi) \mathbf{H}_w'(\chi) d\chi \mathbf{w}_e + \frac{1}{2} \left(\frac{\partial \mathbf{u}_e}{\partial z} \right)^T J \int_{-1}^1 G^* A_2 \mathbf{H}_u^T(\chi) \mathbf{H}_u(\chi) d\chi \left(\frac{\partial \mathbf{u}_e}{\partial z} \right) \\ &= \frac{1}{2} \mathbf{w}_e^T \mathbf{k}_{Gw_e} \mathbf{w}_e + \frac{1}{2} \mathbf{w}_e^T \mathbf{k}_{Gwu_e} \left(\frac{\partial \mathbf{u}_e}{\partial z} \right) + \frac{1}{2} \left(\frac{\partial \mathbf{u}_e}{\partial z} \right)^T \mathbf{k}_{Guw_e} \mathbf{w}_e + \frac{1}{2} \left(\frac{\partial \mathbf{u}_e}{\partial z} \right)^T \mathbf{k}_{Gu_e} \left(\frac{\partial \mathbf{u}_e}{\partial z} \right) \\ &= \frac{1}{2} \mathbf{q}_e^T \mathbf{k}_e \mathbf{q}_e, \end{aligned} \quad (3.35)$$

where the nodal DOF vector of each FE element $\mathbf{q}_e = \left\{ \begin{matrix} \mathbf{u}_e & \mathbf{w}_e & \boldsymbol{\theta}_e & \frac{\partial \mathbf{u}_e}{\partial z} \end{matrix} \right\}^T$ and stiffness

$$\text{matrix of each FE element } \mathbf{k}_e = \begin{bmatrix} \mathbf{0} & \mathbf{0} & \mathbf{0} & \mathbf{0} \\ \mathbf{0} & \mathbf{k}_{Gw_e} & \mathbf{0} & \mathbf{k}_{Gwu_e} \\ \mathbf{0} & \mathbf{0} & \mathbf{0} & \mathbf{0} \\ \mathbf{0} & \mathbf{k}_{Guw_e} & \mathbf{0} & \mathbf{k}_{Gu_e} \end{bmatrix}.$$

Therefore, the FE equation of motion for the whole structure can be derived from eqs. (3.33) and (3.35) by combining each FE matrix as

$$\begin{bmatrix} \mathbf{m}_u & \mathbf{0} & \mathbf{0} & \mathbf{0} \\ \mathbf{0} & \mathbf{m}_w & \mathbf{m}_w & \mathbf{0} \\ \mathbf{0} & \mathbf{m}_w & \mathbf{m}_w & \mathbf{0} \\ \mathbf{0} & \mathbf{0} & \mathbf{0} & \mathbf{0} \end{bmatrix} \ddot{\mathbf{q}} + \begin{bmatrix} \mathbf{0} & \mathbf{0} & \mathbf{0} & \mathbf{0} \\ \mathbf{0} & \mathbf{k}_{Gw} & \mathbf{0} & \mathbf{k}_{Gwu} \\ \mathbf{0} & \mathbf{0} & \mathbf{0} & \mathbf{0} \\ \mathbf{0} & \mathbf{k}_{Guw} & \mathbf{0} & \mathbf{k}_{Gu} \end{bmatrix} \mathbf{q} = \mathbf{f}, \quad (3.36)$$

where the nodal DOF vector of the whole structure is

$$\mathbf{q} = \left\{ u_{2_1} \quad \cdots \quad u_{2_{n+1}} \quad w_1 \quad \theta_1 \quad \cdots \quad w_{n+1} \quad \theta_{n+1} \quad \frac{\partial u_{2_1}}{\partial z} \quad \cdots \quad \frac{\partial u_{2_{n+1}}}{\partial z} \right\}^T \quad (3.37)$$

and the external exciting force vector is

$$\mathbf{f} = \left\{ f_{x_{2_1}} \quad \cdots \quad f_{x_{2_{(n+1)}}} \quad f_{z_1} \quad M_1 \quad \cdots \quad f_{z_{(n+1)}} \quad M_{n+1} \quad f_{s_1} \quad \cdots \quad f_{s_{(n+1)}} \right\}^T, \quad (3.38)$$

where f_{si} refers to the shear force acting on the i -th node.

3.4.4 Coupling method for a laminated beam

All required equations for each layer of HAPCLD treatments have been derived. Therefore, coupling terms which can explain possible mutual interaction between axial and transverse motions of each layer in lamination should be proposed for proper description of HAPCLD treatments' motions. Although the coupling method which describes the axial displacement of viscoelastic layer u_2 as half value of difference between axial displacements in cover and base beam (u_1 and u_3) was proposed by Mead and Markus [2], this method is only valid for a three-layered structure which has a viscoelastic layer as a core layer as in Figure 3.9. Since more complex and laminated structures will be taken into account, a layer-wise approach, as proposed by Ferreira [93], is used, which can express motions in each layer in terms of motion at the neutral axis of a whole structure. For the layer-wise approach, the introduction of extra shape functions is not necessary.

For example, the geometrical deformation of the three-layered structure consisting of an elastic cover beam, a viscoelastic layer and an elastic base beam, shown in Figure 3.9, can be explained again by introducing the neutral axis of a whole structure x_0 as in Figure 3.10. Each layer has a thickness of h_1 , h_2 and h_3 respectively as in Figure 3.5 and local longitudinal axes x_1 , x_2 and x_3 are set up on neutral axes of each layer respectively. Axial displacements u_1 , u_2 and u_3 can be

3. FE MODELLING OF BEAMS WITH HAPCLD TREATMENTS

determined in terms of the axial displacement on x_0 -axis, u_0 , the distances between neutral axes x_i ($i = 1, 2$ and 3) and x_0 -axis, rotation θ and shear deformation of the viscoelastic layer.

Since transverse displacement and rotation at all points over a cross-section are the same in the structure, axial displacement, u , transverse displacement, w , and rotation of the cross section, θ , of each layer can be expressed as

$$\begin{aligned} u_1 &= u_0 - \left(\frac{h_1}{2} + \frac{h_3}{2} - d_3 \right) q_0 + h_2 \frac{\partial u_0}{\partial z}, \quad w_1 = w_0, \quad \theta_1 = \theta_0, \quad \frac{\partial u_1}{\partial z} = 0, \\ u_2 &= u_0 - \left(\frac{h_3}{2} - d_3 \right) \theta_0 + \frac{h_2}{2} \frac{\partial u_0}{\partial z}, \quad w_2 = w_0, \quad \theta_2 = 0, \quad \frac{\partial u_2}{\partial z} = \frac{\partial u_0}{\partial z} \text{ and} \\ u_3 &= u_0 + d_3 \theta_0, \quad w_3 = w_0, \quad \theta_3 = \theta_0, \quad \frac{\partial u_3}{\partial z} = 0. \end{aligned} \quad (3.39)$$

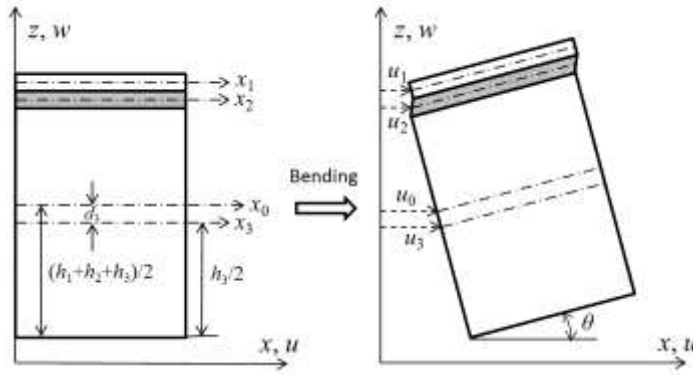


Figure 3.10 Basic concept of layer-wise approach model for a sandwich beam with a viscoelastic core

Therefore, if eq. (3.39) is expressed in a matrix form as

$$\begin{Bmatrix} \mathbf{u}_1 \\ \mathbf{u}_2 \\ \mathbf{u}_3 \end{Bmatrix} = \mathbf{C} \mathbf{u}_0,$$

where local displacement vectors $\mathbf{u}_1 = \left\{ u_1 \quad w_1 \quad q_1 \quad \frac{\partial u_1}{\partial z} \right\}^T$, $\mathbf{u}_2 = \left\{ u_2 \quad w_2 \quad q_2 \quad \frac{\partial u_2}{\partial z} \right\}^T$,

$\mathbf{u}_3 = \left\{ u_3 \quad w_3 \quad q_3 \quad \frac{\partial u_3}{\partial z} \right\}^T$ and global displacement vector $\mathbf{u}_0 = \left\{ u_0 \quad w_0 \quad q_0 \quad \frac{\partial u_0}{\partial z} \right\}^T$, a

coupling matrix of a three-layered beam explaining the relation between DOFs on the neutral axis of a whole system and of each layer can be expressed as

3. FE MODELLING OF BEAMS WITH HAPCLD TREATMENTS

$$\mathbf{C} = \begin{bmatrix} 1 & 0 & 0 & 0 & 1 & 0 & 0 & 0 & 1 & 0 & 0 & 0 \\ 0 & 1 & 0 & 0 & 0 & 1 & 0 & 0 & 0 & 1 & 0 & 0 \\ -\left(\frac{h_1}{2} + \frac{h_3}{2} - d_3\right) & 0 & 1 & 0 & -\left(\frac{h_3}{2} - d_3\right) & 0 & 0 & 0 & d_3 & 0 & 1 & 0 \\ h_2 & 0 & 0 & 0 & \frac{h_2}{2} & 0 & 0 & 1 & 0 & 0 & 0 & 0 \end{bmatrix}^T \quad (3.40)$$

Similarly, the relationship between local and global force vectors can be expressed using a coupling matrix as

$$\begin{Bmatrix} \mathbf{f}_1 \\ \mathbf{f}_2 \\ \mathbf{f}_3 \end{Bmatrix} = \mathbf{C} \mathbf{f}_0,$$

where local force vectors $\mathbf{f}_1 = \begin{Bmatrix} f_{x1} & f_{z1} & M_1 & f_{s1} \end{Bmatrix}^T$, $\mathbf{f}_2 = \begin{Bmatrix} f_{x2} & f_{z2} & M_2 & f_{s2} \end{Bmatrix}^T$, $\mathbf{f}_3 = \begin{Bmatrix} f_{x3} & f_{z3} & M_3 & f_{s3} \end{Bmatrix}^T$ and global force vector $\mathbf{f}_0 = \begin{Bmatrix} f_{x0} & f_{z0} & M_0 & f_{s0} \end{Bmatrix}^T$.

By multiplying this coupling matrix and the transverse matrix of the coupling matrix in eq. (3.39) to mass and stiffness matrices, equivalent mass and stiffness matrices can be derived.

$$\begin{aligned} & \left(-\mathcal{W}^2 \mathbf{M}_{\text{lami}} + \mathbf{K}_{\text{lami}} \right) \begin{Bmatrix} \mathbf{u}_1 \\ \mathbf{u}_2 \\ \mathbf{u}_3 \end{Bmatrix} = \begin{Bmatrix} \mathbf{f}_1 \\ \mathbf{f}_2 \\ \mathbf{f}_3 \end{Bmatrix} \\ & \Rightarrow \mathbf{C}^T \left(-\mathcal{W}^2 \mathbf{M}_{\text{lami}} + \mathbf{K}_{\text{lami}} \right) \mathbf{C} \mathbf{u}_0 = \mathbf{f}_0 \\ & \Rightarrow \left(-\mathcal{W}^2 \mathbf{M}_{\text{eq}} + \mathbf{K}_{\text{eq}} \right) \mathbf{u}_0 = \mathbf{f}_0, \end{aligned} \quad (3.41)$$

$$\text{where } \mathbf{M}_{\text{lami}} = \begin{bmatrix} \mathbf{M}_1 & \mathbf{0} & \mathbf{0} \\ \mathbf{0} & \mathbf{M}_2 & \mathbf{0} \\ \mathbf{0} & \mathbf{0} & \mathbf{M}_3 \end{bmatrix} \text{ and } \mathbf{K}_{\text{lami}} = \begin{bmatrix} \mathbf{K}_1 & \mathbf{0} & \mathbf{0} \\ \mathbf{0} & \mathbf{K}_2 & \mathbf{0} \\ \mathbf{0} & \mathbf{0} & \mathbf{K}_3 \end{bmatrix}, \mathbf{M}_{\text{eq}} = \mathbf{C}^T \mathbf{M}_{\text{lami}} \mathbf{C} \text{ and}$$

$\mathbf{K}_{\text{eq}} = \mathbf{C}^T \mathbf{K}_{\text{lami}} \mathbf{C}$. \mathbf{M}_i and \mathbf{K}_i are mass and stiffness matrices of i-th layer which can be obtained from eq. (3.10) for elastic beams and eq. (3.36) for viscoelastic layers.

3. FE MODELLING OF BEAMS WITH HAPCLD TREATMENTS

Moreover, as has been done in this section, the equivalent mass and stiffness matrices of more complex and laminated structures can be obtained by considering the geometrical deformation and relationship between each layer.

3.5 FE model for a beam with HAPCLD treatment

Simply by introducing the FE model for a piezoelectric beam explained in Section 3.3 as a cover beam to the FE model for a laminated beam with a viscoelastic layer constrained between two elastic beams in Section 3.4.3, an FE model for a beam with HAPCLD treatment can be obtained. For example, for a beam with active constrained layer damping (ACL D) treatment shown in Figure 3.11, in which the cover layer is replaced with a piezoelectric material, matrix equations of motion with global mass and stiffness matrices can be expressed from local matrices as follows.

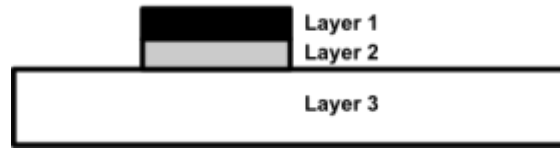





Figure 3.11 Configuration of a beam with ACLD treatment;  : elastic beam,  : viscoelastic layer and  : piezoelectric patch

The equations of motion in the cover layer (piezoelectric beam) are obtained from eq. (3.25) as

$$\begin{bmatrix} \mathbf{m}_{u_1} & 0 & 0 & 0 & 0 \\ 0 & \mathbf{m}_{w_1} & \mathbf{m}_{w_1} & 0 & 0 \\ 0 & \mathbf{m}_{w_1} & \mathbf{m}_{w_1} & 0 & 0 \\ 0 & 0 & 0 & 0 & 0 \\ 0 & 0 & 0 & 0 & 0 \end{bmatrix} \ddot{\mathbf{q}}_1 + \begin{bmatrix} \mathbf{k}_{u_1} & 0 & 0 & 0 & \mathbf{k}_{u\phi} \\ 0 & \mathbf{k}_{w_1} & \mathbf{k}_{w_1} & 0 & 0 \\ 0 & \mathbf{k}_{w_1} & \mathbf{k}_{w_1} & 0 & 0 \\ 0 & 0 & 0 & 0 & 0 \\ \mathbf{k}_{\phi u} & 0 & 0 & 0 & -k_{\phi\phi} \end{bmatrix} \mathbf{q}_1 = \mathbf{M}_1 \ddot{\mathbf{q}}_1 + \mathbf{K}_1 \mathbf{q}_1 = \mathbf{f}_1,$$

$$\text{where } \mathbf{q}_1 = \left\{ u_{1_1} \quad \cdots \quad u_{1_{n+1}} \quad w_{1_1} \quad \theta_{1_1} \quad \cdots \quad w_{1_{n+1}} \quad \theta_{1_{n+1}} \quad \frac{\partial u_{1_1}}{\partial z} \quad \cdots \quad \frac{\partial u_{1_{n+1}}}{\partial z} \quad \phi_1 \right\}^T \text{ and}$$

$$\mathbf{f}_1 = \left\{ f_{x_1 1} \quad \cdots \quad f_{x_1(n+1)} \quad f_{z_1 1} \quad M_{1_1} \quad \cdots \quad f_{z_1(n+1)} \quad M_{1_{n+1}} \quad f_{s_1 1} \quad \cdots \quad f_{s_1(n+1)} \quad Q_1 \right\}^T,$$

where each term is the same as is used in eq. (3.25).

3. FE MODELLING OF BEAMS WITH HAPCLD TREATMENTS

The core layer (viscoelastic material) equations are obtained from eq. (3.36) as

$$\begin{bmatrix} \mathbf{m}_{u_2} & 0 & 0 & 0 & 0 \\ 0 & \mathbf{m}_{w_2} & \mathbf{m}_{w_2} & 0 & 0 \\ 0 & \mathbf{m}_{w_2} & \mathbf{m}_{w_2} & 0 & 0 \\ 0 & 0 & 0 & 0 & 0 \\ 0 & 0 & 0 & 0 & 0 \end{bmatrix} \ddot{\mathbf{q}}_2 + \begin{bmatrix} 0 & 0 & 0 & 0 & 0 \\ 0 & \mathbf{k}_{Gw} & 0 & \mathbf{k}_{Gwu} & 0 \\ 0 & 0 & 0 & 0 & 0 \\ 0 & \mathbf{k}_{Guw} & 0 & \mathbf{k}_{Gu} & 0 \\ 0 & 0 & 0 & 0 & 0 \end{bmatrix} \mathbf{q}_2 = \mathbf{M}_2 \ddot{\mathbf{q}}_2 + \mathbf{K}_2 \mathbf{q}_2 = \mathbf{f}_2,$$

where $\mathbf{q}_2 = \left\{ u_{2_1} \quad \cdots \quad u_{2_{n+1}} \quad w_{2_1} \quad \theta_{2_1} \quad \cdots \quad w_{2_{n+1}} \quad \theta_{2_{n+1}} \quad \frac{\partial u_{2_1}}{\partial z} \quad \cdots \quad \frac{\partial u_{2_{n+1}}}{\partial z} \quad \phi_2 \right\}^T$ and

$$\mathbf{f}_2 = \left\{ f_{x_{2_1}} \quad \cdots \quad f_{x_{2_{(n+1)}}} \quad f_{z_{2_1}} \quad M_{2_1} \quad \cdots \quad f_{z_{2_{(n+1)}}} \quad M_{2_{n+1}} \quad f_{s_{2_1}} \quad \cdots \quad f_{s_{2_{(n+1)}}} \quad Q_2 \right\}^T,$$

where each term is the same as is used in eq. (3.36).

The base layer (elastic beam) equations are obtained from eqs. (3.8) and (3.9) as

$$\begin{bmatrix} \mathbf{m}_{u_3} & 0 & 0 & 0 & 0 \\ 0 & \mathbf{m}_{w_3} & \mathbf{m}_{w_3} & 0 & 0 \\ 0 & \mathbf{m}_{w_3} & \mathbf{m}_{w_3} & 0 & 0 \\ 0 & 0 & 0 & 0 & 0 \\ 0 & 0 & 0 & 0 & 0 \end{bmatrix} \ddot{\mathbf{q}}_3 + \begin{bmatrix} \mathbf{k}_{u_3} & 0 & 0 & 0 & 0 \\ 0 & \mathbf{k}_{w_3} & \mathbf{k}_{w_3} & 0 & 0 \\ 0 & \mathbf{k}_{w_3} & \mathbf{k}_{w_3} & 0 & 0 \\ 0 & 0 & 0 & 0 & 0 \\ 0 & 0 & 0 & 0 & 0 \end{bmatrix} \mathbf{q}_3 = \mathbf{M}_3 \ddot{\mathbf{q}}_3 + \mathbf{K}_3 \mathbf{q}_3 = \mathbf{f}_3,$$

where $\mathbf{q}_3 = \left\{ u_{3_1} \quad \cdots \quad u_{3_{n+1}} \quad w_{3_1} \quad \theta_{3_1} \quad \cdots \quad w_{3_{n+1}} \quad \theta_{3_{n+1}} \quad \frac{\partial u_{3_1}}{\partial z} \quad \cdots \quad \frac{\partial u_{3_{n+1}}}{\partial z} \quad \phi_3 \right\}^T$ and

$$\mathbf{f}_3 = \left\{ f_{x_{3_1}} \quad \cdots \quad f_{x_{3_{(n+1)}}} \quad f_{z_{3_1}} \quad M_{3_1} \quad \cdots \quad f_{z_{3_{(n+1)}}} \quad M_{3_{n+1}} \quad f_{s_{3_1}} \quad \cdots \quad f_{s_{3_{(n+1)}}} \quad Q_3 \right\}^T,$$

where each term is the same as is used in eqs. (3.8) and (3.9).

Therefore, after stacking mass and stiffness matrices for local coordinates into one matrix respectively according to the order of layer, the coupling matrix \mathbf{C} can be expressed as follows:

$$\mathbf{C} = \begin{bmatrix} 1 & 0 & 0 & 0 & 0 & 1 & 0 & 0 & 0 & 0 & 1 & 0 & 0 & 0 & 0 \\ 0 & 1 & 0 & 0 & 0 & 0 & 1 & 0 & 0 & 0 & 0 & 1 & 0 & 0 & 0 \\ -\left(\frac{h_1}{2} + \frac{h_3}{2} - d_3\right) & 0 & 1 & 0 & 0 & -\left(\frac{h_3}{2} - d_3\right) & 0 & 0 & 0 & 0 & d_3 & 0 & 1 & 0 & 0 \\ h_2 & 0 & 0 & 0 & 0 & h_2/2 & 0 & 0 & 1 & 0 & 0 & 0 & 0 & 0 & 0 \\ 0 & 0 & 0 & 0 & 1 & 0 & 0 & 0 & 0 & 0 & 0 & 0 & 0 & 0 & 0 \end{bmatrix}^T$$

3. FE MODELLING OF BEAMS WITH HAPCLD TREATMENTS

By multiplying this coupling matrix and the transverse matrix of the coupling matrix to the stacked mass and stiffness matrices, equivalent mass and stiffness matrices can be derived as explained in the previous section.

Finally, the global matrix equation of motion can be obtained by applying boundary conditions after multiplying the coupling matrix as

$$\mathbf{M}\ddot{\mathbf{q}} + \mathbf{K}\mathbf{q} = \mathbf{f}, \quad (3.42)$$

$$\text{where } \mathbf{M} = \mathbf{C}^T \begin{bmatrix} \mathbf{M}_1 & \mathbf{0} & \mathbf{0} \\ \mathbf{0} & \mathbf{M}_2 & \mathbf{0} \\ \mathbf{0} & \mathbf{0} & \mathbf{M}_3 \end{bmatrix} \mathbf{C}, \quad \mathbf{K} = \mathbf{C}^T \begin{bmatrix} \mathbf{K}_1 & \mathbf{0} & \mathbf{0} \\ \mathbf{0} & \mathbf{K}_2 & \mathbf{0} \\ \mathbf{0} & \mathbf{0} & \mathbf{K}_3 \end{bmatrix} \mathbf{C},$$

$$\mathbf{q} = \left\{ u_1 \quad \cdots \quad u_{n+1} \quad w_1 \quad \theta_1 \quad \cdots \quad w_{n+1} \quad \theta_{n+1} \quad \frac{\partial u_1}{\partial z} \quad \cdots \quad \frac{\partial u_{n+1}}{\partial z} \quad \phi \right\}^T \text{ and}$$

$$\mathbf{f} = \left\{ f_{x1} \quad \cdots \quad f_{x(n+1)} \quad f_{z1} \quad M_1 \quad \cdots \quad f_{z(n+1)} \quad M_{n+1} \quad f_{s1} \quad \cdots \quad f_{s(n+1)} \quad Q \right\}^T.$$

When applying boundary conditions to this kind of structure, which has a small patch covering a part of the structure, shear deformation terms which do not exist on nodes where a viscoelastic layer does not cover must be eliminated carefully. Since the electrical difference term ϕ is the same along all nodes covered by electrodes, it is constant in the whole structure.

If the elastic constraining patch is added in other configurations as shown in Figure 3.12, mass and stiffness matrices of the base layer can be reused by using different coupling matrices.



Figure 3.12 Configuration of a beam with (a) APCLD treatment, (b) AC/PCLD treatment and (c) AC/PSOLD treatment;
 : elastic beam and patch, : viscoelastic layer and : piezoelectric patch

Eq. (3.39) is valid only for an ACLD treatment. Continuity of displacement can be written for an APCLD treatment as shown in Figure 3.12 (a). If a constraining patch is defined with subscript 'c' (subscript '1' means piezoelectric patch, '2' viscoelastic layer and '3' elastic base beam as ACLD case), axial and transverse displacements and rotations in each case as in Figure 3.12 (a) can be defined:

3. FE MODELLING OF BEAMS WITH HAPCLD TREATMENTS

$$\begin{aligned}
u_c &= u_0 - \left(\frac{h_c}{2} + h_1 + \frac{h_3}{2} - d_3 \right) \theta_0 + h_2 \frac{\partial u_0}{\partial z}, \quad w_c = w_0, \quad \theta_c = \theta_0, \quad \frac{\partial u_c}{\partial z} = 0, \\
u_1 &= u_0 - \left(\frac{h_1}{2} + \frac{h_3}{2} - d_3 \right) \theta_0 + h_2 \frac{\partial u_0}{\partial z}, \quad w_1 = w_0, \quad \theta_1 = \theta_0, \quad \frac{\partial u_1}{\partial z} = 0, \\
u_2 &= u_0 - \left(\frac{h_3}{2} - d_3 \right) \theta_0 + \frac{h_2}{2} \frac{\partial u_0}{\partial z}, \quad w_2 = w_0, \quad \theta_2 = 0, \quad \frac{\partial u_2}{\partial z} = \frac{\partial u_0}{\partial z} \text{ and} \\
u_3 &= u_0 + d_3 \theta_0, \quad w_3 = w_0, \quad \theta_3 = \theta_0, \quad \frac{\partial u_3}{\partial z} = 0.
\end{aligned} \tag{3.43}$$

For an AC/PCLD treatment as shown in Figure 3.12 (b), the relationship between displacements of each layer becomes

$$\begin{aligned}
u_c &= u_0 - \left(\frac{h_c}{2} + \frac{h_3}{2} - d_3 \right) \theta_0 + h_2 \frac{\partial u_0}{\partial z}, \quad w_c = w_0, \quad \theta_c = \theta_0, \quad \frac{\partial u_c}{\partial z} = 0, \\
u_2 &= u_0 - \left(\frac{h_3}{2} - d_3 \right) \theta_0 + \frac{h_2}{2} \frac{\partial u_0}{\partial z}, \quad w_2 = w_0, \quad \theta_2 = 0, \quad \frac{\partial u_2}{\partial z} = \frac{\partial u_0}{\partial z}, \\
u_3 &= u_0 + d_3 \theta_0, \quad w_3 = w_0, \quad \theta_3 = \theta_0, \quad \frac{\partial u_3}{\partial z} = 0 \text{ and} \\
u_1 &= u_0 - \left(-\frac{h_1}{2} - \frac{h_3}{2} - d_3 \right) \theta_0, \quad w_1 = w_0, \quad \theta_1 = \theta_0, \quad \frac{\partial u_1}{\partial z} = 0.
\end{aligned} \tag{3.44}$$

Finally, for an AC/PSOLD treatment as shown in Figure 3.12 (c), the relationship between displacements in each layer becomes

$$\begin{aligned}
u_c &= u_0 - \left(\frac{h_c}{2} + h_1 + \frac{h_3}{2} - d_3 \right) \theta_0 + h_2 \frac{\partial u_0}{\partial z}, \quad w_c = w_0, \quad \theta_c = \theta_0, \quad \frac{\partial u_c}{\partial z} = 0, \\
u_2 &= u_0 - \left(\frac{h_1}{2} + \frac{h_3}{2} - d_3 \right) \theta_0 + \frac{h_2}{2} \frac{\partial u_0}{\partial z}, \quad w_2 = w_0, \quad \theta_2 = 0, \quad \frac{\partial u_2}{\partial z} = \frac{\partial u_0}{\partial z}, \\
u_1 &= u_0 - \left(\frac{h_1}{2} + \frac{h_3}{2} - d_3 \right) \theta_0, \quad w_1 = w_0, \quad \theta_1 = \theta_0, \quad \frac{\partial u_1}{\partial z} = 0 \text{ and} \\
u_3 &= u_0 + d_3 \theta_0, \quad w_3 = w_0, \quad \theta_3 = \theta_0, \quad \frac{\partial u_3}{\partial z} = 0.
\end{aligned} \tag{3.45}$$

3. FE MODELLING OF BEAMS WITH HAPCLD TREATMENTS

Therefore, coupling matrices for other configurations can be derived from these equations as done for eq. (3.40).

3.6 Calculation of FRF using FE beam models

Mass and stiffness matrices of FE beam models were established to obtain FRFs of beams with various HAPCLD treatments. Two methods have been used through the thesis.

The first method of FRF calculation is the Inverse Matrix Method. When harmonic forces are applied to a system, the response of the system is also harmonic. Therefore, the dynamic stiffness matrix can be derived from mass and stiffness matrices with the assumption of harmonic excitation and motion as done in eq. (3.41). By multiplying the inverse matrix of the dynamic stiffness matrix to eq. (3.41), displacement vector of the system can be obtained. If the displacement at the node of interest is divided by the excitation force at the node of excitation, the receptance of the system can be derived.

The other method is the Modal Matrix Method. As explained in Appendix B.2 with the beam theory, modal displacements can be derived with eigenvalues and eigenvectors which can be obtained from mass and stiffness matrices established in previous sections of this chapter. Eigenvalues and eigenvectors of the system can be obtained with mass matrix and real part of stiffness matrix. Then, equation of modal motion can be expressed by multiplying this eigenvector to complex stiffness matrix as [94]

$$-\omega^2 m_i X_i(\omega) + \left(1 + i\eta(\omega)\right) k_i X_i(\omega) = p_i(\omega), \quad (3.46)$$

where m_i is modal mass, k_i is modal stiffness, X_i is modal displacement, p_i is modal force of i -th mode and η is loss factor. Therefore, displacement of the system can be obtained from eq. (B.17) as [94]

$$W(x) = \sum_{i=1}^N \frac{\phi_i(x_{input}) \phi_i(x)}{M \left((1 + i\eta(\omega)) \omega_i^2 - \omega^2 \right)} f(x_{input}), \quad (3.47)$$

where $\phi_i(x_{input})$ is eigenvector value at the point of excitation, $\phi_i(x)$ is eigenvector value at the point of interest, M is the mass of the system, ω_i is i -th resonance frequency and $f(x_{input})$ is excitation force at the point of excitation.

3. FE MODELLING OF BEAMS WITH HAPCLD TREATMENTS

In general, both methods have been used through the thesis. However, when quicker calculation was required by decreasing the sizes of matrices, the Modal Matrix Method was used with enough number of modes from the 1st mode to give as similar results as with the Inverse Matrix Method within the frequency range of interest. Since some differences can be made in the Modal Matrix Method by residual modes even in low-frequency range [94], enough number of modes should be used in calculation to prevent this issue.

3.7 Summary and conclusions

In this chapter, FE mass and stiffness matrices for each layer of arbitrarily laminated beam structures are derived based on the Euler beam theory for elastic and piezoelectric layers and the Timoshenko beam theory for viscoelastic layer. By using the constitutive equation for piezoelectric material, the piezoelectric effect happening under mechanical deformation in a piezoelectric layer is considered. For a viscoelastic layer, in order to describe shear deformation of a viscoelastic layer, the shear modulus proposed in the GHM method is introduced. Finally, equivalent FE mass and stiffness matrices are derived by a coupling matrix based on a layer-wise approach to describe mutual effects between each layer of a composite beam and combine separate layers into one equivalent beam.

What has been done in this chapter has been partly done by other researchers. However, to establish FE models for beams with various HAPCLD treatments is a fundamental step for the design of active vibration control with velocity feedback using HAPCLD treatment. Furthermore, a deeper understanding of beam structure and its motion, including modal analysis, was obtained.

In the next chapter, FE models for beams with HAPCLD treatment established in this chapter will be validated by experiments such as the impact hammer test and measurement of transfer functions when mechanical and electrical signals are applied.

4 PARAMETER ESTIMATION OF FE BEAM MODELS THROUGH EXPERIMENT

In this chapter, for parameter estimation of the FE beam models proposed in the previous chapter, experimental measurements for various beam models will be compared with simulation results using FE models established in Chapter 3. Moreover, using the experimental results, material properties, e.g. the Young's modulus, density and modal loss factors of the base structure (an aluminium beam), could be updated to realise the material properties used for FE beam models. This update can guarantee more accurate active control results with FE beam models later. Material properties of piezoelectric and viscoelastic materials were referred to manufacturers' data and experimental data measured in [11]. Moreover, in order to implement active vibration control, the transfer functions need to be clarified. Frequency responses of systems by excitation with a shaker and a PZT actuator will be measured and compared with simulated results of established FE beam models.

4.1 Model update and parameter estimation by impact hammer test of beams

In this section, FE beam models for an elastic beam and a beam with a PCLD patch will be updated and their material properties be estimated through impact hammer tests. PCLD treatment is used here as a representative of other HAPCLD treatments to verify if FE modelling method described in the previous chapter can explain the motion of constrained structures with viscoelastic materials well. The configuration of PCLD treatment used in this section is basically the same configuration shown in Figure 3.8, but no electric signal was applied to the piezoelectric layer of ACLD treatment in Figure 3.8 and the piezoelectric layer acts as a sort of elastic layer generating an electrical signal according to deformation of the layer. Through this experiments, the accuracy of active control simulation using established FE beam models can be guaranteed.

4.1.1 Elastic beam model

For an experiment with FE elastic beam model, an aluminium beam 40 cm long, 3cm wide and 2.92 mm thick, as shown in Figure 4.1, was used. The beam was suspended by sellotape to a

4. PARAMETER ESTIMATION OF FE BEAM MODELS THROUGH EXPERIMENT

frame to simulate free-free boundary conditions. Prior to impact hammer tests, resonance frequencies of the FE beam model with the same dimensions, boundary conditions and material properties given in Table 4.2, which were obtained from the measured data, were compared with those of the beam theory explained in Appendix B. The accuracy of resonance frequencies of the FE beam model was calculated as given in Table 4.1.

Table 4.1 Resonance frequency comparison between beam theory and FE beam models

	Beam Theory	FE Beam (6 elements)	FE Beam (16 elements)	FE Beam (20 elements)	FE Beam (50 elements)
Mode 1	0 Hz	0 Hz	0 Hz	0 Hz	0 Hz
Mode 2	94.147 Hz	91.616 Hz (-2.762 %)	93.758 Hz (-0.414 %)	93.896 Hz (-0.267 %)	94.105 Hz (-0.045 %)
Mode 3	259.512 Hz	236.903 Hz (-9.544 %)	255.623 Hz (-1.521 %)	257.966 Hz (-0.599 %)	259.100 Hz (-0.159 %)
Mode 4	508.748 Hz	428.692 Hz (-18.675 %)	492.996 Hz (-3.195 %)	498.385 Hz (-2.079 %)	507.017 Hz (-0.341 %)
Mode 5	840.992 Hz	639.961 Hz (-31.413 %)	798.007 Hz (-5.387 %)	812.238 Hz (-3.540 %)	836.051 Hz (-0.591 %)
Mode 6	1256.282 Hz	808.537 Hz (-55.377 %)	1163.153 Hz (-8.007 %)	1192.818 Hz (-5.321 %)	1245.024 Hz (-0.904 %)

When these results of beam theory were compared with FE model ones as shown in Table 4.1, they are very similar with each other. And, the more elements were used for FE models, the more precise analysis results can be obtained as known from Table 4.1. However, since more calculation load is required with more FE elements, proper number of FE elements used in FE analysis should be determined considering the analysis accuracy. In Table 4.1, results using 50 FE elements are precise enough up to 6th mode with higher than 99 % accuracy.

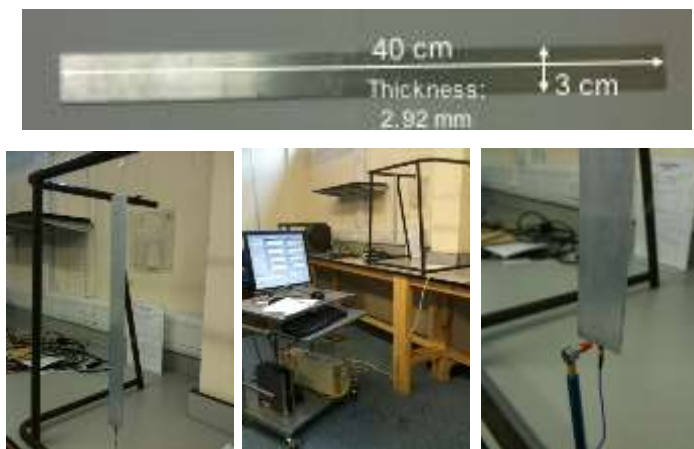


Figure 4.1 Setup of impact hammer test for an aluminium beam

4. PARAMETER ESTIMATION OF FE BEAM MODELS THROUGH EXPERIMENT

For impact hammer tests, an accelerometer (PCB 352C22) was attached to the lower end. The impact point was set to be the same as the accelerometer, but on the other side of the beam to get clear anti-resonance peaks and to distinguish each mode distinctly in the point FRF. The impact hammer (PCB 086E80) and accelerometer were connected to a signal analyser, and the signal from the impact hammer was used as the reference. The sensitivities of the accelerometer and impact hammer were calibrated precisely with a suspended mass. The possibility for error, which can happen in the measurement of sensitivities of two measurement devices, was minimised by averaging three measured data in high coherence over 90 %. The measurement frequency range was set from 0 to 1600 Hz, and the frequency resolution varied between 0.25, 0.125 and 0.0625 Hz. In order to prevent double hitting with the impact hammer, a medium soft tip was used. The measured signals were inspected carefully in each measurement.

The measured point accelerances of an elastic beam were compared with the results simulated by the numerical (FEM by MATLAB and Patran/Nastran) and analytical (modal analysis) methods as explained in Section 3.2 and Appendix B respectively. As shown in Figure 4.2, simulation results by numerical (FE) and analytical (modal analysis) methods for a free-free thin aluminium beam are in good agreement with the measured results.

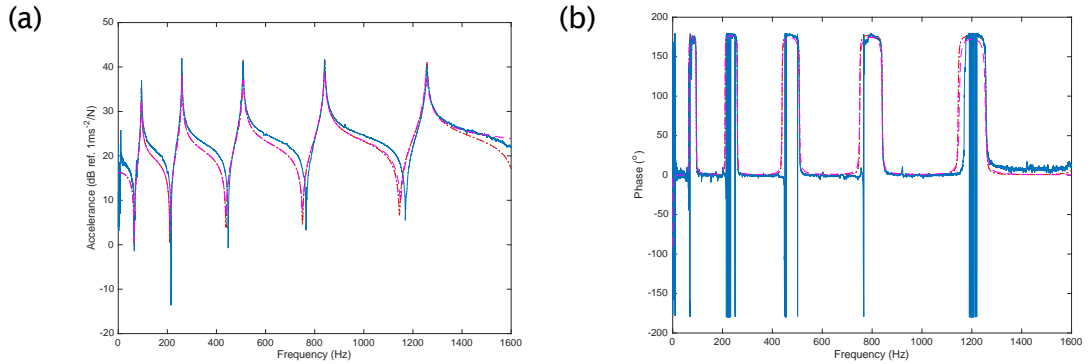


Figure 4.2 Input accelerance of a free-free beam (a) Magnitude and (b) Phase: - - - FEM (MATLAB); - - - Analytical (modal analysis); — Experiment; ··· FEM (Patran/Nastran)

The material properties used for numerical (FEM by MATLAB and Patran/Nastran) and analytical (modal analysis) models of an aluminium beam are listed in Table 4.2 according to measured data. Since the same aluminium alloy was used for experiment, these material properties had been used for aluminium base beams in other result comparison between experimental and numerical results. The natural frequencies and loss factors η , which are double of damping ratios ζ , of this aluminium beam were obtained by the circle fit method from measured data as explained in [94]. These modal loss factors were also used for FE and modal analysis models. In order to reduce errors, sufficient sample data were measured for the circle fit method used to

4. PARAMETER ESTIMATION OF FE BEAM MODELS THROUGH EXPERIMENT

determine the natural frequencies and loss factors. Each material property was selected to minimise errors between measurement and simulation results. First of all, the density of beam was easily determined by measuring the mass of the beam and the dimensions of the beam. Next, the Young's modulus could be determined by making the estimated natural frequencies match well with the measured ones by adjusting the Young's modulus and using the density calculated above.

Table 4.2 Material properties and sensitivity of a free-free beam

Young's modulus of Beam		68 GPa
Density of Beam		2700 kg/m ³
Natural frequencies (Loss factor)		94.15 Hz (0.0118)
		259.51 Hz (0.0034)
		508.75 Hz (0.0042)
		840.99 Hz (0.0029)
		1256.28 Hz (0.0032)
Sensitivity	Impact hammer	22.39 mV/N (± 10 % error)
	Accelerometer	0.98 mV/ms ⁻² (± 10 % error)

The Young's modulus and density in Table 4.2 are within the realms of various data provided by many other references.

Since FE and analytical modal analyses used the same dynamic stiffness matrix, the natural frequencies and the frequency responses obtained by these methods have to be identical in principle. However, there are small differences between two results in Figure 4.2 (a). This is because the number of modes used in modal analysis is fewer than the one used in the FE model. Since each node of the beam structures has three DOFs, the number of modes used in the FE model is equal to the total DOFs for the FE model, which must be three times of the total node numbers. On the other hand, a reduced number of modes was used for modal analysis for faster calculation. Therefore, as some components of higher order modes, other than number of used modes, were not included in the modal analysis, this caused small differences at anti-resonance frequencies in the relatively high frequency range. This effect can be explained with the results in Table 4.1. Since the increase of element used in analysis means the increase of mode involved in analysis, larger improvement of analysis accuracy in higher modes can be found than in lower modes in Table 4.1.

4. PARAMETER ESTIMATION OF FE BEAM MODELS THROUGH EXPERIMENT

Measured accelerances are in good agreement with numerical and analytical results as mentioned above. However, there are some opposite changes in the phase between results as shown in Figure 4.2 (b). This is because of low signal-to-noise ratio at anti-resonance frequencies. At these frequencies, an accelerometer becomes very sensitive to noise due to low accelerances. Moreover, since the whole structure is light, noise at anti-resonance frequencies could be measured easily. Therefore, considering this fact, accelerances of three results are in good agreement.

4.1.2 Elastic beam with a layered patch with a PZT and viscoelastic material model

Based on the results for a thin beam, the model update and parameter estimation were expanded to a thin beam with a layered patch with a PZT and viscoelastic material. In this experiment, since no electric signal was applied to the PZT patch, this patch acted as an elastic constraining layer for PCLD treatment, not an actuating patch for ACLD treatment. However, since the PZT patch was open-circuited and generated electricity according to the deformation of the PZT patch, the electricity generated by the PZT patch in the real structure and the FE model can be compared to validate if the FE model was properly established with material properties given in Tables 4.3 and 4.4 as well as the constraining effect of the constraining layer (the PZT layer in this case). Since this beam model will be used for active vibration control, this experimental validation is important in determining the accuracy of the active control study which will be performed later.

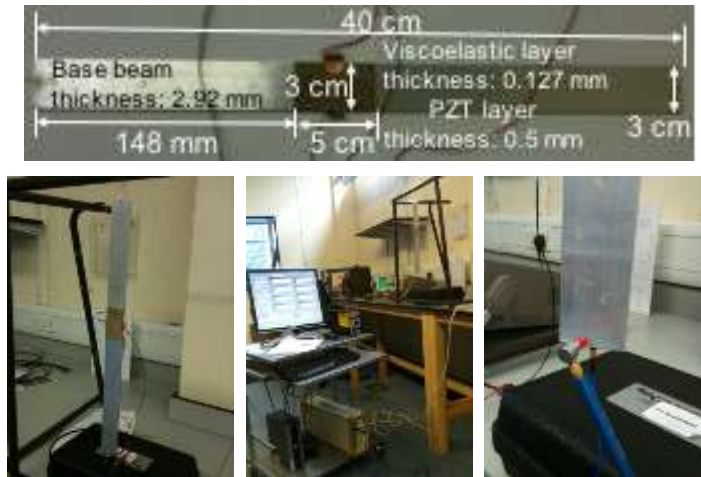


Figure 4.3 Setup of impact hammer test for an aluminium beam with PZT and viscoelastic layered patch

The left end of the patch, which consists of the 0.5 mm thick PZT patch and the 0.127 mm thick viscoelastic layer, is located 148 mm away from the suspension point as shown in Figure

4. PARAMETER ESTIMATION OF FE BEAM MODELS THROUGH EXPERIMENT

4.3. The length and width of the patch are 5 cm and 3 cm respectively. Accelerometer mounting and hammer impact points were the same as in the case of the aluminium beam test performed above. The PZT layer was connected to the signal analyser via a B&K charge amplifier type 2635 to measure the electrical signal generated by the PZT layer. The overall setup is shown in Figure 4.3.

The gain of the charge amplifier was carefully adjusted for measured signal not to exceed the measurement limit value of a signal analyser. Finally, in order to remove any remaining electrical charge in the PZT patch, which can cause noise in the measured data, the PZT patch was discharged shortly before measurements were taken.

The measured results were compared with the simulated ones which were calculated using the FE beam model established in Chapter 3. Each parameter used for eq. (3.30) of the GHM method explained in Section 3.4.1 is given in Table 4.3 for the viscoelastic layer [11, 91]. The shear modulus and loss factor in the frequency domain obtained by eq. (3.30) with these given parameters are shown in Figure 3.6.

Table 4.3 Parameters used for the GHM method [11]

G^{\forall} (MPa)	k	α_k	$\hat{\zeta}_k$	$\hat{\omega}_k$
0.1633	1	4.8278	22.013	28045
	2	14.548	3.1275	41494
	3	40.043	0.6165	41601

Figure 4.4 shows the accelerances of the beam with PZT and viscoelastic layers. The frequency response characteristics of the voltage generated by the PZT patch are shown in Figure 4.5.

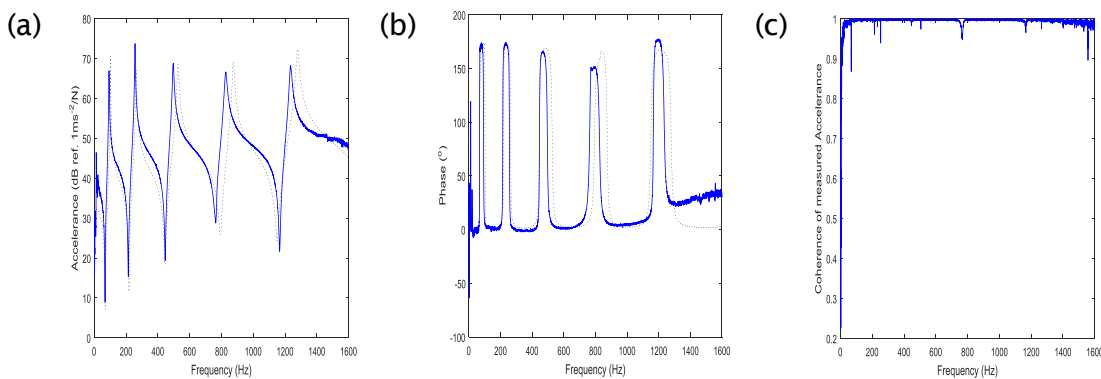


Figure 4.4 Input accelerance of a free-free beam with PZT and viscoelastic layered patch (a) Magnitude, (b) Phase and (c) Coherence of measured data: - - - FEM; — Experiment

4. PARAMETER ESTIMATION OF FE BEAM MODELS THROUGH EXPERIMENT

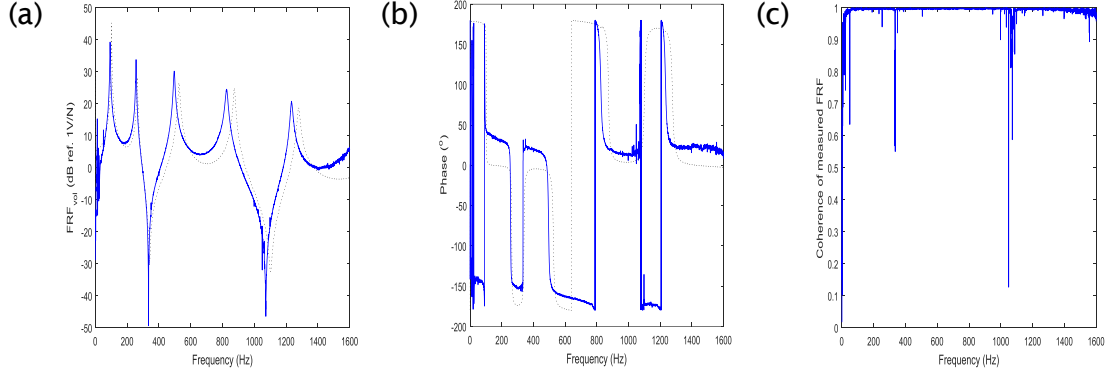


Figure 4.5 Voltage of a free-free beam with PZT and viscoelastic layered patch (a) Magnitude, (b) Phase and (c) Coherence of measured data: - - - FEM; — Experiment

Differences can be found at anti-resonance frequencies in Figures 4.4 and 4.5. Since these differences may be caused by the dynamic characteristics of PZT patch, the dynamics of PZT patch can be studied for various boundary conditions; free, simply supported and clamped for edges, as given in Figure 4.6. Since the PZT patch is indirectly connected to the base beam with the constrained viscoelastic layer, the differences are not thought to be caused by the dynamics of PZT patch. Since the location of PZT patch has some distance from the one of excitation point, this is thought as the main reason of the differences.

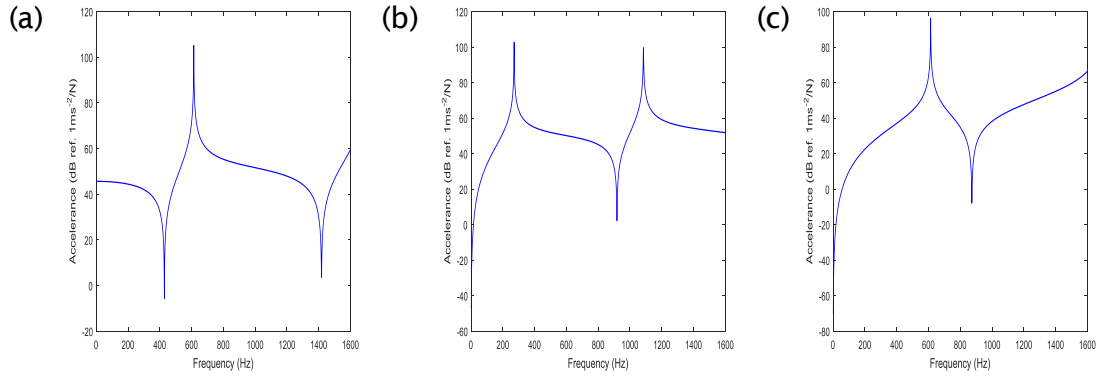


Figure 4.6 Dynamics of PZT patch with different boundary conditions; (a) free, (b) simply supported and (c) clamped

The used material properties of an aluminium beam given in Table 4.2 and the sensitivity of the impact hammer and accelerometer are the same as those used for an aluminium beam measurement. The material properties of the viscoelastic material and the PZT are given in Tables 4.3 and 4.4 respectively. All values in Table 4.4 except modified elastic modulus of PZT, which was adjusted to meet the resonance peaks in Figures 4.4 and 4.5, were the same as the manufacturers' data. The natural frequencies and loss factors, which were obtained by the circle fit method from the measured data as in the case of an aluminium beam measurement, are provided in Table 4.4 as well [94]. Due to the effect of the viscoelastic layer's shear modulus, the loss

4. PARAMETER ESTIMATION OF FE BEAM MODELS THROUGH EXPERIMENT

factors for this beam model are generally four times larger than those for the aluminium beam alone as shown in Tables 4.3 and 4.4. Moreover, as the result of the increased mass by the attachment of patch and the increased stiffness by the constraining effect of the patch, the natural frequencies slightly decrease, on average 1.95 %, compared with those of the aluminium beam. When considering the effect of increased added mass only, about 3.06% decrease of natural frequencies can be predicted. But, increased stiffness by the constraining layer reduced such an effect.

Table 4.4 Material properties of a free-free beam with PZT and a viscoelastic layered patch

Density of viscoelastic material		1130 kg/m ³
Density of PZT		7800 kg/m ³
Modified elastic modulus of PZT		62.11 GPa
Piezoelectric constant of PZT		-11.18 C/m ²
Dielectric constant of PZT		9.96×10 ⁻⁹ F/m
Natural frequencies (Loss factor)		92.20 Hz (0.0267)
		255.59 Hz (0.0122)
		495.39 Hz (0.0163)
		824.68 Hz (0.0180)
		1235.83 Hz (0.0117)
Sensitivity	Impact hammer	22.39 mV/N (±10 % error)
	Accelerometer	0.93 mV/ms ⁻² (±10 % error)

4.2 Transfer function measurement of beams with hybrid control patches

In this section, the transfer functions between excitation by a shaker or a PZT actuator and velocities were measured. These measured transfer functions were compared with simulation results using FE beam models established in Chapter 3. The objective was to validate transfer functions which will be used later in the design of the active control system. Explanation of each component of the overall system set-up for measurement is given below.

Firstly, an aluminium cantilever beam with dimensions 40 cm × 3 cm × 2.58 mm was newly made as a base structure to apply four types of HAPCLD treatments shown in Figure 3.1 at a different point 3.5 cm away from the clamped end as shown in Figure 4.7 (a). Through impact

4. PARAMETER ESTIMATION OF FE BEAM MODELS THROUGH EXPERIMENT

hammer tests, the Young's modulus and density of the beam were measured as 78.5 GPa and 3124.8 kg/m³ respectively by comparing resonance peaks and measuring the mass of a base beam. With a changed boundary condition, the modified Young's modulus of new base beam was determined larger than the case of free-free boundary condition in the previous section. Moreover, the passive modal loss factors of each test case with four types of HAPCLD treatments were calculated by the circle fit method from the measured data for the impact hammer test as given in Figure 4.7 (b) [94]. Only modal loss factors, which are double of damping ratios [94], of an aluminium base beam were used in FE models.

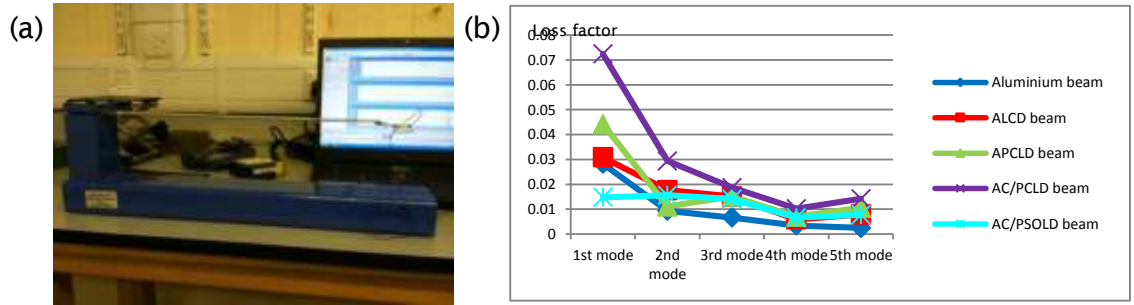


Figure 4.7 (a) Base aluminium cantilever beam for beam control experiment and (b) modal loss factors in each case

Secondly, PZT patches made of PIC255 (5 cm × 3 cm × 0.54 mm, d_{31} direction polarisation, density: 7185.9 kg/m³ by mass measurement) were used for the piezoelectric layer. The viscoelastic material used for the viscoelastic layers was the 3M viscoelastic damping polymer 112P05 with dimensions 5 cm × 3 cm × 0.127 mm and density 1130 kg/m³. The elastic constraining layers were aluminium sheet (5 cm × 3 cm × 0.36 mm, density: 2249.7 kg/m³ by mass measurement). HAPCLD treatments which consist of these three materials were located 1 cm away from the clamped end of the beam.

Finally, since a shaker attached at a free end of cantilever beam was observed to constrain the motion at the free end, a shaker was located at as close a point to the centre of HAPCLD treatments as possible within the allowance of the system set-up (see figure 4.9). This would be useful later to reduce the possibility of instability of the controller due to collocation problems.

In the next subsection, measurement of the transfer functions of systems with HAPCLD treatments will be explained.

4.2.1 Measurement of transfer functions of hybrid system

An active vibration control scheme for beams can be represented by the block diagram as shown in Figure 4.8. In this block diagram, F_e is the primary/disturbance exciting force, v_s is the

4. PARAMETER ESTIMATION OF FE BEAM MODELS THROUGH EXPERIMENT

measured error velocity at a reference point, v_e is the measured velocity at a control target point, g is the feedback control gain and V_c is the control voltage determined by multiplying v_s by the feedback control gain g . H_{ce}^f is the transfer function between the force at the excitation point, F_e , and the velocity at the control target point, v_c , and H_{se}^f is the transfer function between the force at the excitation point, F_e , and the velocity at the error sensor point, v_s . H_{cs}^v and H_{es}^v are the transfer functions between the voltage V_c applied to the PZT patch and the velocities measured at the control target point, v_c , and at the error sensor point, v_s , respectively.

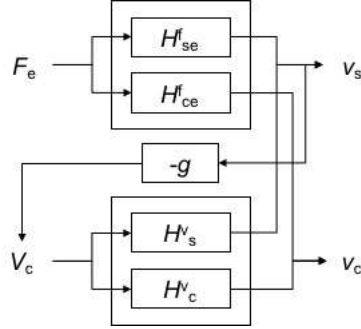


Figure 4.8 Block diagram of the system for a general case

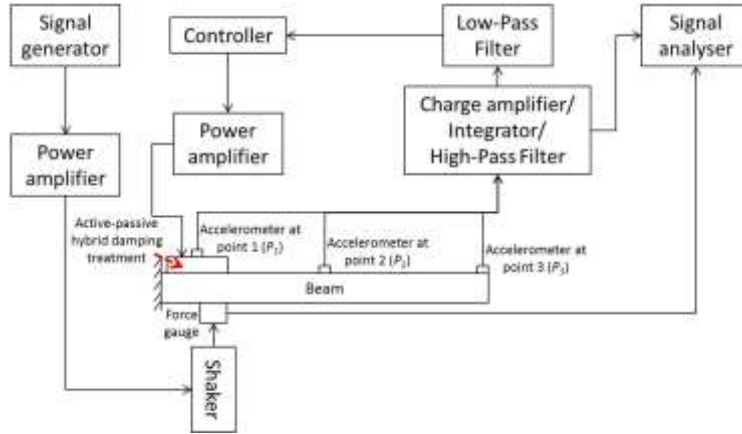


Figure 4.9 Schematic diagram of a control system set-up for beams

Measurement positions were determined considering the base cantilever beam and the position of the PZT actuator as shown in Figure 4.9. Generated control moments were applied at the edges of the patch. The disturbance excitation was applied at a point 5 cm away from the clamped end. In order to compare the performance of different control strategies further, the velocities v_i at the points P_i ($i = 1, 2$ and 3), P_1 : error sensor position at the centre point of the hybrid damping treatment to minimise the collocation problem between the error signal and control moment (3.5 cm away from the clamped end), P_2 : centre point of the beam (20 cm away from the clamped end) and P_3 : free end of the beam (40 cm away from the clamped end), were also measured as error and monitor signals for the various different control strategies. The error signal is used as an input signal to the feedback controller. The monitor signal is used to observe

4. PARAMETER ESTIMATION OF FE BEAM MODELS THROUGH EXPERIMENT

the behaviour of the structure at further points. Velocity v_1 was the error signal, and velocity v_2 and v_3 were used for monitoring purposes.

Following determination of error and monitor points, the measurements of transfer functions with shaker and PZT patch excitations were conducted.

Firstly, H_v^s , FRF velocity per unit voltage applied to the PZT patch, were measured. In order to analyse and record measured data, a Data Physics Quattro signal analyser was used. A pseudo-random signal with an rms level of $1/\sqrt{2}$ V was applied as an input signal. This input signal was sent to a PI E-507 High-Voltage-PZT (HVPZT) piezo amplifier module with a gain factor of 100 via a KEMO low-pass filter with a cut-off frequency of 2 kHz. Electrically driven rectangular PZT patches generated resulting opposite bending moments at each tip, and the beam was excited by these moments. Accelerations at points P_1 , P_2 and P_3 were measured by B&K accelerometers types 4344, 4375 and 4374 with B&K charge amplifiers type 2635. Each measured acceleration was respectively filtered by the charge amplifiers with a high-pass filter of 10 Hz cut-off frequency in order to reduce noise at a low frequency. Considering a pseudo-random signal as an input signal, the rectangular window was used. 100 samples were averaged, and the measured transfer function of the system was adjusted to eliminate the effects of accelerometers (mass) and shaker (mass, stiffness and damping) for a comparison with simulation results after the experiment [95]. The experiment setup is shown in Figure 4.10.

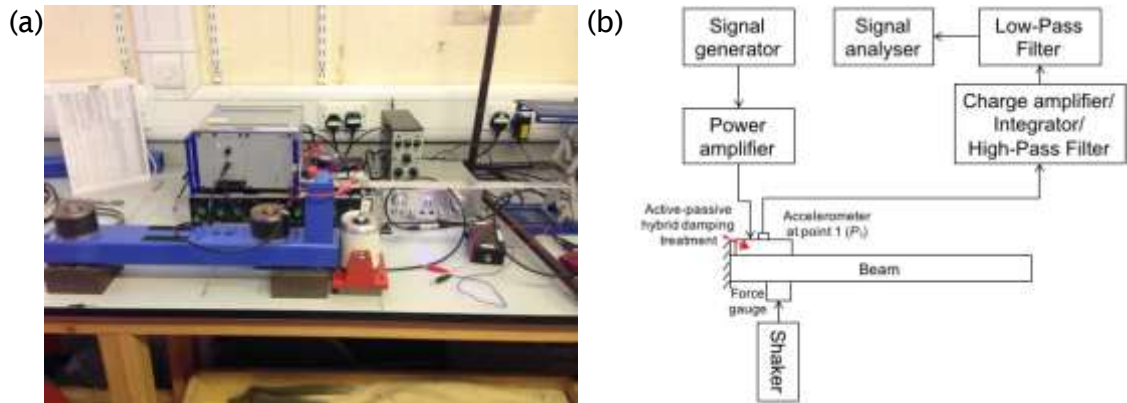


Figure 4.10 Experiment set-up for measurement of FRFs of velocity per unit volt with electric pseudo-random excitation; (a) real system and (b) schematic diagram

In Figure 4.10, the shaker was electrically disconnected, i.e., open-circuited and completely unpowered, but mechanically attached to the beam to create as similar a condition to the control experiment as possible. The beam was excited by the bending moments generated by the PZT patch receiving the pseudo-random signal filtered by the low-pass filter with a cut-off frequency of 2 kHz. The shaker, force gauge and accelerometer acted as added mass, stiffness and damping to the whole structure.

4. PARAMETER ESTIMATION OF FE BEAM MODELS THROUGH EXPERIMENT

Red one-dotted chain lines in Figures 4.12 (a) and (b) show the magnitude and phase of the measured FRF: H_s^v . The measurements have been carried out for all four HAPCLD treatments as given in Figure 3.1. However, only the measurements for the ACLD treatment are shown here as being representative of general behaviour of HAPCLD treatments. The FRF of H_s^v show very well separated resonance frequencies at 83.8, 229.0 441.6 and 725.5 Hz for four of the first five. The first resonance frequency, 13.8 Hz, which was expected from the modal analysis of the FEM model, cannot be seen here due to noise measured by the accelerometer in low frequency range.

Secondly, FRF H_{se}^f at the error measurement point P_1 by pseudo-random force excitation was measured. Similar to the piezoelectric excitation case, a pseudo-random signal was applied to the shaker through an audio power amplifier (Ariston AX-910), where the signal was adjusted to supply current with a maximum of 0.2 A rms into the shaker to avoid the damage on the shaker. As in the previous case, the rectangular window was used considering a pseudo-random input signal. Moreover, 100 samples were averaged, and the effects of accelerometers (mass), force gauge (mass) and shaker (mass, stiffness and damping) were considered [95]. The experimental setup for these measurements is shown in Figure 4.11. The shaker was attached to a point 5 cm away from the clamp with a stinger and a PCB force gauge Model 208C01, which was not used to measure the applied force as the reference signal for FRF. Instead of the applied force, the electrical input current signal to the shaker, which was measured by extra current meter and adjusted to a maximum of 0.2 A rms, was used as the reference signal for FRF to avoid the differences in resonance frequencies between two FRFs, H_s^v and H_{se}^f . The same accelerometers and charge amplifiers were used as for the measurements of FRF H_s^v of velocity, which is integrated data of measured acceleration in the signal analyser, per unit volt. In order to obtain as similar transfer functions for the system as possible to those used in the control experiment, the dynamics of the shaker were included in the measurement.

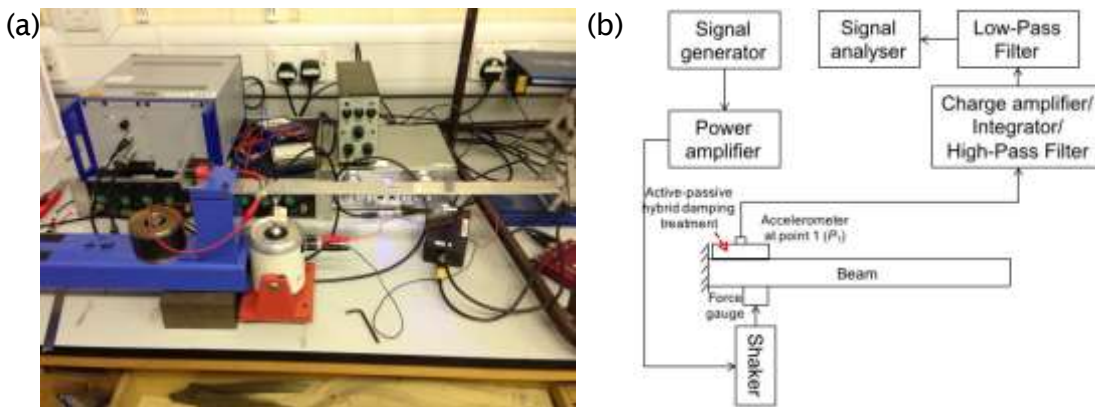


Figure 4.11 Experimental set up for measurement of mobilities with shaker excitation; (a) real system and (b) schematic diagram

4. PARAMETER ESTIMATION OF FE BEAM MODELS THROUGH EXPERIMENT

The FRF with pseudo-random force excitation was measured and its magnitude and phase are shown in Figures 4.13 (a) and (b) as red one-dotted chain lines. Noise is apparent below 100 Hz, especially below 10 Hz. For the measurement of low frequency vibration below 10 Hz, a special low frequency accelerometer, which must use “Quiet” electronics for low frequency noise and have high sensitivity to overcome monitor noise, were usually used. Since a general accelerometer was used in these measurements, noise is thought of as being measured in the low frequency range.

4.2.2 Result comparison of FE models with measured transfer functions

In order to check the FE beam models established in Chapter 3 adding to the model update and parameter estimation performed in the previous section, measured FRFs and phases under two different excitations, by shaker and piezoelectric actuator, were compared with those of FEM beam models using the following figures for an ACLD treatment case. Measured FRFs and phases are generally in good agreement with numerical results obtained by FEM beam models. However, there are some differences in phases as seen in Figure 4.12 and 4.13.

When checking the difference between experimental set-up and FE model, the application of a low-pass filter is the main reason of these differences in Figures 4.12 and 4.13. Since the KEMO low-pass filter, which is an 8th order Butterworth Filter, is used with the cut-off frequency of 300 Hz in the experiment, such a low-pass filter was included as the form of transfer function in the model as well. Results were compared with the measured results in Figure 4.14 and 4.15. With consideration of a low-pass filter effect, more accurate simulation results are obtained for the phase as shown in Figures 4.14 (b) and 4.15 (b). However, amplitudes of FRFs are the same as the previous results regardless of a low-pass filter effect.

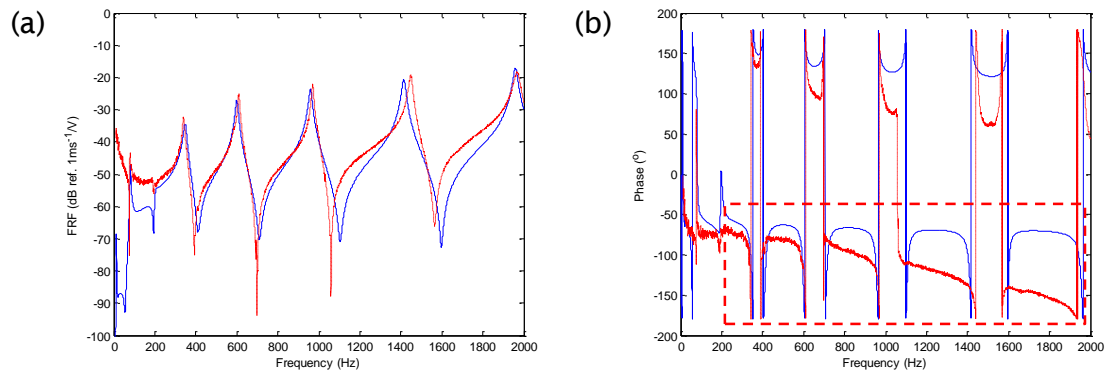


Figure 4.12 (a) FRFs of velocity per unit volt at point P_1 (H'_{v_s}) and (b) phases of velocity per unit volt at point P_1 for a beam with ACLD treatment when an electrical signal is applied to a PZT patch; — FE model and - - - measured data

4. PARAMETER ESTIMATION OF FE BEAM MODELS THROUGH EXPERIMENT

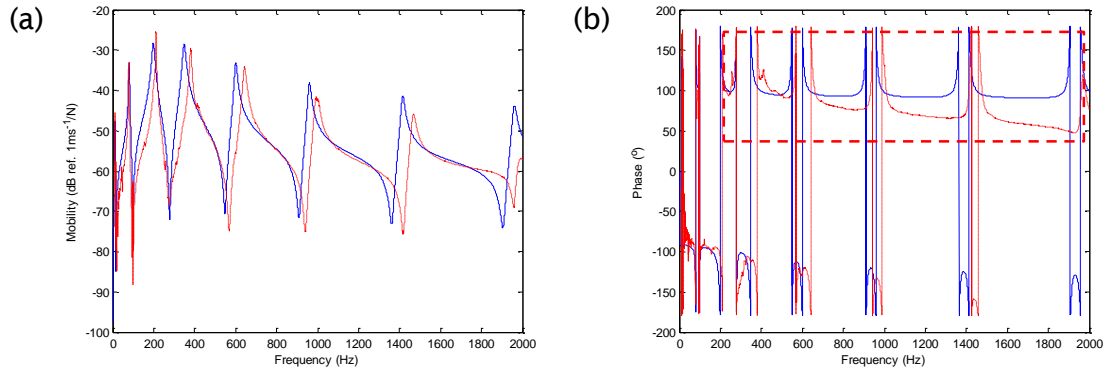


Figure 4.13 (a) Mobility at point P_1 (H_{se}^f) and (b) phases of Mobility at point P_1 for a beam with ACLD treatment when pseudo-random force is applied; — FE model and - - - measured data

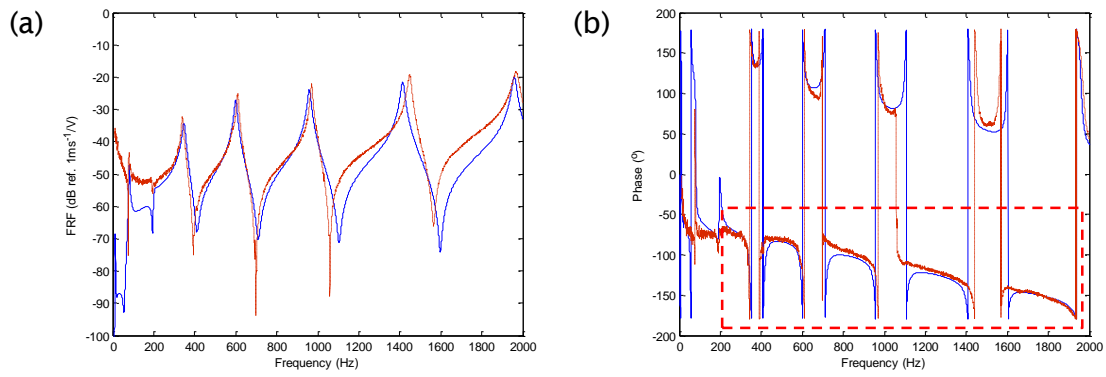


Figure 4.14 (a) FRFs of velocity per unit volt with the effect of a low-pass filter at point P_1 (H_{vs}) and (b) phases of velocity per unit volt with the effect of a low-pass filter at point P_1 for a beam with ACLD treatment when an electrical signal is applied to a PZT patch; — FE model and - - - measured data

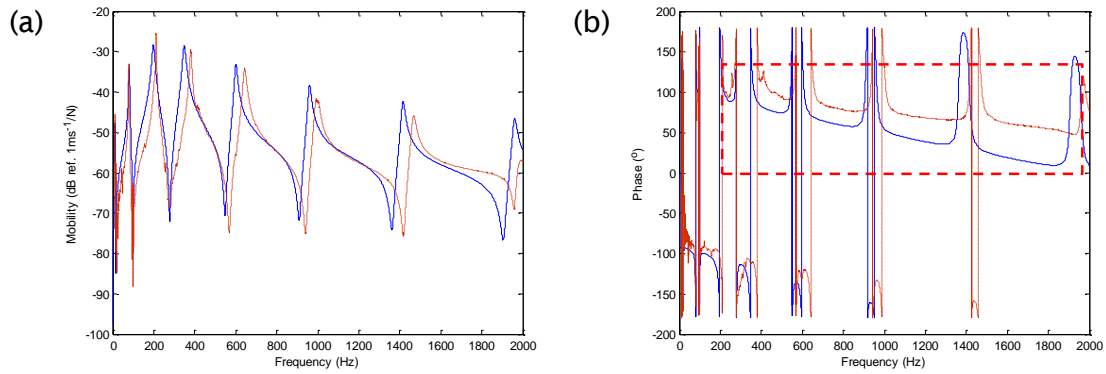


Figure 4.15 (a) Mobility with the effect of a low-pass filter at point P_1 (H_{se}^f) and (b) phases of Mobility with the effect of a low-pass filter at point P_1 for a beam with ACLD treatment when a pseudo-random force is applied; — FE model and - - - measured data

4.3 Summary and conclusion

In this chapter, through impact hammer tests and measurement of transfer functions with two different excitation cases, i.e. pseudo-random exciting force by a shaker or pseudo-random electrical signal using a PZT patch, simulated and measured results were compared with each other. As a result of the comparison, FE beam models established in the previous section were confirmed to express the motion of structures with HAPCLD treatments. Hence, simulation results can be used for controller design, which requires a repetitive process of optimisation. As can be understood from the result comparison, it is clearly shown that, for more accurate simulation results, every component of the experimental set-up, including control target structures themselves as well as all connected equipment such as an accelerometer, the low-pass filter, etc. should be considered in FE models. As explained in Section 4.2.1 and [95], effects of sensors such as accelerometers and a force gauge were considered as additional mass. Mass, stiffness and damping of the shaker were referred to in the technical measurement report and were added to FE models. Phase delay caused by a low-pass filter was also considered according to the filter characteristics.

In the next chapter, the design of optimised controllers, control simulations and experiments relating to four different beam structures with a designed controller will be discussed. Moreover, through the comparison of each result, the HAPCLD treatment with better control performances will be found.

5 VELOCITY FEEDBACK HYBRID ACTIVE-PASSIVE CONTROL OF BEAMS

In this chapter, the design of active controllers using HAPCLD treatments is considered. One of objectives of this chapter is to give design guidelines for the controller to minimise the kinetic energy of the whole structure, or to maximise the energy absorbed by the controller [96]. Another guideline is the maximisation of the stability margin of the control. Moreover, applicability of the conclusion in [3] to structures having more DOFs than beams will be confirmed with different system configurations and a control algorithm in this procedure. The controllers with simple velocity feedback control instead of LQR are applied to the FE beam models with different types of HAPCLD treatments. Finally, experimental results will be obtained and compared to numerical simulations. The bandwidth of the controller and the effect of the low-pass filter for alleviating spill-over effects will be discussed.

5.1 Velocity feedback controller design for beams

Basic study of active control is done in Appendix C. Effect of displacement, velocity and acceleration feedback control is studied with a single-degree-of-freedom (SDOF) system in the same appendix. Moreover, many possible problems in active control due to collocation and duality are studied as well.

In order to design a proper velocity feedback controller for beams, the stability of the controller should be secured by controlling the range of control gain as studied in C.2.3. For an unconditional stable control, optimal control gain can be determined by considering the kinetic energy of a whole structure and the absorbed power by a controller as studied in C.2.3. When active control is applied to a system, the motion of a system, which is related to the kinetic energy of a structure, will be controlled with energy reduction by the application of active control, which will be equal to the absorbed power of the controller. This reduced motion of a system will lead to the minimisation of the kinetic energy of a system as expressed in eq. (C.7).

$$S_k(\omega) = \frac{M}{2R} \sum_{r=1}^R \left| \tilde{v}_r(\omega) \right|^2, \quad (C.7)$$

where M is mass of the whole structure, R is the number of measuring points and $\left| \tilde{v}_r(\omega) \right|$ is the mean square value of the velocity measured by the r -th accelerometer.

5. VELOCITY FEEDBACK HYBRID ACTIVE-PASSIVE CONTROL OF BEAMS

Moreover, the power spectral density of power absorbed by the control actuator is expressed as

$$S_p(\omega) = \frac{1}{2} \beta \left| \tilde{v}_c(\omega) \right|^2, \quad (\text{C.8})$$

where β is the control gain and $\left| \tilde{v}_c(\omega) \right|$ denotes the mean square value of the control velocity.

In the next section, based on the controller design study, the design process for a controller for real systems of beams with HAPCLD treatments will be studied.

5.2 Experimental controller design of a beam with HAPCLD treatment

In this section, the controller design mentioned in the previous section will be applied to real beam structures described in Sections 3.5. Various configurations of HAPCLD treatments will be considered. In the next subsection, the determination of control gains based on the open loop Nyquist plots for each configuration will be studied.

5.2.1 Determination of control gain margins

For the beam structures in the four different configurations of HAPCLD treatments explained in Chapter 3, the Nyquist plots for open loops can be obtained. FE beam models established in Chapter 3 and experimental data will be used to obtain optimal control gains. Beam structures were clamped in a cantilever beam configuration. Beams with the four different HAPCLD treatments are shown in Figures 5.1 to 5.4. Copper electrodes were attached to top and bottom surfaces of PZT patches to provide electrical signal.

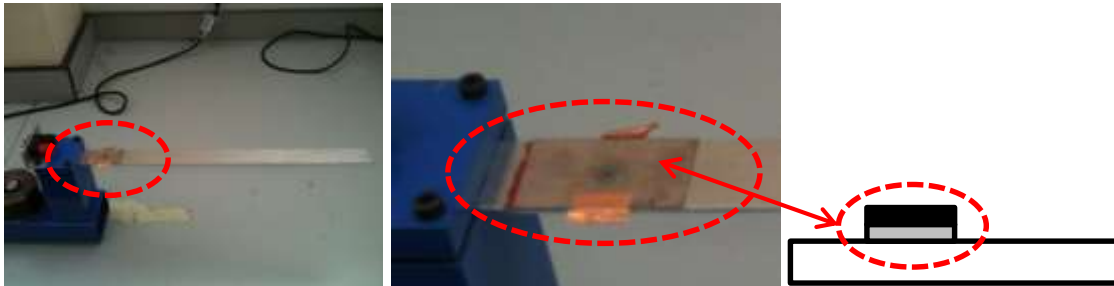





Figure 5.1 Beam with ACLD treatment for experiment;  : elastic beam,  : viscoelastic layer and  : piezoelectric patch

5. VELOCITY FEEDBACK HYBRID ACTIVE-PASSIVE CONTROL OF BEAMS

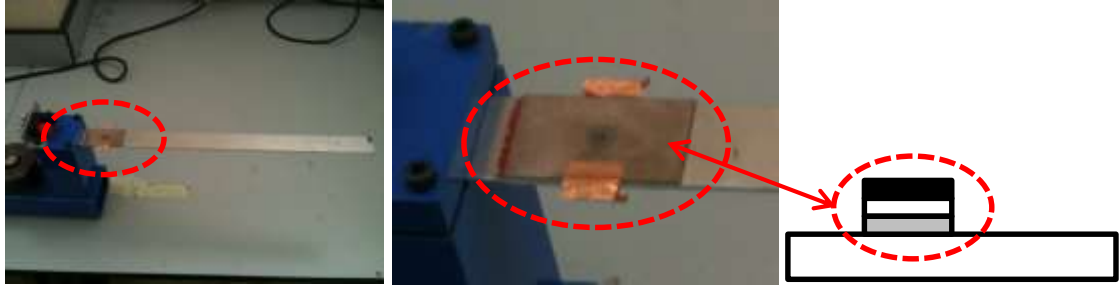





Figure 5.2 Beam with APCLD treatment for experiment;  : elastic beam,  : viscoelastic layer and  : piezoelectric patch

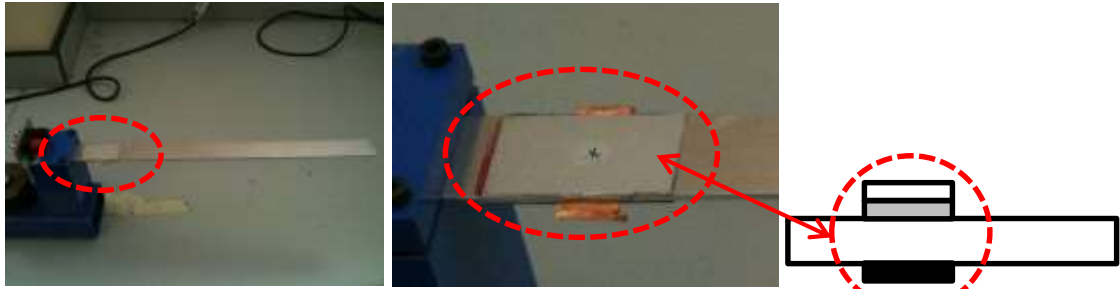





Figure 5.3 Beam with AC/PCLD treatment for experiment;  : elastic beam,  : viscoelastic layer and  : piezoelectric patch

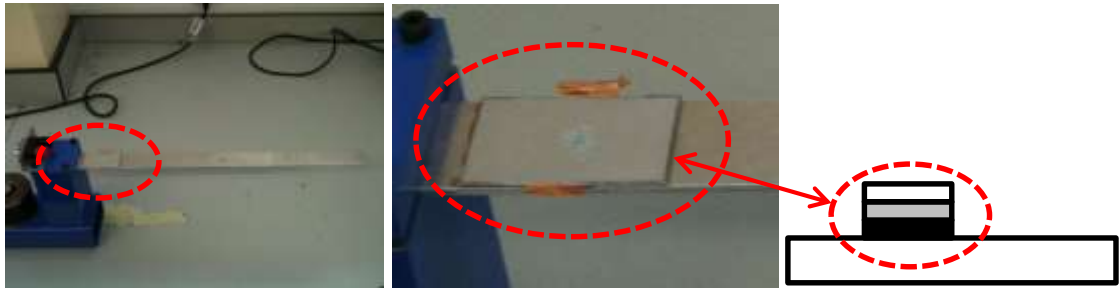





Figure 5.4 Beam with AC/PSOLD treatment for experiment;  : elastic beam,  : viscoelastic layer and  : piezoelectric patch

The experimental set-up for measurement of FRFs of velocity per unit volt with pseudo-random excitation by a piezoelectric actuator shown in Figure 4.17 in Section 4.2.2 was adopted. The Nyquist plot for the open loop for each configuration can be obtained from the measured FRFs of HAPCLD treatments in Section 4.2.2. The FRFs were then measured without or with a KEMO low-pass filter to check the effect of a low-pass filter on the control input signal.

The Nyquist plots for an open loop system without any low-pass filter are shown in Figure 5.5. As can be noted from Figure 5.5, for ACLD, APCLD and AC/PSOLD treatments the circles of Nyquist plot move from the positive real area to the negative after the third circle and the radius

5. VELOCITY FEEDBACK HYBRID ACTIVE-PASSIVE CONTROL OF BEAMS

of the circles also increases. This means there is a higher possibility of instability of control at the higher frequencies. This is the reason why Trindade and Benjeddou used only the first three modes for beam control to avoid potential negative effects of active control in their paper [3]. Therefore, for stable control, the introduction of a method to filter high frequency components out from the signal is necessary to use only positive real parts of control force. Here, a low-pass filter, which can eliminate higher frequency components than a cut-off frequency, was used as a filtering method for this purpose.

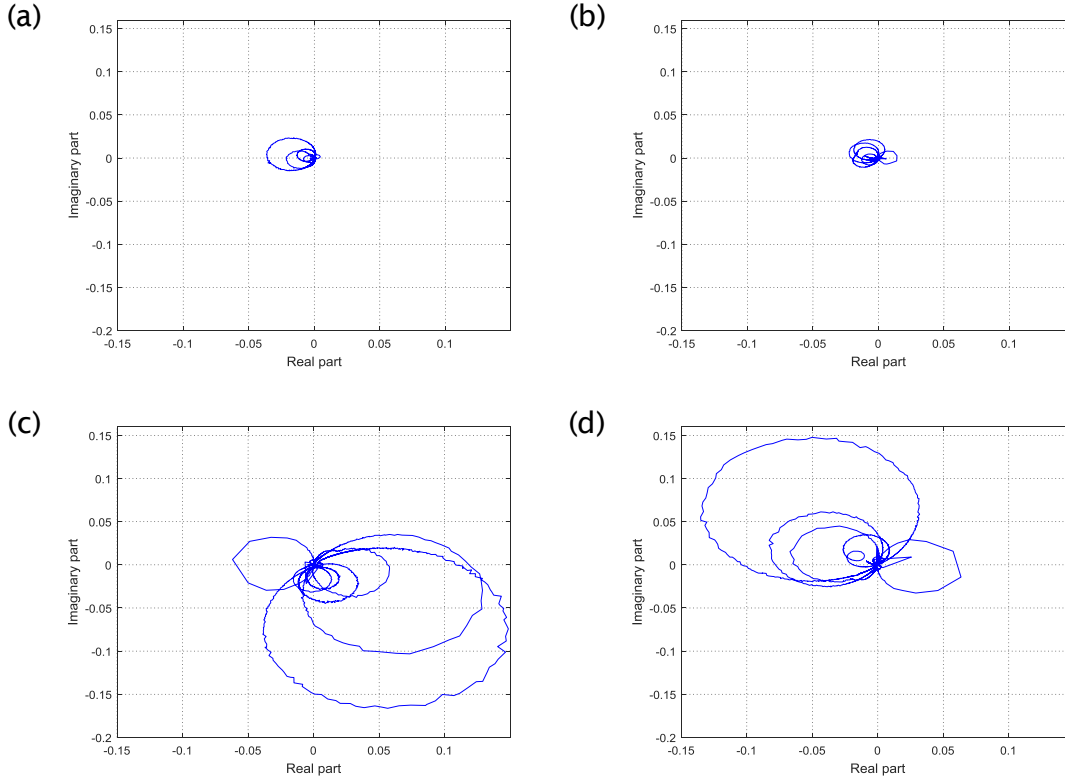


Figure 5.5 The Nyquist plots for the open loop of beam structures without a KEMO low-pass filter: (a) ACLD treatment, (b) APCLD treatment, (c) AC/PCLD treatment and (d) AC/PSOLD treatment

A KEMO low-pass filter with an 8 Pole Butterworth filter was applied to the system to use only positive parts of open loops in Figure 5.5 to minimise the effect of negative parts on control stability. The cut-off frequency was set to 300 Hz, which causes higher modes than the 3rd mode to be eliminated from the control signal. As a result, the Nyquist plots for open loop were changed as shown in Figure 5.6 with the application of the low-pass filter.

5. VELOCITY FEEDBACK HYBRID ACTIVE-PASSIVE CONTROL OF BEAMS

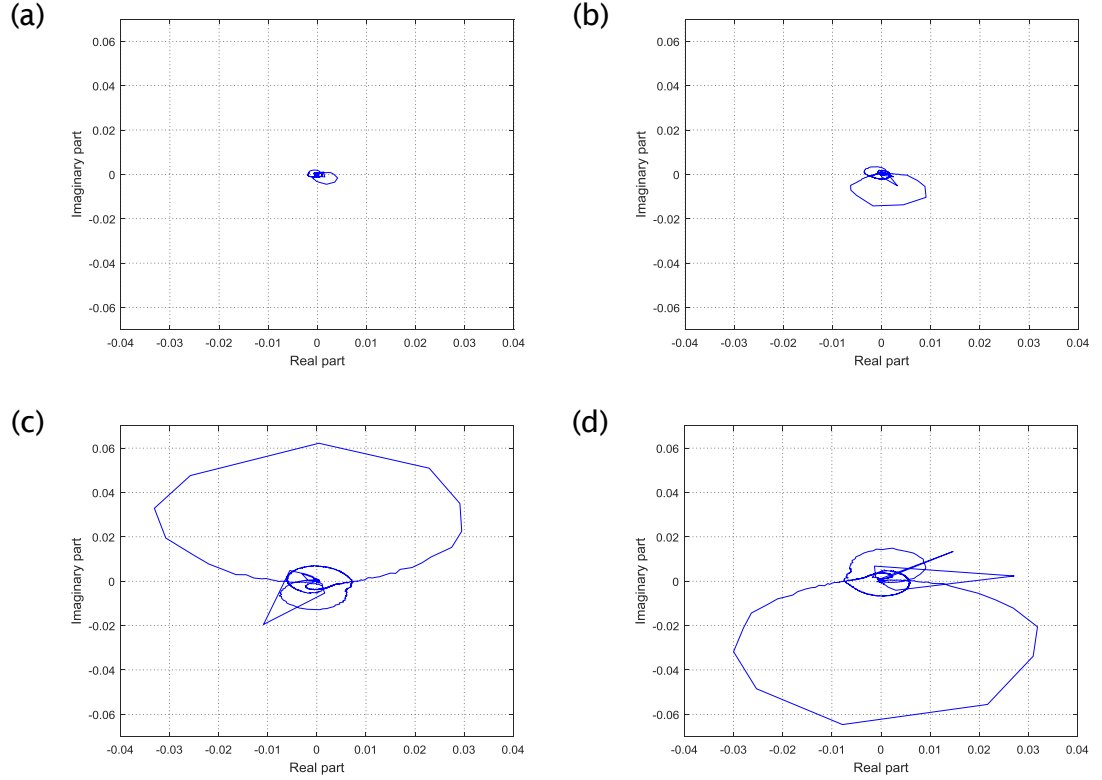


Figure 5.6 The Nyquist plots for the open loop of beam structures with a KEMO low-pass filter (Cut-off frequency: 300 Hz): (a) ACLD treatment, (b) APCLD treatment, (c) AC/PCLD treatment and (d) AC/PSOLD treatment

Although the low-pass filter reduces the high frequency components, it also causes a phase shift in filtered signals. When a control is implemented for harmonically excited systems, an attempt to cancel the phase shift may be tried with an all-pass filter, which adds even more phase shift to the signals and finally eliminates the phase shift caused by a low-pass filter by rotating the total phase shift over 360° . However, for a broadband control like this case, this method will only cause larger deformation of the Nyquist plot and make the problem more severe.

For a broadband control, an ideal low-pass filter shown in Figure 5.7, which can precisely cut off the input signal at the cut-off frequency and does not provide the phase shift, is required. However, since it is physically impossible to eliminate phase delay, which is caused by time delay within filters for signal processing [97], realisation of this ideal low-pass filter may be impossible. Therefore, how to compensate this delayed phase for a similar result with an ideal low-pass filter can be studied by using various methods such as the introduction of individual serial combinations of band-pass filters and all-pass filters in the next subsection.

5. VELOCITY FEEDBACK HYBRID ACTIVE-PASSIVE CONTROL OF BEAMS

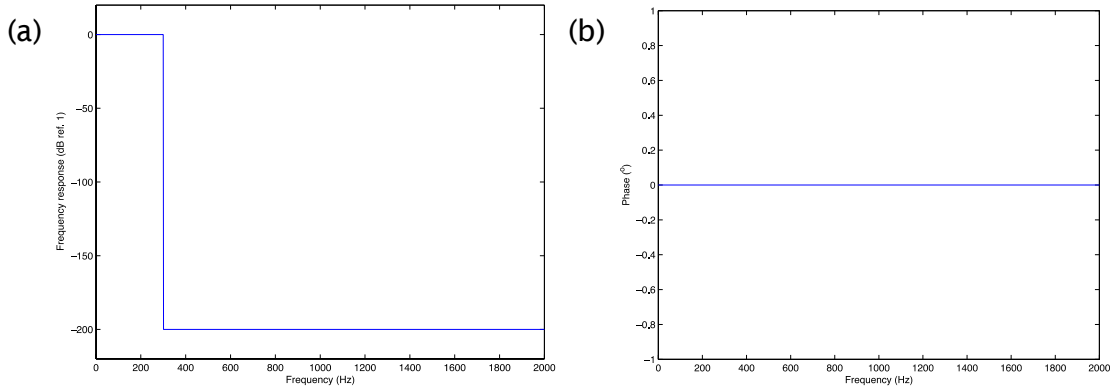


Figure 5.7 An ideal low-pass filter with 300 Hz cut-off frequency: (a) Frequency response and (b) Phase response

If this ideal low-pass filter or other filtering methods with a similar effect to an ideal low-pass filter can be applied to the system, the Nyquist plot for the open loop can be changed from Figure 5.5 to Figure 5.8 with reduced frequency components above a cut-off frequency. Signal phase shift is minimised with the application of this ideal low-pass filter.

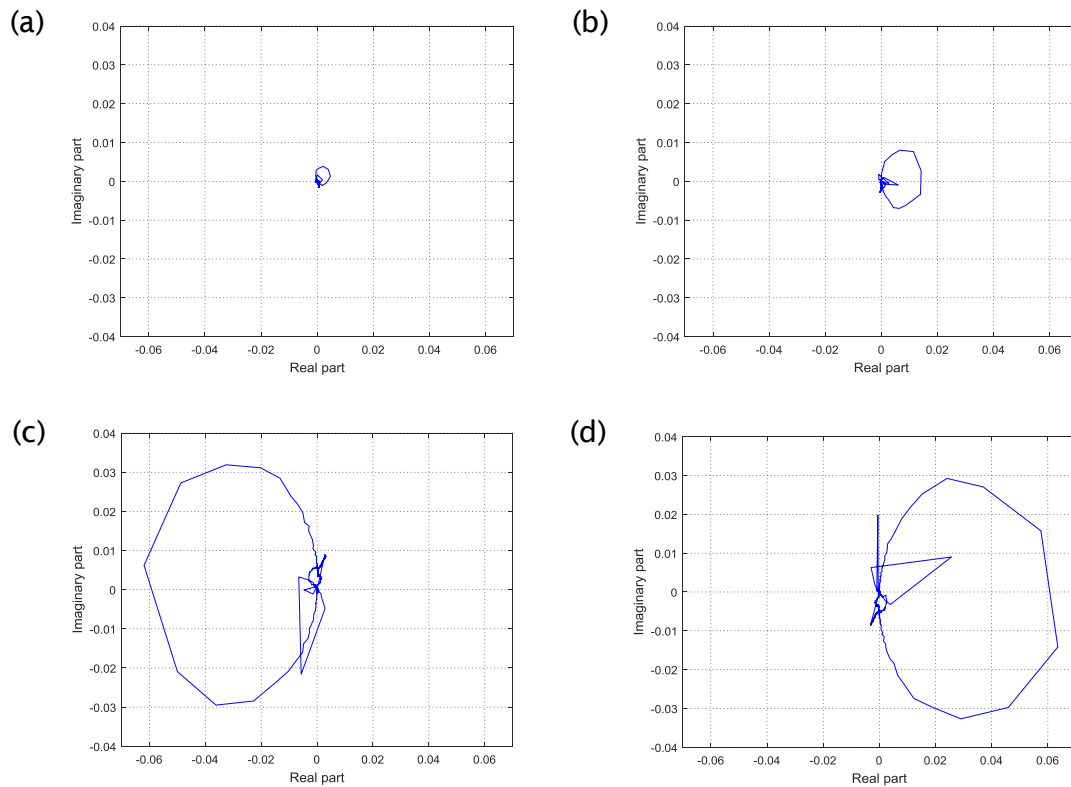


Figure 5.8 The Nyquist plots for the open loop of beam structures with an ideal low-pass filter (Cut-off frequency: 300 Hz): (a) ACLD treatment, (b) APCLD treatment, (c) AC/PCLD treatment and (d) AC/PSOLD treatment

5. VELOCITY FEEDBACK HYBRID ACTIVE-PASSIVE CONTROL OF BEAMS

Table 5.1 G_{3dB} for each configuration according to the application of a low-pass filter

	Without filter	With a KEMO low-pass filter	Ratio to 'w/o filter' case	With an ideal low-pass filter	Ratio to 'w/o filter' case
ACLD	14.09	261.97	18.59	825.10	58.56
APCLD	24.58	167.61	6.82	1240	50.45
AC/PCLD	8.42	61.79	7.34	8.42	1
AC/PSOLD	4.79	69.77	14.57	1302	271.82

In summary, control gains for stable control with a 3 dB gain margin in each case, G_{3dB} , can be shown as in Table 5.1. The method used to calculate 3 dB gain margin from a Nyquist plot of transfer function is explained in Appendix C.2.3 with an example. Introduction of a low-pass filter can give a positive influence on the increase in control gain for stable control. AC/PSOLD treatment can provide the largest increase in control gain out of four types and it can result in the possible estimation of the best control result with HAPCLD treatment as concluded in [3]. When considering the phase shift caused by the inner signal processing procedure of the low-pass filter circuit, the advantage of an ideal filter is obvious in Table 5.1 and its design for realisation will be explored more in the next subsection.

5.2.2 Study of a realisation method for an ideal low-pass filter by means of an all-pass filter or phase compensator

As mentioned in the previous subsection, in the case of harmonic excitation, an all-pass filter is usually used to compensate for the phase shift caused by a low-pass filter. An all-pass filter does not affect the amplitude of an input signal, but only the phase up to a cut-off frequency as shown in Figure 5.9. If a filtered signal, which went through a low-pass filter and an all-pass filter in series, has an additional 360° phase shift in total through a series of filters at a specific target frequency, the output signal seems to have no phase shift as a consequence. Therefore, an introduction of an all-pass filter is very useful in compensation for phase shift for the control of harmonically excited system.

5. VELOCITY FEEDBACK HYBRID ACTIVE-PASSIVE CONTROL OF BEAMS

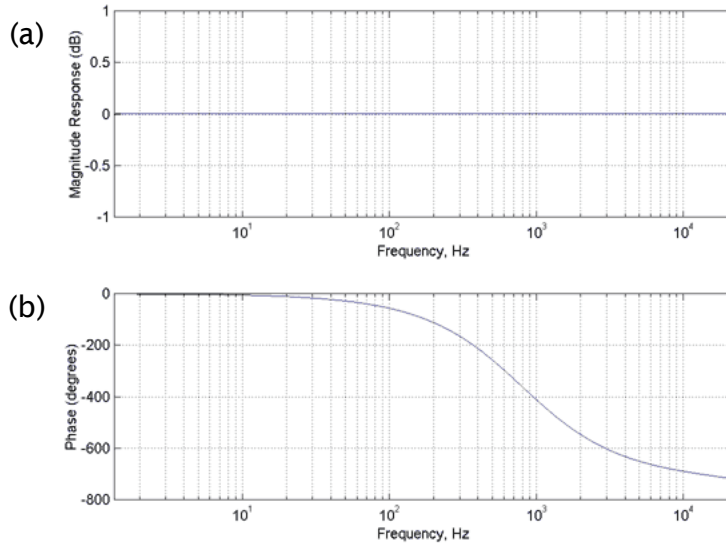


Figure 5.9 Frequency response of an all-pass filter from [<http://www.uaudio.com/blog/allpass-filters>] (a) Magnitude Response and (b) Phase

However, in the case of broadband excitation or multi-mode control, as used in this thesis, the introduction of an all-pass filter to compensate for a phase shift at a specific target frequency can cause problems in other modes. For example, when the phase shift through a low-pass filter at the first mode is compensated for by an all-pass filter, all other frequency components of the signal are under the influence of the shifted phase resulting from an all-pass filter as well. Therefore, when compensating for the filtered signal at the second mode, a second all-pass filter should be designed considering added phase shift resulting from an all-pass filter at the first mode. For other modes, this procedure should be repeated to effectively eliminate all phase shifts from previously applied all-pass filters from input signal. Thus, the introduction of an all-pass filter can make a phase shift problem due to a filter more severe in this manner for broadband excitation or multi-mode control.

As a method for minimisation of phase shift, the selection of a lower-order filter, which has a smaller phase shift, can be considered. A filter of a lower order generally causes a smaller phase shift in the input signal. However, in this case, since the attenuation of amplitude of the signal after a cut-off frequency is smaller than when using higher-order filters, reduced trimming effect is expected.

On the other hand, a so-called counter all-pass filter, which has the same frequency response but the opposite phase change to a general all-pass filter, could be proposed. Unfortunately, a counter all-pass filter does not exist and it would be impossible to realise when considering the operational logic of filtering. During the process of signal conversions between time and frequency domains such as FFT and IFFT, the group delay in the signal happens and it results in a phase shift. Therefore, since this phase shift is the result of a time gap between unfiltered and

5. VELOCITY FEEDBACK HYBRID ACTIVE-PASSIVE CONTROL OF BEAMS

filtered signals [97], it is impossible to eliminate the phase shift itself by adding another filter such as a counter all-pass filter.

However, the efficiency of all-pass filters in phase compensation cannot be ignored, although it is valid in narrow band control as mentioned above. In order to overcome this weakness of all-pass filter in broad band control, the combination of band-pass filters and all-pass filters as shown in Figure 5.10 can be proposed as an alternative method of phase compensation and real-time signal decomposition in a frequency domain. The application of a band-pass filter to a velocity input signal was proposed for stable modal vibration control of non-collocated structures in [98]. In the case that sensors and actuators are not collocated, the phases of some modes are in out-of-phase status, which can cause the range of control gain for stable control to be limited or control itself to be unstable as explained in Sections C.2.2 and C.2.3. However, by applying a modal filter consisting of high-pass filters, band-pass filters or low-pass filters according to the kind of input signal, i.e. displacement, velocity or acceleration signal for each mode, stable control can be achieved in each mode.

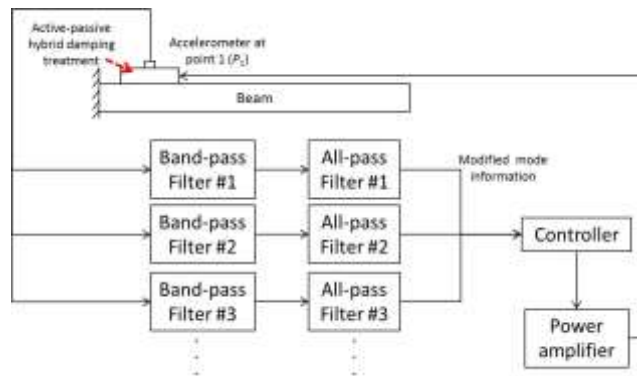


Figure 5.10 Phase shift minimisation method in real-time active control using a combination of a band-pass filter and an all-pass filter

Each band-pass filter is used for filtering real-time signals within frequency bands around each resonance frequency of interest. This means that the centre frequencies of each band-pass filter are determined by the resonance frequencies of each mode of interest. Bandwidth of the band-pass filters can be set to the bandwidth of each mode, i.e. the differences of half-power frequencies of each mode. Additional phase shift can occur during the filtering of a signal around each resonance frequency of interest using band-pass filters. This phase shift can be physically eliminated by adding more phase shift using all-pass filters to make a total phase shift of 360° through the combination of filters. As a result of signal filtering, the effect of phase shift by filters for mode selection for active control can be physically removed and the possibility of unstable control can be minimised. The filtering system described in Figure 5.10 can be a bit heavy for the case that there are many modes to be controlled. However, when considering that

5. VELOCITY FEEDBACK HYBRID ACTIVE-PASSIVE CONTROL OF BEAMS

first some modes are subject of active control in general, the size of system should be efficiently determined according to the number of controlled modes.

In this section, the way to keep the magnitude of a signal the same but can eliminate or minimise the effects of phase shift due to other filters for signal control such as a low-pass filter was discussed. The objective of this discussion is to only clarify the active control of velocity feedback control with systems used in this thesis regardless of unexpected phase distortion by the application of a low-pass filter. In the next section, the control results using an ideal filter realised by a combination of band-pass filters will be discussed. Measured FRFs of beam structures shown in Sections 4.2.2 and 4.2.3 will be used.

5.2.3 Optimal control gains with the proposed ideal filter

As mentioned at the end of the previous section, estimated control results with the ideal filter shown in Figure 5.7 will be discussed in this section.

Control results and phases with ACLD treatment for three cases, i.e. without filter, with a KEMO low-pass filter and with an ideal filter, are obtained as shown in Figure 5.11 and 5.12 respectively using control gain G_{3dB} with the 3 dB gain margins given in Table 5.1.

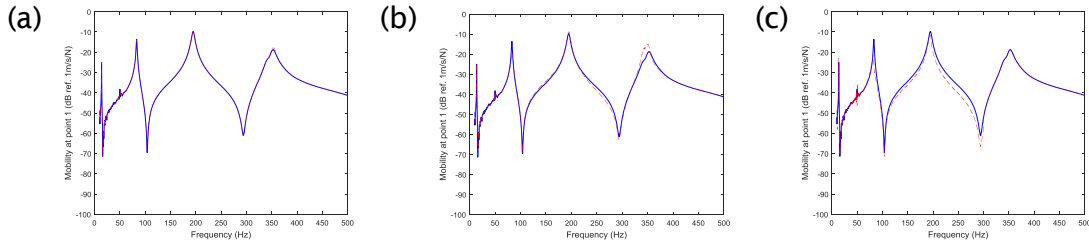


Figure 5.11 Control results for ACLD treatment on a beam with (a) No filter ($G_{3dB} = 14.09$), (b) a KEMO low-pass filter ($G_{3dB} = 261.97$) and (c) a proposed ideal filter ($G_{3dB} = 825.10$); — No control; - - with control

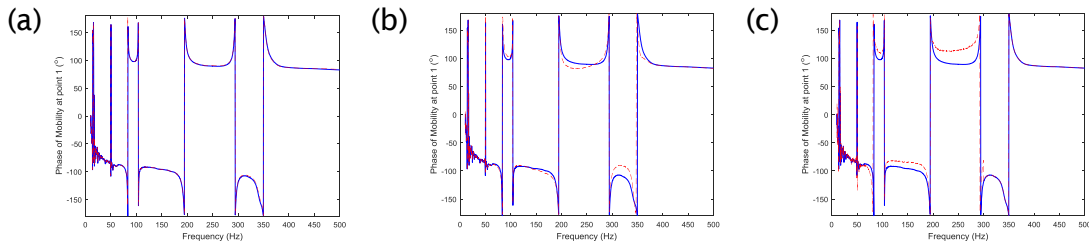


Figure 5.12 Phases for ACLD treatment on a beam with (a) No filter ($G_{3dB} = 14.09$), (b) a KEMO low-pass filter ($G_{3dB} = 261.97$) and (c) a proposed ideal filter ($G_{3dB} = 825.10$); — No control; - - with control

5. VELOCITY FEEDBACK HYBRID ACTIVE-PASSIVE CONTROL OF BEAMS

The peak values in the uncontrolled case and the changes in those values for each control case are summarised in Table 5.2.

Table 5.2 Change of peak values in the case of active control using ACLD treatment in beams

		1st mode	2nd mode	3rd mode
Only with passive control effect of ACLD (Peak amplitude)		-24.99 dB	-13.62 dB	-9.758 dB
Changes by active control using G_{3dB}	w/o filter	+0.03 dB	-0.27 dB	-0.038 dB
	w/ KEMO filter	+1.01 dB	-5.76 dB	+9.036 dB
	w/ ideal filter	+2.05 dB	-8.12 dB	-1.762 dB

As seen in Figure 5.11 and Table 5.2, the ideal filter is advantageous and the vibration of the beam at the sensor point is controlled most effectively. Moreover, the active control effect using a PZT actuator is dominant for the 2nd mode in the current position. The maximum reduction in all cases of active control is obtained at the frequency of the 2nd mode with the ideal filter. Relatively small reduction in the 3rd mode will be discussed with other cases. Control of the 4th mode also shows a change of resonance frequency for the related mode as shown in Figure 5.11. It was caused by the additional damping added by the active control, which can cause the pinning effect as explained in Appendix C with a very high control gain, with the ideal filter.

The same simulation was repeated for other configurations. Obtained results are arranged below. Figures 5.13, 5.14 and 5.15 show the results for APCLD, AC/PCLD and AC/PSOLD treatments respectively. Phase plots for Figure 5.13, 5.14 and 5.15 can be found in Appendix C.2.4. As expected, the most reduction with active control is obtained using AC/PSOLD treatment in all four cases.

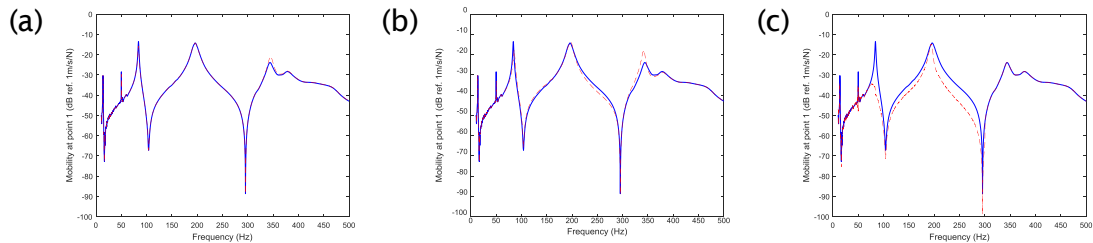


Figure 5.13 Control results for APCLD treatment on a beam with (a) No filter ($G_{3dB} = 24.58$), (b) a KEMO low-pass filter ($G_{3dB} = 167.61$) and (c) a proposed ideal filter ($G_{3dB} = 1240$); — No control; — with control

5. VELOCITY FEEDBACK HYBRID ACTIVE-PASSIVE CONTROL OF BEAMS

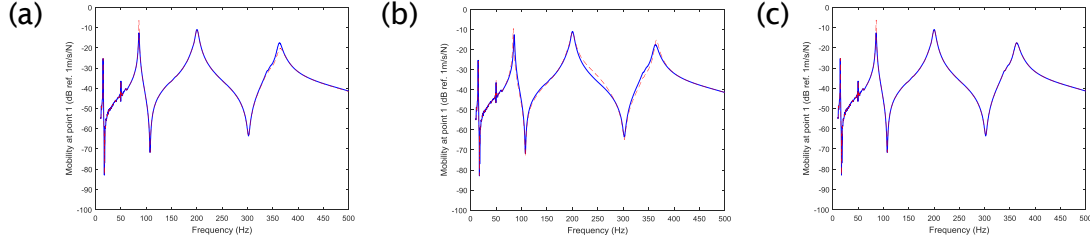


Figure 5.14 Control results for AC/PCLD treatment on a beam with (a) No filter ($G_{3dB} = 8.42$), (b) a KEMO low-pass filter ($G_{3dB} = 61.79$) and (c) a proposed ideal filter ($G_{3dB} = 8.42$); — No control; - - with control

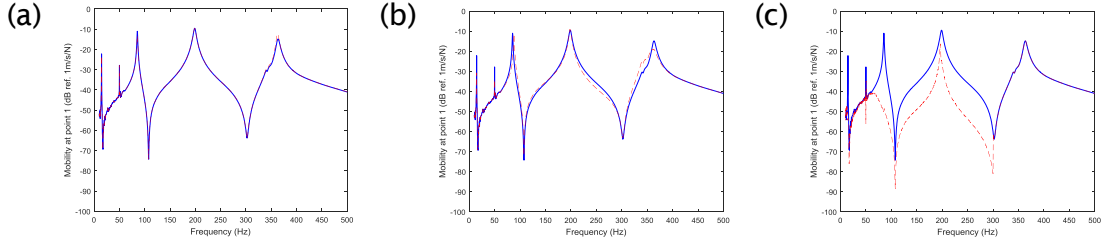


Figure 5.15 Control results for AC/PSOLD treatment on a beam with (a) No filter ($G_{3dB} = 4.79$), (b) a KEMO low-pass filter ($G_{3dB} = 69.77$) and (c) a proposed ideal filter ($G_{3dB} = 1302$); — No control; - - with control

As discussed with ACLD treatment, the motion of a PZT patch at the current location on the beam as shown in Figures 5.1 to 5.4 is confirmed to affect the 2nd mode most out of the first three modes presented in the figures. When considering the difference between ACLD treatment and other configurations, the application of an additional constraining layer is assumed to give an influence on control results by adding a constraining effect on whole systems even during active control. When a piezoelectric layer acts as an actuator during active control, a constraining effect of the piezoelectric layer is reduced compared with when it is in a passive control state. It should be noted that ACLD treatment is the only configuration in which a PZT patch has the double role of piezoelectric actuator and constraining layer out of the four configurations used in this study. However, since an additional constraining layer maintains a constraining effect during active control for other configurations, more reduced control results could be obtained from the other three configurations.

For comparison, vibration control simulations with 3dB control gains for a proposed ideal filter of each configurations were conducted and the results are shown in Figure 5.16. Due to some differences in phase, especially for the third mode, the reduction pattern in the related mode is different between measured and simulation results. However, general reduction patterns in two cases are similar. The simulation results for phases are given in Appendix C.2.4.

5. VELOCITY FEEDBACK HYBRID ACTIVE-PASSIVE CONTROL OF BEAMS

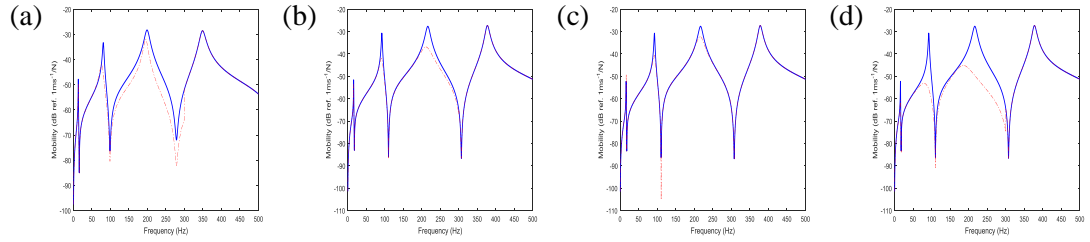


Figure 5.16 Control simulation results with a proposed ideal filter and G_{3dB} for (a) ACLD, (b) APCLD, (c) AC/PCLD and (d) AC/PSOLD treatments

Peak value reductions in each case shown in Figures 5.13 to 5.15 are arranged in Tables 5.3, 5.4 and 5.5 respectively. As is shown in the tables, the peak value reductions with APCLD and AC/PSOLD treatments are larger than with ACLD treatment. Due to the reverse polarization of the PZT patch for AC/PCLD treatment, the expected reduction is not achieved. According to the results, although the lower peak amplitude change by passive control is measured in the case of APCLD treatment, the increase in passive damping by APCLD treatment is not certain since different base beams were used in each case. More exact comparison of passive control can be found in Figure 4.6 and related discussion is presented in Section 4.2. As can be noticed from Figures 5.11, 13, 14 and 15, the reductions in 3rd mode are relatively smaller than other modes. When checking the changes in Figure 5.15, modal stiffness and mass of 3rd mode were increased by active control rather than modal damping. The mismatch between input signal, i.e. velocity, and control moment generated by the PZT patch, which is called duality problem as studied in Appendix C, caused these results.

Table 5.3 Change of peak values in the case of active control using APCLD treatment in a beam

		1st mode	2nd mode	3rd mode
Only with passive control effect of APCLD (Peak amplitude)		-30.39 dB	-13.62 dB	-14.28 dB
Changes by active control using G_{3dB}	w/o filter	+0.20 dB	-2.24 dB	-0.05 dB
	w/ KEMO filter	+0.44 dB	-4.74 dB	+0.41 dB
	w/ ideal filter	-4.05 dB	-20.92 dB	-0.56 dB

5. VELOCITY FEEDBACK HYBRID ACTIVE-PASSIVE CONTROL OF BEAMS

Table 5.4 Change of peak values in the case of active control using AC/PCLD treatment in a beam

		1st mode	2nd mode	3rd mode
Only with passive control effect of AC/PCLD (Peak amplitude)		-24.34 dB	-12.62 dB	-11.04 dB
Changes by active control using G_{3dB}	w/o filter	+0.27 dB	+6.343 dB	+0.21 dB
	w/ KEMO filter	-2.64 dB	+5.072 dB	-1.16 dB
	w/ ideal filter	+0.27 dB	+6.343 dB	+0.21 dB

Table 5.5 Change of peak values in the case of active control using AC/PSOLD treatment in a beam

		1st mode	2nd mode	3rd mode
Only with passive control effect of AC/PSOLD (Peak amplitude)		-22.19 dB	-11.01 dB	-9.511 dB
Changes by active control using G_{3dB}	w/o filter	-1.02 dB	-2.32 dB	-0.098 dB
	w/ KEMO filter	-8.72 dB	-3.21 dB	+0.925 dB
	w/ ideal filter	-28.08 dB	-29.77 dB	-6.799 dB

The effectiveness of AC/PSOLD treatment for active control is assured by the tables given above as can be noted in Figures 5.13 to 5.15. Therefore, the conclusion about active control simulations for the first three modes of a cantilever beam using four different HAPCLD treatments conducted in [3] was confirmed as applicable with different control strategies through related experiments and simulations. Since a similar base structure, e.g. cantilever beams with different dimensions, and similar configurations were used as was done in [3], the frequency responses of PZT actuators were similar. Therefore, used controllers gave a positive effect for the first three modes only. However, although simple velocity feedback control was used in this study instead of the LQR used in [3], control results were determined by structural relationships between a base structure and a controller rather than an applied control strategy, if stability problem could be solved by an additional method as explained in this chapter. With this result, the application of controllers and a control strategy used for beams in this chapter can be expanded towards more complex structures such as plates.

5.3 Summary and conclusions

In this chapter, active control of a beam structure using HAPCLD treatments has been studied. The conclusions by Trindade and Benjeddou [3] related to HAPCLD treatments were validated even with a simple velocity feedback, which is different from the one used in [3], Linear Quadratic Regulator (LQR). Although LQR was used as a control algorithm for parameter study in [3], other various control algorithms including ‘Proportional and/or Derivative’ and ‘Direct Velocity Feedback’ was used in their references. Thus, a simple control algorithm such as ‘Direct Velocity Feedback’ was selected from the control algorithms listed in [3] as a control algorithm instead of LQR in this study to verify the applicability of various HAPCLD treatments and their applicability for stable control is guaranteed as described in [3].

In addition to this, the modal decomposition method, which can be implemented in real-time active control, without phase shift and minimising the possibility of unstable control caused by the application of a filter was investigated. Combined application of band-pass filters and all-pass filters can eliminate the effect of phase shift in each mode caused by any kind of filters and guarantee stable active control.

As result of the study in this chapter, four types of HAPCLD treatments and velocity feedback control strategy have been validated as being applicable to beams and their application to more complex structures such as plates can be studied based on this result. Therefore, the application of HAPCLD treatments and a velocity feedback control strategy should be studied in the following chapters.

In the next chapter, an FE modelling method for 2-D structures such as plates will be studied to establish the foundation of an active control feasibility study with 2-D structures using HAPCLD treatments.

6 FE MODELLING OF FLAT PLATES

According to consideration of shear deformation as was carried out for the beam models, two kinds of plate models are developed; one is according to the Kirchhoff plate theory and the other is the Mindlin-Reissner plate theory. The former ignores the shear deformation of the cross section with the assumption of a thin plate, that is, the thickness of the plate is relatively thin compared to the length and width of plate and is subject to a small deflection, while the latter considers the first order of shear deformation. Shear deformation is ignored for elastic and piezoelectric layers, but considered for the viscoelastic layer in this study. The Kirchhoff plate theory is then used for elastic and piezoelectric sheets, and the Mindlin-Reissner plate theory is utilised for the viscoelastic layer. In order to describe the shear deformation of the viscoelastic layer, the shear modulus of the GHM method is expanded to plates. Finally, the coupling method based on a layer-wise approach is introduced to plates as well. The objective of the research carried out in this chapter is the establishment of FE plate models to verify if the study of FE modelling of beams can successfully be expanded to more complex structures, that is, plates. Individual research topics in this chapter have already been studied by other researchers. However, such topics have been used together for the first time here to model complex laminate structures such as ACLD, APCLD, AC/PCLD and AC/PSOLD treatments.

6.1 Overview of flat plates with HAPCLD treatments

The final objective for FE modelling for plates with HAPCLD treatments is to establish FE models of plates as was done for beams in Chapter 3. In summary, all configurations of the structures are given in Figure 6.1. All configurations consist of a combination of elastic base plate, viscoelastic layer, elastic constraining layer and piezoelectric layer. In order to establish full FE models, FE models of each layer are derived from equations of motions in each layer. After this, final FE models will be established for each configuration considering the mutual relations between the motions of each layer.

6. FE MODELLING OF FLAT PLATES

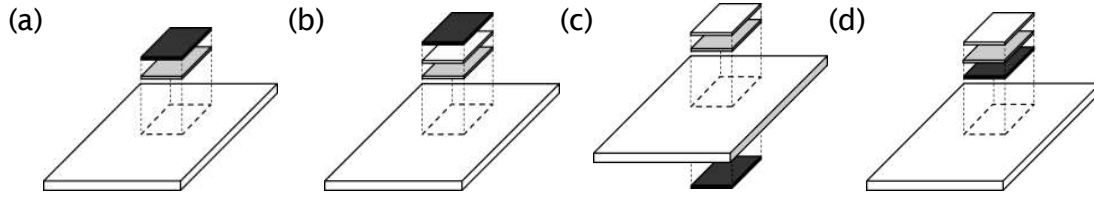





Figure 6.1 Configuration of a plate with (a) ACLD treatment, (b) APCLD treatment, (c) AC/PCLD treatment and (d) AC/PSOLD treatment;  : elastic plate and patch,  : viscoelastic layer and  : piezoelectric patch

6.2 FE model of an elastic plate

Here an isotropic elastic plate with a constant cross section is considered. Deflection of a Kirchhoff plate and establishment of FE global mass and stiffness matrices based on the Kirchhoff plate theory are explained in this section.

6.2.1 Basic assumption of a Kirchhoff plate

When a plate is subject to bending deformation, the deflection of the plate can be considered in the x and y directions individually as in Figure 6.2. This means that a plate can be treated as a beam which is stretched in the x and y directions respectively. Therefore, the basic assumption of a Euler beam, where there is no shear deformation in a cross section of the beam, which is explained in Section 3.2, can be applied to a plate as well [84]. The concept and assumption for small deflection on the x -axis shown in Figures 3.2 and 3.3 in Section 3.2.1 can be applied for the x - and y -axes in exactly the same way in this case as shown in Figure 6.2 (b) and (c).

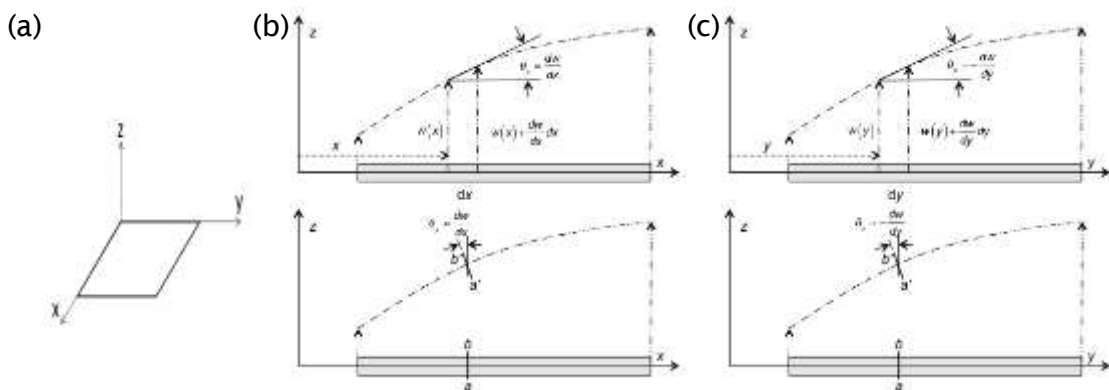


Figure 6.2 (a) The coordinate system of a plate (b) Deflection of plate in the x direction (c) Deflection of a plate in the y direction

For this reason, eqs. (3.3) and (3.4) for displacement equations of a beam can be expanded for a plate element as [84]

$$u(x, y, z) = u(x, y, 0) - z \frac{dw(x, y)}{dx} = u(x, y) - z \frac{dw(x, y)}{dx} = u(x, y) - z q_y(x, y), \quad (6.1)$$

$$v(x, y, z) = v(x, y, 0) - z \frac{dw(x, y)}{dy} = v(x, y) - z \frac{dw(x, y)}{dy} = v(x, y) + z q_x(x, y), \quad (6.2)$$

$$w(x, y, z) = w(x, y, 0) = w(x, y). \quad (6.3)$$

As explained in Section 3.2, each equation for displacements can describe the bending motion of the plate at one point in each axis, and cross sections of the plate element in the x and y -axes can remain straight.

6.2.2 FE formulation for an elastic Kirchhoff plate

Considering eqs. (6.1), (6.2) and (6.3), the potential energy of a Kirchhoff plate element with length in the x -direction of $2a$, in the y -direction of $2b$, thickness of h , a constant cross section and constant material properties, that is, constant Young's modulus E and density ρ can be expressed as

$$U_e = \frac{1}{2} \int_{-b-a}^b \int_{-a-h/2}^a \int_{-h/2}^{h/2} (\tau_{xx} \varepsilon_{xx} + \tau_{xy} \varepsilon_{xy} + \tau_{yx} \varepsilon_{yx} + \tau_{yy} \varepsilon_{yy}) dz dx dy,$$

where strain and stress relating to the z -axis can be ignored,

$$\tau_{xx} = \frac{E}{1-\nu^2} (\varepsilon_{xx} + \nu \varepsilon_{yy}), \quad \tau_{yy} = \frac{E}{1-\nu^2} (\varepsilon_{yy} + \nu \varepsilon_{xx}), \quad \tau_{xy} = \tau_{yx} = 2G \varepsilon_{xy} = \frac{E}{1+\nu} \varepsilon_{xy}, \quad (6.4)$$

ν denotes the Poisson's ratio and G refers to the Shear modulus of isotropic elastic plate.

With eq. (6.4) defining the relation between strain and stress of a plate,

$$U_e = \frac{E}{2(1-\nu^2)} \int_{-b-a}^b \int_{-a-h/2}^a \int_{-h/2}^{h/2} \{ \varepsilon_{xx}^2 + 2\nu \varepsilon_{xx} \varepsilon_{yy} + \varepsilon_{yy}^2 + 2(1-\nu) \varepsilon_{xy}^2 \} dz dx dy, \quad (6.5)$$

$$\text{where } \varepsilon_{xx} = \frac{\partial u}{\partial x} - z \frac{\partial^2 w}{\partial x^2}, \quad \varepsilon_{yy} = \frac{\partial v}{\partial y} - z \frac{\partial^2 w}{\partial y^2}, \quad \varepsilon_{xy} = \varepsilon_{yx} = \frac{1}{2} \left(\frac{\partial u}{\partial y} + \frac{\partial v}{\partial x} \right) - z \frac{\partial^2 w}{\partial x \partial y}. \quad (6.6)$$

6. FE MODELLING OF FLAT PLATES

Therefore, by substituting eq. (6.6) into eq. (6.5), eq. (6.5) can be rewritten as

$$U_e = \frac{C}{2} \int_{-b}^b \int_{-a}^a \left[\left(\frac{\partial u}{\partial x} \right)^2 + \left(\frac{\partial v}{\partial y} \right)^2 + 2\nu \frac{\partial u}{\partial x} \frac{\partial v}{\partial y} + \frac{1-\nu}{2} \left(\frac{\partial u}{\partial y} + \frac{\partial v}{\partial x} \right)^2 \right] dx dy$$

$$+ \frac{D}{2} \int_{-b}^b \int_{-a}^a \left[\left(\frac{\partial^2 w}{\partial x^2} \right)^2 + \left(\frac{\partial^2 w}{\partial y^2} \right)^2 + 2\nu \frac{\partial^2 w}{\partial x^2} \frac{\partial^2 w}{\partial y^2} + 2(1-\nu) \left(\frac{\partial^2 w}{\partial x \partial y} \right)^2 \right] dx dy, \quad (6.7)$$

where the extensional stiffness is $C = \frac{Eh}{1-\nu^2}$ and the bending rigidity is $D = \frac{Eh^3}{12(1-\nu^2)}$.

In the case of kinetic energy, since $z\dot{\theta}_x(x, y)$, $z\dot{\theta}_y(x, y)$, $(z\dot{\theta}_x(x, y))^2$ and $(z\dot{\theta}_y(x, y))^2$ terms can be ignored for the same reason as explained for eq. (3.6) in Section 3.2.2, the kinetic energy of a Kirchhoff plate can be defined as

$$T_e = \frac{1}{2} \int_{-b}^b \int_{-a}^a \left(\rho h \dot{u}(x, y)^2 + \rho h \dot{v}(x, y)^2 + \rho h \dot{w}(x, y)^2 \right) dx dy. \quad (6.8)$$

When the definition of displacement for an FE element is expressed with shape functions of in-plane and out-of-plane displacements as in eqs. (A.9) and (A.10) in Appendix A.3, the final formulas for the kinetic and potential energy of a Kirchhoff plate can easily be derived from eqs. (6.7) and (6.8) as has been done in Appendix A.4. The matrix form of equations for each energy is same as the final one for beams given in eqs. (3.8) and (3.9) of Section 3.2 respectively.

Finally, the FE equation of motion for a Kirchhoff plate is derived as

$$\mathbf{M}\ddot{\mathbf{q}} + \mathbf{K}\mathbf{q} = \mathbf{f} \rightarrow (\mathbf{K} - \omega^2 \mathbf{M})\mathbf{q} = \mathbf{K}_D \mathbf{q} = \mathbf{f}, \quad (6.9)$$

where the nodal DOF vector of the whole structure \mathbf{q} is defined as

$$\mathbf{q} = \{\mathbf{u} \quad \mathbf{w}\}^T, \quad \mathbf{u} = \left\{ \begin{matrix} u_1 & v_1 & \cdots & u_{m+1} & v_{m+1} \end{matrix} \right\} \text{ and}$$

$$\mathbf{w} = \left\{ \begin{matrix} w_1 & \theta_{x1} & \theta_{y1} & w_{xy1} & \cdots & w_{m+1} & \theta_{x(m+1)} & \theta_{y(m+1)} & w_{xy(m+1)} \end{matrix} \right\}.$$

Moreover, an external exciting force vector \mathbf{f} is defined as

$$\mathbf{f} = \{\mathbf{f}_u \quad \mathbf{f}_w\}^T, \quad \mathbf{f}_u = \left\{ \begin{matrix} f_{x1} & f_{y1} & \cdots & f_{x(m+1)} & f_{y(m+1)} \end{matrix} \right\} \text{ and}$$

$$\mathbf{f}_w = \left\{ \begin{matrix} f_{z1} & M_{x1} & M_{y1} & M_{xy1} & \cdots & f_{z(m+1)} & M_{x(m+1)} & M_{y(m+1)} & M_{xy(m+1)} \end{matrix} \right\}.$$

In this section, FE mass and stiffness matrices of an elastic plate structure are derived from kinetic and potential energy equations using the assumption of Kirchhoff plate theory. In the next section, a method to consider the electromechanical effect of piezoelectric materials in two-dimensional space will be studied based on the same assumption as this section.

6.3 FE model for a piezoelectric plate

In this section, an isotropic piezoelectric plate with constant cross section is considered. Since this piezoelectric plate is assumed as a Kirchhoff plate model, the kinetic energy related to the motion of plate is same as one for an elastic plate. Moreover, by using the constitutive equations of a piezoelectric material for 2-D structures, the piezoelectric effect of a piezoelectric plate is considered in deriving a stiffness matrix.

6.3.1 The constitutive equations of piezoelectric material for a 2D element

For the same reason explained in Section 3.3.1, the constitutive equations of piezoelectric material should be considered to understand the electrical characteristics of piezoelectric plates. The general constitutive equations of piezoelectric material are given in eq. (3.14).

For 2-D structures, y -directional components of strain and stress must not be neglected unlike in the case of 1-D elements. However, the assumption regarding the z -axis can be applied to this 2-D element in xy -space by assuming $\tau_{zz} \approx 0$. The resultant kinematic assumptions yield

$$\varepsilon_{zz} = \frac{1}{c_{33}} (e_{33} E_z - c_{13} \varepsilon_{xx} - c_{23} \varepsilon_{yy}). \quad (6.10)$$

Thus, substituting eq. (6.10) into eq. (3.14) leads us to obtain

6. FE MODELLING OF FLAT PLATES

$$\begin{aligned}
 \begin{Bmatrix} t_{xx} \\ t_{yy} \\ t_{yz} \\ t_{zx} \\ t_{xy} \end{Bmatrix} &= \begin{bmatrix} c_{11}^* & c_{12}^* & 0 & 0 & 0 \\ c_{21}^* & c_{22}^* & 0 & 0 & 0 \\ 0 & 0 & c_{44} & 0 & 0 \\ 0 & 0 & 0 & c_{55} & 0 \\ 0 & 0 & 0 & 0 & c_{66} \end{bmatrix} \begin{Bmatrix} e_{xx} \\ e_{yy} \\ e_{yz} \\ e_{zx} \\ e_{xy} \end{Bmatrix} - \begin{bmatrix} 0 & 0 & e_{31}^* \\ 0 & 0 & e_{32}^* \\ 0 & e_{24} & 0 \\ e_{15} & 0 & 0 \\ 0 & 0 & 0 \end{bmatrix} \begin{Bmatrix} E_x \\ E_y \\ E_z \end{Bmatrix}, \\
 \begin{Bmatrix} D_x \\ D_y \\ D_z \end{Bmatrix} &= \begin{bmatrix} 0 & 0 & 0 & e_{15} & 0 \\ 0 & 0 & e_{24} & 0 & 0 \\ e_{31}^* & e_{32}^* & 0 & 0 & 0 \end{bmatrix} \begin{Bmatrix} e_{xx} \\ e_{yy} \\ e_{yz} \\ e_{zx} \\ e_{xy} \end{Bmatrix} + \begin{bmatrix} dc_{11} & 0 & 0 \\ 0 & dc_{22} & 0 \\ 0 & 0 & dc_{33}^* \end{bmatrix} \begin{Bmatrix} E_x \\ E_y \\ E_z \end{Bmatrix}, \quad (6.11)
 \end{aligned}$$

where $c_{11}^* = c_{11} - c_{13}^2/c_{33}$, $c_{12}^* = c_{12} - c_{13}c_{23}/c_{33}$, $c_{21}^* = c_{21} - c_{13}c_{23}/c_{33}$, $c_{22}^* = c_{22} - c_{23}^2/c_{33}$, $e_{31}^* = e_{31} - e_{33}c_{13}/c_{33}$, $e_{32}^* = e_{32} - e_{33}c_{23}/c_{33}$, $\epsilon_{33}^* = \epsilon_{33} + e_{33}^2/c_{33}$ and c_{11} , c_{12} , c_{21} and c_{22} are elastic moduli of piezoelectric materials, c_{44} , c_{55} and c_{66} are shear moduli of piezoelectric materials, e_{31} , e_{32} , e_{24} and e_{15} are piezoelectric stress constants of piezoelectric materials, dc_{11} , dc_{22} and dc_{33}^* are dielectric constants of piezoelectric materials, τ_{xx} and τ_{yy} are extensional stresses, τ_{yz} , τ_{zx} and τ_{xy} are shear stresses, D_x and D_y are axial electric displacements and D_z is the transverse electric displacement.

6.3.2 FE formulation for a piezoelectric Kirchhoff plate

In this section, only the mechanical and electrical potential energy caused by a piezoelectric layer will be discussed as done for the case in Section 3.3.2. Firstly, the mechanical potential energy can be determined in the specific form of strain and stress for a 2-D structure from the first term of eq. (3.18) as

$$U_e = \frac{1}{2} \int_{V_e} \left\{ \epsilon_{xx} \quad \epsilon_{yy} \quad \epsilon_{yz} \quad \epsilon_{zx} \quad \epsilon_{xy} \right\} \left\{ \tau_{xx} \quad \tau_{yy} \quad \tau_{yz} \quad \tau_{zx} \quad \tau_{xy} \right\}^T dV.$$

By substituting the definition of stress obtained from eq. (6.11),

$$U_e = \frac{1}{2} \int_{V_e} \left\{ \begin{matrix} \varepsilon_{xx} & \varepsilon_{yy} & \varepsilon_{yz} & \varepsilon_{zx} & \varepsilon_{xy} \end{matrix} \right\} \left\{ \begin{matrix} c_{11}^* \varepsilon_{xx} + c_{12}^* \varepsilon_{yy} - e_{31}^* E_z \\ c_{21}^* \varepsilon_{xx} + c_{22}^* \varepsilon_{yy} - e_{32}^* E_z \\ c_{44} \varepsilon_{yz} - e_{24} E_y \\ c_{55} \varepsilon_{zx} - e_{15} E_x \\ c_{66} \varepsilon_{xy} \end{matrix} \right\} dV. \quad (6.12)$$

Since this model is considered a Kirchhoff plate, every shear strain term between in-plane and out-of-plane directions should be neglected, i.e. $\varepsilon_{yz} = 0$ and $\varepsilon_{zx} = 0$. It is assumed that the piezoelectric plate has thickness h_p and d_{31} mode polarisation, which means this piezoelectric layer is polarised in the thickness direction. The electric difference term between the upper and lower surface in the case of flat-rectangular-plate-shaped piezoelectric structures can be expressed as [88, 89]

$$E_x = -\frac{e_{15}}{e_{11}} \left(\frac{\partial w}{\partial y} + q_y \right) = 0, \quad E_y = -\frac{e_{24}}{e_{22}} \left(\frac{\partial w}{\partial y} - q_x \right) = 0 \text{ and } E_z = -\frac{\phi}{h_p}, \quad (6.13)$$

and, by considering that the electric potential is constant over the face of the element, eq. (6.12) can be rewritten with eq. (6.13) as

$$\begin{aligned} U_e &= \frac{1}{2} \int_{V_e} \left(\varepsilon_{xx} c_{11}^* \varepsilon_{xx} + \varepsilon_{xx} c_{12}^* \varepsilon_{yy} - \varepsilon_{xx} e_{31}^* E_z + \varepsilon_{yy} c_{21}^* \varepsilon_{xx} + \varepsilon_{yy} c_{22}^* \varepsilon_{yy} - \varepsilon_{yy} e_{32}^* E_z + \varepsilon_{xy} c_{66} \varepsilon_{xy} \right) dV \\ &= \frac{1}{2} \int_{V_e} \left(\left(\frac{\partial u}{\partial x} - z \frac{\partial^2 w}{\partial x^2} \right) c_{11}^* \left(\frac{\partial u}{\partial x} - z \frac{\partial^2 w}{\partial x^2} \right) + \left(\frac{\partial u}{\partial x} - z \frac{\partial^2 w}{\partial x^2} \right) c_{12}^* \left(\frac{\partial v}{\partial y} - z \frac{\partial^2 w}{\partial y^2} \right) + \left(\frac{\partial u}{\partial x} - z \frac{\partial^2 w}{\partial x^2} \right) e_{31}^* \frac{f_e}{h_p} \right. \\ &\quad + \left(\frac{\partial v}{\partial y} - z \frac{\partial^2 w}{\partial y^2} \right) c_{21}^* \left(\frac{\partial u}{\partial x} - z \frac{\partial^2 w}{\partial x^2} \right) + \left(\frac{\partial v}{\partial y} - z \frac{\partial^2 w}{\partial y^2} \right) c_{22}^* \left(\frac{\partial v}{\partial y} - z \frac{\partial^2 w}{\partial y^2} \right) + \left(\frac{\partial v}{\partial y} - z \frac{\partial^2 w}{\partial y^2} \right) e_{32}^* \frac{f_e}{h_p} \\ &\quad \left. + \left(\frac{1}{2} \left(\frac{\partial u}{\partial x} + \frac{\partial v}{\partial y} \right) - z \frac{\partial^2 w}{\partial x \partial y} \right) c_{66} \left(\frac{1}{2} \left(\frac{\partial u}{\partial x} + \frac{\partial v}{\partial y} \right) - z \frac{\partial^2 w}{\partial x \partial y} \right) \right) dV. \end{aligned}$$

By integrating in the thickness direction and changing the coordinate system from xyz -space to $\xi\eta z$ -space with the Jacobian matrix \mathbf{J} in Appendix A.1,

$$\begin{aligned} U_e &= \frac{1}{2} \int_{-1}^1 \int_{-1}^1 \left(h_p \left(\frac{1}{J_x^2} \frac{\partial u}{\partial \xi} c_{11}^* \frac{\partial u}{\partial \xi} + \frac{1}{J_x} \frac{1}{J_y} \frac{\partial u}{\partial \xi} c_{12}^* \frac{\partial v}{\partial \eta} + \frac{1}{J_x} \frac{1}{J_y} \frac{\partial v}{\partial \eta} c_{21}^* \frac{\partial u}{\partial \xi} + \frac{1}{J_y^2} \frac{\partial v}{\partial \eta} c_{22}^* \frac{\partial v}{\partial \eta} \right) \right. \\ &\quad \left. + h_p \left(\frac{1}{J_x} \frac{\partial u}{\partial \xi} e_{31}^* \frac{\phi_e}{h_p} + \frac{1}{J_y} \frac{\partial v}{\partial \eta} e_{32}^* \frac{\phi_e}{h_p} \right) + \frac{h_p^3}{12} \left(\frac{1}{J_x^4} \frac{\partial^2 w}{\partial \xi^2} c_{11}^* \frac{\partial^2 w}{\partial \xi^2} + \frac{1}{J_x^2} \frac{1}{J_y^2} \frac{\partial^2 w}{\partial \xi^2} c_{12}^* \frac{\partial^2 w}{\partial \eta^2} \right. \right. \\ &\quad \left. \left. + \frac{1}{J_x^2} \frac{1}{J_y^2} \frac{\partial^2 w}{\partial \eta^2} c_{21}^* \frac{\partial^2 w}{\partial \xi^2} + \frac{1}{J_y^4} \frac{\partial^2 w}{\partial \eta^2} c_{22}^* \frac{\partial^2 w}{\partial \eta^2} \right) \right) d\xi d\eta \end{aligned}$$

6. FE MODELLING OF FLAT PLATES

$$\begin{aligned}
& + \frac{1}{J_x^2} \frac{1}{J_y^2} \frac{\partial^2 w}{\partial \eta^2} c_{21}^* \frac{\partial^2 w}{\partial \xi^2} + \frac{1}{J_y^4} \frac{\partial^2 w}{\partial \eta^2} c_{22}^* \frac{\partial^2 w}{\partial \eta^2} \Bigg) + \frac{h_p}{4} \left(\frac{1}{J_x} \frac{\partial u}{\partial \xi} + \frac{1}{J_y} \frac{\partial v}{\partial \eta} \right) c_{66} \left(\frac{1}{J_x} \frac{\partial u}{\partial \xi} + \frac{1}{J_y} \frac{\partial v}{\partial \eta} \right) \\
& + \frac{h_p^3}{12} \frac{1}{J_x^2 J_y^2} \frac{\partial^2 w}{\partial \xi \partial \eta} c_{66} \frac{\partial^2 w}{\partial \xi \partial \eta} \Bigg) J_x d\xi J_y d\eta. \tag{6.14}
\end{aligned}$$

Using shape functions in eqs. (A.9) and (A.10) of Appendix A.3 and, since the electric potential difference ϕ_e is constant, eq. (6.14) can be changed into the FE approximate form as

$$\begin{aligned}
U_e &= \frac{1}{2} \mathbf{u}_e^T J_x J_y \int_{-1}^1 \int_{-1}^1 h_p \mathbf{B}_{in}^T \mathbf{D}_p \mathbf{B}_{in} d\xi d\eta \mathbf{u}_e + \frac{1}{2} \mathbf{w}_e^T J_x J_y \int_{-1}^1 \int_{-1}^1 \frac{h_p^3}{12} \mathbf{B}_{out}^T \mathbf{D}_p \mathbf{B}_{out} d\xi d\eta \mathbf{w}_e \\
&+ \frac{1}{2} \mathbf{u}_e^T J_x J_y \int_{-1}^1 \int_{-1}^1 h_p \frac{e_{31}^*}{h_p} \mathbf{B}_{in}^T d\xi d\eta \phi_e \\
&= \frac{1}{2} \mathbf{u}_e^T \mathbf{k}_{in_e} \mathbf{u}_e + \frac{1}{2} \mathbf{w}_e^T \mathbf{k}_{out_e} \mathbf{w}_e + \frac{1}{2} \mathbf{u}_e^T \mathbf{k}_{u\phi_e} \phi_e, \tag{6.15}
\end{aligned}$$

where the matrix of material constants of a piezoelectric plate

$$\mathbf{D}_p = \begin{bmatrix} \frac{c_{11}^*}{1-\nu_p^2} & \frac{c_{12}^* \nu_p}{1-\nu_p^2} & 0 \\ \frac{c_{21}^* \nu_p}{1-\nu_p^2} & \frac{c_{22}^*}{1-\nu_p^2} & 0 \\ 0 & 0 & \frac{c_{66}}{2(1+\nu_p)} \end{bmatrix} \text{ and other definitions of each matrix are the same as eq.}$$

(A.18) in Appendix A.4.

Furthermore, the electrical potential energy can be defined as [89]

$$W_e = \frac{1}{2} \int_{V_e} \mathbf{E}^T \mathbf{D} dV.$$

In the specific form of strain and stress for a 2-D structure,

$$W_e = \frac{1}{2} \int_{V_e} \left\{ \begin{matrix} E_x & E_y & E_z \end{matrix} \right\} \left\{ \begin{matrix} D_x \\ D_y \\ D_z \end{matrix} \right\} dV.$$

By substituting the definition of electrical displacement obtained from eq. (6.13),

$$W_e = \frac{1}{2} \int_{V_e} \left\{ \begin{matrix} E_x & E_y & E_z \end{matrix} \right\} \left\{ \begin{matrix} e_{15} e_{zx} + dc_{11} E_x \\ e_{24} e_{yz} + dc_{22} E_y \\ e_{31}^* e_{xx} + e_{32}^* e_{yy} + dc_{33}^* E_z \end{matrix} \right\} dV. \quad (6.16)$$

Applying the assumption of a Kirchhoff plate and eq. (6.13) to eq. (6.16) gives

$$\begin{aligned} W_e &= \frac{1}{2} \int_{V_e} (E_z e_{31}^* \epsilon_{xx} + E_z e_{32}^* \epsilon_{yy} + E_z dc_{33}^* E_z) dV \\ &= \frac{1}{2} \int_{V_e} \left(-\frac{f_e}{h_p} e_{31}^* \left(\frac{\partial u}{\partial x} - z \frac{\partial^2 w}{\partial x^2} \right) - \frac{f_e}{h_p} e_{32}^* \left(\frac{\partial v}{\partial y} - z \frac{\partial^2 w}{\partial y^2} \right) + dc_{33}^* \left(\frac{f_e}{h_p} \right)^2 \right) dV. \end{aligned}$$

By integrating this equation in the thickness direction, i.e. for the out-of-plane displacement z from $-\frac{h}{2}$ to $\frac{h}{2}$ with the consideration that this plate has constant cross sections in all directions,

$$W_e = \frac{1}{2} \int_{-b}^b \int_{-a}^a h_p \left(-\frac{f_e}{h_p} e_{31}^* \frac{\partial u}{\partial x} - \frac{f_e}{h_p} e_{32}^* \frac{\partial v}{\partial y} + dc_{33}^* \left(\frac{f_e}{h_p} \right)^2 \right) dx dy.$$

With the Jacobian matrix \mathbf{J} in Appendix A.1, the coordinate system is changed from xyz -space to $\xi\eta z$ -space as

$$W_e = \frac{1}{2} \int_{-1}^1 \int_{-1}^1 h_p \left(-\frac{1}{J_x} \frac{f_e}{h_p} e_{31}^* \frac{\partial u}{\partial \xi} - \frac{1}{J_y} \frac{f_e}{h_p} e_{32}^* \frac{\partial v}{\partial \eta} + dc_{33}^* \left(\frac{f_e}{h_p} \right)^2 \right) J_x dx J_y dy dh. \quad (6.17)$$

As was done for eq. (6.14), eq. (6.17) can be changed to FE discrete form as

$$\begin{aligned} W_e &= \frac{1}{2} \phi_e J_x J_y \int_{-1}^1 \int_{-1}^1 -h_p \frac{e_{31}^*}{h_p} \mathbf{B}_m d\xi d\eta \mathbf{u}_e + \frac{1}{2} 4 J_x J_y \frac{dc_{33}^*}{h_p^2} \phi_e^2 \\ &= -\frac{1}{2} \phi_e \mathbf{k}_{\phi \mathbf{u}_e} \mathbf{u}_e + \frac{1}{2} \phi_e k_{\phi \phi}^e \phi_e. \end{aligned} \quad (6.18)$$

Therefore, from eqs. (6.15) and (6.18), the effective stiffness matrix of a piezoelectric plate can be obtained from $\mathbf{U} - \mathbf{W}_e$. Finally, for a piezoelectric Kirchhoff plate, the electrical characteristics of piezoelectric material should be considered. Such characteristics can be represented

6. FE MODELLING OF FLAT PLATES

by the added state electrical potential difference ϕ_e . The FE equation of a piezoelectric Kirchhoff plate can be derived by considering this term as

$$\begin{bmatrix} \mathbf{m}_{in} & \mathbf{0} & \mathbf{0} \\ \mathbf{0} & \mathbf{m}_{out} & \mathbf{0} \\ \mathbf{0} & \mathbf{0} & 0 \end{bmatrix} \ddot{\mathbf{q}} + \begin{bmatrix} \mathbf{k}_{in} & \mathbf{0} & \mathbf{k}_{u\phi} \\ \mathbf{0} & \mathbf{k}_{out} & \mathbf{0} \\ \mathbf{k}_{\phi u} & \mathbf{0} & -k_{\phi\phi} \end{bmatrix} \mathbf{q} = \mathbf{f}, \quad (6.19)$$

where the nodal DOF vector of the whole structure including the electrical potential generated by the piezoelectric material \mathbf{q} is defined as

$$\mathbf{q} = \{\mathbf{u} \quad \mathbf{w} \quad \phi\}^T, \quad u = \left\{ u_1 \quad v_1 \quad \cdots \quad u_{n+1} \quad v_{n+1} \right\} \text{ and}$$

$$\mathbf{w} = \left\{ w_1 \quad \theta_{x1} \quad \theta_{y1} \quad w_{xy1} \quad \cdots \quad w_{n+1} \quad \theta_{x(n+1)} \quad \theta_{y(n+1)} \quad w_{xy(n+1)} \right\}.$$

Moreover, an external exciting force vector \mathbf{f} is defined as

$$\mathbf{f} = \{\mathbf{f}_u \quad \mathbf{f}_w \quad Q\}^T, \quad \mathbf{f}_u = \left\{ f_{x1} \quad f_{y1} \quad \cdots \quad f_{x(n+1)} \quad f_{y(n+1)} \right\},$$

$$f_w = \left\{ f_{z1} \quad M_{x1} \quad M_{y1} \quad M_{xy1} \quad \cdots \quad f_{z(n+1)} \quad M_{x(n+1)} \quad M_{y(n+1)} \quad M_{xy(n+1)} \right\}$$

and Q refers to electrical charge.

6.4 FE model for a laminated plate with one viscoelastic layer

In the previous section, FE mass and stiffness matrices of a piezoelectric plate are derived from kinetic and potential energy equations using the assumption of Kirchhoff plate theory and constitutive equations of piezoelectric materials. In this section, FE modelling considering shear deformation of viscoelastic materials when the viscoelastic layer is under deformation in the form of a sandwich structure will be studied based on the Mindlin-Reissner plate theory. Here the model of a viscoelastic layer constrained between two Kirchhoff plates is considered to describe the motion of viscoelastic layer used in HAPCLD treatments. Mindlin-Reissner plate assumptions are used for shear deformation. The viscoelasticity of the material is considered by introducing the GHM method.

6.4.1 Basic assumptions for a viscoelastic layer constrained between two elastic plates

As was done in Section 3.4.1 for a beam, the Mead and Markus model proposed in [2] is adopted. The sandwich plate theory provided in [99, 100] is the 2-D expansion of the Mead and Markus's 1-D theory. By using the theory, the equations of motion are derived with FEM modelling. For a sandwich plate with a viscoelastic layer as shown in Figure 6.3, the following assumptions are applied [99, 100]:

- (1) Shear strains in the base and cover plates are negligible: $\frac{\partial u_1}{\partial z} \approx 0$, $\frac{\partial v_1}{\partial z} \approx 0$, $\frac{\partial u_3}{\partial z} \approx 0$ and

$$\frac{\partial v_3}{\partial z} \approx 0, \text{ and longitudinal direct strains in the viscoelastic layer are negligible: } \frac{\partial u_2}{\partial x} \approx 0$$

$$\text{and } \frac{\partial v_2}{\partial x} \approx 0.$$

- (2) Transverse direct strains in the viscoelastic layer, base and cover plates are also neglected; so the transverse displacements w of all points on the same cross-section of all layers before deformation are equal: $w_1 = w_2 = w_3$.

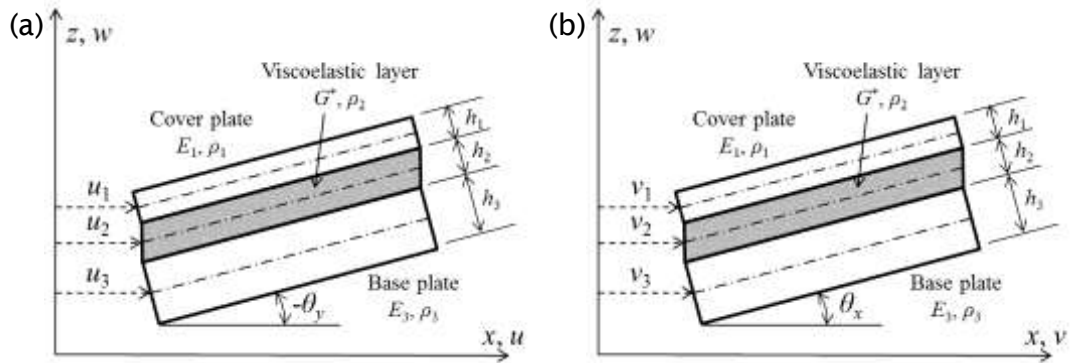


Figure 6.3 Geometric concept of a viscoelastic layer constrained between two elastic plates (a) in the x-axis and (b) y-axis

The shear strains on the centre plane of a viscoelastic layer can be defined like eq. (3.30) in Section 3.4.2 as

$$\gamma_{x,2} = \frac{\partial w}{\partial x} + \frac{\partial u_2(x, y, 0)}{\partial z} = \frac{\partial w}{\partial x} + \frac{\partial u_2(x, y)}{\partial z} \text{ and}$$

$$\gamma_{y,2} = \frac{\partial w}{\partial y} + \frac{\partial v_2(x, y, 0)}{\partial z} = \frac{\partial w}{\partial y} + \frac{\partial v_2(x, y)}{\partial z}, \quad (6.20)$$

6. FE MODELLING OF FLAT PLATES

where u_i and v_i are the in-plane displacement of any point in the viscoelastic core. Subscript $i = 1$ is used for the cover plate. Subscripts 2 and 3 are used for the viscoelastic layer and the base plate respectively. Thus, the shear stresses in the viscoelastic layer are

$$\begin{aligned} Q_{x,2} &= G^* \int_{-h_2/2}^{h_2/2} \gamma_{x,2} dz = G^* h_2 \left(\frac{\partial w}{\partial x} + \frac{\partial u_2}{\partial z} \right) \text{ and} \\ Q_{y,2} &= G^* \int_{-h_2/2}^{h_2/2} \gamma_{y,2} dz = G^* h_2 \left(\frac{\partial w}{\partial y} + \frac{\partial v_2}{\partial z} \right), \end{aligned} \quad (6.21)$$

where G^* is the complex shear modulus of the viscoelastic core which can be obtained by using eq. (3.29) in Section 3.4.1 [91].

6.4.2 FE formulation of a viscoelastic layer constrained between two elastic plates

If a plate element has a length of $2a$ and $2b$ in the x -direction and y -direction respectively, the kinetic energy of the plate element for viscoelastic layer constrained between two elastic plates can be defined as [99, 100]

$$T_e = \frac{1}{2} \rho_2 h_2 \int_{-b-a}^b \int_{-a}^a (\dot{u}_2^2 + \dot{v}_2^2 + \dot{w}_2^2) dx dy .$$

After the coordinate system is changed from the absolute xyz -space to the local $\xi\eta z$ -space with the Jacobian matrix \mathbf{J} in Appendix A.1, applying shape functions in eqs. (A.9) and (A.10) of Appendix A.3 can give

$$\begin{aligned} T_e &= \frac{1}{2} \dot{\mathbf{u}}_e^T J_x J_y \int_{-1}^1 \int_{-1}^1 \rho_2 h_2 \mathbf{H}_{in}^T \mathbf{H}_{in} d\xi J_y d\eta \dot{\mathbf{u}}_e + \frac{1}{2} \dot{\mathbf{w}}_e^T J_x J_y \int_{-1}^1 \int_{-1}^1 \rho_2 h_2 \mathbf{H}_{out}^T \mathbf{H}_{out} d\xi J_y d\eta \dot{\mathbf{w}}_e \\ &= \frac{1}{2} \dot{\mathbf{u}}_e^T \mathbf{m}_{in_e} \dot{\mathbf{u}}_e + \frac{1}{2} \dot{\mathbf{w}}_e^T \mathbf{m}_{out_e} \dot{\mathbf{w}}_e \\ &= \frac{1}{2} \dot{\mathbf{q}}_e^T \mathbf{m}_e \dot{\mathbf{q}}_e, \end{aligned} \quad (6.22)$$

$$\text{where } \dot{\mathbf{q}}_e = \left\{ \begin{matrix} \dot{\mathbf{u}}_e & \dot{\mathbf{v}}_e & \dot{\mathbf{w}}_e & \dot{\theta}_e & \frac{\partial \dot{\mathbf{u}}_e}{\partial z} & \frac{\partial \dot{\mathbf{v}}_e}{\partial z} \end{matrix} \right\}^T, \quad \mathbf{m}_e = \begin{bmatrix} \mathbf{m}_{in_e} & \mathbf{0} & \mathbf{0} & \mathbf{0} & \mathbf{0} & \mathbf{0} \\ \mathbf{0} & \mathbf{m}_{in_e} & \mathbf{0} & \mathbf{0} & \mathbf{0} & \mathbf{0} \\ \mathbf{0} & \mathbf{0} & \mathbf{m}_{out_e} & \mathbf{m}_{out_e} & \mathbf{0} & \mathbf{0} \\ \mathbf{0} & \mathbf{0} & \mathbf{m}_{out_e} & \mathbf{m}_{out_e} & \mathbf{0} & \mathbf{0} \\ \mathbf{0} & \mathbf{0} & \mathbf{0} & \mathbf{0} & \mathbf{0} & \mathbf{0} \\ \mathbf{0} & \mathbf{0} & \mathbf{0} & \mathbf{0} & \mathbf{0} & \mathbf{0} \end{bmatrix}.$$

Moreover, when considering only shear deformation exists in the viscoelastic layer, the potential energy can be defined as [99, 100]

$$U_e = \frac{1}{2} \int_{-b}^b \int_{-a}^a (\mathcal{Q}_{x,2} \gamma_{x,2} + \mathcal{Q}_{y,2} \gamma_{y,2}) dx dy, \quad (6.23)$$

where $\mathcal{Q}_{x,2}$, $\mathcal{Q}_{y,2}$ are shear stresses in a viscoelastic layer defined in eq. (6.21) which can lead the change of eq. (6.23) as

$$U_e = \frac{1}{2} \int_{-b}^b \int_{-a}^a \left(G^* h_2 \left(\frac{\partial w}{\partial x} + \frac{\partial u_2}{\partial z} \right)^2 + G^* h_2 \left(\frac{\partial w}{\partial y} + \frac{\partial v_2}{\partial z} \right)^2 \right) dx dy.$$

After the coordinate system is changed from xyz -space to $\xi\eta z$ -space with the Jacobian matrix \mathbf{J} in Appendix A.1, applying shape functions in eqs. (A.9) and (A.10) of Appendix A.3 can give

$$\begin{aligned} U_e &= \frac{1}{2} \mathbf{w}_e^T J_x J_y \int_{-1}^1 \int_{-1}^1 h_2 \mathbf{H}_{out}^T \mathbf{G} \mathbf{H}'_{out} d\xi d\eta \mathbf{w}_e + \frac{1}{2} \mathbf{w}_e^T J_x J_y \int_{-1}^1 \int_{-1}^1 h_2 \mathbf{H}_{out}^T \mathbf{G} \mathbf{H}_{in} d\xi d\eta \frac{\partial \mathbf{u}_e}{\partial z} \\ &\quad + \frac{1}{2} \frac{\partial \mathbf{u}_e^T}{\partial z} J_x J_y \int_{-1}^1 \int_{-1}^1 h_2 \mathbf{H}_{in}^T \mathbf{G} \mathbf{H}'_{out} d\xi d\eta \mathbf{w}_e + \frac{1}{2} \frac{\partial \mathbf{u}_e^T}{\partial z} J_x J_y \int_{-1}^1 \int_{-1}^1 h_2 \mathbf{H}_{in}^T \mathbf{G} \mathbf{H}_{in} d\xi d\eta \frac{\partial \mathbf{u}_e}{\partial z} \\ &= \frac{1}{2} \mathbf{w}_e^T \mathbf{k}_{Gw_e} \mathbf{w}_e + \frac{1}{2} \mathbf{w}_e^T \mathbf{k}_{Gw_e} \frac{\partial \mathbf{u}_e}{\partial z} + \frac{1}{2} \frac{\partial \mathbf{u}_e^T}{\partial z} \mathbf{k}_{Gu_e} \mathbf{w}_e + \frac{1}{2} \frac{\partial \mathbf{u}_e^T}{\partial z} \mathbf{k}_{Gu_e} \frac{\partial \mathbf{u}_e}{\partial z} \\ &= \frac{1}{2} \mathbf{q}_e^T \mathbf{k}_e \mathbf{q}_e, \end{aligned} \quad (6.24)$$

$$\text{where } \mathbf{q}_e = \left\{ \begin{matrix} \mathbf{u}_e & \mathbf{v}_e & \mathbf{w}_e & \theta_e & \frac{\partial \mathbf{u}_e}{\partial z} & \frac{\partial \mathbf{v}_e}{\partial z} \end{matrix} \right\}^T, \quad \mathbf{G} = \begin{bmatrix} G^* & 0 \\ 0 & G^* \end{bmatrix},$$

6. FE MODELLING OF FLAT PLATES

$$\mathbf{k}_e = \begin{bmatrix} \mathbf{0} & \mathbf{0} & \mathbf{0} & \mathbf{0} & \mathbf{0} & \mathbf{0} \\ \mathbf{0} & \mathbf{0} & \mathbf{0} & \mathbf{0} & \mathbf{0} & \mathbf{0} \\ \mathbf{0} & \mathbf{0} & \mathbf{k}_{Gw_e} & \mathbf{0} & \mathbf{k}_{Gwu_e} & \mathbf{k}_{Gwu_e} \\ \mathbf{0} & \mathbf{0} & \mathbf{0} & \mathbf{0} & \mathbf{0} & \mathbf{0} \\ \mathbf{0} & \mathbf{0} & \mathbf{k}_{Guw_e} & \mathbf{0} & \mathbf{k}_{Gu_e} & \mathbf{0} \\ \mathbf{0} & \mathbf{0} & \mathbf{k}_{Guw_e} & \mathbf{0} & \mathbf{0} & \mathbf{k}_{Gu_e} \end{bmatrix}.$$

6.4.3 Coupling method for a laminated plate

In order to calculate displacements of each layer of laminated plates the Kantrovich-Krylov method, which is based on the Mead-Markus method [2], was used in [99, 100]. However, as explained in Section 3.4.4, this coupling method is valid only for sandwich structures. Thus, for more complex configurations of HAPCLD treatment than sandwich structures, the coupling matrix derived by a layer-wise approach will be introduced for a plate as was done for a beam in Section 3.4.4. The coupling matrix for a laminated plate can be obtained from the geometric relationships between the deformations of each layer. The deformation of a cross section for a bending motion described in Figure 3.10 in Section 3.4.4 in the x -direction can be applied to the y -direction as well as in Figure 6.4.

Therefore, the relationship between each displacement component can be derived as

$$\begin{aligned} u_1 &= u_0 - \left(\frac{h_1}{2} + \frac{h_3}{2} - d_3 \right) q_{y0} + h_2 \frac{\partial u_0}{\partial z}, \quad v_1 = v_0 + \left(\frac{h_1}{2} + \frac{h_3}{2} - d_3 \right) q_{x0} + h_2 \frac{\partial v_0}{\partial z}, \quad w_1 = w_0, \\ \theta_{x1} &= \theta_{x0}, \quad \theta_{y1} = \theta_{y0}, \quad w_{xy1} = w_{xy0}, \quad \frac{\partial u_1}{\partial z} = 0, \quad \frac{\partial v_1}{\partial z} = 0, \\ u_2 &= u_0 - \left(\frac{h_3}{2} - d_3 \right) q_{y0} + \frac{h_2}{2} \frac{\partial u_0}{\partial z}, \quad v_2 = v_0 + \left(\frac{h_3}{2} - d_3 \right) q_{x0} + \frac{h_2}{2} \frac{\partial v_0}{\partial z}, \quad w_2 = w_0, \\ q_{x2} &= 0, \quad q_{y2} = 0, \quad w_{xy2} = 0, \quad \frac{\partial u_2}{\partial z} = \frac{\partial u_0}{\partial z}, \quad \frac{\partial v_2}{\partial z} = \frac{\partial v_0}{\partial z} \quad \text{and} \\ u_3 &= u_0 + d_3 q_{y0}, \quad v_3 = v_0 - d_3 q_{x0}, \quad w_3 = w_0, \\ q_{x3} &= q_{x0}, \quad q_{y3} = q_{y0}, \quad w_{xy3} = w_{xy0}, \quad \frac{\partial u_3}{\partial z} = 0, \quad \frac{\partial v_3}{\partial z} = 0, \end{aligned} \quad (6.25)$$

where subscripts 1, 2, 3 and 0 refer to cover plate, viscoelastic layer, base plate and neutral axis of the whole plate respectively.

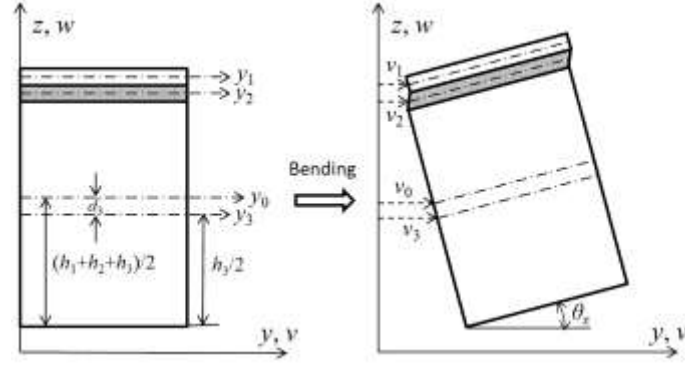


Figure 6.4 Basic concept of a layer-wise approach model for a sandwich plate with a viscoelastic core on the y-axis

From eq. (6.25), the coupling matrix for a laminated plate described in Figures 3.10 and 6.4 can be obtained as

$$\mathbf{C} = [\mathbf{C}_1 \quad \mathbf{C}_2 \quad \mathbf{C}_3]^T, \quad (6.26)$$

$$\text{where } \mathbf{C}_1 = \begin{bmatrix} 1 & 0 & 0 & 0 & -\left(\frac{h_1}{2} + \frac{h_3}{2} - d_3\right) & 0 & h_2 & 0 \\ 0 & 1 & 0 & \frac{h_1}{2} + \frac{h_3}{2} - d_3 & 0 & 0 & 0 & h_2 \\ 0 & 0 & 1 & 0 & 0 & 0 & 0 & 0 \\ 0 & 0 & 0 & 1 & 0 & 0 & 0 & 0 \\ 0 & 0 & 0 & 0 & 1 & 0 & 0 & 0 \\ 0 & 0 & 0 & 0 & 0 & 1 & 0 & 0 \\ 0 & 0 & 0 & 0 & 0 & 0 & 1 & 0 \\ 0 & 0 & 0 & 0 & 0 & 0 & 0 & 1 \end{bmatrix},$$

$$\mathbf{C}_2 = \begin{bmatrix} 1 & 0 & 0 & 0 & -\left(\frac{h_3}{2} - d_3\right) & 0 & \frac{h_2}{2} & 0 \\ 0 & 1 & 0 & \frac{h_3}{2} - d_3 & 0 & 0 & 0 & \frac{h_2}{2} \\ 0 & 0 & 1 & 0 & 0 & 0 & 0 & 0 \\ 0 & 0 & 0 & 0 & 0 & 0 & 0 & 0 \\ 0 & 0 & 0 & 0 & 0 & 0 & 0 & 0 \\ 0 & 0 & 0 & 0 & 0 & 0 & 0 & 0 \\ 0 & 0 & 0 & 0 & 0 & 0 & 1 & 0 \\ 0 & 0 & 0 & 0 & 0 & 0 & 0 & 1 \end{bmatrix} \text{ and}$$

6. FE MODELLING OF FLAT PLATES

$$\mathbf{C}_3 = \begin{bmatrix} 1 & 0 & 0 & 0 & d_3 & 0 & 0 & 0 \\ 0 & 1 & 0 & -d_3 & 0 & 0 & 0 & 0 \\ 0 & 0 & 1 & 0 & 0 & 0 & 0 & 0 \\ 0 & 0 & 0 & 1 & 0 & 0 & 0 & 0 \\ 0 & 0 & 0 & 0 & 1 & 0 & 0 & 0 \\ 0 & 0 & 0 & 0 & 0 & 1 & 0 & 0 \\ 0 & 0 & 0 & 0 & 0 & 0 & 0 & 0 \\ 0 & 0 & 0 & 0 & 0 & 0 & 0 & 0 \end{bmatrix}.$$

\mathbf{C}_i is coupling the local coordinate components, that is, the in-plane displacements, out-of-plane displacements and shear deformation of the i -th layer to the related global coordinate components to derive equivalent equations of motion. Therefore, by multiplying this coupling matrix \mathbf{C} and the transverse matrix of the coupling matrix \mathbf{C}^T to mass and stiffness matrices, equivalent mass and stiffness matrices can be derived.

6.5 FE model for a plate with HAPCLD treatment

Simply by introducing the FE model for a piezoelectric plate explained in Section 6.3 to an FE model of a laminated plate with a viscoelastic layer, an FE model for a plate with HAPCLD treatment can be obtained as was done in Section 3.5 for a beam. For example, for a plate with ACLD treatment, as in Figure 6.5, matrix equations of motion, displacement and force vectors for each layer can be expressed as before, where cover layer is replaced with a piezoelectric material.

As discussed in Section 3.5, when applying boundary conditions to this kind of structure, which has a small patch covering a part of the structure, shear deformation terms, which do not exist on nodes where a viscoelastic layer does not cover, must be eliminated carefully. Since the electrical difference term ϕ is the same along all nodes, it does not need to be eliminated considering nodes covered by a patch. If there are more than two patches attached, more electrical difference terms generated by each piezoelectric layer should be used as individual displacement terms in the displacement vector.

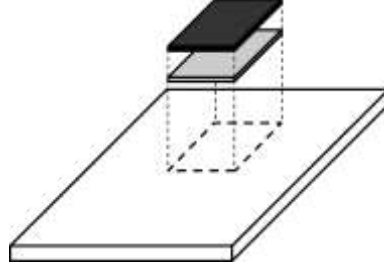





Figure 6.5 Configuration of a plate with ACLD treatment;  : elastic plate,  : viscoelastic layer and  : piezoelectric patch

Equations for the cover layer (piezoelectric plate) are given by

$$\begin{bmatrix} \mathbf{m}_{in_1} & \mathbf{0} & \mathbf{0} & \mathbf{0} \\ \mathbf{0} & \mathbf{m}_{out_1} & \mathbf{0} & \mathbf{0} \\ \mathbf{0} & \mathbf{0} & \mathbf{0} & \mathbf{0} \\ \mathbf{0} & \mathbf{0} & \mathbf{0} & \mathbf{0} \end{bmatrix} \ddot{\mathbf{q}}_1 + \begin{bmatrix} \mathbf{k}_{in_1} & \mathbf{0} & \mathbf{0} & \mathbf{k}_{u\phi} \\ \mathbf{0} & \mathbf{k}_{out_1} & \mathbf{0} & \mathbf{0} \\ \mathbf{0} & \mathbf{0} & \mathbf{0} & \mathbf{0} \\ \mathbf{k}_{\phi u} & \mathbf{0} & \mathbf{0} & -k_{\phi\phi} \end{bmatrix} \mathbf{q}_1 = \mathbf{M}_1 \ddot{\mathbf{q}}_1 + \mathbf{K}_1 \mathbf{q}_1 = \mathbf{f}_1,$$

$$\text{where } \mathbf{q}_1 = \left\{ \mathbf{u}_1 \quad \mathbf{w}_1 \quad \frac{\partial \mathbf{u}_1}{\partial z} \quad f_1 \right\}^T, \quad \mathbf{u}_1 = \left\{ u_{1_1} \quad v_{1_1} \quad \cdots \quad u_{1_{n+1}} \quad v_{1_{n+1}} \right\},$$

$$\mathbf{w}_1 = \left\{ w_{1_1} \quad \theta_{x1_1} \quad \theta_{y1_1} \quad w_{xy1_1} \quad \cdots \quad w_{1_{n+1}} \quad \theta_{x1_{n+1}} \quad \theta_{y1_{n+1}} \quad w_{xy1_{n+1}} \right\},$$

$$\frac{\partial \mathbf{u}_1}{\partial z} = \left\{ \frac{\partial u_{1_1}}{\partial z} \quad \frac{\partial v_{1_1}}{\partial z} \quad \cdots \quad \frac{\partial u_{1_{n+1}}}{\partial z} \quad \frac{\partial v_{1_{n+1}}}{\partial z} \right\} \text{ and}$$

$$\mathbf{f}_1 = \left\{ \mathbf{f}_{in_1} \quad \mathbf{f}_{out_1} \quad \mathbf{f}_{s_1} \quad Q_1 \right\}^T, \quad \mathbf{f}_{in_1} = \left\{ f_{x_1 1} \quad f_{y_1 1} \quad \cdots \quad f_{x_1(n+1)} \quad f_{y_1(n+1)} \right\},$$

$$\mathbf{f}_{out_1} = \left\{ f_{z_1 1} \quad M_{x_1 1} \quad M_{y_1 1} \quad M_{xy_1 1} \quad \cdots \quad f_{z_1(n+1)} \quad M_{x_1(n+1)} \quad M_{y_1(n+1)} \quad M_{xy_1(n+1)} \right\},$$

$$\mathbf{f}_{s_1} = \left\{ f_{s_{x_1} 1} \quad f_{s_{y_1} 1} \quad \cdots \quad f_{s_{x_1}(n+1)} \quad f_{s_{y_1}(n+1)} \right\},$$

where each term is the same as those used in eq. (6.19).

Equations for the core layer (viscoelastic material) are given by

6. FE MODELLING OF FLAT PLATES

$$\begin{bmatrix} \mathbf{m}_{\text{in}_2} & \mathbf{0} & \mathbf{0} & \mathbf{0} \\ \mathbf{0} & \mathbf{m}_{\text{out}_2} & \mathbf{0} & \mathbf{0} \\ \mathbf{0} & \mathbf{0} & \mathbf{0} & \mathbf{0} \\ \mathbf{0} & \mathbf{0} & \mathbf{0} & \mathbf{0} \end{bmatrix} \ddot{\mathbf{q}}_2 + \begin{bmatrix} \mathbf{0} & \mathbf{0} & \mathbf{0} & \mathbf{0} \\ \mathbf{0} & \mathbf{k}_{\text{Gw}} & \mathbf{k}_{\text{Gwu}} & \mathbf{0} \\ \mathbf{0} & \mathbf{k}_{\text{Guw}} & \mathbf{k}_{\text{Gu}} & \mathbf{0} \\ \mathbf{0} & \mathbf{0} & \mathbf{0} & \mathbf{0} \end{bmatrix} \mathbf{q}_2 = \mathbf{M}_2 \ddot{\mathbf{q}}_2 + \mathbf{K}_2 \mathbf{q}_2 = \mathbf{f}_2,$$

$$\text{where } \mathbf{q}_2 = \left\{ \mathbf{u}_2 \quad \mathbf{w}_2 \quad \frac{\partial \mathbf{u}_2}{\partial z} \quad \phi_2 \right\}^T, \quad \mathbf{u}_2 = \left\{ u_{2_1} \quad v_{2_1} \quad \cdots \quad u_{2_{n+1}} \quad v_{2_{n+1}} \right\},$$

$$\mathbf{w}_2 = \left\{ w_{2_1} \quad \theta_{x2_1} \quad \theta_{y2_1} \quad w_{xy2_1} \quad \cdots \quad w_{2_{n+1}} \quad \theta_{x2_{n+1}} \quad \theta_{y2_{n+1}} \quad w_{xy2_{n+1}} \right\},$$

$$\frac{\partial \mathbf{u}_2}{\partial z} = \left\{ \frac{\partial u_{2_1}}{\partial z} \quad \frac{\partial v_{2_1}}{\partial z} \quad \cdots \quad \frac{\partial u_{2_{n+1}}}{\partial z} \quad \frac{\partial v_{2_{n+1}}}{\partial z} \right\} \text{ and}$$

$$\mathbf{f}_2 = \left\{ \mathbf{f}_{\text{in}_2} \quad \mathbf{f}_{\text{out}_2} \quad \mathbf{f}_{s_2} \quad \mathcal{Q}_2 \right\}^T, \quad \mathbf{f}_{\text{in}_2} = \left\{ f_{x_2 1} \quad f_{y_2 1} \quad \cdots \quad f_{x_2(n+1)} \quad f_{y_2(n+1)} \right\},$$

$$\mathbf{f}_{\text{out}_2} = \left\{ f_{z_2 1} \quad M_{x_2 1} \quad M_{y_2 1} \quad M_{xy_2 1} \quad \cdots \quad f_{z_2(n+1)} \quad M_{x_2(n+1)} \quad M_{y_2(n+1)} \quad M_{xy_2(n+1)} \right\},$$

$$\mathbf{f}_{s_2} = \left\{ f_{s_{x_2} 1} \quad f_{s_{y_2} 1} \quad \cdots \quad f_{s_{x_2}(n+1)} \quad f_{s_{y_2}(n+1)} \right\},$$

where each term is the same as those used in eqs. (6.22) and (6.24).

Equations for the base layer (elastic plate) are given by

$$\begin{bmatrix} \mathbf{m}_{\text{in}_3} & \mathbf{0} & \mathbf{0} & \mathbf{0} \\ \mathbf{0} & \mathbf{m}_{\text{out}_3} & \mathbf{0} & \mathbf{0} \\ \mathbf{0} & \mathbf{0} & \mathbf{0} & \mathbf{0} \\ \mathbf{0} & \mathbf{0} & \mathbf{0} & \mathbf{0} \end{bmatrix} \ddot{\mathbf{q}}_3 + \begin{bmatrix} \mathbf{k}_{\text{in}_3} & \mathbf{0} & \mathbf{0} & \mathbf{0} \\ \mathbf{0} & \mathbf{k}_{\text{out}_3} & \mathbf{0} & \mathbf{0} \\ \mathbf{0} & \mathbf{0} & \mathbf{0} & \mathbf{0} \\ \mathbf{0} & \mathbf{0} & \mathbf{0} & \mathbf{0} \end{bmatrix} \mathbf{q}_3 = \mathbf{M}_3 \ddot{\mathbf{q}}_3 + \mathbf{K}_3 \mathbf{q}_3 = \mathbf{f}_3,$$

$$\text{where } \mathbf{q}_3 = \left\{ \mathbf{u}_3 \quad \mathbf{w}_3 \quad \frac{\partial \mathbf{u}_3}{\partial z} \quad \phi_3 \right\}^T, \quad \mathbf{u}_3 = \left\{ u_{3_1} \quad v_{3_1} \quad \cdots \quad u_{3_{n+1}} \quad v_{3_{n+1}} \right\},$$

$$\mathbf{w}_3 = \left\{ w_{3_1} \quad \theta_{x3_1} \quad \theta_{y3_1} \quad w_{xy3_1} \quad \cdots \quad w_{3_{n+1}} \quad \theta_{x3_{n+1}} \quad \theta_{y3_{n+1}} \quad w_{xy3_{n+1}} \right\},$$

$$\frac{\partial \mathbf{u}_3}{\partial z} = \left\{ \frac{\partial u_{3_1}}{\partial z} \quad \frac{\partial v_{3_1}}{\partial z} \quad \cdots \quad \frac{\partial u_{3_{n+1}}}{\partial z} \quad \frac{\partial v_{3_{n+1}}}{\partial z} \right\} \text{ and}$$

$$\mathbf{f}_3 = \left\{ \mathbf{f}_{\text{in}_3} \quad \mathbf{f}_{\text{out}_3} \quad \mathbf{f}_{s_3} \quad \mathcal{Q}_3 \right\}^T, \quad \mathbf{f}_{\text{in}_3} = \left\{ f_{x_3 1} \quad f_{y_3 1} \quad \cdots \quad f_{x_3(n+1)} \quad f_{y_3(n+1)} \right\},$$

$$\mathbf{f}_{\text{out}_3} = \left\{ \begin{matrix} f_{z_3 1} & M_{x_3 1} & M_{y_3 1} & M_{xy_3 1} & \cdots & f_{z_3(n+1)} & M_{x_3(n+1)} & M_{y_3(n+1)} & M_{xy_3(n+1)} \end{matrix} \right\},$$

$$\mathbf{f}_{s_3} = \left\{ \begin{matrix} f_{s_{x_3} 1} & f_{s_{y_3} 1} & \cdots & f_{s_{x_3}(n+1)} & f_{s_{y_3}(n+1)} \end{matrix} \right\},$$

where each term is the same as those used in eqs. (A.16) and (A.18).

Therefore, after stacking mass and stiffness matrices for local coordinates into one matrix according to the order of layer, the coupling matrix \mathbf{C} of eq. (6.26) is given by the three sub-matrices which are same as the three sub-matrices in eq. (6.26) except the coupling term for the electrical difference generated by PZT patch.

Finally, the global matrix equation of motion can be obtained as

$$\mathbf{M}\ddot{\mathbf{q}} + \mathbf{K}\mathbf{q} = \mathbf{f},$$

$$\text{where } \mathbf{M} = \mathbf{C}^T \begin{bmatrix} \mathbf{M}_1 & \mathbf{0} & \mathbf{0} \\ \mathbf{0} & \mathbf{M}_2 & \mathbf{0} \\ \mathbf{0} & \mathbf{0} & \mathbf{M}_3 \end{bmatrix} \mathbf{C}, \quad \mathbf{K} = \mathbf{C}^T \begin{bmatrix} \mathbf{K}_1 & \mathbf{0} & \mathbf{0} \\ \mathbf{0} & \mathbf{K}_2 & \mathbf{0} \\ \mathbf{0} & \mathbf{0} & \mathbf{K}_3 \end{bmatrix} \mathbf{C},$$

$$\mathbf{q} = \left\{ \mathbf{u} \quad \mathbf{w} \quad \frac{\partial \mathbf{u}}{\partial z} \quad \phi \right\}^T, \quad \mathbf{u} = \left\{ \begin{matrix} u_1 & v_1 & \cdots & u_{n+1} & v_{n+1} \end{matrix} \right\},$$

$$\mathbf{w} = \left\{ \begin{matrix} w_1 & \theta_{x_1} & \theta_{y_1} & w_{xy_1} & \cdots & w_{n+1} & \theta_{x_{n+1}} & \theta_{y_{n+1}} & w_{xy_{n+1}} \end{matrix} \right\},$$

$$\frac{\partial \mathbf{u}}{\partial z} = \left\{ \begin{matrix} \frac{\partial u_1}{\partial z} & \frac{\partial v_1}{\partial z} & \cdots & \frac{\partial u_{n+1}}{\partial z} & \frac{\partial v_{n+1}}{\partial z} \end{matrix} \right\} \text{ and}$$

$$\mathbf{f} = \{\mathbf{f}_{\text{in}} \quad \mathbf{f}_{\text{out}} \quad \mathbf{f}_s \quad Q\}^T, \quad \mathbf{f}_{\text{in}} = \left\{ \begin{matrix} f_{x_1} & f_{y_1} & \cdots & f_{x(n+1)} & f_{y(n+1)} \end{matrix} \right\},$$

$$\mathbf{f}_{\text{out}} = \left\{ \begin{matrix} f_{z_1} & M_{x_1} & M_{y_1} & M_{xy_1} & \cdots & f_{z(n+1)} & M_{x(n+1)} & M_{y(n+1)} & M_{xy(n+1)} \end{matrix} \right\},$$

$$\mathbf{f}_s = \left\{ \begin{matrix} f_{s_x 1} & f_{s_y 1} & \cdots & f_{s_x(n+1)} & f_{s_y(n+1)} \end{matrix} \right\}.$$

Furthermore, if an elastic constraining patch is added as in the three cases in Figure 6.6, mass and stiffness matrices of the base layer can be used for it. The coupling matrices and the equations of motion for these three cases are derived as explained in Appendix D.

6. FE MODELLING OF FLAT PLATES

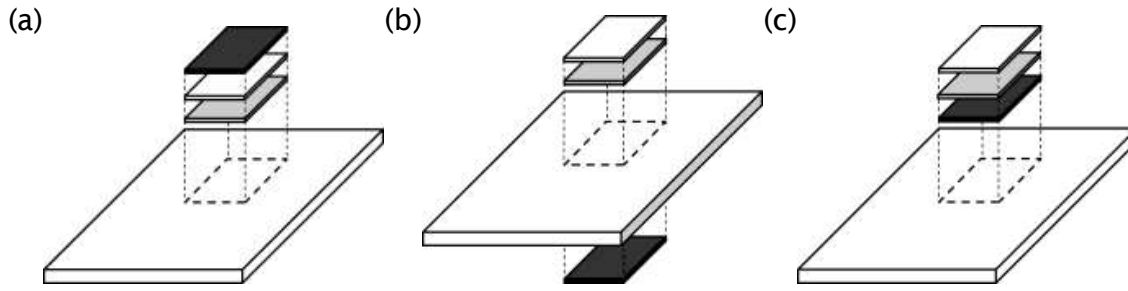


Figure 6.6 Configuration of a plate with (a) APCLD treatment, (b) AC/PCLD treatment and (c) AC/PSOLD treatment;

□ : elastic plate, □ : viscoelastic layer and ■ : piezoelectric patch

6.6 Validation of FE flat plate models

Flat plate models have been validated with the beam experiment results in Section 4.1. The beam structures as shown in Figures 4.1 and 4.3 (a free-free beam and a free-free beam with a PZT patch and a viscoelastic layer of 40 cm long, 3cm wide and 2.92 mm thick) and with the material properties which were modified in the previous comparison were used as given in Tables 4.2, 4.3 and 4.4 of Section 4.1. These structures can be thought of as narrow plates. Moreover, since other in-plane displacement in the y-axis was considered in this validation, the equivalent Young's modulus of structures was adjusted differently from the validation of beam models. As done for FE beam models in Section 4.1, resonance frequencies of FE plate models were compared with those of beam theory in Table 6.1. According to the comparison, FE plate models can give more accurate results than FE beam models. Since the effect of deformation in y-direction which is ignored in the beam theory in general is involved in models with increased number of elements in y-direction, higher resonance frequencies are obtained in those FE models.

As shown in Figures 6.7, 6.8 and 6.9, FEM and experimental results are in good agreement with each other. Figure 6.7 shows an input accelerance comparison for a free narrow plate. In Figures 6.8 and 6.9, input accelerances and electric voltage generated by the PZT patch of a free narrow plate with a PZT and viscoelastic layered patch are shown respectively. There are some changes in phase in Figure 6.7 (b) due to noise measured at anti-resonance frequencies and residuals truncated during modal analysis using FE models. Moreover, since more DOFs at each node were considered, from three to six in the modal analysis with an FE plate model than in an FE beam model and in-plane shear deformation which cannot be considered with an FE beam model was also considered as a result of nodal DOF increase, more similar results were obtained in the higher frequency range than are shown in Figures 4.2 and 4.4 of an FE beam model in Section 4.1. Secondly, results on a free-free beam with a PZT patch and a viscoelastic layer

6. FE MODELLING OF FLAT PLATES

were compared to the numerical model. As shown in Figures 6.8 and 6.9, experimental and numerical results are in good agreement.

Table 6.1 Resonance frequency comparison between beam theory and FE plate models

	Beam Theory	FE Plate (2×6 elements)	FE Plate (2×16 elements)	FE Plate (2×20 elements)	FE Plate (4×50 elements)
Mode 1	0 Hz	0 Hz	0 Hz	0 Hz	0 Hz
Mode 2	94.147 Hz	93.787 Hz (-0.384 %)	94.121 Hz (-0.027 %)	94.144 Hz (-0.003 %)	94.180 Hz (0.035 %)
Mode 3	259.512 Hz	256.289 Hz (-1.258 %)	259.277 Hz (-0.091 %)	259.499 Hz (-0.005 %)	259.867 Hz (0.137 %)
Mode 4	508.748 Hz	497.286 Hz (-2.305 %)	507.774 Hz (-0.192 %)	508.648 Hz (-0.020 %)	510.158 Hz (0.276 %)
Mode 5	840.992 Hz	810.493 Hz (-3.763 %)	838.262 Hz (-0.326 %)	840.574 Hz (-0.050 %)	844.744 Hz (0.444 %)
Mode 6	1256.282 Hz	1156.300 Hz (-8.647 %)	1250.227 Hz (-0.484 %)	1255.060 Hz (-0.097 %)	1264.219 Hz (0.628 %)

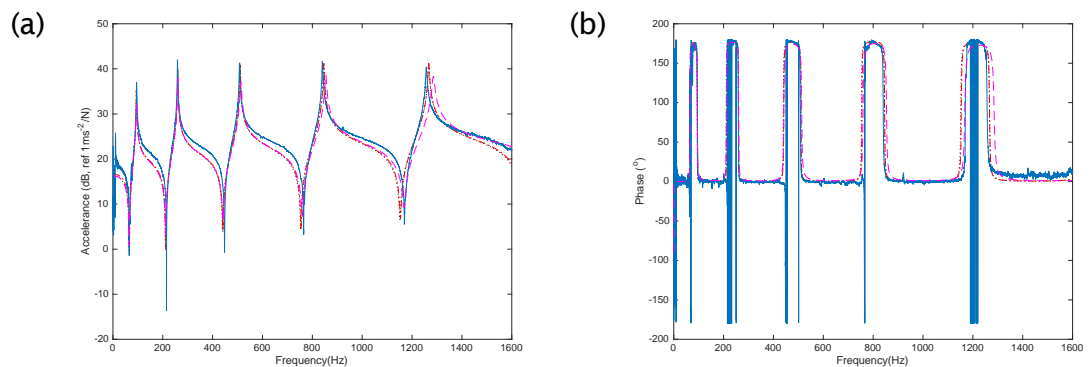


Figure 6.7 Input acceleration for a free narrow plate using 2-D FEM (a) Magnitude and (b) Phase: --- FEM (MATLAB); - - - Analytic (modal analysis); — Experiment; - - - FEM (Patran/Nastran)

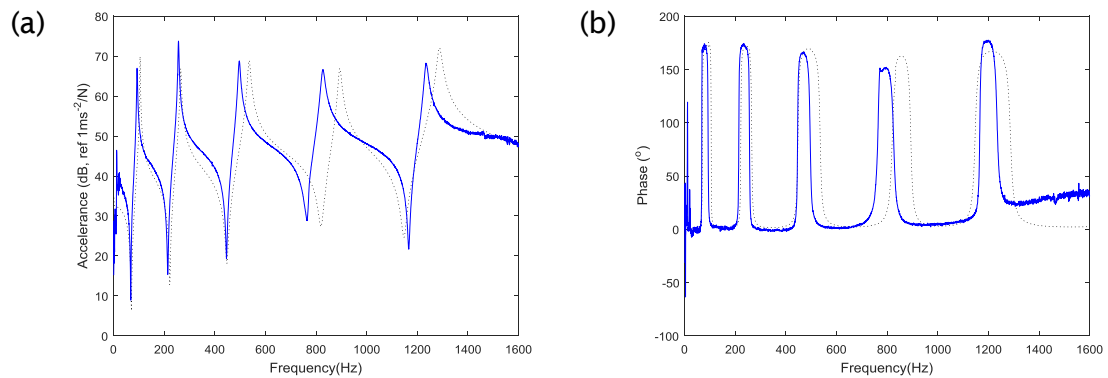


Figure 6.8 Input acceleration for a free narrow plate with PZT and a viscoelastic layered patch using 2-D FEM (a) Magnitude and (b) Phase: --- FEM; — Experiment

6. FE MODELLING OF FLAT PLATES

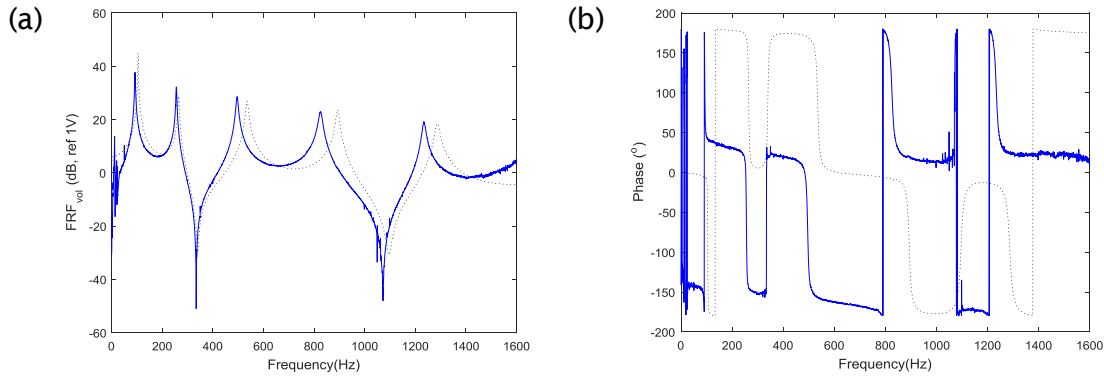


Figure 6.9 Voltage of a free narrow plate with PZT and a viscoelastic layered patch using 2-D FEM (a) Magnitude and (b) Phase: ---- FEM; — Experiment

6.7 Summary and conclusions

In this chapter, FE mass and stiffness matrices for each layer of arbitrarily laminated flat plate structures have been derived based on the Kirchhoff plate theory for elastic and piezoelectric layers and on the Mindlin-Reissner plate theory for a viscoelastic layer. By using the constitutive equation for a piezoelectric material, the electro-mechanical piezoelectric effect is modelled. For a viscoelastic layer, in order to describe shear deformation of a viscoelastic layer caused by viscoelasticity, the shear modulus proposed in the GHM method is introduced, as was done for a beam, and expanded for 2-D structures. Moreover, equivalent FE mass and stiffness matrices are derived by a coupling matrix based on a layer-wise approach to describe mutual effects between each layer of a composite plate and to combine separate layers into one equivalent beam. Finally, established FE plate models were validated through impact hammer tests with real test beams used in Chapter 4 for the model updating and response comparison of FE beam models subject to the assumption of thin plates.

FE modelling performed in this chapter is a good foundation for the active vibration control of flat plates using HAPCLD treatments, especially using APCLD, AC/PCLD and AC/PSOLD treatments later and will be expanded to curved plates with an introduction on curvature in the next chapter. The objective of the research carried out in this chapter as described in the introduction, the study of FE modelling of beams, has been successfully expanded to more complex structures, namely plates.

In the next chapter, firstly, FE modelling and its investigation for curved plates will be carried out considering the coordinates transfer due to curvature. A comparison between flat and curved

6. FE MODELLING OF FLAT PLATES

plates in terms of mechanical behaviour such as mode shapes and the effects of curvatures on control performance in each case will follow.

7 FE MODELLING OF CURVED PLATES

In the previous chapter, FE modelling and its validation of flat plates with HAPCLD treatments were studied. However, when considering applicability to various areas such as aeroplanes and automobiles, curved plates, i.e. shells, are much more generally and commonly used than flat plates. For example, outer surfaces of airplanes and cars, structural hull of ships, and other many machineries consist of curved plates with various shapes as shown in Figure 7.1. Therefore, based on the FE flat plate models established in Chapter 6, FE models for curved plates should be studied.

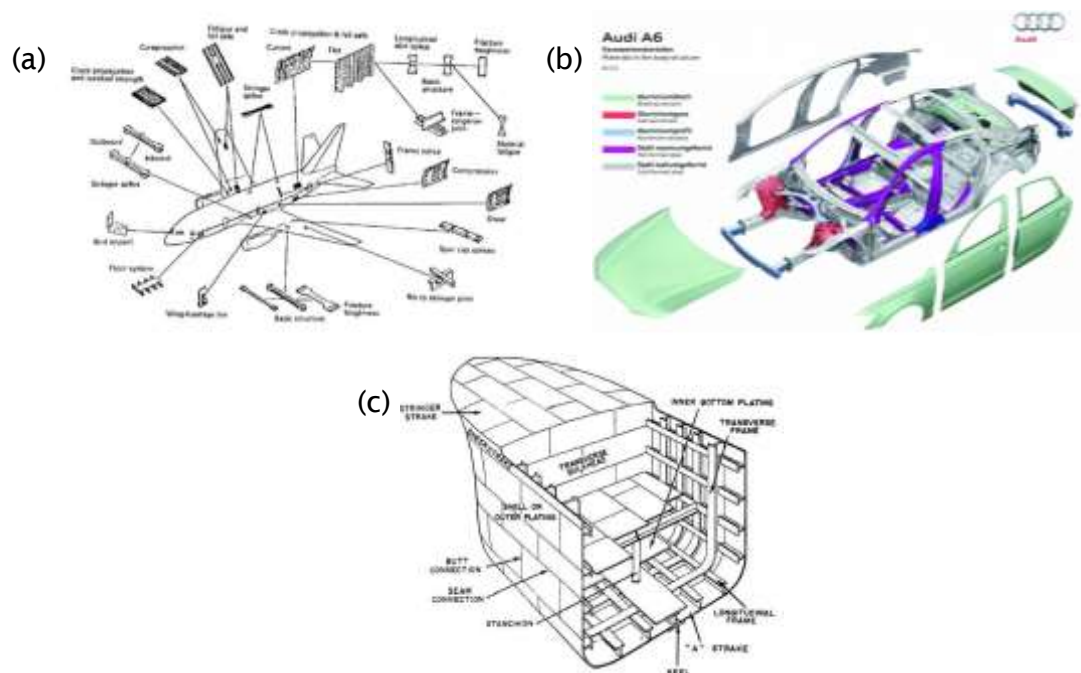


Figure 7.1 Examples of curved plate application in machinery (a) airplane
[\[http://hendrynoya.wordpress.com/2011/04/17/aircraft-load-part-i/\]](http://hendrynoya.wordpress.com/2011/04/17/aircraft-load-part-i/), (b) car
[\[http://www.boronextrication.com/2011/08/02/2012-audi-a6-body-structure/\]](http://www.boronextrication.com/2011/08/02/2012-audi-a6-body-structure/) and (c) ship
[\[http://navyadministration.tpub.com/12966/css/12966_302.htm\]](http://navyadministration.tpub.com/12966/css/12966_302.htm)

In this chapter, firstly, FE modelling and validation for curved plates will be studied. By introducing the coordinate transfer methods between flat and curved plates, FE models established for flat plates in Chapter 6 will be transformed to FE models for curved plates. Using this method, the Cartesian coordinates for a flat plate will be changed to the curved coordinates where a curved plate is treated like a flat plate in the Cartesian coordinates. The comparison between flat and curved plates in terms of mechanical behaviour such as mode shapes in each case will follow this modelling study. The change of each mode according to the increase in curvature and the relationship between modes of flat and curved plates will be studied in this chapter.

7. FE MODELLING OF CURVED PLATES

7.1 FE modelling of a slightly curved plate

The focus for the research topic moves from a flat plate to a curved plate now. In fact, slightly curved plates are more commonly used in many cases, such as cars and aeroplanes, than flat plates. In this section, a slightly curved plate is treated as a flat plate, but local coordinates are set along the curved surface of this structure. A flat plate is a specific example of a curved plate with infinite curvatures in the x - and y -directions. Therefore, the coordinate transfer between a flat plate and a slightly curved plate will be studied. In the following subsection, the FE modelling of a slightly curved plate based on the FE modelling of a plate in Chapter 6 will be discussed.

7.1.1 Basic assumption for a slightly curved plate

According to Warburton [101], a slightly curved plate may be regarded as a shallow shell, whose smallest radius of curvature at any point is large compared with the largest length measured along the middle surface of the shell. Alternatively, a slightly curved plate should be a thin-walled structure with a comparatively small rise above the base plane covered by the structure as defined by Vlasov [101]. Therefore, a slightly curved plate can be treated as a thin plate with small curvatures compared with its length, and the FE modelling method explained in Section 6.5 for a laminated flat plate can be used for the FE modelling of a slightly curved plate by considering coordinate transfer due to these curvatures as described in Figure 7.2. After an FE laminated model is derived in the global coordinates from 2-D FE elements of each layer in local coordinates, an FE model of a slightly curved plate can be derived from it by introducing the change of coordinates from flat rectangular coordinates to curved coordinates.

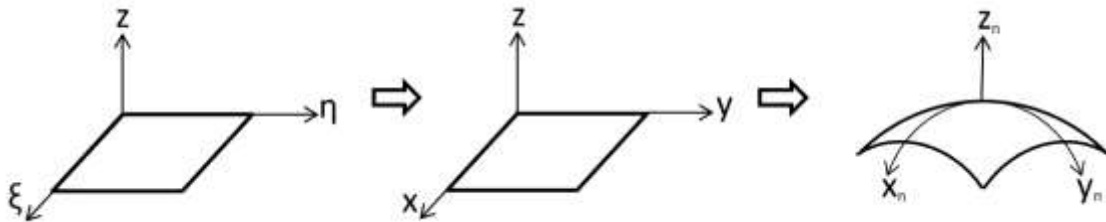


Figure 7.2 Change of coordinates for a slightly curved plate from an FE element

A general slightly curved plate can be described as in Figure 7.3. A slightly curved plate is bent with the radii of curvatures R_x and R_y in the x - and y -directions respectively, which are con-

7. FE MODELLING OF CURVED PLATES

stant along the surface of a slightly curved plate. Arc lengths of L_x and L_y are constant along each y - and x -direction as well. Displacement components on the neutral plane of the plate, u and v , are in the x - and y -directions respectively, and w is normal to the surface.

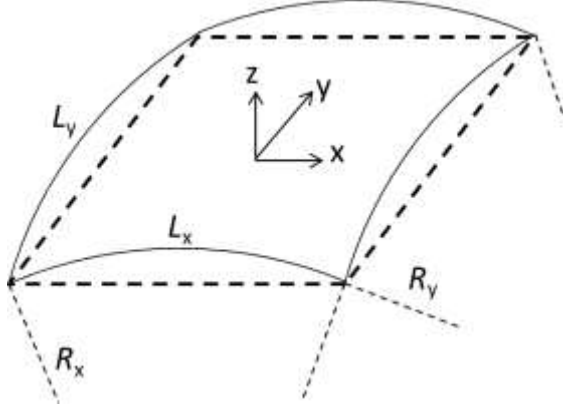


Figure 7.3 Basic concept of a slightly curved plate

The strains at a distance z from the neutral plane of a plate are related to the strains on the neutral plane of a plate and changes in curvature with the assumption that the thickness of the plate is thin enough comparing with the lengths of the arc [101]. The strains on the neutral plane of a plate, allowing for the double curvatures, are expressed considering eqs. (6.1), (6.2) and (6.3) as [101, 102]

$$e_{xx}(x, y, z) = \frac{\eta u(x, y)}{\eta x} - z \frac{\eta^2 w(x, y)}{\eta x^2} + \frac{w(x, y)}{R_x},$$

$$e_{yy}(x, y, z) = \frac{\eta v(x, y)}{\eta y} - z \frac{\eta^2 w(x, y)}{\eta y^2} + \frac{w(x, y)}{R_y},$$

$$\text{and } \varepsilon_{xy}(x, y, z) = \varepsilon_{yx}(x, y, z) = \frac{1}{2} \left(\frac{\partial u(x, y)}{\partial y} + \frac{\partial v(x, y)}{\partial x} \right) - z \frac{\partial^2 w(x, y)}{\partial x \partial y}. \quad (7.1)$$

As shown in eq. (7.1), the in-plane strains of a slightly curved plate are derived by combining the in-plane and out-of-plane displacements. Therefore, the larger out-of-plane deflections occur in the motion of plates, the larger the in-plane strains that there are.

The changes in curvature and twist are the same as those for flat plate theory as

$$\kappa_x = -\frac{\partial^2 w}{\partial x^2}, \quad \kappa_y = -\frac{\partial^2 w}{\partial y^2} \quad \text{and} \quad \kappa_{xy} = -\frac{\partial^2 w}{\partial x \partial y}. \quad (7.2)$$

7. FE MODELLING OF CURVED PLATES

The potential energy of a slightly curved plate can be obtained by substituting eqs. (7.1) and (7.2) into the potential energy equation of a flat plate in eq. (6.5). In this case, a and b in eq. (6.5) are matched to $L_x/2$ and $L_y/2$ in eq. (7.3).

$$\begin{aligned}
 U = & \frac{C}{2} \int_{-L_y/2}^{L_y/2} \int_{-L_x/2}^{L_x/2} \left[\left(\frac{\partial u}{\partial x} \right)^2 + \left(\frac{\partial v}{\partial y} \right)^2 + 2n \frac{\partial u}{\partial x} \frac{\partial v}{\partial y} + \frac{1-n}{2} \left(\frac{\partial u}{\partial y} + \frac{\partial v}{\partial x} \right)^2 \right] dx dy \\
 & + \frac{C}{2} \int_{-L_y/2}^{L_y/2} \int_{-L_x/2}^{L_x/2} \left[\left(\frac{w}{R_x} + \frac{w}{R_y} \right)^2 - 2(1-n) \frac{w}{R_x} \frac{w}{R_y} + 2(1+n) \left(\frac{w}{R_x} + \frac{w}{R_y} \right) \left(\frac{\partial u}{\partial x} + \frac{\partial v}{\partial y} \right) \right] dx dy \\
 & + \frac{D}{2} \int_{-L_y/2}^{L_y/2} \int_{-L_x/2}^{L_x/2} \left[\left(\frac{\partial^2 w}{\partial x^2} \right)^2 + \left(\frac{\partial^2 w}{\partial y^2} \right)^2 + 2n \frac{\partial^2 w}{\partial x^2} \frac{\partial^2 w}{\partial y^2} + 2(1-n) \left(\frac{\partial^2 w}{\partial x \partial y} \right)^2 \right] dx dy, \quad (7.3)
 \end{aligned}$$

where the extensional stiffness is $C = \frac{Eh}{1-\nu^2}$ and the bending rigidity is $D = \frac{Eh^3}{12(1-\nu^2)}$. As

has been derived from the second equation in eq. (7.3), an increase in potential energy in a curved plate due to curvatures is expected.

The kinetic energy of a slightly curved plate is derived from the equivalent for a flat plate considering eq. (7.1).

$$T_e = \frac{1}{2} \int_{-L_y/2}^{L_y/2} \int_{-L_x/2}^{L_x/2} \left[\rho h \left(\dot{u}(x,y)^2 + \dot{v}(x,y)^2 + \dot{w}(x,y)^2 \right) \right] dx dy. \quad (7.4)$$

7.1.2 Coordinate transfer and FE modelling

In order to establish FE models for a slightly curved plate, the interpolation functions for a slightly curved plate should be defined based on FE models for a flat plate as explained in Section 7.1.1. From the strains of a slightly curved plate in eq. (7.1), the first derivative matrix of in-plane displacement can be derived as [103]

$$\mathbf{B}_{\text{in}} = \begin{bmatrix} \frac{\partial}{\partial x} & 0 \\ 0 & \frac{\partial}{\partial y} \\ \frac{\partial}{\partial y} & \frac{\partial}{\partial x} \end{bmatrix} \mathbf{H}_{\text{in}} + \begin{bmatrix} \frac{1}{R_x} & 0 & 0 & 0 \\ \frac{1}{R_y} & 0 & 0 & 0 \\ 0 & 0 & 0 & 0 \end{bmatrix} \mathbf{H}_{\text{out}}, \quad (7.5)$$

where the linear shape functions \mathbf{H}_{in} for the in-plane displacement and the Hermite cubic shape function \mathbf{H}_{out} for the out-of-plane displacement are defined in eqs. (A.9) and (A.10). Eq. (7.5) shows the change of in-plane displacement in thickness direction which is caused by the curvature. Since the changes in curvature and twist are the same as those for flat plate theory as mentioned for eq. (7.2), it is confirmed that the first derivative matrix of out-of-plane displacement \mathbf{B}_{out} is the same as that for a flat plate expressed in eq. (A.18) as

$$\mathbf{B}_{\text{out}} = \begin{bmatrix} \frac{\partial^2}{\partial x^2} \\ \frac{\partial^2}{\partial y^2} \\ \frac{\partial^2}{\partial x \partial y} \end{bmatrix} \mathbf{H}_{\text{out}}. \quad (7.6)$$

Since the nodal in-plane displacements calculated by FE models for a slightly curved plate are placed along a curved surface and the nodal out-of-plane displacements are normal to a surface, these displacements should be defined in terms of Cartesian coordinates instead of curved local coordinates. For this, each nodal displacement should be transferred considering the angle from the z -axis at one point on a surface. Therefore, by substituting eqs. (7.5) and (7.6) into eqs. (A16) and (A.18), the kinetic and potential energy matrices of a slightly curved plate can be derived.

If a slightly curved plate, which has a single curvature in one direction, that is, it is a cylindrically-curved plate, is divided into N elements and each element is defined as in Figure 7.4, the maximum angle of a slightly curved plate can be calculated as

$$\theta = \cos^{-1} \left(\frac{R_s - z_c}{R_s} \right), \quad (7.7)$$

where R_s is the radius of curvature of a slightly curved plate. Therefore, the angle φ_i between radial direction of curved plate, which is the transferred z -axis of curved plate, and the original z -axis at the i -th node can be obtained as

7. FE MODELLING OF CURVED PLATES

$$j_i = j_{i-1} - \frac{j_1}{N} = j_1 \left(1 - \frac{i-1}{N}\right) = q \left(1 - \frac{i-1}{N}\right) = \cos^{-1} \left(\frac{R_s - z_c}{R_s} \right) \left(1 - \frac{i-1}{N}\right). \quad (7.8)$$

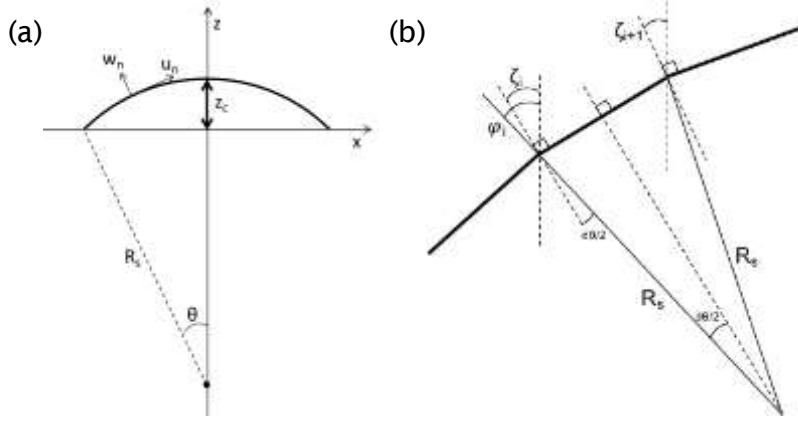


Figure 7.4 FE model of a slightly curved plate; (a) the relationship between the global coordinates and the local co-ordinates in a slightly curved plate and (b) rotation of an FE element along the curvature

Therefore, the transformation matrix of a coordinate corresponding to a rotation of an angle φ_i from the z -axis for a doubly curved plate including a piezoelectric component, which is derived from the one for a cylindrically curved plate given in [96] to have the transfer matrix as given in [99] for strain components, can be given as

$$\mathbf{T}_{\text{coord}} = \begin{bmatrix} \cos j_{x_i} & -\sin j_{x_i} \sin j_{y_i} & -\sin j_{x_i} \cos j_{y_i} & 0 & 0 & 0 & 0 & 0 & 0 \\ 0 & \cos j_{y_i} & -\sin j_{y_i} & 0 & 0 & 0 & 0 & 0 & 0 \\ \sin j_{x_i} & \cos j_{x_i} \sin j_{y_i} & \cos j_{x_i} \cos j_{y_i} & 0 & 0 & 0 & 0 & 0 & 0 \\ 0 & 0 & 0 & 1 & 0 & 0 & 0 & 0 & 0 \\ 0 & 0 & 0 & 0 & 1 & 0 & 0 & 0 & 0 \\ 0 & 0 & 0 & 0 & 0 & 1 & 0 & 0 & 0 \\ 0 & 0 & 0 & 0 & 0 & 0 & 1 & 0 & 0 \\ 0 & 0 & 0 & 0 & 0 & 0 & 0 & 1 & 0 \\ 0 & 0 & 0 & 0 & 0 & 0 & 0 & 0 & 1 \end{bmatrix}, \quad (7.9)$$

where j_{x_i} and j_{y_i} are the rotation angles in x - and y -directions at the i -th node respectively.

For a doubly curved plate such as a spherically curved plate and an elliptically-curved plate, an angle at one node from the z -axis should be calculated by considering angles on the x - and y -axes together.

With this transformation matrix $\mathbf{T}_{\text{coord}}$, the local coordinates located along the curved surface can be transferred to the Cartesian coordinates (including an electric potential difference ϕ) as

$$\left\{ \begin{matrix} \mathbf{u}_n & \mathbf{w}_n & \frac{\partial \mathbf{u}_n}{\partial z} & f \end{matrix} \right\}^T = \mathbf{T} \left\{ \begin{matrix} \mathbf{u} & \mathbf{w} & \frac{\partial \mathbf{u}}{\partial z} & f \end{matrix} \right\}^T. \quad (7.10)$$

Displacement vectors \mathbf{u} , \mathbf{w} and $\frac{\partial \mathbf{u}}{\partial z}$ are defined in Section 6.5 and displacement vectors of the curved surface \mathbf{u}_n , \mathbf{w}_n and $\frac{\partial \mathbf{u}_n}{\partial z}$ are described in Figure 7.4.

7.1.3 Comparison with approximated theoretical results

In this subsection, the established FE models for a slightly curved plate with double curvature will simply be validated by comparing the fundamental frequencies obtained by eq. (7.11) [96] and the FE model.

$$W_{11}^2 = W_0^2 \left[1 + \frac{192(1 - \nu^2)}{\rho^4} \left(\frac{z_c}{h} \right)^2 \right], \quad (7.11)$$

where W_0 is the fundamental frequency in a bending motion of a simply supported square flat plate with side length L in x - and y -directions. Levy-type solutions, which use the Fourier trigonometric functions for displacements of plates, was used in eq. (7.11). This equation is derived with the assumption $z_c/L \leq 0.05$ and $2R_s z_c = (L/2)^2$. Therefore, the maximum rise at the centre of curved plates should be limited to meet the ratio with side length. According to [96], this assumption and the use of the arc length rather than the chord length can cause small errors, ≤ 1.2 per cent for $z_c/L \leq 0.05$ in the frequency ratio W_{11}/W_0 with Poisson's ratio 0.3.

When a simply-supported aluminium doubly curved plate with a maximum rise of 1mm, square arc length of 21cm, 2.58mm thickness and Poisson's ratio 0.33 is considered, the changes in the fundamental frequency compared with an aluminium flat plate with the same side length and thickness is given in Table 7.1. Since similar number of FE elements was used for analysis in both cases, the fundamental frequencies of curved plates can be thought to converge on a certain steady value as flat plates. Although considering inherent errors caused from the basic assumption in eq. (7.11), values obtained by FE models seem a bit larger than those acceptable from the Warburton's equation.

7. FE MODELLING OF CURVED PLATES

Table 7.1 Fundamental frequency comparison of flat and curved plates

Flat plate			Slightly doubly curved plate		
Exact	FEM (Matlab)		Warburton's [96]	FEM (Matlab)	
281.70 Hz	7×7	14×14	316.69 Hz	8×8	12×12
	281.67 Hz	281.70 Hz		358.4 Hz	357.7 Hz

In order to check the change of fundamental frequency of doubly curved plates according to the increase of curvature, the maximum rise at the centre was changed from 0.1mm to 10.5mm, which is the maximum allowable value with the Warburton's assumption in eq. (7.11), i.e. $z_c/L \leq 0.05$ and the change of fundamental frequencies with the same plate used for Table 7.1 are obtained as shown in Figure 7.5.

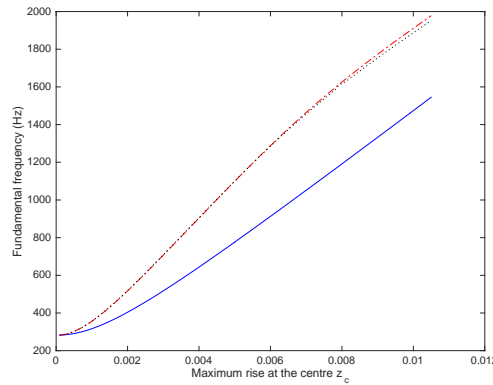


Figure 7.5 Change of fundamental frequency according to the increase of maximum rise at the centre: — Warburton's theory; - - - FEM (Matlab, 8X8); FEM (Matlab, 12X12)

The same comparisons were conducted to check the result in Figure 7.5 for the changes of second and third resonance frequencies of flat plate according to the increase of curvature. The resonance frequency equation for a doubly curved square plate in eq. (7.12) based on the Warburton's equation in eq. (7.11) [114] was used for theoretical values of frequencies with the values of flat plate at (2, 1) and (2, 2) modes which are relevant to the second and third resonance frequencies. Results comparison is given in Figure 7.6.

$$W_{mn}^2_{\text{curved square}} = W_{mn}^2_{\text{square}} \left(1 + \frac{768(1-n^2)}{\rho^4(m^2+n^2)^2} \left(\frac{z_c}{h} \right)^2 \right) \quad (7.12)$$

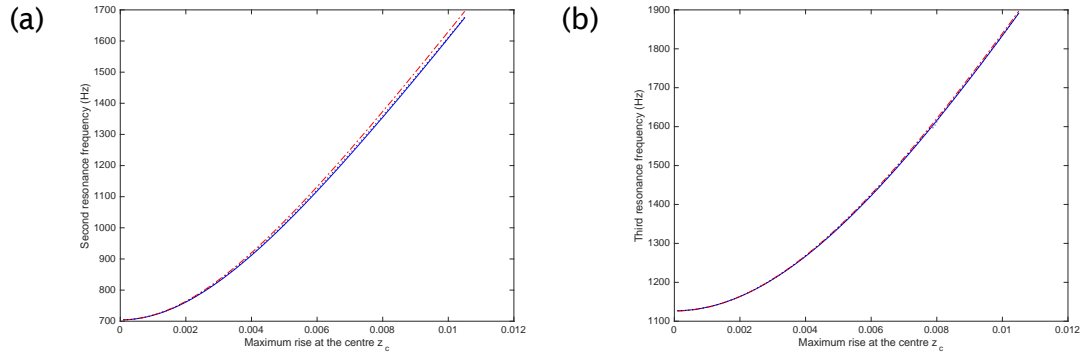


Figure 7.6 Change of resonance frequency according to the increase of maximum rise at the centre; (a) second resonance frequency and (b) third resonance frequency: — Warburton's theory; - - - FEM (Matlab, 8X8); FEM (Matlab, 12X12)

Since assumptions are used as explained above, eqs. (7.11) and (7.12) are approximate expressions for the resonance frequencies of doubly curved plates. Some differences between the frequency obtained by theoretical equations and the one obtained using the FE model, which also involves some assumption, are found in the above results. Therefore, in order to clarify these differences, further verification through experiments is required.

Regardless of the differences, increase in stiffness by the curvature of a slightly curved plate results in increase in fundamental frequency from a flat plate. By considering the increase in strain in a slightly curved plate caused by the curvature, this effect is considered relatively well in the FE modelling of a slightly curved plate.

7.2 Experimental investigation of FE curved plate models

7.2.1 Impact hammer test with curved plates

An FE plate model for curved plates was compared with measured results from impact hammer tests as carried out for free-free beams in Chapter 4. For this comparison, a singly curved plate was hung to a test rig with strings attached to upper corners of a plate as shown in Figure 7.7. An accelerometer was attached to the centre of the plate as the most flexible point of the whole structure, and the opposite centre point was excited by an impact hammer.

7. FE MODELLING OF CURVED PLATES



Figure 7.7 Impact hammer test for a singly curved plate

The length and width of the plate were 42 cm and 40 cm respectively to avoid the overlap of modes in the x - and y -directions. The thickness of the plate was 2 mm and the maximum rise at the centre point was 20 mm. The equivalent density of the plate was calculated by measuring the mass and dimensions of real curved plates as 2620.4 kg/m^3 and the Poisson's ratio was assumed to be 0.33. The equivalent Young's modulus for a plate was adjusted to 68 GPa to match as many peaks at resonance frequencies of out-of-plane motion as relatively possible by comparing resonance frequencies of simulated and measured results.

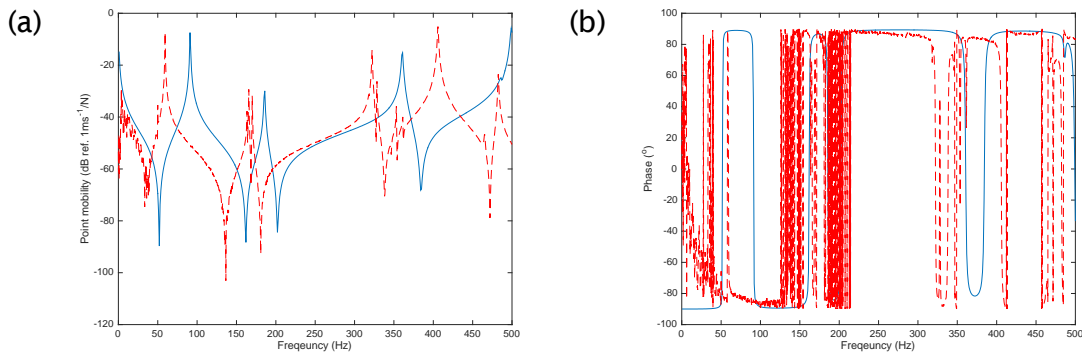


Figure 7.8 Result comparison for an impact hammer test between an FE plate model and a real curved plate (a) point mobility and (b) phase: — FEM (MATLAB); - - - Experiment

The comparison between the point mobilities at the centre of the plate of a curved plate FE model (MATLAB) and the measured point mobility by impact hammer test was conducted. The result is given in Figure 7.8. As shown in Figure 7.8, there are some differences between the two results. The difference in the first peak is understood with results in Figure 7.5. For other modes, according to the results in Figure 7.6 which show the accuracy of the FE model, the irregularity of curvature in real plate, which made by a hand roller, is thought as the main reason.

7.2.2 Effect of curvature on mode shapes and resonance frequencies with FE plate models

For more accurate discussion, mode shapes of curved plates are compared to mode shapes of a flat plate. The mode shapes of a flat and curved plate with the dimensions $42 \text{ cm} \times 40 \text{ cm} \times 2 \text{ mm}$ is studied. The mode shapes for the out-of-plane motion of a free-free flat plate are shown in Figure 7.9. The determination of modes for a free-free plate is based on [106]. The mode shapes for a free-free curved plate with a maximum rise of 10 mm and 20 mm are shown in Figures 7.10 and 7.11 respectively.

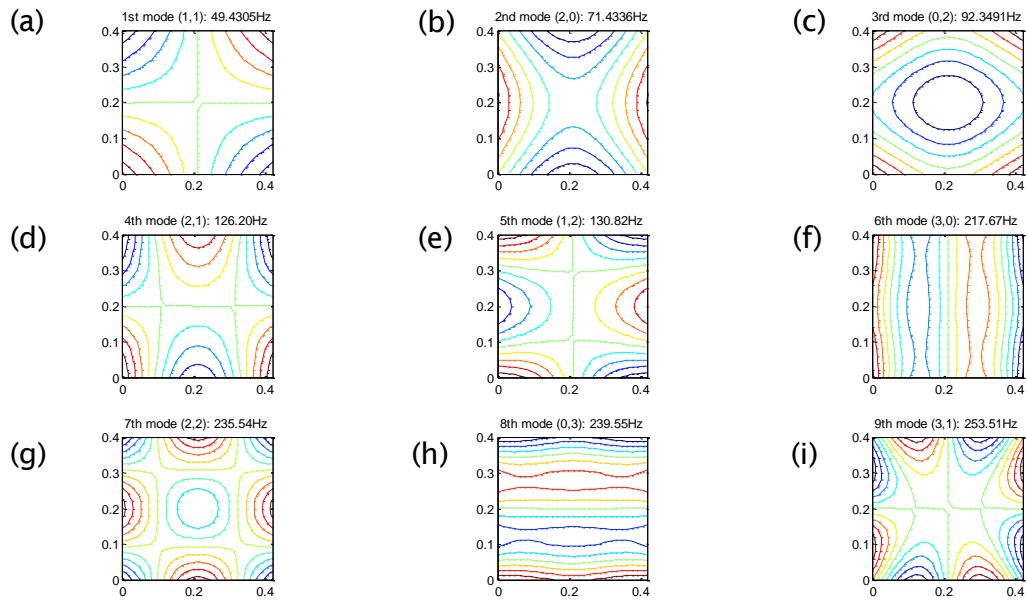


Figure 7.9 Mode shapes for a free-free flat plate for out-of-plane motion (a) 1st mode (1, 1) at 49.4305 Hz, (b) 2nd mode (2, 0) at 71.4336 Hz, (c) 3rd mode (0, 2) at 92.3491 Hz, (d) 4th mode (2, 1) at 126.20 Hz, (e) 5th mode (1, 2) at 130.82 Hz, (f) 6th mode (3, 0) at 217.67 Hz, (g) 7th mode (2, 2) at 235.54 Hz, (h) 8th mode (0, 3) at 239.55 Hz and (i) 9th mode (3, 1) at 253.51 Hz

7. FE MODELLING OF CURVED PLATES

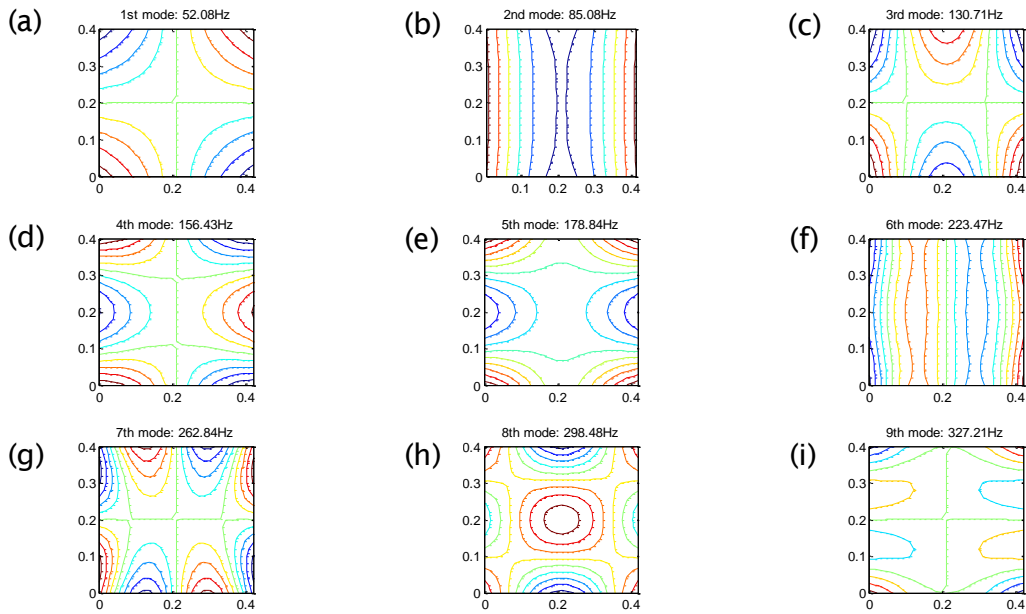


Figure 7.10 Mode shapes for a free-free curved plate with the maximum rise of 10 mm for out-of-plane motion (a) 1st mode at 52.08 Hz, (b) 2nd mode at 85.08 Hz, (c) 3rd mode at 130.71 Hz, (d) 4th mode at 156.43 Hz, (e) 5th mode at 178.84 Hz, (f) 6th mode at 223.47 Hz, (g) 7th mode at 262.84 Hz, (h) 8th mode at 298.48 Hz and (i) 9th mode at 327.21 Hz

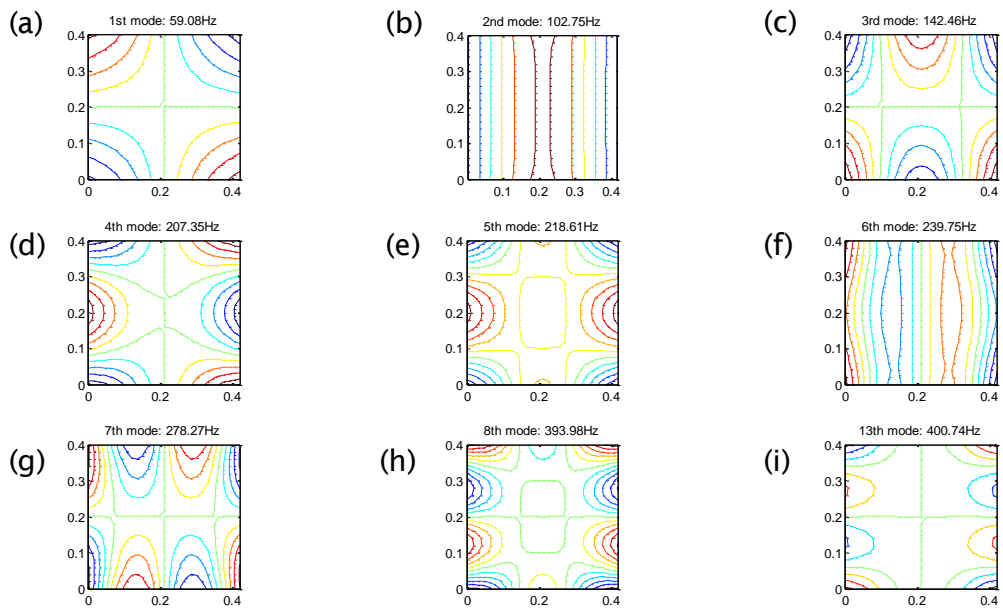


Figure 7.11 Mode shapes for a free-free curved plate with the maximum rise of 20 mm for out-of-plane motion (a) 1st mode at 59.08 Hz, (b) 2nd mode at 102.75 Hz, (c) 3rd mode at 142.46 Hz, (d) 4th mode at 207.35 Hz, (e) 5th mode at 218.61 Hz, (f) 6th mode at 239.75 Hz, (g) 7th mode at 278.27 Hz, (h) 8th mode at 393.98 Hz and (i) 9th mode at 400.74 Hz

After mode shapes were calculated for each case as above, using the Modal Assurance Criterion (MAC) method explained by eq. (7.13) [94], the relationship between modes of a curved plate and a flat plate with the same dimensions was studied.

$$\text{MAC}(p, x) = \frac{\left| \sum_{j=1}^n (\phi_x)_j (\phi_p)_j^* \right|^2}{\sum_{j=1}^n (\phi_x)_j (\phi_x)_j^* \sum_{j=1}^n (\phi_p)_j (\phi_p)_j^*}, \quad (7.13)$$

where p and x are the modes compared. n denotes the node number for the FEM model. $(\phi_i)_j$ is the mode shape for the i -th mode at the j -th node and $(\phi_i)_j^*$ is the conjugate of $(\phi_i)_j$. Considering maximum rises of 10 mm and 20 mm, the results, as shown in Figure 7.12, were obtained.

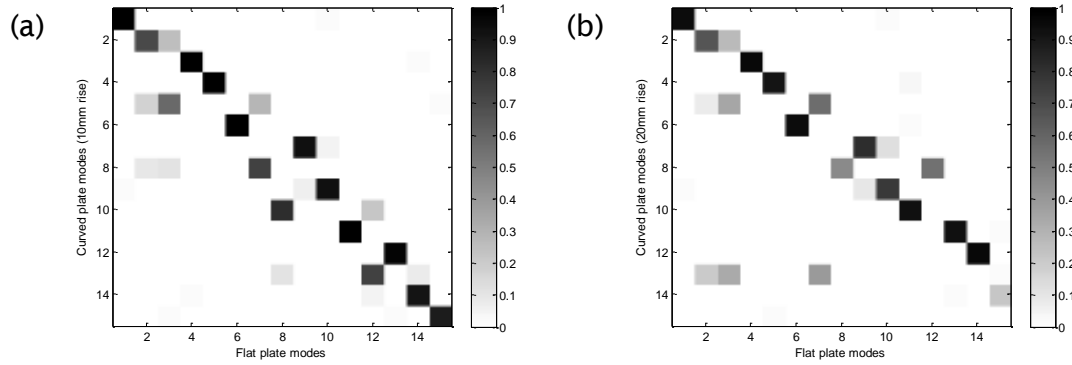


Figure 7.12 The MAC result between a flat plate and (a) a curved plate with 10 mm rise and (b) a curved plate with 20 mm rise

The 2nd mode of a flat plate is mainly related to the 2nd modes of two curved plates. However, due to the curvature, it is partly related to the 5th and 8th modes of a curved plate with a 10 mm rise and the 5th and 13th modes of a curved plate with a 20 mm rise respectively. These relationships of modes between curved plates with 10 mm and 20 mm rises are clear for the 7th mode of a flat plate. Moreover, the 8th and 12th modes of a flat plate are mainly related to the 10th and 13th modes of a curved plate with a 10 mm rise and the 8th modes of a curved plate with a 20 mm rise respectively. According to the results, the 10th and 13th modes of a curved plate with a 10 mm rise seem related to the 8th mode and one higher than the 15th modes of a curved plate with a 20 mm rise respectively. As shown by Figures 7.10 and 7.11, mode shapes for the 8th mode of curved plates with 10 mm rises and 20 mm rises are different. This means that (m, n) modes in each case are different due to curvature. Especially for modes higher than the 10th mode for curved plates, orders of (m, n) modes in two cases are showing larger differ-

7. FE MODELLING OF CURVED PLATES

ence from each other. It is because the effect of curvature on stiffness is larger in higher modes than in lower modes.

Based on the MAC results, it is helpful to go back to the point mobility plots at the centre of plates, where the largest deflection can be found in lower modes which are main target of active vibration control in general, as shown in Figure 7.13. The relationships of modes become clearer. As shown by Figure 7.13, the first three peaks of a flat plate change as the curvature of the plate increases. Since nodal lines are located at the centre of a plate for other modes, as shown by Figure 7.9, the change of other modes according to the increase in curvature is not traceable in the point mobility at the centre.

Figure 7.14 shows the changes in the first three mode shapes of out-of-plane displacement shown in Figure 7.13 for a flat plate, a curved plate with a 10 mm rise and a curved plate with a 20 mm rise. The increase in curvature in the x -direction causes an increase in the bending stiffness in the y -direction. Thus, it results in the change of related mode shapes as illustrated in Figure 7.14.

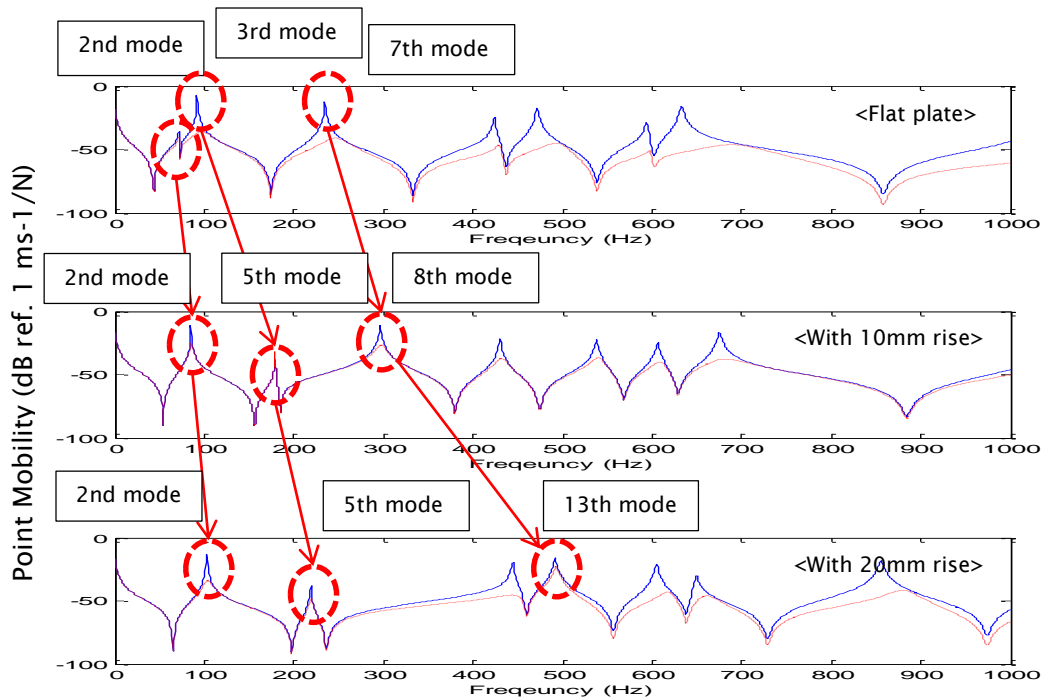


Figure 7.13 The relationship between related modes of plates; Top: a flat plate, Middle: a singly curved plate with a 1cm rise and Bottom: a singly curved plate with 2cm rise (— with ACLD treatment & no active control, - - - with ACLD treatment & active control using control gain $\beta_{min,KE}$)

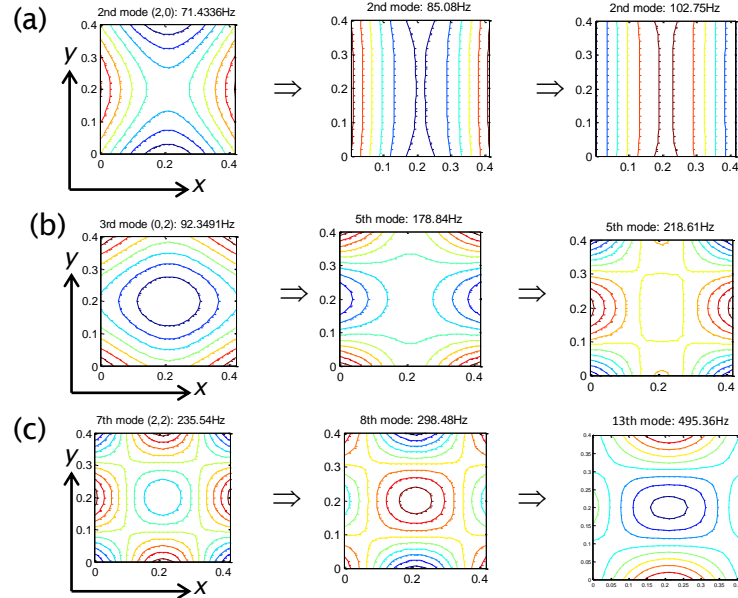


Figure 7.14 The relation between associated modes of plates with mode shapes for (a) 2nd mode, (b) 3rd mode and (c) 7th mode of a flat plate

When changes for each mode are investigated, it is clear that the 2nd mode in a flat plate is the most influenced by the curvature. While the out-of-plane motions are generally symmetrical in the x - and y -directions for other modes in spite of a single curve in the x -direction, the mode shapes for curved plates in Figure 7.14 (a) are asymmetrical due to a single curve in the x -direction. This means that the 2nd modes of curved plates are under a greater influence from curvature than other modes. The first peak in Figure 7.8 is not matched well in spite of other peaks being relatively well-matched, with a modified Young's modulus of theoretical plates, due to the irregularity of curvature in real curved plates as explained above. This difference should be considered when comparing the results of experiment and simulation.

In conclusion, using a singly curved plate without any attachment, the FE models for singly curved plates were validated. Moreover, the reasons for differences between simulations and experimental results were discussed. In the next section, based on this section, control results with a controller design and validated FE curved plate models will be discussed.

7.3 Summary and conclusions

In this chapter, FE curved plate models were derived considering the coordinate transfer due to curvature based on the flat plate models established in Chapter 6. By considering the change of in-plane strain due to curvatures in a slightly curved plate and angles at one point from the z -

7. FE MODELLING OF CURVED PLATES

axis, FE modelling of a slightly curved plate was established. This model was validated and the effect of curvature on mode shapes was illustrated by comparing the mode shapes of a flat plate and curved plate. This coordinate transfer method explained in this chapter can be applied to FE flat plate models with HAPCLD treatments established in Chapter 6 as well for the study in the next chapter.

In the next chapter, from the understanding of flat and curved plates established in Chapters 6 and 7, active vibration control results will be compared, and control performance for all cases will be discussed. Furthermore, from the understanding of flat and curved plates, active vibration control results will be compared, and control performance for all cases will be discussed.

8 HYBRID ACTIVE-PASSIVE CONTROL OF PLATES

In this chapter, by using FE models for flat and curved plates established in Chapters 6 and 7 respectively and real five curved plates which five different types of HAPCLD treatment are individually attached to, the effect of active control by HAPCLD treatments will be studied case by case. These five HAPCLD treatments include four HAPCLD treatments and inverse AC/PCLD treatment which has a piezoelectric actuator and PCLD treatment on different sides from AC/PCLD treatment. While AC/PCLD and inverse AC/PLCD treatments have the same effect on a flat plate, they give a different effect with curved plates due to the direction of curvature and this effect will be studied through real curved plate experiments. In addition to this, active control results with each HAPCLD treatment obtained from simulation and experiment will be compared and studied. Moreover, as studied in the previous chapter, since mode shapes change according to the change of curvature, the effect of active control can vary according to the change of curvature and configuration. Therefore, the effect of curvature on active control will be studied through comparison of each case.

8.1 Numerical study of control applied to FE plate models

With the validated FE models for curved plates in the previous sections, controllers for active control of out-of-plane motions were designed using the method discussed in Chapter 5, and control performances were evaluated. In this section, the control results will be studied and influencing factors, which caused these results, will be discussed. In the following sections, active control will be conducted for various cases including different curvatures of plates and configurations of HAPCLD treatments. Obtained control results will be compared, and which factor causes the differences in results will be discussed.

Flat and singly curved plates with HAPCLD treatments as explained in Chapters 6 and 7 are shown in Figure 8.1. Damping treatments were attached around the centre of the plates, and the error measurement point was set up at the centre point. The primary external exciting force was applied at the same point to give the collocated condition, and mobilities at the centre point were compared in each case of HAPCLD treatment configurations.

8. HYBRID ACTIVE-PASSIVE CONTROL OF PLATES

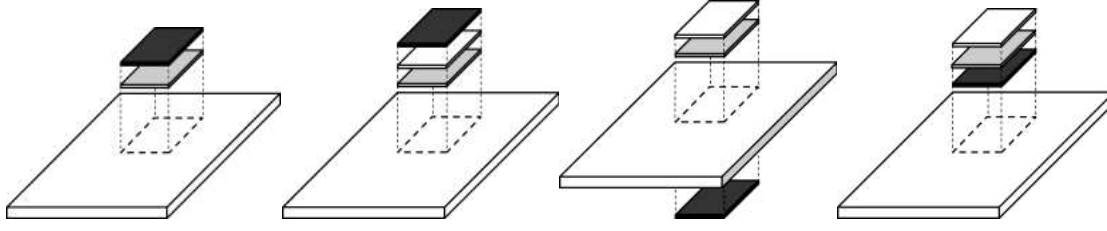





Figure 8.1 Configuration of a plate with (1) ACLD treatment, (2) APCLD treatment, (3) AC/PCLD treatment and (4) AC/PSOLD treatment;  : elastic plate,  : viscoelastic layer and  : piezoelectric patch

8.1.1 Control results for flat plates

As described in Figure 8.1, HAPCLD treatments are assumed to be attached on flat plates. A result was obtained relating to the change in the kinetic energy of whole structures and the absorbed power from actuators as explained in Section 5.1.2.

Firstly, the results of ACLD treatment are given. From the kinetic energy and absorbed power results, the optimised control gain of 1667.5 was obtained to minimise the Kinetic energy of a whole structure as seen in Figure 8.2. The results were calculated by eqs. C.7 (the kinetic energy of a structure) and C.8 (the absorbed power by an actuator) with 9 points equally distributed on the plates and control gains from 0 to 3000.

$$S_k(\omega) = \frac{M}{2R} \sum_{r=1}^R \left| \tilde{v}_r(\omega) \right|^2, \quad (C.7)$$

where M is mass of the whole structure, R is the number of measuring points and $\left| \tilde{v}_r(\omega) \right|$ is the mean square value of the velocity measured by the r -th accelerometer.

$$S_p(\omega) = \frac{1}{2} \beta \left| \tilde{v}_c(\omega) \right|^2, \quad (C.8)$$

where β is the control gain and $\left| \tilde{v}_c(\omega) \right|$ denotes the mean square value of the control velocity.

Since the primary exciting point, the error measurement point and the location of the actuator are collocated in this case, stable control was guaranteed within the frequency range of 1000 Hz. With this calculated control gain, the following control results and the Nyquist plot with the control gain were obtained as shown in Figure 8.3. In Figure 8.3 (a), large reductions can be found in most peaks of the point mobility except the first peak, where an increase in peak size is found. This increase is caused by the control moment which is related to the small circle marked with a red dotted line in Figure 8.3 (b). The reason for the small circle will be discussed in Sec-

8. HYBRID ACTIVE-PASSIVE CONTROL OF PLATES

tion 8.1.3 with other control results. In spite of the existence of this circle, optimised control gain is determined as $G_{\min,KE}$ which is smaller than G_{3dB} .

Furthermore, passive and active loss factors in the system were calculated as given in Table 8.1. Passive damping is the inherent damping of a structure due to the structure itself and the viscoelastic layer. Active damping is additional damping caused by the active control. As shown in Figure 8.3 (a), active control gave a negative effect on the first peak. This result will be discussed and compared with other control results in Section 8.1.3.

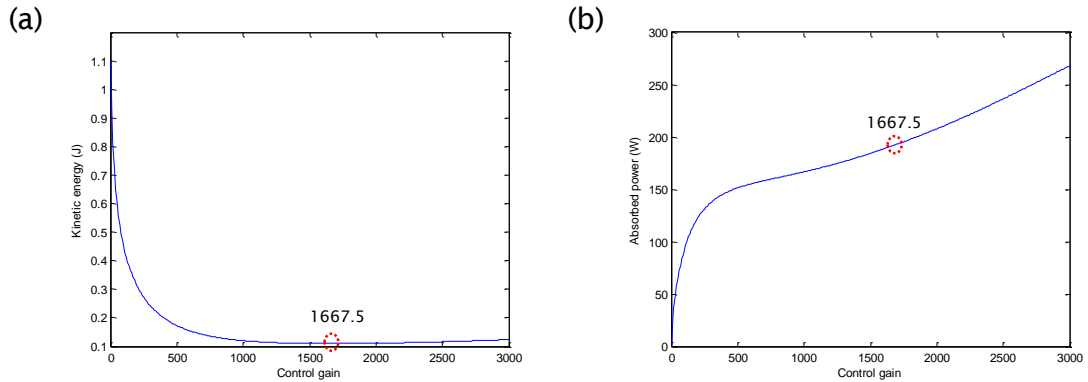


Figure 8.2 The kinetic energy and absorbed power for a flat plate with ACLD treatment with control gains: (a) Change of the kinetic energy of a plate and (b) Change of absorbed power by an actuator

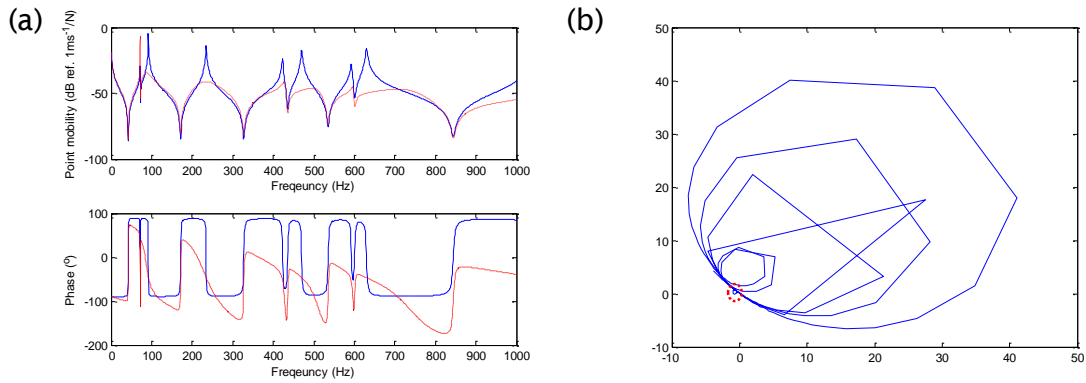


Figure 8.3 Control result for a flat plate with ACLD treatment (a) Magnitude and phase of point mobility; — no control; - - - with control and (b) the Nyquist plot for a closed loop with the optimised control gain of 1667.5; ⊙ circle with negative effect on active control

Table 8.1 Passive and active loss factors for a flat plate with ACLD treatment

Peak order	1	2	3	4	5
Passive	0.0057	0.0057	0.0054	0.0054	0.0057
Passive & Active	0.0005	0.2255	0.2028	0.0268	0.0980

8. HYBRID ACTIVE-PASSIVE CONTROL OF PLATES

With APCLD treatment, the optimised control gain of 814.7 was obtained from the following changes in kinetic energy and absorbed power as shown in Figure E.1 in Section E.1.1. All other results for APCLD, AC/PCLD and AC/PSOLD treatments are given in Section E.1 of Appendix E.

With this control gain, the following control results were obtained. Differently from the ACLD case, control results for all peaks were positive and all circles in Figure E.2 (b) were rotated by about 45° clockwise from those in Figure 8.3 (b). This difference was caused by the increase of passive damping by adding an elastic constraining layer which remains in the same shape even when a PZT patch is in motion to the ACLD treatment where the constraining effect of PZT patch decreases when it is in motions.

Table 8.2 Passive and active loss factors for a flat plate with APCLD treatment

Peak order	1	2	3	4	5
Passive	0.0050	0.0060	0.0055	0.0055	0.0059
Passive & Active	0.0098	0.2190	0.1161	0.0193	0.0591

Control simulations were conducted with AC/PCLD and AC/PSOLD treatments. With AC/PCLD and AC/PSOLD treatments, the optimised control gains of 192.7 and 196.8 were obtained respectively. The changes in kinetic energy and absorbed power for each case were calculated as shown in Figures E.3 and E.5.

Compared with the two other previous cases, although absorbed powers from controllers are smaller due to higher structural constraint, the kinetic energies of whole structures are minimised with smaller control gains. This is because such controllers can directly apply a control force to the base structure. When it is borne in mind that additional elastic bridges are introduced into ACLD treatment to enhance the transmission of control force as shown in Figure 2.7, as Enhanced ACLD treatment, these methods can minimise the dissipation of a control force in the viscoelastic layer and give more efficient active control, which is clarified with smaller $G_{\min,KE}$ than in the previous two cases.

These two HAPCLD treatments have very similar configurations except that a PZT actuator is separated from PCLD treatment or not. Thus, the obtained results were very similar as well. As the location of a PZT patch is on the opposite sides of the base plate in the two cases, control results are expected to be different with the increase in curvature which will cause geometrical asymmetry in structures for curved plates.

8. HYBRID ACTIVE-PASSIVE CONTROL OF PLATES

Table 8.3 Passive and active loss factors for a flat plate with AC/PCLD treatment

Peak order	1	2	3	4	5
Passive	0.0065	0.0053	0.0052	0.0052	0.0054
Passive & Active	0.0166	0.1950	0.0979	0.0209	0.0486

Table 8.4 Passive and active loss factors for a flat plate with AC/PSOLD treatment

Peak order	1	2	3	4	5
Passive	0.0060	0.0055	0.0053	0.0053	0.0056
Passive & Active	0.0257	0.1932	0.1002	0.0210	0.0460

As shown by Figures 8.3 (a), E.2 (a), E.4 (a) and E.6 (a), a phase drop can be found in the mobility with optimised control gain. This is because the total damping of structures increases in each mode with active control using velocity feedback as explained in Section 5.1.1. Due to increased damping, peaks at resonance frequencies were reduced, along with phase drops.

The control simulation results with a flat plate and four different HAPCLD treatments were shown. In the next section, the effects of curvature will be discussed with the control simulation results of singly curved plates with maximum rises of 10 and 20 mm.

8.1.2 Control results for singly curved plates

The same HAPCLD treatments described in Figure 8.3 were applied to singly curved plates as well. In this case, there can be two options for attaching damping treatments; one is where a flat treatment is used and the other is where a singly curved treatment which has exactly the same curvature as a base plate is in use. Here, the latter case is utilised to make the effect of curvature on active control results clearer.

When ACLD treatment is applied to singly curved plates with maximum rises of 10 and 20 mm, optimised control gains of 1795.5 and 1687.3 are calculated respectively from Figures 8.4 and 8.5.

Given the same excitation force but no control force, the kinetic energies of curved plates are smaller than those for a flat plate. This means the out-of-plane motion of curved plates is more

8. HYBRID ACTIVE-PASSIVE CONTROL OF PLATES

constrained than the one for a flat plate due to increased stiffness caused by curvature in the x -direction. In spite of this, the minimum kinetic energies were obtained with larger control gain than for a flat plate. This means that controllers are having less effect on the out-of-plane motion of curved plates. As shown by Figure 8.5, although the absorbed power from the controller is larger than in the other two cases, the minimum kinetic energy is a bit larger than in other cases. This is an effect of the increase in stiffness due to the curvature.

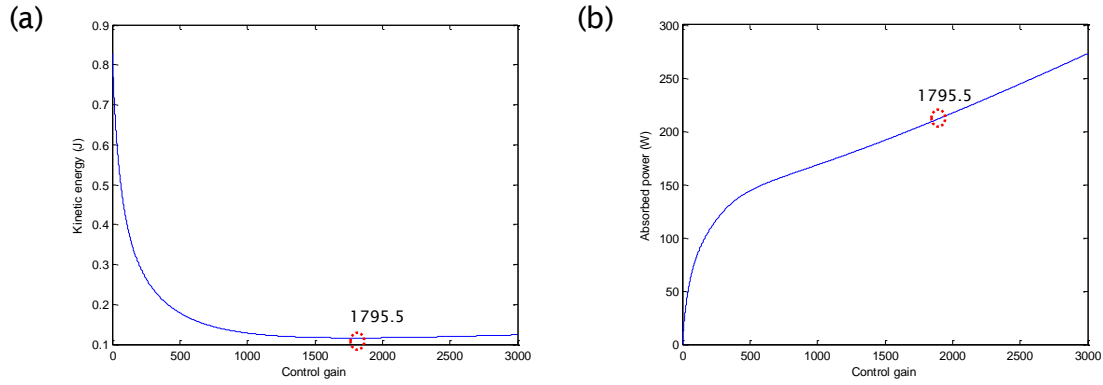


Figure 8.4 The kinetic energy and absorbed power for a singly curved plate with a maximum rise of 10 mm with ACLD treatment with control gains: (a) Change of the kinetic energy of a plate and (b) Change of absorbed power by an actuator

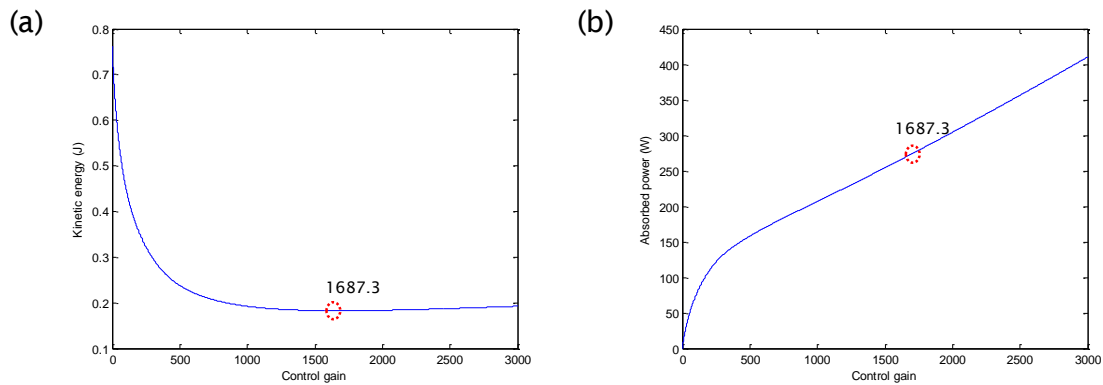


Figure 8.5 The kinetic energy and absorbed power for a singly curved plate with a maximum rise of 20 mm with ACLD treatment with control gains: (a) Change of the kinetic energy of a plate and (b) Change of absorbed power by an actuator

With these optimised control gains, the control results shown in Figures 8.6 and 8.7 were obtained. As shown by comparison with Figure 8.3, active control with singly curved plates has a positive influence on all peaks up to 1000 Hz. This difference can be explained as the effect of curvature on active control. For example, a small circle which can be found in the Nyquist plot for a closed-loop in Figure 8.3 (b) does not exist in the Nyquist plots in Figures 8.6 (b) and 8.7

8. HYBRID ACTIVE-PASSIVE CONTROL OF PLATES

(b). As described for Figures 7.12, 7.13 and 7.14, resonance frequencies and related mode shapes change according to the change in curvatures. Since the influence of active control depends on the mode shape, especially the change pattern of the mode shapes, the effect of active control can change from negative to positive or vice versa. For example, as shown in Figure 7.14, while the directions of a piezoelectric patch's bending motion are the same in the x - and y -directions, the bending directions of a flat plate's 2nd mode are opposite in the x - and y -directions. On the other hand, although the bending directions of curved plates' 2nd modes are not symmetrical, the x -directional bending motion of a piezoelectric patch can contribute mainly to active control in the y -directional bending motion since curvature in the x -axis increases stiffness in the y -direction and constrains related motion.

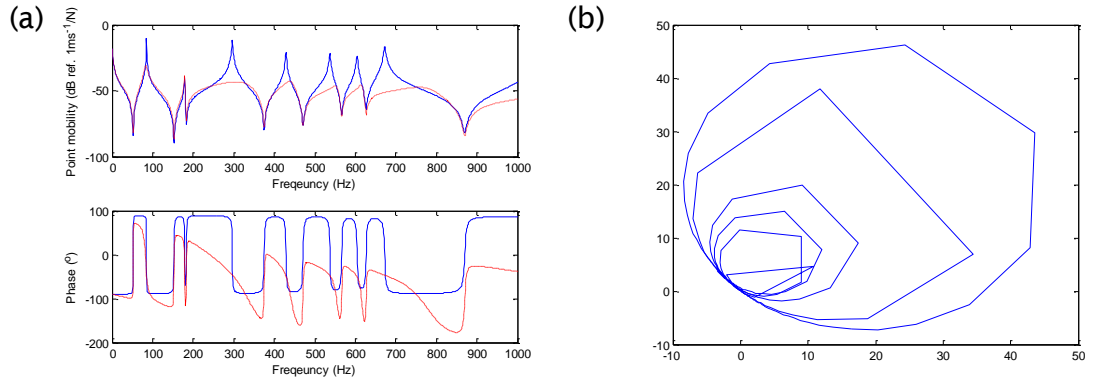


Figure 8.6 Control result for a singly curved plate with a maximum rise of 10 mm with ACLD treatment (a) Magnitude and phase of point mobility; — no control; - - - with control and (b) the Nyquist plot for closed loop with the optimised control gain of 1795.5

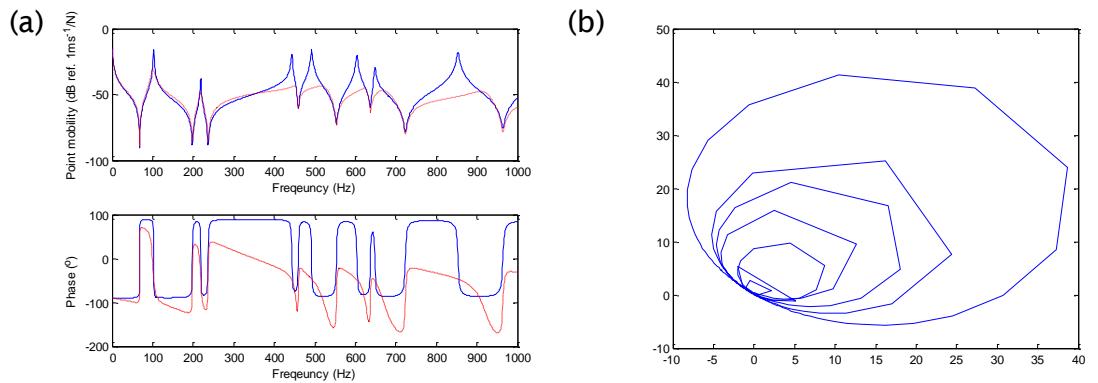


Figure 8.7 Control result for a singly curved plate with a maximum rise of 20 mm with ACLD treatment (a) Magnitude and phase of point mobility; — no control; - - - with control and (b) the Nyquist plot for a closed loop with the optimised control gain of 1687.3

8. HYBRID ACTIVE-PASSIVE CONTROL OF PLATES

The effect of changes in curvature on the mode shapes of plates with HAPCLD treatments is plotted in Figure 8.8. As can be noted from Figure 8.8 (a), the change in the 2nd mode shape is clearly distinguishable from other cases. Only the 2nd mode of a flat plate changes in opposite directions in the x - and y -directions. The motions of a rectangular PZT patch, i.e. bending and extension motions, have bilateral symmetry at opposite ends of the x - and y -directions respectively. Generated forces and moments by a PZT actuator are also bilaterally symmetric. However, since the motion of a base plate is asymmetric in the x - and y -directions, motions in one direction can be amplified by control moments in spite of controlled motions in the other direction. Thus, this asymmetry in mode shapes is assumed to cause unstable active control in the case of a rectangular PZT actuator. On the other hand, the other mode shapes have the same sign of change around the centre point of the plates as shown in Figure 8.8 (b) and (c). These changes guarantee the symmetry of modal motions in base structures, and the bending motions of a PZT actuator can equally contribute to stable active control in the x - and y -directions.

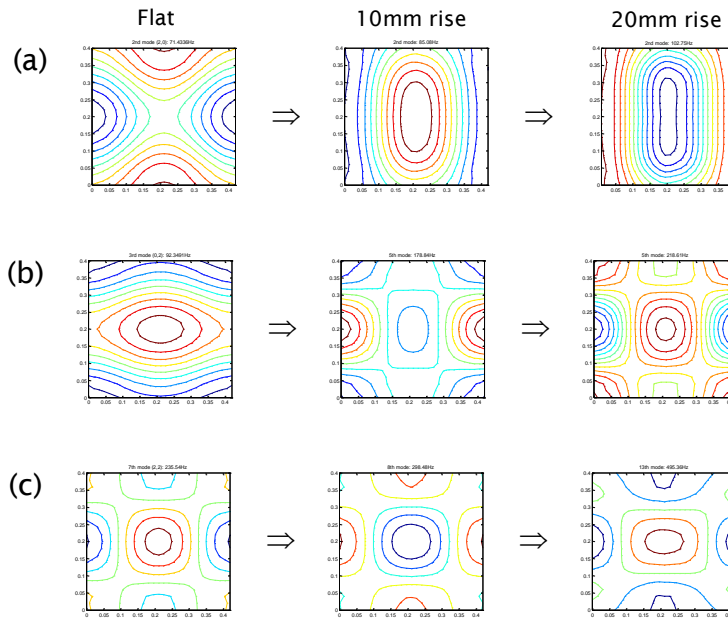


Figure 8.8 The change rate for mode shapes in a plate according to curvature for (a) 2nd peak, (b) 3rd peak and (c) 7th peak

With APCLD treatment, optimised control gains of 670.9 and 720.7 were calculated respectively according to the maximum rises of 10 mm and 20 mm from Figures E.7 and E.9 of Section E.2.1. Comparing these results with those from ACLD treatment, the patterns of changes in control gain, kinetic energy and absorbed power were different from the case of flat plate in Figure E.1. All other study results for APCLD, AC/PCLD and AC/PSOLD treatments are given in Section E.2 as done for the case of flat plate.

8. HYBRID ACTIVE-PASSIVE CONTROL OF PLATES

The reason for this difference can be thought of as follows. For example, the changes in control gain and absorbed power with optimised control gain are arranged in Table 8.5. As shown in Table 8.5, absorbed power by an actuator increases regardless of the change in control gain with ACLD treatment. On the other hand, absorbed power by APCLD treatment does not change as much as by ACLD treatment. This is because of the difference in configurations. Since an additional elastic constraining layer is located between the PZT layer and viscoelastic layer in APCLD treatment, the change in absorbed power in accordance with the curvature can be limited with APCLD treatment more than with ACLD treatment, where the motion of the PZT layer is constrained by the viscoelastic layer only.

With these optimised control gains, control results with APCLD treatments for singly curved plates with maximum rises of 10 mm and 20 mm were obtained as shown in Figures E.8 and E.10 respectively. As shown by Figure E.8 (b), due to the small negative effect of active control, the controlled result of the 3rd peak around 180 Hz in Figure E.8 (a) gets worse than uncontrolled results. This can be explained by Figure 8.8 (b). In general, related mode shapes of plates have a maximum change in curvature around the centre point as can be noted in Figure 8.8, except the 2nd peak without curvature and the 3rd peak with a 10 mm maximum rise. The case of the 2nd peak without curvature has already been discussed above. For the 3rd peak with a 10 mm maximum rise, the change in curvature is not as large as in other cases. Compared with other cases, the curvature around the centre point in this case is relatively flat. As a result, the bending moments generated by a rectangular PZT patch can have a negative influence on the active control.

The cases of AC/PCLD and AC/PSOLD treatments were studied as well. Changes in kinetic energy and absorbed power with AC/PCLD treatment with maximum rises of 10 mm and 20 mm were obtained as shown in Figures E.11 and E.14. As can be noted from Figure E.11, a very different result from the previous result was obtained with the curvature of 10 mm. This is because of the circle for the 2nd peak located in the negative region of the Cartesian complex coordinates as marked in Figure E.13 (b). The effect of this circle is basically negative on active control as explained for the case of a flat plate with ACLD treatment related to Figure 8.3 (b). However, in the previous case, since the location of the circle did not limit the stability of active control, large control gain and stable results were obtained. On the other hand, in this case, the location of the circle limits the range of control gain for stable active control. Therefore, determined control gain is relatively small compared to other cases for stable control. This will be studied in detail below.

In the case of AC/PCLD treatment with a 10 mm maximum rise, the control gain is limited to 41.7 by a 3 dB control gain margin for stability. This value was determined from Figure E.13 (b)

8. HYBRID ACTIVE-PASSIVE CONTROL OF PLATES

to guarantee stable active control as a half value of the control gain of 83.4 with which the small circle of the Nyquist plot in Figure E.13 (b) passes the point $(-1, 0)$ in the Cartesian complex coordinates. When considering the point mobility in Figure E.13 (a), this circle is related to the 2nd peak (5th mode) of point mobility at the centre point. If considering mode shapes in Figure 7.11, the pattern of mode shapes around the centre point for the 2nd mode of a flat plate and the 5th mode of a curved plate with a 10 mm rise, which have circles in the negative region within the Cartesian complex coordinates, can be found to be different from other cases. While nodal lines are located at the centre point or the centre point is enclosed by modal lines in other cases, there is no nodal line and closed modal line around the centre point in the two cases. Related to this issue, more study will be done in Section 8.1.3. While the circle for the 2nd mode of a flat plate does not pass the point $(-1, 0)$ which leads the system response saturated at that frequency, the one for the 5th mode of a curved plate with a 10 mm rise passes the point $(-1, 0)$. The first saturations of kinetic energy and absorbed power, led by the saturation of the system response at the 5th mode with a control gain of 83.4, happen around the control gain of 88 as shown in Figure E.12. On the other hand, the optimised control gain for AC/PCLD treatment with a 20 mm maximum rise is determined to be 137.4 from Figure E.14. With these two control gains, the control results in Figures E.13 and E.15 were obtained for two different curvatures. As discussed above, an unstable control result was obtained only at the 2nd peak in the case of a 10 mm maximum rise due to the negative effect of active control.

The control simulations with AC/PSOLD treatment for plates with 10 mm and 20 mm maximum rises were conducted. The optimised control gains of 161.2 and 151.7 were obtained from Figures E.16 and E.18. With these control gains, active control results were obtained as in Figures E.17 and E.19. It can be noticed from Figures E.16 and E.18 that results for curved plates with AC/PSOLD treatment are different from the ones with AC/PCLD treatment. These results are the same for a flat plate as shown by Figures E.3 and E.5. This will be studied in detail below.

In contrast to the previous cases, only stable control results were obtained with AC/PSOLD treatment. As shown by Figures E.17 (b) and E.19 (b), the control effect of AC/PSOLD treatment is always positive up to 1 kHz. Especially, for the 2nd peak of a curved plate with a 10 mm rise, while unstable control results were obtained with APCLD and AC/PCLD treatments due to the circle in the negative area [107], a stable control result was obtained with AC/PSOLD treatment for the same mode shape. This is because of differences in damping and stiffness of the different configurations of HAPCLD treatment. The mutual interaction in terms of displacement between the constraining layer, PZT layer, viscoelastic layer and base structure can be different according to the order of layering. Thus, it can affect the contribution of the active control force generated by the PZT actuator towards the motion of the overall structure.

8. HYBRID ACTIVE-PASSIVE CONTROL OF PLATES

Moreover, as noticed from the relationship between control gains and Nyquist plots for a controlled closed loop, AC/PCLD and AC/PSOLD treatments can give similar control effects to ACLD and APCLD treatments with smaller control gains. This is because a PZT patch which generates a control bending moment contacts a base structure directly. If a viscoelastic layer is located between a PZT patch and a base structure, control energy generated by a PZT patch would dissipate in a viscoelastic layer during energy transference from a PZT patch to a base structure. In terms of energy dissipation, AC/PCLD and AC/PSOLD treatments are more effective than the other two configurations.

8.1.3 Summary of control simulation of a plate with HAPCLD treatments

As has been studied above, considering the effectiveness of active control, AC/PSOLD treatment provided the best result out of four different HAPCLD treatments. AC/PSOLD treatment gave similar or larger control effects on a base structure with smaller control gain than other HAPCLD treatments. Moreover, it was also shown that the possibility of unstable active control could be minimised by the use of AC/PSOLD treatment regardless of base structures which are flat or curved. In other cases, peak value increase at a certain mode or conditional stable control was found according to the change in curvature in spite of collocation between sensor and actuator. However, stable active control results were obtained with AC/PSOLD treatment in every case. As an example in summary, the changes in control gain and absorbed power with optimised control gain are arranged for all cases in Table 8.5.

Table 8.5 Changes in control gain and maximum absorbed power for all cases according to the change in curvature

		Flat	10 mm	20 mm
Control gain	ACLD	1667.5	1795.5	1687.3
	APCLD	814.7	670.9	720.7
	AC/PCLD	192.7	41.7 (G_{3dB})	137.4
	AC/PSOLD	196.8	161.2	151.7
Absorbed power with optimised control gain (W)	ACLD	≈ 190	≈ 210	≈ 270
	APCLD	≈ 73	≈ 80	≈ 80
	AC/PCLD	≈ 18	≈ 12 (G_{3dB})	≈ 30
	AC/PSOLD	≈ 18	≈ 15	≈ 13

8. HYBRID ACTIVE-PASSIVE CONTROL OF PLATES

In order to investigate the relation between control gains and curvature, the change of control gains according to the curvature was studied as shown in Figure 8.9. As studied in Chapter 7, the control performance of PZT patch is determined in the relation with the change of mode shapes of the base plate. Moreover, when the kinetic energy of whole structure is considered, the effect of increasing stiffness due to the increase of curvature should be considered. Increasing stiffness can constrain the motion of structure, which is followed by the related change of control gain.

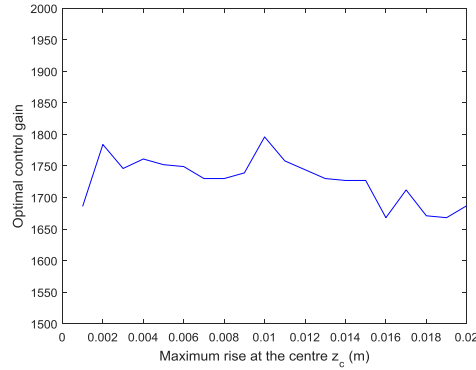


Figure 8.9 The change of control gains according to the curvature (ACLD)

The changes of mobility in each case are summarised in Figure 8.10. The effects of each HAPCLD treatment can become clearer through the normalisation by used control gains as shown in Figure 8.11.

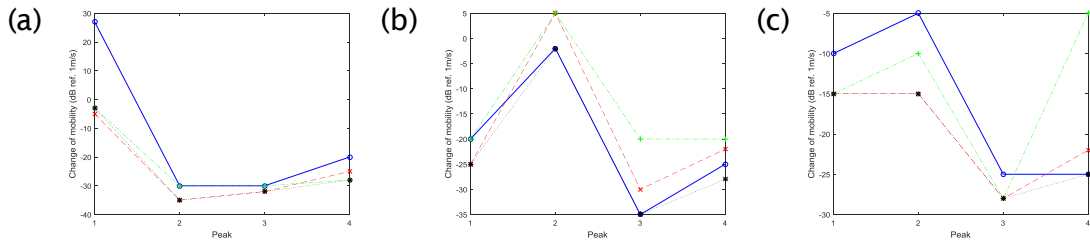


Figure 8.10 The changes of mobility in each case for (a) flat plates, (b) singly curved plates with 10mm rise and (c) singly curved plates with 20mm rise; — ACLD, - - APCLD, - . AC/PCLD and AC/PSOLD

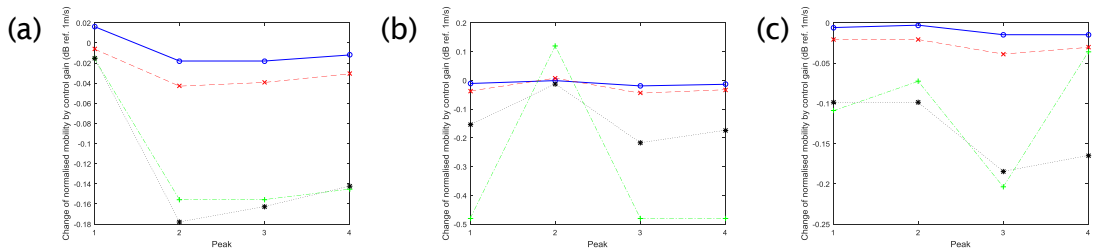


Figure 8.11 The changes of normalised mobility by control gain in each case for (a) flat plates, (b) singly curved plates with 10mm rise and (c) singly curved plates with 20mm rise; — ACLD, - - APCLD, - . AC/PCLD and AC/PSOLD

8. HYBRID ACTIVE-PASSIVE CONTROL OF PLATES

When considering that the reductions in point mobility in each case do not show significant difference with $G_{\min,KE}$, it becomes clear that AC/PSOLD treatment can give the most efficient control result with relatively small control effort, i.e. small control gain and small power absorption in all four cases as shown in Figure 8.11. The absorbed power by controller increases steeply as control gain increases until the kinetic energy of a whole structure reaches the minimum point. After the minimum point of kinetic energy, the efficiency of the controller decreases and maintains a constant rate in terms of absorbed power. Moreover, AC/PSOLD treatment gave the most robust control result in terms of stability in all four cases; in the other three cases it gave an unstable result in a certain situation as summarised in Table 8.6. Negative active control results in Table 8.6 mean that active control forces increase the motions of related modes (highlighted in red colour). In the cases marked as 'Negative', a certain mode out of all the modes got a negative effect from active control leading to an increase in peak or the saturation of kinetic energy in a whole structure with limited stability. As mentioned in relation to Figure 8.8 in Section 8.1.2, these negative effects seem to be caused by the relationship between mode shapes (or their change rate, i.e. strain) and the location of the PZT actuator.

Table 8.6 Active control result summary in each case

		Peaks in mobility (mode)				
		1st (2nd)	2nd (3rd)	3rd (7th)	4 th	5th
Flat						
	ACLD	Negative	Positive	Positive	Positive	Positive
	APCLD	Positive	Positive	Positive	Positive	Positive
	AC/PCLD	Positive	Positive	Positive	Positive	Positive
	AC/PSOLD	Positive	Positive	Positive	Positive	Positive
10mm						
	ACLD	Positive	Positive	Positive	Positive	Positive
	APCLD	Positive	Negative	Positive	Positive	Positive
	AC/PCLD	Positive	Negative	Positive	Positive	Positive
	AC/PSOLD	Positive	Positive	Positive	Positive	Positive
20mm						
	ACLD	Positive	Positive	Positive	Positive	Positive
	APCLD	Positive	Positive	Positive	Positive	Positive
	AC/PCLD	Positive	Positive	Positive	Positive	Positive
	AC/PSOLD	Positive	Positive	Positive	Positive	Positive

8. HYBRID ACTIVE-PASSIVE CONTROL OF PLATES

As discussed in the previous sections, since these negative results were caused by the dynamic characteristics of structure (i.e. mode shapes of free plates), the change of damping treatment location according to the mode shapes can be a radical solution. However, since the application of treatments in different shapes or different positions according to modes was not considered, more common method for robust control should be studied.

The sign of mode shapes around the centre point in each case was studied in Table 8.7. (+) sign denotes that a plate deflects upwards and (-) sign means that a plate deflects downwards. 0 sign means that there is no deflection in the direction. The first sign is for the x -direction and the other is for the y -direction.

As shown by Table 8.7, the main reason for unstable active control is the difference in sign of mode shapes around the centre point for each mode. This factor implies the possibility of unstable active control in the case in which symmetrical control forces or moments are applied to a base structure as studied in this thesis. However, as mentioned in the previous section, this possibility of instability in active control can be mitigated by adding adequate damping to a whole structure with some material with high damping properties such as a viscoelastic material.

Moreover, since HAPCLD treatments considered in this study cause asymmetry in whole structures, change in the neutral axis for 1-D structures or neutral plane for 2-D structures happens as explained in Sections 3.4.4 and 6.4.3. Thus, the effect of control force or moment on a base structure can change according to the distance between actuators such as the PZT layer and this neutral axis or plane. In general, the larger this distance is, the larger the control force or moment becomes. In addition to this, there is an extra movement in the neutral axis or plane inside a curved plate due to the curvature. This asymmetry can give an influence on the active control of PZT patches attached inside or outside a curved plate as discussed in [108]. Therefore, considering the influence of distance from the neutral plane on active control, the effectiveness of AC/PSOLD treatment becomes clearer. Considering the configurations in each case, since the distance between the PZT actuator and neutral plane of a base plate is largest for APCLD treatment in the four cases, APCLD treatment can generate the largest control force in theory. However, as shown by Table 8.5, AC/PCLD and AC/PSOLD treatments can give similar vibration reduction with APCLD treatment even with much smaller control gain and absorbed power. In [109], only the effect of a PZT actuator attached to a base structure according to the curvature is studied. When considering the ratio of dissipated energy in a viscoelastic layer to total generated energy by a PZT actuator, the efficiency of direct active control on a base structure such as AC/PSOLD treatment is verified in this section.

8. HYBRID ACTIVE-PASSIVE CONTROL OF PLATES

Table 8.7 Sign of mode shapes around the centre point for each mode

		Peaks in mobility (mode)			
		1st (2nd)	2nd (3rd)	3rd (7th)	4th
Flat	-	(-)/(+)	(+)/(+)	(+)/(+)	
	ACLD	(+)(-)	(+)/(+)	(+)/(+)	
	APCLD	(+)(-)	(+)/(+)	(+)/(+)	
	AC/PCLD	(+)(-)	(-)(-)	(-)(-)	
	AC/PSOLD	(-)(+)	(+)/(+)	(-)(-)	
10mm	-	(-)/0	(-)/(+)	(-)(-)	
	ACLD	(-)/0	(-)/(+)	(+)/(+)	
	APCLD	(-)/0	(+)(-)	(-)(-)	
	AC/PCLD	(+)/0	(-)/(+)	(+)/(+)	
	AC/PSOLD	(+)/0	(-)/(+)	(+)/(+)	
20mm	-	(-)/0	(-)(-)		(-)(-)
	ACLD	(-)/0	(+)/(+)		(+)/(+)
	APCLD	(+)/0	(-)(-)		(+)/(+)
	AC/PCLD	(-)/0	(+)/(+)		(-)(-)
	AC/PSOLD	(-)/0	(+)/(+)		(+)/(+)

In the next section, the effect of curvature on active control in each case will be discussed adding to control experiment results using singly curved plates with a 20 mm rise attached by various configurations of HAPCLD treatment in comparison with simulation results.

8.2 Study of plate vibration control with measured FRFs and results comparison

In this section, active control simulation with measured FRFs of a system were conducted with singly curved plates with different configurations of HAPCLD treatments attached, for comparison, with simulation results discussed in the previous section. While curved HAPCLD treatments were used in simulation, flat ones were used for experiments due to the difficulty of fab-

8. HYBRID ACTIVE-PASSIVE CONTROL OF PLATES

rication. However, since the damping treatment patches were relatively narrow enough compared with the curvature of the base plate, the gap between plates and patches, which was well filled with epoxy glue, was small enough to be neglected. First of all, passive modal loss factors of plates without and with HAPCLD treatments will be estimated through impact hammer tests.

8.2.1 Experimental results from impact hammer test

Firstly, impact hammer test results for HAPCLD treated plates will be compared with those for non-treated plates, which were measured in Section 7.2.1. Moreover, changes in passive damping in each case with different configurations were measured and compared. Figure E.20 in Section E.3 shows changes in FRFs up to 500 Hz when four different types of HAPCLD treatment were applied to a curved plate. Impact hammer tests were conducted as explained in Section 7.2.1. The centre point of plates hung on a test rig with fishing line was hit by an impact hammer, and velocity was measured on the opposite centre point. The inverse AC/PCLD treatment in Figure E.20 (e) denotes the configuration where the positions of the PZT patch and PCLD treatment were changed from the ones in AC/PCLD treatment to each opposite side of a curved plate. This is introduced to check the effect of curvature direction on active control, although it is not treated in Chapters 6 and 7 as well as Section 8.1. As noted from Figure E.20, a change in passive damping due to additional damping treatments is clear in the over 300 Hz range rather than in the low frequency range including the first and second peaks. Moreover, changes in modal stiffness and mass for 4th and 5th peaks are observed due to the attachment of damping treatments.

Values of passive modal loss factors, when an active control signal is not applied to each PZT actuator, up to the 5th peak in each case were measured by the circle fit method and arranged in Table 8.8. In the table, 'w/o' and 'w/' denote whether a HAPCLD treatment is attached to a plate or not. The most noticeable thing is that differences in passive damping increase between AC/PCLD and inverse AC/PCLD treatments. Although the same plate was not used for comparison, it means that the effectiveness of AC/PCLD treatment can be improved by only changing the position of the attachment, especially the position of a PZT actuator from the inner side of the curvature to the outer side and vice versa for the position of PCLD treatment as shown in Figure 8.12. This is applicable only for a curved structure, because, when a PZT actuator is attached on the outer side of a curved structure, the neutral axis or layer moves toward the centre of curvature and the generated control moment increases as the curvature of the structure increases [108]. In the case of a PZT actuator attached on the inner side, the opposite phenomenon

8. HYBRID ACTIVE-PASSIVE CONTROL OF PLATES

will occur [108]. For flat structures, the effect of this kind of change in configuration cannot make any difference to results.

Table 8.8 Passive modal loss factors up to the 5th peak in each case

		1st peak	2nd peak	3rd peak	4th peak	5th peak
#1 plate (Bare plate)	w/o	0.0060	0.0024	0.0027	0.0031	0.0022
#2 plate (ALCD)	w/o	0.0058	0.0016	0.0024	0.0037	0.0021
	w/	0.0076	0.0015	0.0066	0.0133	0.0035
#3 plate (APCLD)	w/o	0.0061	0.0014	0.0026	0.0036	0.0012
	w/	0.0072	0.0014	0.0116	0.0576	0.0039
#4 plate (AC/PCLD)	w/o	0.0055	0.0016	0.0024	0.0027	0.0019
	w/	0.0086	0.0016	0.0049	0.0044	0.0024
#5 plate (AC/PSOLD)	w/o	0.0056	0.0021	0.0024	0.0022	0.0017
	w/	0.0074	0.0022	0.0040	0.0066	0.0025
#6 plate (Inverse AC/PCLD)	w/o	0.0059	0.0012	0.0026	0.0051	0.0035
	w/	0.0094	0.0016	0.0146	0.0205	0.0053

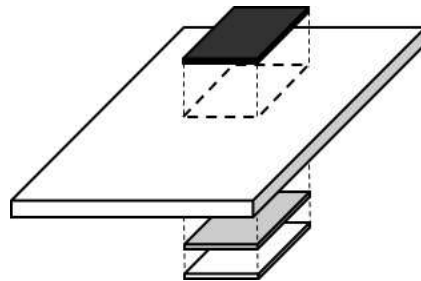
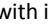




Figure 8.12 Configuration of a plate with inverse AC/PCLD treatment;  : elastic plate and patch,  : viscoelastic layer and  : piezoelectric patch

8. HYBRID ACTIVE-PASSIVE CONTROL OF PLATES

8.2.2 Experiment set-up, measurement procedure and FRF measurement results

In order to apply free-free boundary conditions to plates, plates were hung on a test rig as shown in Figure 7.7. All dimensions and material properties of a plate are the same as explained in Section 7.2.1. For measurement of velocity at the centre point, an accelerometer was attached to the damping treatment patch at the point as shown in Figure 8.13 (a). Application of a signal to the PZT patch was conducted by using electrical copper tapes attached to the PZT patch as shown in Figure 8.13 (b). When connecting electrical cables to the PZT patch, they should be carefully connected so as not to constrain the motions of free-free plates. Especially, for AC/PCLD treatment, since a PZT patch is located on the opposite side of the plate compared to other cases, electrical cables should be connected over a test rig as shown in Figure 8.13 (c). With this set-up, the measurement of FRFs with a pseudo-random input signal can be conducted for all configurations.

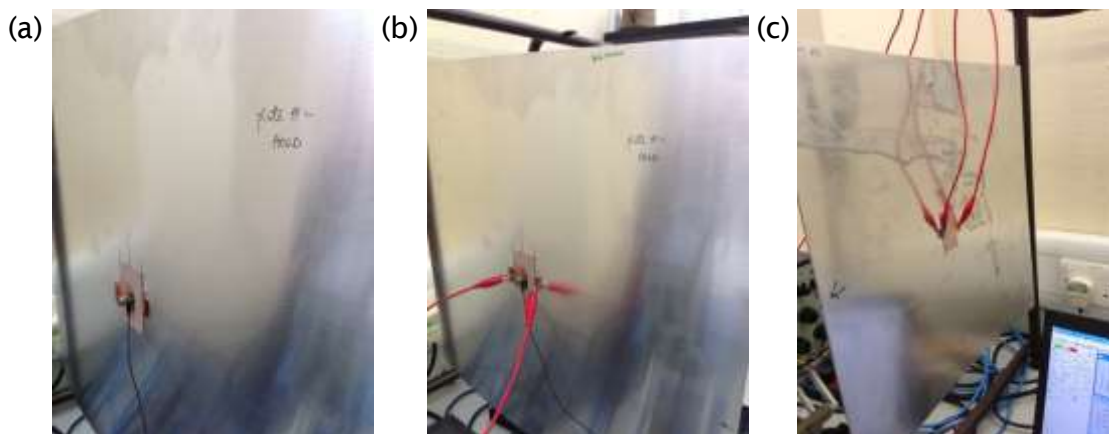


Figure 8.13 Basic connection between accelerometer and electrical cables (a) attachment of accelerometer, (b) connection of electrical cables for ACLD, APCLD and AC/PSOLD treatments and (c) connection of electrical cables for AC/PCLD treatment

In order to apply mechanical excitation with a pseudo-random signal, a shaker should be attached to plates properly by connection using a stinger and a force gauge. The shaker should be adjusted so it stays perpendicular to the plate surfaces. In order to allow free motion of plates, the distance between a shaker and plates should be arranged carefully. Firm attachment of the shaker is required to guarantee that the excitation in the out-of-plane direction was obtained. As a result, the shaker attachment was implemented as shown in Figure 8.14.

With the basic set-up as explained above, input signals have been applied to the PZT patch or to the shaker. The transfer functions were obtained by measuring FRFs for each case. The ex-

8. HYBRID ACTIVE-PASSIVE CONTROL OF PLATES

periment set-up for this was implemented as shown in Figure 8.15. The related schematic diagram for plate control is given in Figure 8.16.

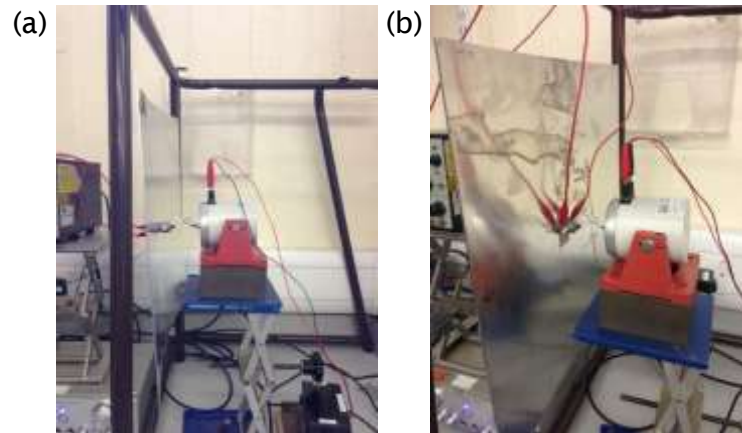


Figure 8.14 Shaker attachment for mechanical pseudo-random excitation for (a) ACDL, APCLD and AC/PSOLD treatments and (b) AC/PCLD treatment

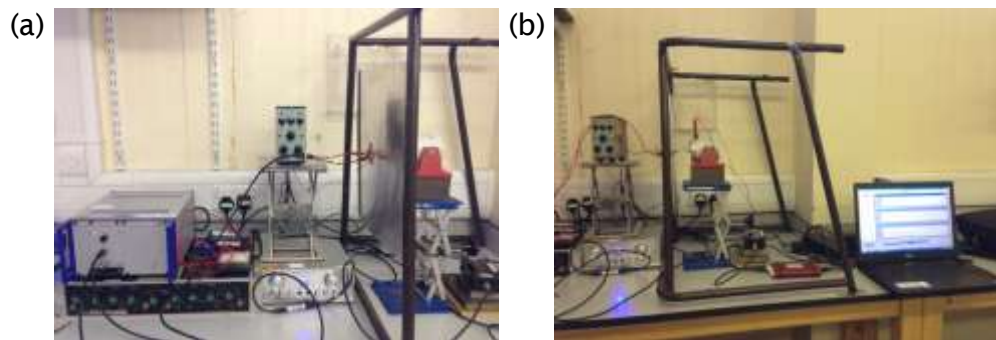


Figure 8.15 Input signal connection for (a) pseudo-random PZT excitation with electrical signal and (b) pseudo-random mechanical excitation by a shaker

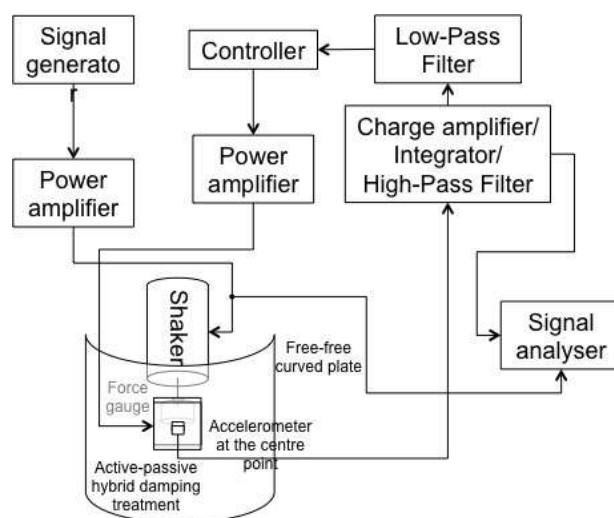


Figure 8.16 Schematic diagram of free-free curved plate control

8. HYBRID ACTIVE-PASSIVE CONTROL OF PLATES

The PZT patch was connected to a high voltage amplifier (PI E-507 High-Voltage-PZT (HVPZT) piezo amplifier Module), which receives a pseudo-random signal filtered by a low-pass filter from a signal generator in Figure 8.15 (a). An electrical input signal was sent to a signal analyser directly. For mechanical excitation, a pseudo-random signal was applied to a shaker from a signal generator through an amplifier, which amplifies the signal so as not to exceed 2 mA. An amplified input signal was sent directly to a signal analyser as a reference signal for FRF instead of measured force by an impedance head to eliminate resonance frequency mismatch between measured force and velocity. An accelerometer was connected to B&K charge amplifiers type 2635 for amplification of measured data, filtering of low frequency noise components below 10 Hz and signal conversion from acceleration to velocity. All the equipment used was the same as that used in section 4.2.1. Therefore, with this experiment set-up, measurements of FRFs with excitations by a shaker and a PZT actuator were conducted. In the next subsection, measured data through impact hammer tests for passive loss factor and FRF measurement with excitations by a shaker and a PZT actuator will be analysed with each other and other previously measured data.

Moreover, FRFs with excitation of pseudo-random bending moments generated by a PZT patch and pseudo-random force generated by a shaker were measured as well for each configuration.

Figures 8.17 and 8.18 show measured FRFs and phases for the ACLD case. In particular, FRF's attenuation over 500 Hz with the KEMO low-pass filter, which is an 8th order Butterworth Filter and was installed as shown in Figure 8.16, and steeper change in phase with a low-pass filter up to the cut-off frequency than without any filter are obvious in Figure 8.16. Moreover, noise in measured data below 50 Hz is clear as well in Figure 8.17. Measurement was repeated for other configurations as well and similar results were obtained.

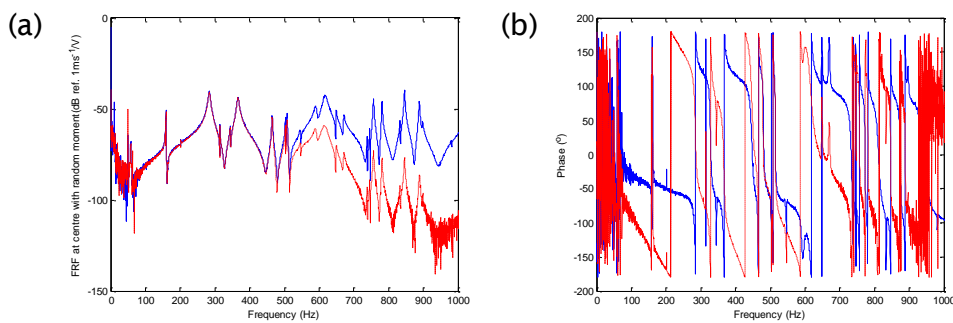


Figure 8.17 (a) FRFs at the centre with a pseudo-random moment by a PZT actuator and (b) phases of FRFs at the centre with a pseudo-random moment by a PZT actuator; — without filter; - - - with a low-pass filter with a cut-off frequency of 500 Hz (ACLD treatment on a curved plate)

8. HYBRID ACTIVE-PASSIVE CONTROL OF PLATES

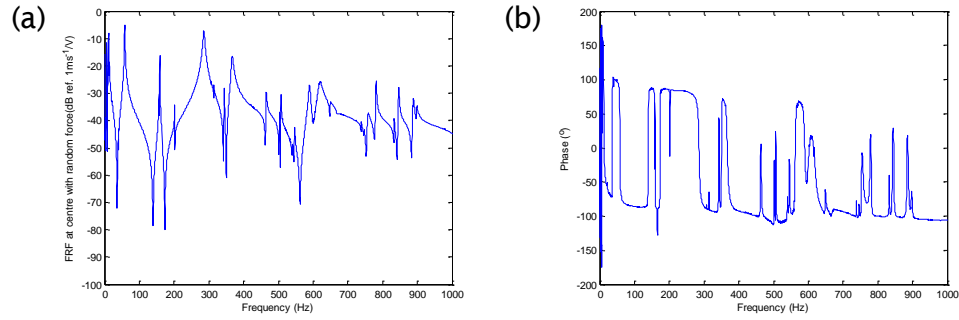


Figure 8.18 (a) FRF at the centre with a pseudo-random force by a shaker and (b) phase of FRF at the centre with a pseudo-random force by a shaker (ACLD treatment on a curved plate)

8.2.3 Active control based on experimental data

By using these measurement data shown in Section 8.2.2, active control results were simulated. Different low-pass filters were considered in order to evaluate the effect of anti-aliasing filters on stability. As explained in Section 5.2.1, a low-pass filter, which is introduced to limit the control frequency range up to the highest mode in interest, can cause the stability issue in active control due to a phase shift in the filtered active control signal. Firstly, with ACLD treatment, Nyquist plots, control gain and controlled results were studied. When no filter is connected to the control signal, control gain with a 3 dB gain margin for stable control was 870.90 (see the Nyquist plot in Figure 8.17 (a)). With this control gain, the control result as shown in Figure 8.19 (b) was obtained. Since the strength of the control force is determined by the radius of the circle in the Nyquist plot for a closed loop and the magnitudes of the control force increase according to frequency as shown in Figure 8.19 (a), mobility reductions in the low frequency range are relatively small (see figure 8.19 (b)). Similar results are obtained for other cases as shown later.

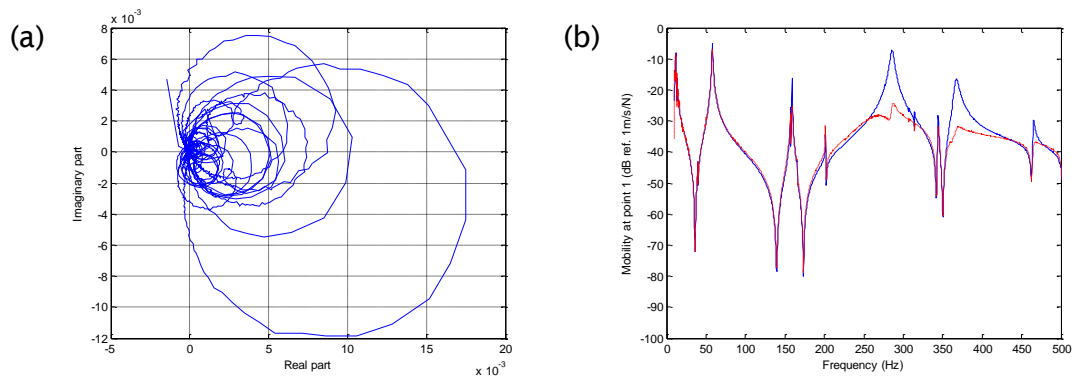


Figure 8.19 (a) Nyquist plot for a closed loop without filter and (b) controlled result without filter (ACLD treatment)

8. HYBRID ACTIVE-PASSIVE CONTROL OF PLATES

However, a low-pass filter with a cut-off frequency of 500 Hz can be used to trim the input control signal. Figure 8.20 shows a control gain with a 3 dB gain margin of 69.35. Circles of the Nyquist plot start rotating according to the change of phase and negative control results were obtained at some peaks.

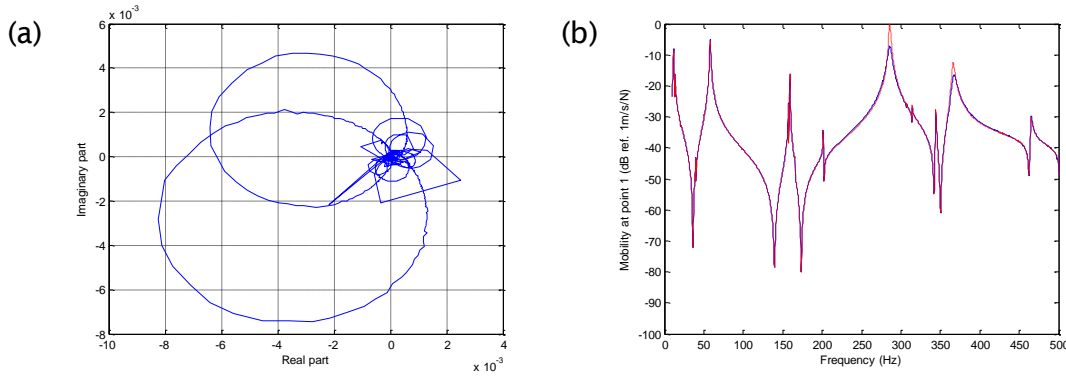


Figure 8.20 (a) Nyquist plot for a closed loop with a low-pass filter with a cut-off frequency of 500 Hz and (b) controlled result with a low-pass filter with a cut-off frequency of 500 Hz (ACLD treatment)

As studied in section 5.2, if an ideal low-pass filter is used for trimming the signal at a cut-off frequency, the results can be changed as shown in Figure 8.21 with control gain with a 3 dB gain margin of 1446.7.

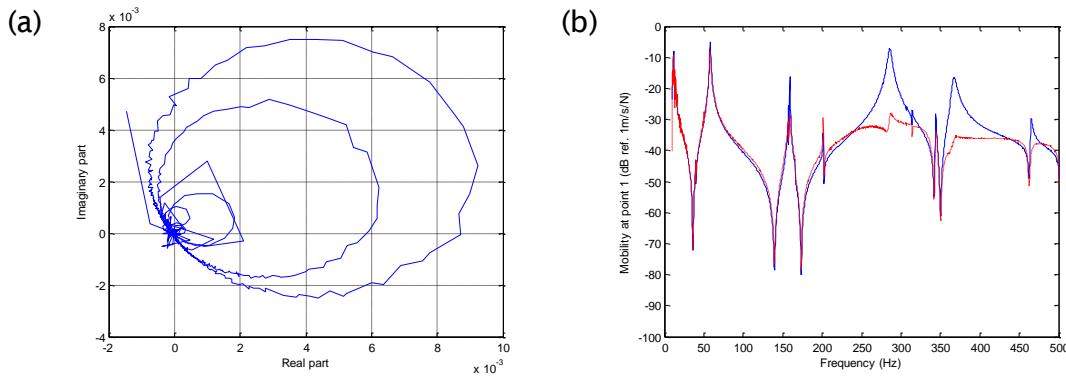


Figure 8.21 (a) Nyquist plot for a closed loop with an ideal low-pass filter with a cut-off frequency of 500 Hz and (b) controlled result with an ideal low-pass filter with a cut-off frequency of 500 Hz (ACLD treatment)

When the Nyquist plot for a closed loop with ACLD treatment in Figures 8.20 is compared with the ones in Figures 8.6 and 8.7, similarity between simulation and experiment results can be found. Due to limits in the realisation of the simulation model in the real structure, small differences are found between the two results, but the overall trends of the Nyquist plots are in good agreement.

Changes in peak values in each case are summarised in Table 8.9. Values in the ‘w/o control’ row refer to the initial peak values of FRF. Other values denote changes in peak values.

8. HYBRID ACTIVE-PASSIVE CONTROL OF PLATES

Table 8.9 Changes in peak values in the case of active control using ACLD treatment in a plate structure

	1 st	2 nd	3 rd
w/o active control (Peak value)	-5.12 dB	-16.33 dB	-7.061 dB
w/o filter	-1.66 dB	-9.09 dB	-16.979 dB
w/ KEMO filter	-0.183 dB	+0.11 dB	+6.8136 dB
w/ ideal filter	-2.807 dB	-12.20 dB	-20.829 dB

As shown in Table 8.9, by trimming off components which can cause instability in active control, a larger control gain can be obtained and better control results follow. However, when a low-pass filter or any other filter is used for trimming unnecessary components off, continuous phase shift which is induced by group delay during the filtering process in a filter can lead to undesirable control results. As explained in Section 5.2, in the case that only one peak (one mode or one component at a specific frequency) should be under active control, the introduction of an all-pass filter can solve this phase shift problem. On the other hand, in the case that more than one mode should be under active control as was the case in this study, phase delays caused by filters should be considered as discussed in Section 5.2.

The same procedure was repeated for other configurations as well. For all results, refer to Section E.4 in Appendix E. Only tables including the changes in peak values for each case are given in this section for comparison.

Larger effects of active control were obtained with APCLD, AC/PCLD, AC/PSOLD and inverse AC/PCLD treatments than with ACLD treatment. With APCLD treatment, although the largest reductions were achieved, the effectiveness of active control was not the best out of all configurations considering control gains, which are decided according to the changes in kinetic energy and absorbed power, and which are relatively larger than those for other configurations. AC/PCLD, AC/PSOLD and inverse AC/PCLD treatments are giving as large reductions in peak values as APCLD treatment with one fifth or sixth of the control gain value used for APCLD treatment. This effectiveness of active control can be thought of as the result of a direct transfer of control force/moment from a PZT patch to a base structure without energy dissipation in a viscoelastic layer as explained in the previous section.

8. HYBRID ACTIVE-PASSIVE CONTROL OF PLATES

Table 8.10 Changes in peak values in the case of active control using APCLD treatment in a plate structure

	G_{3dB}	1 st	2 nd	3 rd
w/o active control (Peak value)	-	-4.51	-16.13	-9.213
w/o filter	382.38	-6.01	-14.04	-17.027
w/ KEMO filter	22.26	-0.45	-0.82	+1.473
w/ ideal filter	943.48	-11.10	-19.99	-24.357

Table 8.11 Changes in peak values in the case of active control using AC/PCLD treatment in a plate structure

	G_{3dB}	1 st	2 nd	3 rd
w/o active control (Peak value)	-	-4.442	-15.58	-12.67
w/o filter	218.82	-21.878	-19.92	-25.42
w/ KEMO filter	4.42	-1.597	+0.96	+5.793
w/ ideal filter	206.67	-21.418	-19.73	-24.95

Table 8.12 Changes in peak values in the case of active control using AC/PSOLD treatment in a plate structure

	G_{3dB}	1 st	2 nd	3 rd
w/o active control (Peak value)	-	-6.815	-16.58	-21.05
w/o filter	175.47	-16.865	-16.22	-13.61
w/ KEMO filter	5.33	-1.640	+0.74	+5.53
w/ ideal filter	160.74	-16.195	-15.56	-12.62

Table 8.13 Changes in peak values in the case of active control using inverse AC/PCLD treatment in a plate structure

	G_{3dB}	1 st	2 nd	3 rd
w/o active control (Peak value)	-	-4.457	-12.94	-18.87
w/o filter	216.28	-17.823	-22.12	-18.39
w/ KEMO filter	12.43	-2.347	+3.362	+5.90
w/ ideal filter	211.71	-17.663	-22.00	-18.23

On the other hand, the effect of curvature on active control using a PZT patch may be unexpected. According to [108], when a PZT patch is attached on the outside of a curved plate, active control effect gets larger than on the inside of the plate due to the outward movement of the neutral plane from the mid-plane of the plate. However, when checking the curvature around the centre on real plates, the curved plate around the centre is flat enough for flat damping treat-

ments, which were used in the experiment, to be attached only with a small gap between plates and treatments. In order to make this effect clearer, a larger PZT actuator such as the one used in [80] and [109], which covers the whole surface or broad part of a curved plate with the same curvature, might be needed.

8.3 Summary and conclusions

In this chapter, numerical and experimental results with curved plates and HAPCLD treatments were analysed. As a result of the study, by using HAPCLD treatments consisting of a constraining layer, a viscoelastic layer and a PZT layer, much larger reduction of local vibration is expected than with the simplest configuration of target configurations, i.e. ACLD treatment. Moreover, configurations which can apply control force/moment to a base structure without energy dissipation in a viscoelastic layer are expected to provide more efficient active control results. As explained in Sections 8.1.2 and 8.2.3, the decrease in control efficiency due to the energy dissipation in a viscoelastic layer is greater than the increase in control force due to the increased length of moment arm with the distance between a PZT actuator and neutral axis of a base structure. As a result, it is evaluated that AC/PSOLD treatment can give the most efficient and robust active control results compared to other cases for plates as well as for beams. However, for the case of collocation between a sensor and actuator, although AC/PCLD treatment can give a similar result with AC/PSOLD treatment for flat structures, the curvature should be carefully considered for stable active control in the application of AC/PCLD treatment to curved structures.

Moreover, FE plate models established in Chapter 5, including elastic plates, viscoelastic materials and piezoelectric materials, were validated by experimental data with impact hammer tests. Based on validated FE plate models, active control results were estimated for flat and curved plates with different curvatures. Finally, FRFs of real curved plates with various HAPCLD treatments were measured with excitation by pseudo-random moments and forces. Moreover, active control results were obtained with these measured FRFs and each result was analysed.

In the next chapter, the study in the thesis will be summarised and final conclusions will be derived based on the results of the study with a comment on the unique elements of this thesis as explained in Section 1.3. Furthermore, future tasks for further study will be presented.

9 CONCLUSIONS AND SUGGESTIONS FOR FUTURE WORK

Four different types of HAPCLD treatments categorised by Trindade and Benjeddou [3] have been applied to beams, flat and curved plates respectively in this thesis. For the study, FE models for each case were established based on a layer-wise approach considering the mutual relationship between each layer of laminated structures and validated with experimental data. Active control was implemented and control results were obtained through simulations and experiments. Discussions of these results were given in every chapter.

In the next subsection, the whole study in this thesis will be summarised. The conclusions and its unique elements will be discussed in Section 9.1.2 based on the summary of study. Moreover, based on the conclusions and novelty, future areas of study will be proposed with references in Section 9.2.

9.1 Summary

One of the objectives of this thesis was to confirm the assessment results in [3] for beams with four different types of HAPCLD treatment. For this objective, numerical beam models for laminated structures including viscoelastic and piezoelectric materials were established with FEM [92, 110] and a layer-wise approach [93] in Chapter 3. Established beam models were validated with analytical continuous beam models explained in Appendix B and [111], and measurements of FRFs from impact hammer tests and pseudo-random excitation tests with piezoelectric actuators or shakers in Chapter 4. With the validated FE beam models and measured data, active controls of beams were executed with optimised control gains considering the changes in kinetic energy of whole structures, absorbed power by actuators according to the changes in control gain, which can minimise the kinetic energy or maximise the absorbed power, and stability of active control in Chapter 5. Moreover, in order to solve instability problems due to the phase shift caused by a low-pass filter, which was used to limit the target control frequency range related to up to the 3rd mode, a new compensation method to eliminate the effect of phase shift was proposed as well in Chapter 5.

Furthermore, in order to investigate the applicability of HAPCLD treatments for beams to more complex structures such as flat and curved plates, which was another objective of this thesis, numerical flat and curved plate models for laminated structures including viscoelastic, elas-

9. CONCLUSIONS AND SUGGESTIONS FOR FUTURE WORK

tic constraining and piezoelectric layers were established with FEM [92, 110] and a layer-wise approach [93] in Chapters 6 and 7. In Chapters 6 and 7, the established FE flat and curved plate models were validated by experimental data such as impact hammer tests and the measurement of FRFs under pseudo-random excitation of force or moment with real experimental flat and curved plates. In addition to the numerical model validation, active control of flat and curved plates was executed with the validated FE flat and curved plate models and the proposed filter in Chapter 8. In addition to this control simulation, active control of curved plates using measured transfer functions of real curved plates was implemented in Chapter 8. During this study, the effect of curvature and induced change of mode shapes in free-free flat and curved plates on active control was studied and discussed.

With this summary of the study in the thesis, the final conclusions and novelty of the thesis will be discussed in the next subsection.

9.2 Conclusions

1. It was experimentally verified that AC/PSOLD treatment can give the most efficient control results in active control as well as passive control out of four HAPCLD treatments categorised from configurations used by many researchers in previously published papers. Moreover, during the process of verification, the reason why Trindade and Benjeddou [3] had used only the first three modes for active control in their study was clarified. With HAPCLD treatments located on cantilever beams as shown from Figures 5.18 to 5.21, active control moments generated by piezoelectric actuators in HAPCLD treatments can give negative effects for over the 4th mode in active control, which can be represented by circles on Nyquist plots located in an imaginary negative area as shown in Figure 5.22. In order to eliminate these negative influences from over the 4th modes, a mode or frequency filtering method should be introduced to limit the target mode range below the 3rd mode. Since a simple negative velocity control was used in this study instead of the LQR algorithm used for the controller in [3], a low-pass filter was introduced to limit target frequency range up to the 3rd mode. However, due to the phase shift, the total amount up to the cut-off frequency is decided by the order of a low-pass filter, and the locations of circles on Nyquist plots can change from the original locations in non-filtered cases. As a result, active control results which were estimated to be positive without the influence of filters can be changed so they are negative in real experiments as explained in Section 5.2.1. Therefore, in order to eliminate or minimise these undesirable changes in active control, additional introduction of filters or signal processing methods is required. In this study, the

9. CONCLUSIONS AND SUGGESTIONS FOR FUTURE WORK

application of serial band-pass filters for each mode was introduced for this purpose based on [98], and expected active control results from simulations using numerical FE models were obtained ignoring the effects of a low-pass filter as explained in Section 5.2.3.

2. The assessment results for HAPCLD treatments were verified for beams and for flat and curved plates as well. With four different configurations of HAPCLD treatment attached to flat or curved plates, simulations of numerical FE models and measurements of FRFs of real structures were conducted. As shown in Sections 8.1.2, 8.1.3 and 8.2.2, the largest reductions at resonance frequencies were obtained with AC/PSOLD treatment of four HAPCLD treatment configurations for flat and curved plates as were carried out for beams. Thus, this means that the configuration like AC/PSOLD treatment has a possibility of expanded application for more efficient control of vibration in curved plates, which can cause structure-borne noise radiated from the surface of a plate, than ACLD treatment, which has been mainly used for structure-borne noise control for curved plates by many researchers. During this study, the impact of the relationship between mode shapes and motions of piezoelectric patches on active control was studied as explained in Section 8.1.2. Differently from the case for control point force generated by shakers, piezoelectric actuators occupy spaces and have their own mode shapes under pseudo-random excitation. Thus, the effect of control force or moment generated by piezoelectric actuators on base structures rely on dynamic characteristics of piezoelectric actuators according to the mode shapes of plates.
3. Easily composable numerical models for beams, flat and curved plates were established using FEM and a layer-wise approach in this study. As explained in Chapters 3 and 6, individual numerical mass and stiffness matrices for each layer were derived from the energy conservation equation using potential and kinetic energy of structures without consideration of the relationship between local displacements of each layer. Each mass and stiffness matrix can be shared by layers having the same material properties and dimensions. A coupling matrix was derived from the relationships between local displacements of each layer from an equivalent neutral axis or plane of laminated structures as explained in Sections 3.4.3 and 6.4.3. In this process, distances between neutral axes in each layer take on a large role in defining the relationship between each displacement term. Equivalent mass and stiffness matrices of whole structures can be obtained by simply multiplying the coupling matrix to the stacked mass and stiffness matrices in the order of lamination from top to bottom. These numerical models were validated by analytic models and experimental measurements as explained in Chapter 4 and Sections 6.6 and 7.2.
4. More complex configurations than ACLD treatment were applied to flat and curved plates

9. CONCLUSIONS AND SUGGESTIONS FOR FUTURE WORK

as explained in Section 1.2. The control performances of these HAPCLD treatments applied to flat and curved plates were studied. As expected from the results of beams, these configurations can give much more efficient control results than ACLD treatment can. In particular, AC/PSOLD treatment can give more robust active control than other treatments regardless of the change in curvature and mode shapes. Therefore, they can be considered better for control results in flat and curved plate vibration control, which can be utilised for outward sound radiation control and inner cavity noise control in airplanes, automobiles and pipelines.

9.3 Suggestions for future work

1. Some unconsidered factors relating to HAPCLD treatments can be studied. According to [3], a piezoelectric actuator can be attached separately from PCLD treatment in AC/PCLD treatment. Thus, considering mode shapes and the control contribution of active and passive control according to frequency, AC and PCLD treatment can be applied to different points. AC can be applied to the point where low-frequency components are dominant, and PCLD treatment can be applied to the point for higher modes respectively. The control effect in this case can be compared with the case in which AC and PCLD treatment are applied as the configuration of AC/PCLD treatment at the same point.
2. Study with the application of other various boundary conditions, as studied by Huang et al. [112], can be investigated using the configurations of HAPCLD treatment attached to flat and curved plates as studied in this thesis. Like the study of Wang et al. [99, 100] in which the Mead-Markus model for sandwich beams with a viscoelastic core was expanded to plates, the study in [112] can also be applied to plates according to Wang et al.'s study to begin to know the dynamic characteristics of structures. Moreover, the change in active control effects generated by the same actuator type at the same actuator location as done in this study could be researched according to the changes in boundary conditions, which are strongly related to the mode shapes of structures.
3. Different shapes of piezoelectric actuator such as a triangle-shaped PZT patch studied by Hong et al. [113] could be utilised for active control and HAPCLD treatments. Due to the dynamic characteristics of piezoelectric materials, while rectangular piezoelectric actuators mainly generate two pairs of bending moments at every edge, triangular piezoelectric actuators generate vertical force at the most narrow-angled tip of the three tips. In order to avoid the duality problem, these kinds of piezoelectric actuators can be used for velocity

9. CONCLUSIONS AND SUGGESTIONS FOR FUTURE WORK

feedback control instead of rectangular actuators. Moreover, the effects of HAPCLD treatment by triangle-shaped piezoelectric actuators can be studied as well.

4. Solid piezoelectric actuators in HAPCLD treatments can be replaced by polyvinylidene fluoride (PVDF) film type actuators based on Zhang et al.'s study [114] for cavity noise control. Since these PVDF actuators are more easily bent according to the curvatures of curved structures than solid piezoelectric actuators, they are commonly used for vibration and radiated sound control of shell structures as in [109] and [114]. However, since the constraining effect of solid piezoelectric actuators cannot be expected from PVDF actuators, the dynamic characteristics of PVDF actuators should be studied more in order to apply them to HAPCLD treatments. Moreover, solid piezoelectric actuators can be replaced by active fibre composites as was done in Ray's studies [16 ~ 23] or different types of piezoelectric composite actuators which are explained in Chopra's review [115].
5. Study about the applicability of HAPCLD treatment for vibro-acoustic problems related to vortex induced vibration (VIV) and structure-borne noise of pipelines could be considered. As concluded in the previous section, since HAPCLD treatments can give better performance in both passive and active controls than conventional active controls, it would be useful to utilise them for this kind of control application. When the thickness of HAPCLD treatments, which are generally thicker than active control (AC) consisting of a single piezoelectric actuator, can limit the range of application, the usage of PVDF films mentioned in the paragraph above can be helpful, if they can generate a large enough power to suppress the motions of pipes as solid piezoelectric actuators.
6. New concepts of controller such as a Lyapunov-based control strategy used by Dadfarnia et al. [116] could be introduced for HAPCLD treatments instead of the simple negative velocity feedback control used in this thesis. According to [116], a Lyapunov-based control strategy, which replaced a conventional PD control strategy, could give very effective control results for vibration suppression in a moving robot arm model. Based on these results, a new control strategy could be introduced to discover the possibility of more effective and efficient control results.

APPENDIX A FINITE ELEMENT MODELLING METHOD

A.1 Shape functions and the Jacobian matrix of a 1-D element

In Finite Element Analysis (FEA), since a structure can be assumed to be the sum of its small elements, the simple FE elements are usually used for analysis. In the case of a 1-D problem, this FE element is a straight beam element with length 2 and has 2 nodes, 3 DOFs at each node as shown in Figure A.1.



Figure A.1 FE beam element

The nodes have displacements u and w along the element axis, and a rotation θ . The subscripts 1 and 2 indicate the numbers of the node. The coordinates $\xi = -1$ and 1 at nodes 1 and 2 respectively.

A continuous system is divided into a finite number of 1-D elements, and each element has the same nodes and DOFs.

Shape functions are used to approximate the change of displacement in the element. For the axial displacement, the values of displacement change linearly along the length of the element. Therefore, the linear shape functions are used for the axial displacement defined as [110]

$$H_1(\xi) = \frac{1}{2}(1 - \xi), \quad H_2(\xi) = \frac{1}{2}(1 + \xi). \quad (\text{A.1})$$

The geometry of a single axial element is shown in Figure A.2. The origin is set at the half point of an element, and if the FE element shown in Figure A.1 is used, the ratio of length between a real element and an FE element is a . The axial displacement of the element can be expressed as [92]

$$u = \begin{bmatrix} H_1(\xi) & H_2(\xi) \end{bmatrix} \begin{bmatrix} u_1 \\ u_2 \end{bmatrix} = \mathbf{H}_u(\xi) \mathbf{u}_e. \quad (\text{A.2})$$

APPENDIX A FINITE ELEMENT MODELLING METHOD

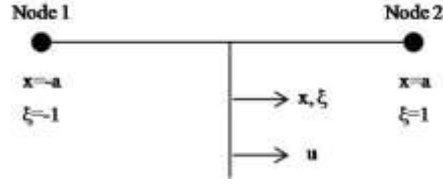


Figure A.2 Geometry of a single axial element

On the other hand, for the bending motion of a beam element, the transverse displacement w and the rotation angle $\theta = \partial w / \partial x$ should be taken as degrees of freedom at each node. Therefore, the Hermite cubic shape functions are used for the bending motion. They are defined as [110]

$$H_1^0(\xi) = \frac{1}{4}(2 - 3\xi + \xi^3), \quad H_2^0(\xi) = \frac{1}{4}(2 + 3\xi - \xi^3),$$

$$H_1^1(\xi) = \frac{1}{4}(1 - \xi - \xi^2 + \xi^3), \quad H_2^1(\xi) = \frac{1}{4}(-1 - \xi + \xi^2 + \xi^3). \quad (\text{A.3})$$

A single bending element is shown in Figure A.3. The origin is allocated at the half point of an element as well, and the ratio of length is the same as for a single axial element. The transverse displacement and rotation angle of the element can be expressed as [92]

$$w = \begin{bmatrix} H_1^0(\xi) & JH_1^1(\xi) & H_2^0(\xi) & JH_2^1(\xi) \end{bmatrix} \begin{Bmatrix} w_1 \\ \theta_1 \\ w_2 \\ \theta_2 \end{Bmatrix} = \mathbf{H}_w(\xi) \mathbf{w}_e, \quad (\text{A.4})$$

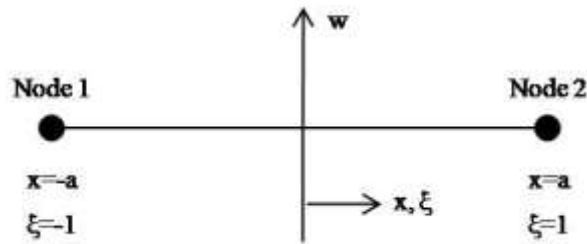


Figure A.3 Geometry of a single bending element

where J is the ratio of the lengths of the element in the x and ξ coordinates, i.e., the Jacobian matrix of a 1-D element which will be explained below.

When an element in the global coordinate (x, y, z) is transformed to the FE element in the local coordinates (ξ, η, ζ) through the mapping, since the dimension of the element is changed accord-

ing to the ratio between two elements, displacement, force, and so on should be changed with that ratio. This ratio is called the Jacobian matrix generally defined as [92, 110]

$$\begin{bmatrix} dx \\ dy \\ dz \end{bmatrix} = \mathbf{J} \begin{bmatrix} d\chi \\ dh \\ dz \end{bmatrix} = \begin{bmatrix} \frac{\partial x}{\partial \chi} & \frac{\partial x}{\partial h} & \frac{\partial x}{\partial z} \\ \frac{\partial y}{\partial \chi} & \frac{\partial y}{\partial h} & \frac{\partial y}{\partial z} \\ \frac{\partial z}{\partial \chi} & \frac{\partial z}{\partial h} & \frac{\partial z}{\partial z} \end{bmatrix} \begin{bmatrix} d\chi \\ dh \\ dz \end{bmatrix}. \quad (\text{A.5})$$

Therefore, in the case of a 1-D problem, since the Jacobian matrix relates to the transformation between coordinates x and ξ , the Jacobian matrix of a 1-D problem should be the ratio of length of the elements in the two coordinate systems. For example, for elements shown in figures A.2 and A.3, the value of the Jacobian term for straight beam elements should be

$$J = \frac{\partial x}{\partial \xi} = \frac{a - (-a)}{1 - (-1)} = a.$$

A.2 Assembly of global matrices of a 1-D element

In general, in order to calculate the mass and stiffness matrices, numerical integration using the Gauss-Legendre method is used. When a function $g(\chi)$ is integrated from -1 to 1, the integral of that function can be evaluated as [110]

$$\int_{-1}^1 g(\xi) d\xi = \sum_{j=1}^n W_j g(\xi_j), \quad (\text{A.6})$$

where W_j are the weight coefficients and ξ_j are the sampling points. These values are determined according to how many sampling points are chosen for integration. Detailed information about integration points and weight coefficients for the Gauss integration formula is shown in Table A.1.

The mass and stiffness matrices of each element can be obtained through the Gauss integration. With these mass and stiffness matrices, the global dynamic stiffness matrix can be obtained. Firstly, the vector of global DOFs is defined. If there are n elements in a one-dimensional system, there are $n+1$ FE nodes in that system, and the DOFs of these FE nodes form the vector of global DOFs. Therefore, the global mass and stiffness matrices can be assembled as shown in

Figure A.4 by inserting the matrices of the individual elements in a position related to the nodal DOFs of the element.

N	$\pm \xi_j$	W_j
1	0	2
2	$1/3^{1/2}$	1
3	$(0.6)^{1/2}$ 0	$5/9$ $8/9$
4	$\left[\frac{3+4.8^{1/2}}{7} \right]^{1/2}$ $\left[\frac{3-4.8^{1/2}}{7} \right]^{1/2}$	$\left[\frac{1}{2} - \frac{30^{1/2}}{36} \right]^{1/2}$ $\left[\frac{1}{2} + \frac{30^{1/2}}{36} \right]^{1/2}$

[illegible]

Once the global mass and stiffness matrices are assembled, the equation of motion can be obtained according to d'Alembert's principle that the sum of the forces acting on the system is equal to zero. Therefore, the FE equation of motion can be expressed as

164

A.3 Shape functions and the Jacobian matrix of a 2-D element

As explained for a beam element in Appendix A.1, the general 2-D FE element which is used for the FE analysis of a plate has the square shape with length 2 on each side, 4 nodes and 5 or 6 DOFs at each node as shown in Figure 1. DOF can be changed according to the conformity of the element. If non-conforming elements are used, each element has 5 DOFs. Otherwise, it has 6 DOFs which include the twisting term $w_{xy} = \partial^2 w / \partial x \partial y$ added to 5 DOFs shown in Figure A.5.

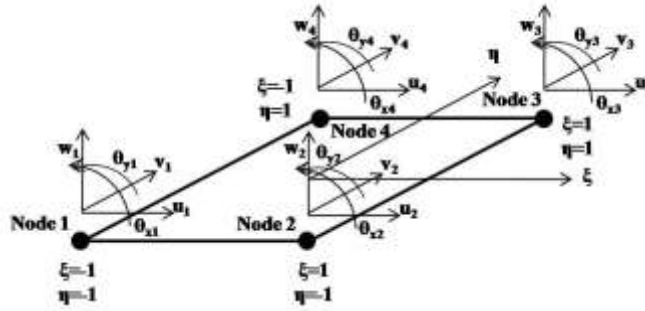


Figure A.5 2-D FE element

In Figure A.5, the slope θ_x and θ_y can be defined as

$$\theta_x = \frac{\partial w}{\partial y}, \quad \theta_y = -\frac{\partial w}{\partial x}. \quad (\text{A.8})$$

The formulation of 2-D FEM is basically the same as that for the 1-D case. For in-plane displacement, i.e. u and v , the linear interpolation functions are used, and for out-of-plane displacement, i.e. w and other slope terms, the Hermite cubic shape functions are used. Therefore, eq. (A.2) and (A.4) in appendix A.1 can be applied here as [92]

$$u = \begin{bmatrix} H_{in_1} & 0 & H_{in_2} & 0 & H_{in_3} & 0 & H_{in_4} & 0 \\ 0 & H_{in_1} & 0 & H_{in_2} & 0 & H_{in_2} & 0 & H_{in_4} \end{bmatrix} \begin{bmatrix} u_1 \\ v_1 \\ u_2 \\ v_2 \\ u_3 \\ v_3 \\ u_4 \\ v_4 \end{bmatrix} = \mathbf{H}_{in} \mathbf{u}_e, \quad (\text{A.9})$$

$$\mathbf{w} = \left[\begin{array}{cccc} \mathbf{H}_{\text{out}_1} & \mathbf{H}_{\text{out}_2} & \mathbf{H}_{\text{out}_3} & \mathbf{H}_{\text{out}_4} \end{array} \right] \left\{ \begin{array}{c} w_1 \\ \theta_{x1} \\ \theta_{y1} \\ w_{xy1} \\ \vdots \\ w_4 \\ \theta_{x4} \\ \theta_{y4} \\ w_{xy4} \end{array} \right\} = \mathbf{H}_{\text{out}} \mathbf{w}_e, \quad (\text{A.10})$$

$$\text{where } H_j^{\text{in}} = \frac{1}{4} (1 + \xi_j \xi) (1 + \eta_j \eta), \quad (\text{A.11})$$

$$\mathbf{H}_{\text{out}_j}^T(\xi, \eta) = \begin{bmatrix} f_j(\xi) f_j(\eta) \\ J_y f_j(\xi) g_j(\eta) \\ -J_x g_j(\xi) f_j(\eta) \\ J_x J_y g_j(\xi) g_j(\eta) \end{bmatrix}, \quad (\text{A.12})$$

$f_j(\xi) = \frac{1}{4} (2 + 3\xi_j \xi - \xi_j \xi^3)$, $g_j(\xi) = \frac{1}{4} (-\xi_j - \xi + \xi_j \xi^2 + \xi^3)$ and j refers to the nodal number of the element in every equation which varies from 1 to 4.

In eq. (A.12), J_x and J_y are the ratio of a real element and an FE element in the x - and y -directions respectively. As explained in Appendix A.1, this is called the Jacobian matrix generally defined as [92, 110]

$$\begin{bmatrix} dx \\ dy \\ dz \end{bmatrix} = \mathbf{J} \begin{bmatrix} d\xi \\ d\eta \\ d\zeta \end{bmatrix} = \begin{bmatrix} \frac{\partial x}{\partial \xi} & \frac{\partial x}{\partial \eta} & \frac{\partial x}{\partial \zeta} \\ \frac{\partial y}{\partial \xi} & \frac{\partial y}{\partial \eta} & \frac{\partial y}{\partial \zeta} \\ \frac{\partial z}{\partial \xi} & \frac{\partial z}{\partial \eta} & \frac{\partial z}{\partial \zeta} \end{bmatrix} \begin{bmatrix} d\xi \\ d\eta \\ d\zeta \end{bmatrix}. \quad (\text{A.13})$$

In the case of a 2-D problem, this matrix can be reduced as

$$\mathbf{J} = \begin{bmatrix} \frac{\partial x}{\partial \xi} & \frac{\partial x}{\partial \eta} \\ \frac{\partial y}{\partial \xi} & \frac{\partial y}{\partial \eta} \end{bmatrix}. \quad (\text{A.14})$$

However, for a rectangular plane plate, since $\frac{\partial x}{\partial \eta}$ and $\frac{\partial y}{\partial \xi}$ are equal to nought, $\frac{\partial x}{\partial \xi}$ and $\frac{\partial y}{\partial \eta}$ can be used individually. Therefore, $\frac{\partial x}{\partial \xi}$ is equal to J_x and $\frac{\partial y}{\partial \eta}$ can mean J_y respectively.

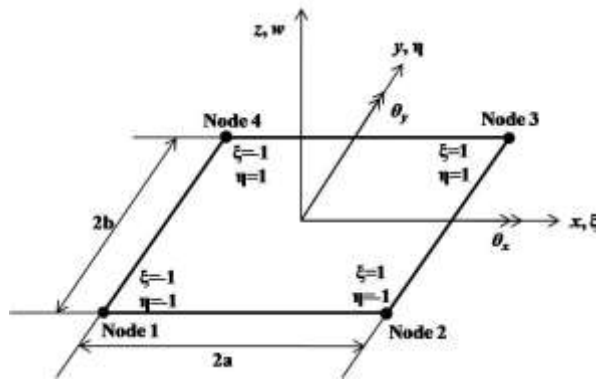


Figure A.6 Geometry of a single plate element

If the geometry of a single plate element is the same as that shown in Figure A.10, the values for each ratio can be replaced with $J_x = \frac{\partial x}{\partial \xi} = \frac{a - (-a)}{1 - (-1)} = a$, $J_y = \frac{\partial y}{\partial \eta} = \frac{b - (-b)}{1 - (-1)} = b$.

A.4 Composition of global matrices of a 2-D element

Basically, the composition method for a 2-D element is the same as for 1-D. However, since 2-D FE elements are not connected with other neighbour elements in the order as is the case for a 1-D element, each node number for each element has to be memorised in order to be used for composition.

According to [104], the kinetic energy of a single element can be calculated as

$$T_e = \frac{1}{2} \int_{A_e} \rho(x, y) h(x, y) (\dot{u}^2 + \dot{v}^2 + \dot{w}^2) dA$$

APPENDIX A FINITE ELEMENT MODELLING METHOD

$$= \frac{1}{2} \int_{-1}^1 \int_{-1}^1 \rho(\xi, \eta) h(\xi, \eta) (\dot{u}^2 + \dot{v}^2 + \dot{w}^2) J_x J_y d\xi d\eta. \quad (\text{A.15})$$

If eqs. (A.9) and (A.10) are considered, eq. (A.15) can be rewritten as

$$\begin{aligned} T_e &= \frac{1}{2} \dot{\mathbf{u}}_e^T J_x J_y \int_{-1}^1 \int_{-1}^1 \rho(\xi, \eta) h(\xi, \eta) \mathbf{H}_{\text{in}}^T \mathbf{H}_{\text{in}} d\xi d\eta \dot{\mathbf{u}}_e + \frac{1}{2} \dot{\mathbf{w}}_e^T J_x J_y \int_{-1}^1 \int_{-1}^1 \rho(\xi, \eta) h(\xi, \eta) \mathbf{H}_{\text{out}}^T \mathbf{H}_{\text{out}} d\xi d\eta \dot{\mathbf{w}}_e \\ &= \frac{1}{2} \dot{\mathbf{u}}_e^T \mathbf{m}_{\text{in}_e} \dot{\mathbf{u}}_e + \frac{1}{2} \dot{\mathbf{w}}_e^T \mathbf{m}_{\text{out}_e} \dot{\mathbf{w}}_e \\ &= \frac{1}{2} \dot{\mathbf{q}}_e^T \mathbf{m}_e \dot{\mathbf{q}}_e, \end{aligned} \quad (\text{A.16})$$

$$\text{where, } \dot{\mathbf{q}}_e = \begin{Bmatrix} \dot{\mathbf{u}}_e & \dot{\mathbf{w}}_e \end{Bmatrix}^T, \mathbf{m}_e = \begin{bmatrix} \mathbf{m}_{\text{in}_e} & \mathbf{0} \\ \mathbf{0} & \mathbf{m}_{\text{out}_e} \end{bmatrix}.$$

Furthermore, the potential energy of a single element can be defined as [110]

$$\begin{aligned} U_e &= \frac{1}{2} \int_{A_e} h(x, y) \boldsymbol{\varepsilon}^T \mathbf{D} \boldsymbol{\varepsilon} dA + \frac{1}{2} \int_{A_e} \frac{h^3(x, y)}{12} \boldsymbol{\chi}^T \mathbf{D} \boldsymbol{\chi} dA \\ &= \frac{1}{2} \int_{-1}^1 \int_{-1}^1 h(\xi, \eta) \boldsymbol{\varepsilon}^T \mathbf{D} \boldsymbol{\varepsilon} J_x J_y d\xi d\eta + \frac{1}{2} \int_{-1}^1 \int_{-1}^1 \frac{h^3(\xi, \eta)}{12} \boldsymbol{\chi}^T \mathbf{D} \boldsymbol{\chi} J_x J_y d\xi d\eta, \end{aligned} \quad (\text{A.17})$$

$$\text{where the matrix of material constants } \mathbf{D} = \begin{bmatrix} \frac{E}{1-\nu^2} & \frac{E\nu}{1-\nu^2} & 0 \\ \frac{E\nu}{1-\nu^2} & \frac{E}{1-\nu^2} & 0 \\ 0 & 0 & G = \frac{E}{2(1+\nu)} \end{bmatrix} \text{ for isotropic ma-}$$

terials, E is the Young's modulus, ν is the Poisson's ratio of the material,

$$\boldsymbol{\varepsilon} = \begin{bmatrix} \partial u / \partial x \\ \partial v / \partial y \\ \partial u / \partial y + \partial v / \partial x \end{bmatrix}, \text{ and } \boldsymbol{\chi} = \begin{bmatrix} \partial^2 w / \partial x^2 \\ \partial^2 w / \partial y^2 \\ 2 \partial^2 w / \partial x \partial y \end{bmatrix}.$$

Substituting eqs. (A.9) and (A.10) into eq. (A.17) gives

$$\begin{aligned}
 U_e &= \frac{1}{2} \mathbf{u}_e^T J_x J_y \int_{-1}^1 \int_{-1}^1 h(\xi, \eta) \mathbf{B}_{\text{in}}^T \mathbf{D} \mathbf{B}_{\text{in}} d\xi d\eta \mathbf{u}_e + \frac{1}{2} \mathbf{w}_e^T J_x J_y \int_{-1}^1 \int_{-1}^1 \frac{h^3(\xi, \eta)}{12} \mathbf{B}_{\text{out}}^T \mathbf{D} \mathbf{B}_{\text{out}} d\xi d\eta \mathbf{w}_e \\
 &= \frac{1}{2} \mathbf{u}_e^T \mathbf{k}_{\text{in}_e} \mathbf{u}_e + \frac{1}{2} \mathbf{w}_e^T \mathbf{k}_{\text{out}_e} \mathbf{w}_e \\
 &= \frac{1}{2} \mathbf{q}_e^T \mathbf{k}_e \mathbf{q}_e, \tag{A.18}
 \end{aligned}$$

$$\text{where } \mathbf{q}_e = \{\mathbf{u}_e \quad \mathbf{w}_e\}^T, \mathbf{k}_e = \begin{bmatrix} \mathbf{k}_{\text{in}_e} & \mathbf{0} \\ \mathbf{0} & \mathbf{k}_{\text{out}_e} \end{bmatrix}, \mathbf{B}_{\text{in}} = \begin{bmatrix} \frac{\partial}{\partial x} & 0 \\ 0 & \frac{\partial}{\partial y} \\ \frac{\partial}{\partial y} & \frac{\partial}{\partial x} \end{bmatrix} \mathbf{H}_{\text{in}} = \begin{bmatrix} \frac{1}{J_x} \frac{\partial}{\partial \xi} & 0 \\ 0 & \frac{1}{J_y} \frac{\partial}{\partial \eta} \\ \frac{1}{J_y} \frac{\partial}{\partial \eta} & \frac{1}{J_x} \frac{\partial}{\partial \xi} \end{bmatrix} \mathbf{H}_{\text{in}}(\xi, \eta)$$

$$\text{and } \mathbf{B}_{\text{out}} = \begin{bmatrix} \frac{\partial^2}{\partial x^2} \\ \frac{\partial^2}{\partial y^2} \\ \frac{\partial^2}{\partial x \partial y} \end{bmatrix} \mathbf{H}_{\text{out}} = \begin{bmatrix} \frac{1}{J_x^2} \frac{\partial^2}{\partial \xi^2} \\ \frac{1}{J_y^2} \frac{\partial^2}{\partial \eta^2} \\ \frac{2}{J_x J_y} \frac{\partial^2}{\partial \xi \partial \eta} \end{bmatrix} \mathbf{H}_{\text{out}}(\xi, \eta).$$

The Gauss integration formula is applied for the numerical integration in the ξ and η directions as in Appendix A.2. However, since the integration is done in both directions, the weight coefficients have to be multiplied by each other according to the integration points along the ξ and η directions. For example, if 9 integration points are used, the integration points and weight coefficients are decided by Table A.1 as shown in Figure A.7. With the integration point and weight coefficients in Figure A.7, eqs. (A.17) and (A.18) can be integrated, and local mass and stiffness matrices are obtained.

APPENDIX A FINITE ELEMENT MODELLING METHOD

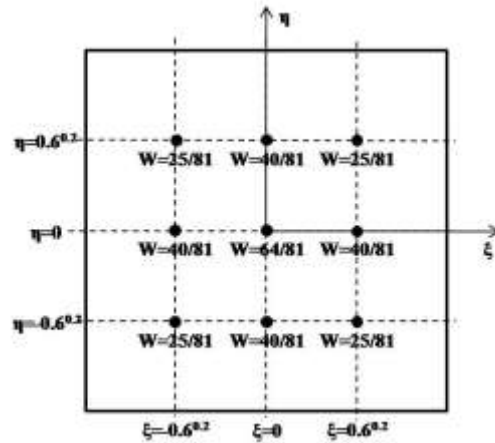


Figure A.7 Integration points and weight coefficients for 9-point Gauss integration for a 2-D element

The global mass and stiffness matrices for 2-D structures can be obtained by inserting these local mass and stiffness matrices in a position related to the nodal DOFs of each element as for 1-D structures in Figure A.4. Since 2-D elements are assembled in the x - and y -directions, an element of 2-D structures does not share nodes with other elements as a 1-D element does. Therefore, when arranging each component of the local matrices in a global matrix, they should be located in the correct positions by carefully considering related nodes.

APPENDIX B ANALYTICAL MODELS OF BEAMS

In this section, the exact solution, the natural frequencies and the mode shape of a Euler beam derived from the equation of motion will be discussed. Using this information, the analytical analyses using the transfer matrix method and the modal approach will be followed.

B.1 Exact solution of a Euler beam

When the forces and moments acting on a Euler beam element are considered, those can be described as shown in Figure B.1. V is the shear force, M is a bending moment, and $p(x)$ is a uniform distributed load acting on a unit length of the beam [111].

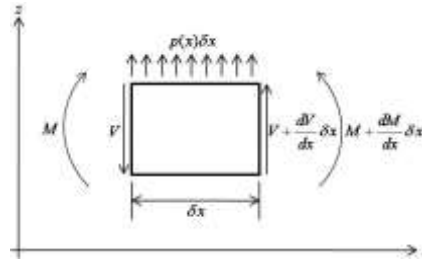


Figure B.1 Forces and moments acting on a Euler beam element

If the forces in the y -direction and the moments acting on the element are considered respectively, the summation of each component can be written as

$$V + \frac{dV}{dx} \delta x - V + p(x) \delta x = 0, \quad (\text{B.1})$$

$$V \frac{\delta x}{2} + V \frac{\delta x}{2} + \frac{dV}{dx} \delta x \frac{\delta x}{2} - M + M + \frac{dM}{dx} \delta x = 0. \quad (\text{B.2})$$

From eqs. (B.1) and (B.2), the relationship between the force and moment can be obtained as

$$\frac{dV}{dx} = -p(x), \quad (\text{B.3})$$

$$\frac{dM}{dx} = -V - \frac{1}{2} \frac{dV}{dx} (\delta x)^2 \approx -V. \quad (\text{B.4})$$

If the cross section of the beam is bent as shown in Figure B.2, the moment acting on the section can be expressed as

APPENDIX B ANALYTIC MODELS OF BEAMS

$$\begin{aligned}
 M &= b \int_{-h/2}^{h/2} \sigma z dz \\
 &= b \int_{-h/2}^{h/2} E z^2 \frac{\partial^2 w}{\partial x^2} dz \\
 &= EI \frac{\partial^2 w}{\partial x^2}.
 \end{aligned} \tag{B.5}$$

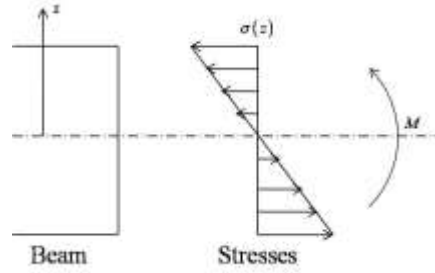


Figure B.2 Stress distribution in a bent beam

If the force equilibrium is considered in Figure B.1, the equation can be expressed by using eqs. (B.4) and (B.5) as

$$\rho A \delta x \frac{\partial^2 w}{\partial t^2} = V + \frac{dV}{dx} \delta x - V + p \delta x \rightarrow \rho A \frac{\partial^2 w}{\partial t^2} = -EI \frac{\partial^4 w}{\partial x^4} + p. \tag{B.6}$$

Therefore, the equation of motion for a Euler beam is written as

$$EI \frac{\partial^4 w}{\partial x^4} + \rho A \frac{\partial^2 w}{\partial t^2} = p. \tag{B.7}$$

Since the motion of the beam is time-harmonic, expressed as $w(x, t) = W(x) e^{i\omega t}$, eq. (B.7) can be rewritten as

$$EI \frac{\partial^4 W}{\partial x^4} - \rho A \omega^2 W = p \quad \rightarrow \quad \frac{\partial^4 W}{\partial x^4} - \beta^4 W = p, \tag{B.8}$$

$$\text{where } \beta^4 = \rho A \frac{\omega^2}{EI}.$$

From eq. (B.8), the equation of transverse displacement and natural frequencies of a beam which satisfies eq. (B.8) in the case of free vibration can be derived as

$$W = A \cosh \beta x + B \sinh \beta x + C \cos \beta x + D \sin \beta x = e^{\alpha x}, \quad (\text{B.9})$$

$$\omega_n = \beta_n^2 \sqrt{\frac{EI}{\rho A}} = (\beta_n l)^2 \sqrt{\frac{EI}{\rho A l^4}}, \quad (\text{B.10})$$

where $\alpha = \pm \beta$ and $\pm i\beta$, and l is the length of the beam.

B.2 Modal analysis of a Euler beam

By applying boundary conditions to eq. (B.9), the dispersion relationship can be obtained. Firstly, for free end there is no moment and shear force applied in a free vibration. Therefore, the boundary conditions of the free end can be expressed as

$$\left. \frac{\partial^2 W}{\partial x^2} \right|_{x=0 \text{ or } l} = 0, \quad \left. \frac{\partial^3 W}{\partial x^3} \right|_{x=0 \text{ or } l} = 0. \quad (\text{B.11})$$

Secondly, if the end tip is clamped, there is no deflection and strain. Therefore, the boundary conditions of a clamped end are like

$$W|_{x=0 \text{ or } l} = 0, \quad \left. \frac{\partial W}{\partial x} \right|_{x=0 \text{ or } l} = 0. \quad (\text{B.12})$$

Finally, when the beam end is simply supported, the end tip of the beam doesn't move but it is free for moments. Therefore, the boundary conditions of a simply supported end can be shown as

$$W|_{x=0 \text{ or } l} = 0, \quad (\text{B.13})$$

In the case of a cantilever beam, the boundary conditions for this model are the clamped-free conditions. With these conditions and eq. (B.9), the dispersive equation, natural frequencies and the modal function are derived as

$$\cosh \beta l \cos \beta l = -1, \quad (\text{B.14})$$

$$\omega_1 = (1.8755)^2 \sqrt{\frac{EI}{\rho A l^4}}, \quad \omega_2 = (4.6941)^2 \sqrt{\frac{EI}{\rho A l^4}}, \quad \omega_3 = (7.8548)^2 \sqrt{\frac{EI}{\rho A l^4}},$$

APPENDIX B ANALYTIC MODELS OF BEAMS

$$\omega_4 = (10.9955)^2 \sqrt{\frac{EI}{\rho Al^4}}, \quad \omega_5 = (14.1372)^2 \sqrt{\frac{EI}{\rho Al^4}}, \quad \omega_6 = (17.2787)^2 \sqrt{\frac{EI}{\rho Al^4}}, \quad (\text{B.15})$$

$$\begin{aligned} \phi(x) = & \cosh(\beta x) - \frac{\cosh(\beta l) + \cos(\beta l)}{\sinh(\beta l) + \sin(\beta l)} \sinh(\beta x) \\ & - \cosh(\beta x) + \frac{\cosh(\beta l) + \cos(\beta l)}{\sinh(\beta l) + \sin(\beta l)} \sinh(\beta x). \end{aligned} \quad (\text{B.16})$$

Using natural frequencies and modal function, the modal displacement can be obtained as [53]

$$W(x) = \sum_{n=1}^N \frac{\phi_n(x_{input}) \phi_n(x)}{M(\omega_n^2 - \omega^2)} f(x_{input}), \quad (\text{B.17})$$

where $\phi_n(x_{input})$ is the mode shape at the point of input power, $\phi_n(x)$ is the mode shape at the point of output displacement, M is the mass of the beam, ω_n refers to the natural frequencies of the beam, and ω is the input power frequency.

B.3 Transfer matrix method for analysis of a Euler beam

Also, by using another form of exact solution $W = Ae^{\beta x} + Be^{-\beta x} + Ce^{i\beta x} + De^{-i\beta x}$ and boundary conditions, the displacement of a beam can be estimated through the transfer matrix method expressed as

$$\begin{bmatrix} 1 & 1 & 1 & 1 \\ b & -b & ib & -ib \\ b^2 e^{bl} & b^2 e^{-bl} & -b^2 e^{ibl} & -b^2 e^{-ibl} \\ b^3 e^{bl} & -b^3 e^{-bl} & -ib^3 e^{ibl} & ib^3 e^{-ibl} \end{bmatrix} \begin{Bmatrix} A \\ B \\ C \\ D \end{Bmatrix} = \begin{Bmatrix} W|_{x=0} \\ q|_{x=0} \\ \frac{M|_{x=l}}{EI} \\ \frac{V|_{x=l}}{EI} \end{Bmatrix}. \quad (\text{B.18})$$

By multiplying the inverse matrix of the transfer matrix of the left side to eq. (B.18), the displacement coefficients at each end tip of the beam can be calculated. These displacement coefficients are the amplitudes of displacement for each wave component existing in the beam.

APPENDIX C BASIC STUDY OF ACTIVE CONTROL

In this section, a different controller will be designed for general cases considering the kinetic energy of the whole structure, the absorbed power by the controller and the stability of active control as optimising functions. Firstly, in order to study the effects of the control input signal, active control using a single degree of freedom (SDOF) system will be considered. Secondly, this study will be expanded to a 2 degrees of freedom (DOF) system, which is a slightly more complex system than an SDOF system and has potential possibilities for unstable control due to the increasing DOF.

C.1 Effect of active control on an SDOF system

When a control force $f_c = \alpha x + \beta \dot{x} + \gamma \ddot{x}$ is applied to an SDOF system, the equation for motion of the system is

$$m\ddot{x} + c\dot{x} + kx = f + f_c = f - (\alpha x + \beta \dot{x} + \gamma \ddot{x}) \quad (\text{C.1})$$

If harmonic motion is considered, $x(t) = Xe^{i\omega t}$ and $f(t) = Fe^{i\omega t}$, eq. (C.1) can be rewritten as

$$\left(-\omega^2(m + g) + i(kh + \omega b) + (k + a) \right) X = F. \quad (\text{C.2})$$

Eq. (C.2), the controlled equation of motion, normalised by mass, can be rewritten as

$$\frac{X}{X_0} = \frac{1}{\left(1 + a_n \right) - \frac{\omega^2}{\omega_n^2} \left(1 + g_n \right) + i \frac{\omega}{\omega_n} 2\zeta \left(1 + b_n \right)}, \quad (\text{C.3})$$

where X_0 is the uncontrolled displacement, ω denotes excitation frequency, ω_n the natural frequency, ζ is the damping ratio of the system, mass-normalised control gains $a_n = a/k$, $b_n = b/c$ and $g_n = \gamma/m$.

As shown in eq. (C.2), control force alters the effective dynamical properties of the global system; mass, damping and stiffness. Control gain of the displacement feedback, α , will have the effect of increasing the mass of the system, control gain of the velocity feedback, β , will affect the damping, and control gain of the acceleration feedback, γ , will have an influence on the

APPENDIX C BASIC STUDY OF ACTIVE CONTROL

stiffness. When an SDOF system is considered, the frequency responses of the system change as in Figure C.1.

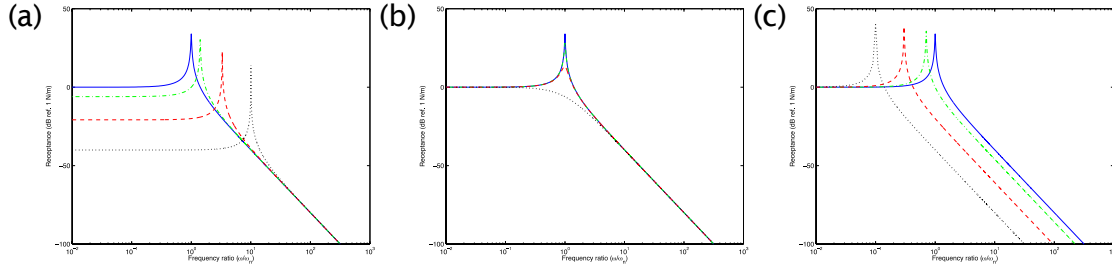


Figure C.1 Change of receptances of a system under control (a) Displacement control, (b) Velocity control and (c) Acceleration control; — No control; - - $\alpha, \beta, \gamma = 1$; - - $\alpha, \beta, \gamma = 10$; $\alpha, \beta, \gamma = 100$ [Label in x-axis: Frequency ratio (ω/ω_n), Label in y-axis: Receptance (dB ref. 1 N/m)]

As shown in Figure C.1 (a), the increase of α results in an increase in total stiffness of the system. Therefore, the natural frequency of the system increases, although changes are relatively minute due to the small ratio of the inherent stiffness of the structure and additional stiffness by displacement control. On the other hand, the increase of γ gives the same effect in terms of increasing the total mass of the system. As a result, the natural frequency of the system decreases. In contrast to the former two cases, β affects the damping, hence the peak value at the natural frequency. Since the natural frequency is determined by mass and stiffness, the increase in damping, i.e. the increase in β , reduces the motion of the system without the change in natural frequency. While the main objective of mass or stiffness change is to avoid the overlap in resonance frequency and exciting frequency, an increase in damping results in the reduction of modal peaks. Decreasing the frequency responses around resonance frequencies is the main objective of this research. Therefore, only the velocity feedback control of total damping for the system will be used later.

C.2 Optimisation of velocity feedback control

When a system is under velocity feedback active control, the dynamic motion of a system is reduced by control up to a certain level according to the increase in control gain. When control gain exceeds a certain threshold, undesirable results can be obtained and the dynamic motion of a system increases again with control gain. In fact, control force or moment gives a pinning effect to the system: that is the control force can constrain the motions of the structure [117].

As a result of this kind of undesirable control result, the kinetic energy of the whole system decreases and increases again after it reaches a minimum point. On the other hand, for the same

reason, the absorbed power by a controller keeps increasing until it shows a maximum level. After the maximum point, the absorbed power does not increase any more or even decrease. Therefore, control gains to minimise the kinetic energy or to maximise the absorbed power can be obtained [96].

For a system with sensors and actuators which are not collocated in terms of position, that is, not attached at the same point, a controller can also have an instability problem in feedback control in a general manner [118]. In order to guarantee a stable control result for a situation when unstable control is expected as is the case when there is a collocation issue, a control gain should be limited up to the point within the 3 dB control gain margin from a pole located at $(-1, 0)$ in a Nyquist plot for Cartesian complex coordinates. From this, control gain to guarantee the stability of active control with a 3 dB control gain margin can be obtained.

The effect of collocation between sensors and control actuators will be briefly studied in the next subsection with an example of a 2 DOF system.

C.2.1 Effect of collocation on active control for a 2 DOF system

If a 2 DOF system, which consists of connected-in-parallel masses m_1 and m_2 by dampers c_1 and c_2 , and two springs k_1 and k_2 as in Figure C.2, is considered, the equation of motion can be expressed as

$$\begin{bmatrix} m_1 & 0 \\ 0 & m_2 \end{bmatrix} \begin{Bmatrix} \ddot{x}_1 \\ \ddot{x}_2 \end{Bmatrix} + \begin{bmatrix} c_1 + c_2 & -c_2 \\ -c_2 & c_2 \end{bmatrix} \begin{Bmatrix} \dot{x}_1 \\ \dot{x}_2 \end{Bmatrix} + \begin{bmatrix} k_1 + k_2 & -k_2 \\ -k_2 & k_2 \end{bmatrix} \begin{Bmatrix} x_1 \\ x_2 \end{Bmatrix} = \begin{Bmatrix} f_1 \\ f_2 \end{Bmatrix} + \begin{Bmatrix} f_1^c \\ f_2^c \end{Bmatrix}, \quad (\text{C.4})$$

where x_1 and x_2 are the displacements at each mass, f_1 and f_2 the forces at each mass which can be considered to be exciting forces, and f_1^c and f_2^c the control forces at mass m_1 and m_2 respectively.

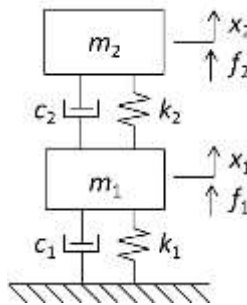


Figure C.2 General 2-DOF system

APPENDIX C BASIC STUDY OF ACTIVE CONTROL

There are four possible different simple velocity control feedback controls that can be considered. The normalised equation of motion for an SDOF system, eq. (C.3), can be expanded for a 2-DOF system considering four cases of velocity control as follows:

$$\begin{Bmatrix} f_1^c \\ f_2^c \end{Bmatrix} = - \begin{bmatrix} \beta \delta(i-1) & \beta \delta(i-2) \\ \beta \delta(i-3) & \beta \delta(i-4) \end{bmatrix} \begin{Bmatrix} \dot{x}_1 \\ \dot{x}_2 \end{Bmatrix},$$

where β is a control gain and $\delta(i-n)$ is the Dirac delta function where n denotes the Case numbers from 1 to 4.

In Cases 1 and 4, the control force is applied to the same mass where the error signal is measured. For Case 1, \dot{x}_1 is the error signal and f_c is applied to the mass m_1 only, i.e. f_1^c is applied to the system as a control force. For Case 4, the error signal \dot{x}_2 is measured at mass m_2 and f_c is also applied to the mass m_2 , i.e. f_2^c is applied to the system as a control force.

On the other hand, the control force is applied to a different mass where the error signal is measured in Cases 2 and 3. For Case 2, \dot{x}_2 is the error signal and $f_c (= f_1^c)$ is applied to the mass m_1 . For Case 3, the error signal \dot{x}_1 is measured at mass m_1 and $f_c (= f_2^c)$ is applied to the mass m_2 .

Therefore, mass-normalised equations of motion for each case can be expressed as

$$\begin{bmatrix} \frac{X_1}{X_{1_0}} \\ \frac{X_2}{X_{2_0}} \end{bmatrix} = \left(\begin{bmatrix} -\frac{W^2}{W_1^2} & 0 \\ 0 & -\frac{W^2}{W_2^2} \end{bmatrix} + i2 \begin{bmatrix} Z_1 \frac{W}{W_1} \left(1 + \frac{c_2}{c_1} + b_1 \delta(i-1) \right) & -Z_1 \frac{W}{W_1} \left(\frac{c_2}{c_1} - b_1 \delta(i-2) \right) \\ -Z_2 \frac{W}{W_2} \left(1 - b_2 \delta(i-3) \right) & Z_2 \frac{W}{W_2} \left(1 + b_2 \delta(i-4) \right) \end{bmatrix} + \begin{bmatrix} 1 + \frac{k_2}{k_1} & -\frac{k_2}{k_1} \\ -1 & 1 \end{bmatrix} \right)^{-1} \begin{Bmatrix} f_1 \\ f_2 \end{Bmatrix},$$

where normalised control gains by each damping $b_1 = \frac{b}{c_1}$ and $b_2 = \frac{b}{c_2}$, and i means a case number from 1 to 4. According to the case number, additional damping by control signal can be added to the system damping matrix.

APPENDIX C BASIC STUDY OF ACTIVE CONTROL

A single exciting force is assumed to be applied to mass m_2 , that is, $f_1 = 0$. Normalised displacements $\frac{X_1}{X_{1_0}}$ and $\frac{X_2}{X_{2_0}}$ are shown in Figures C.3, C.4, C.5 and C.6 as the velocity control gain β is changed.

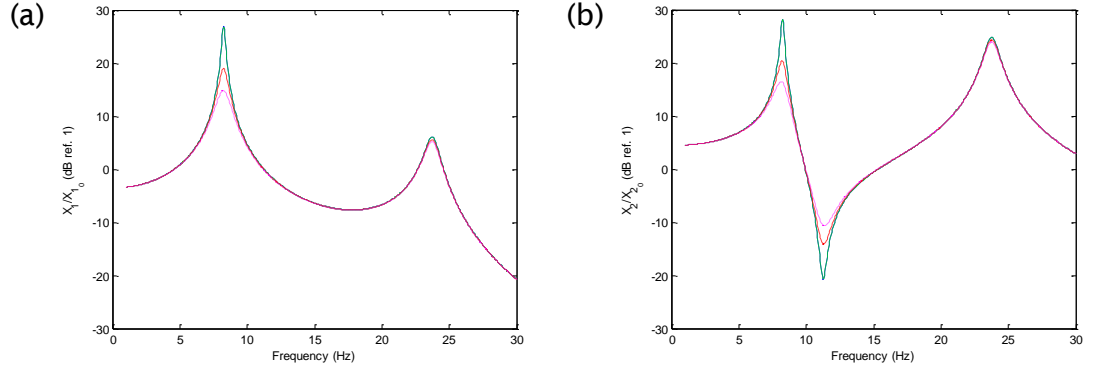


Figure C.3 (a) Normalised displacement at mass m_1 for Case 1 (b) Normalised displacement at mass m_2 for Case 1;

— No control; - - $\beta = 1$; - . $\beta = 150$; . . $\beta = 300$

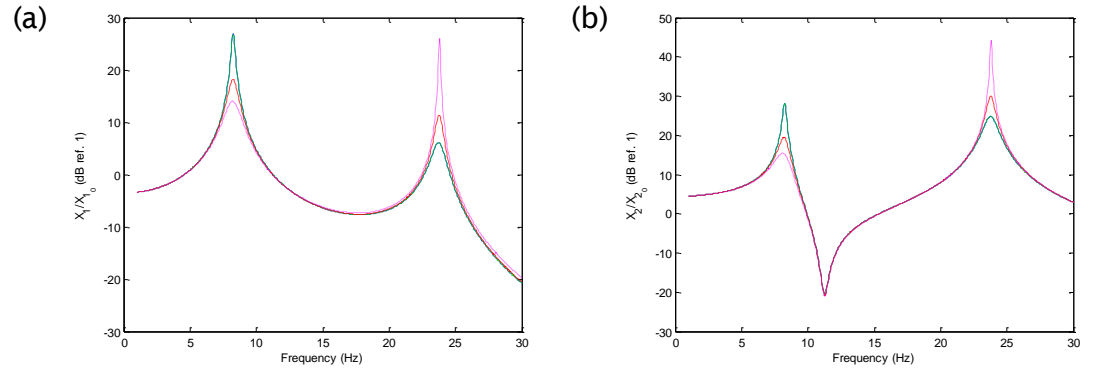


Figure C.4 (a) Normalised displacement at mass m_1 for Case 2 (b) Normalised displacement at mass m_2 for Case 2;

— No control; - - $\beta = 1$; - . $\beta = 150$; . . $\beta = 300$

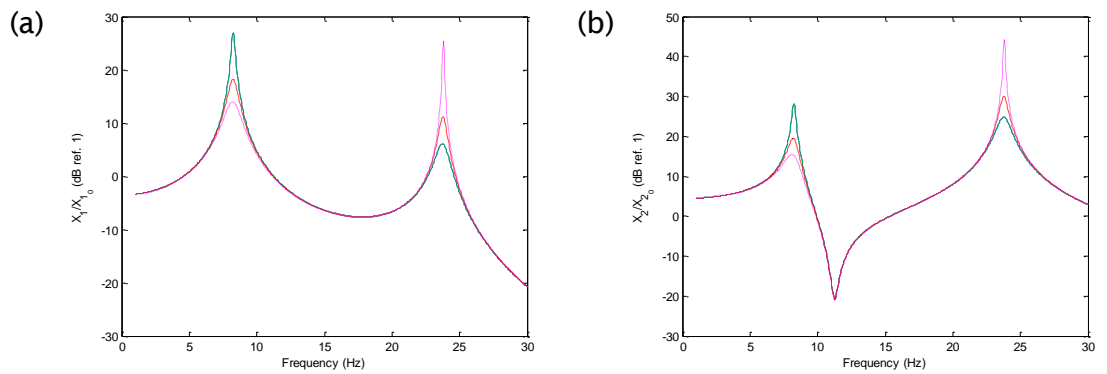


Figure C.5 (a) Normalised displacement at mass m_1 for Case 3 (b) Normalised displacement at mass m_2 for Case 3;

— No control; - - $\beta = 1$; - . $\beta = 150$; . . $\beta = 300$

APPENDIX C BASIC STUDY OF ACTIVE CONTROL

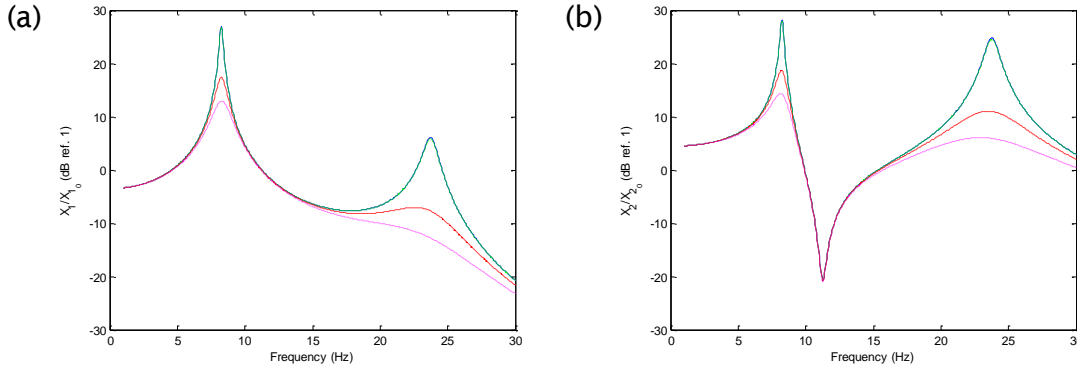


Figure C.6 (a) Normalised displacement at mass m_1 for Case 4 (b) Normalised displacement at mass m_2 for Case 4;

— No control; — $\beta = 1$; — $\beta = 150$; — $\beta = 300$

In Case 4 (Figure C.6), since the primary force is applied to the mass m_2 , the disturbance, the control force and the error signal are all collocated. As a result of perfect collocation, the best control results for all cases are obtained for both of mass m_1 and m_2 . On the other hand, although the same error signal is used for control in Case 2, increased responses at the second mode are shown due to the control force being applied to the mass m_1 , which is not collocated. Similar results as those in Case 2 are obtained in Case 3. Finally, in Case 1, the effect of control is mainly dominant for the 1st mode rather than the 2nd mode as shown by Figure C.3. When considering that two masses are moving in phase at the 1st mode and moving out of phase at the 2nd mode in a 2 DOF system, only the motion at the 1st mode is controlled in Case 1 because the control force is applied to the motion of the mass m_1 which is induced by the mutual reaction between masses m_1 and m_2 . At the 1st mode, since motions of the masses m_1 and m_2 are in phase, control effect in the motion of mass m_1 can affect the overall motion of the system. However, since two motions are out of phase at the 2nd mode, the control force cannot control the motion of mass m_2 , the primary source of the whole system. Therefore, the importance of collocation in active control is confirmed in this study.

C.2.2 Effect of collocation on active control of a beam

A cantilever beam is taken into account to see the effect of collocation and spill-over on multi-degrees of freedom systems. When a cantilever beam is considered, each case as explained in Figure C.7 can be obtained, if we consider one control force f_c , one error signal and one controller with control gain β (see figure C.7).

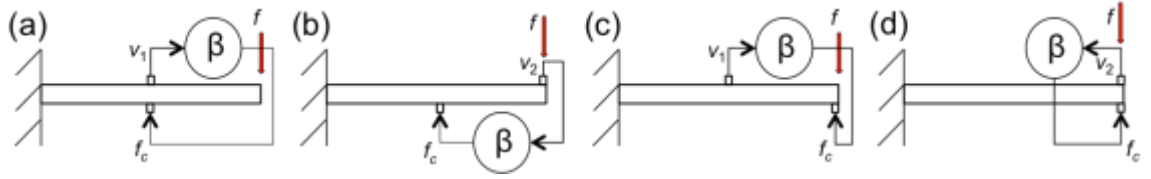


Figure C.7 Control case for 4-element FE cantilever beam mode (a) Case 1 (Collocated), (b) Case 2 (Non-collocated), (c) Case 3 (Non-collocated) and (d) Case 4 (Collocated)

Modified transfer functions between a primary exciting force f and velocities measured at the centre v_1 and tip v_2 can be expressed as follows:

$$\text{Case 1: } v_1 = \frac{H_{12}}{1 + \beta H_{11}} f \quad \text{and} \quad v_2 = \frac{H_{22} + \beta(H_{11}H_{22} - H_{12}H_{21})}{1 + \beta H_{11}} f$$

$$\text{Case 2: } v_1 = \frac{H_{12} + \beta(H_{12}H_{21} - H_{11}H_{22})}{1 + \beta H_{21}} f \quad \text{and} \quad v_2 = \frac{H_{22}}{1 + \beta H_{21}} f$$

$$\text{Case 3: } v_1 = \frac{H_{12}}{1 + \beta H_{12}} f \quad \text{and} \quad v_2 = \frac{H_{22}}{1 + \beta H_{12}} f$$

$$\text{Case 4: } v_1 = \frac{H_{12}}{1 + \beta H_{22}} f \quad \text{and} \quad v_2 = \frac{H_{22}}{1 + \beta H_{22}} f, \quad (\text{C.5})$$

where H_{ij} refers to the transfer functions between i and j (1 denotes the centre and 2 refers to the tip), v_i is velocities measured at the point i and f denotes the primary exciting force applied to the tip of the cantilever beam. Control force f_c is determined by velocity feedback as $f_c = -\beta v_i$.

Changes in velocities with control gain are shown in Figures C.8, C.9, C.10 and C.11. As shown in Figure C.11 (b), the most efficient control results are obtained with the collocated case of the exciting force, the error signal and the control force. On the other hand, because of instability issues, increased control results with large control gain may be unrealistic. Changes of resonant peaks are seen when control gain becomes very large. In these cases, control force gives a ‘pinning effect’ to a system, which refers to the point at which the applied control force is pinned. As a result, equivalent stiffness increases and resonance frequencies change. However, the effect of the control force is different for every mode according to the point of control force application and the error signal. A pinning effect does not happen at some peaks even when it happens at other peaks in some cases. For example, a change in peaks in FRF can be found as shown by the red dashed circle in Figure C.11 (a). On the other hand, controllable modes are limited for the other cases.

APPENDIX C BASIC STUDY OF ACTIVE CONTROL

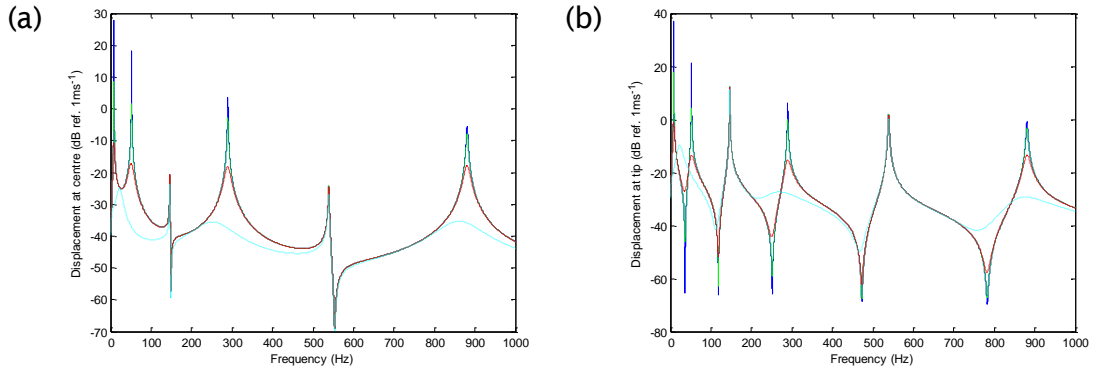


Figure C.8 (a) Displacement at the centre for Case 1 (b) Displacement at the tip for Case 1; — No control; - - $\beta = 1$; — $\beta = 10$; - - $\beta = 100$

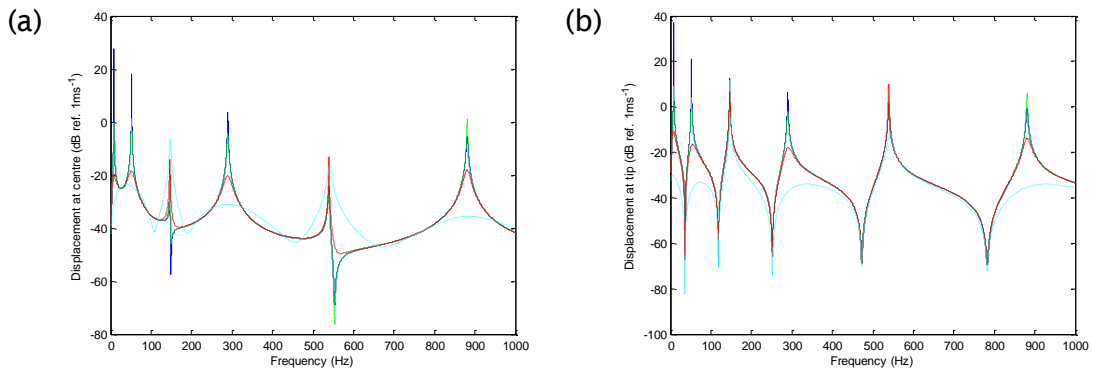


Figure C.9 (a) Displacement at the centre for Case 2 (b) Displacement at the tip for Case 2; — No control; - - $\beta = 1$; — $\beta = 10$; - - $\beta = 100$

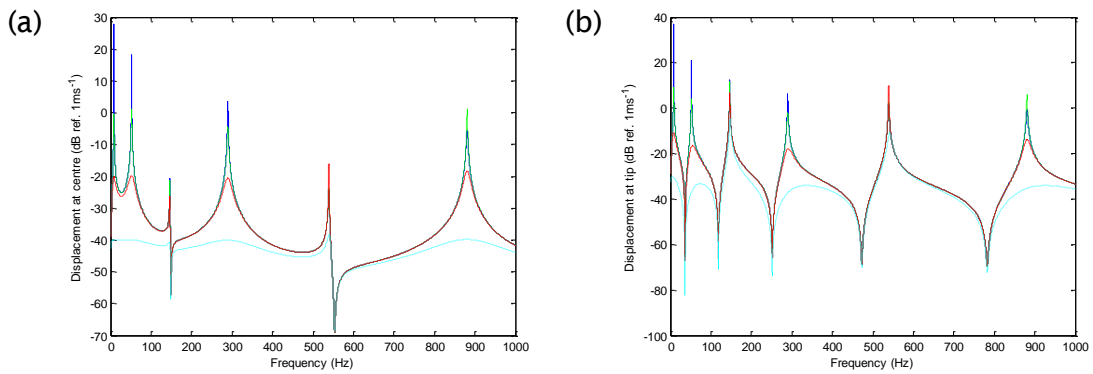


Figure C.10 (a) Displacement at the centre for Case 3 (b) Displacement at the tip for Case 3; — No control; - - $\beta = 1$; — $\beta = 10$; - - $\beta = 100$

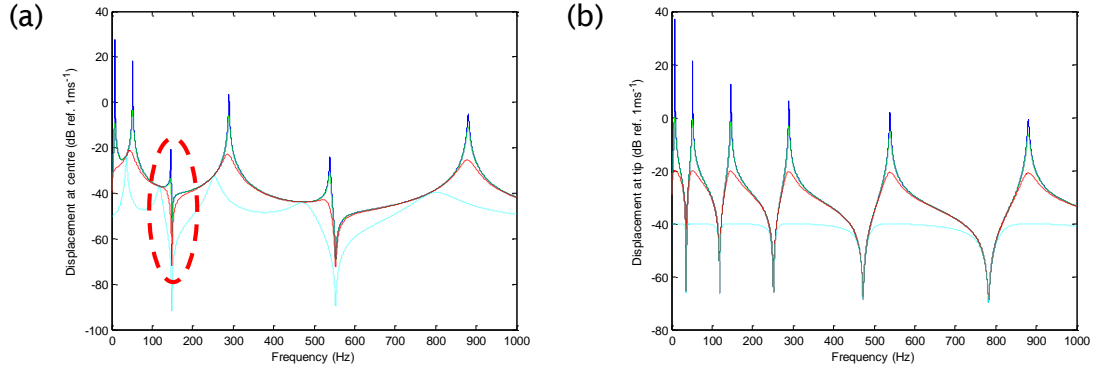


Figure C.11 (a) Displacement at the centre for Case 4 (b) Displacement at the tip for Case 4; — No control; - - $\beta = 1$; — $\beta = 10$; - - $\beta = 100$

In this section, theory related to active control with a single actuator applied to simple structures has been explained. As mentioned above, collocation has an effect also on the stability threshold. Moreover, even with stable control, the pinning effect can happen when too large a control gain is in use. In conclusion, control gain should be optimised in the aspect of efficiency to avoid the pinning effect. In the next section, a method to determine an optimised control gain considering these factors will be discussed.

C.2.3 Determination of optimal control gains

Following the previous section, the determination of an optimised control gain will be explained in this section. Stability limit for control gain will constitute a boundary to optimisation. If the stability of control is guaranteed, the kinetic energy of the whole system or the absorbed power by the controller may be considered. Due to the pinning effect explained in the previous section, although the motion at the point where an actuator is installed can be controlled completely by active control, motions in other parts can increase due to the excitation by the actuator when large control forces are applied. Instead, the absorbed power by control reduces to a minimum until the point when the pinning effect happens and increases by induced motion in other parts of the structure after the pinning effect. A detailed explanation will follow below. For the simulation, the control cases and the FEM model of the previous section are used.

Firstly, the limit of control gain for a 3 dB gain margin will be studied. Nyquist plots for $\beta=1$ for the open loop referred to in eq. (C.5) will be considered. The systems for Figure C.7 are considered. Modified transfer functions for each case are the same as in eq. (C.5).

APPENDIX C BASIC STUDY OF ACTIVE CONTROL

Therefore, the open loops for a controller, which are the transfer functions between error and velocity due to the control force, are given as eq. (C.6). Their Nyquist plots are given in Figure C.12.

Case 1: βH_{11} , Case 2: βH_{21} , Case 3: βH_{12} and Case 4: βH_{22} . (C.6)

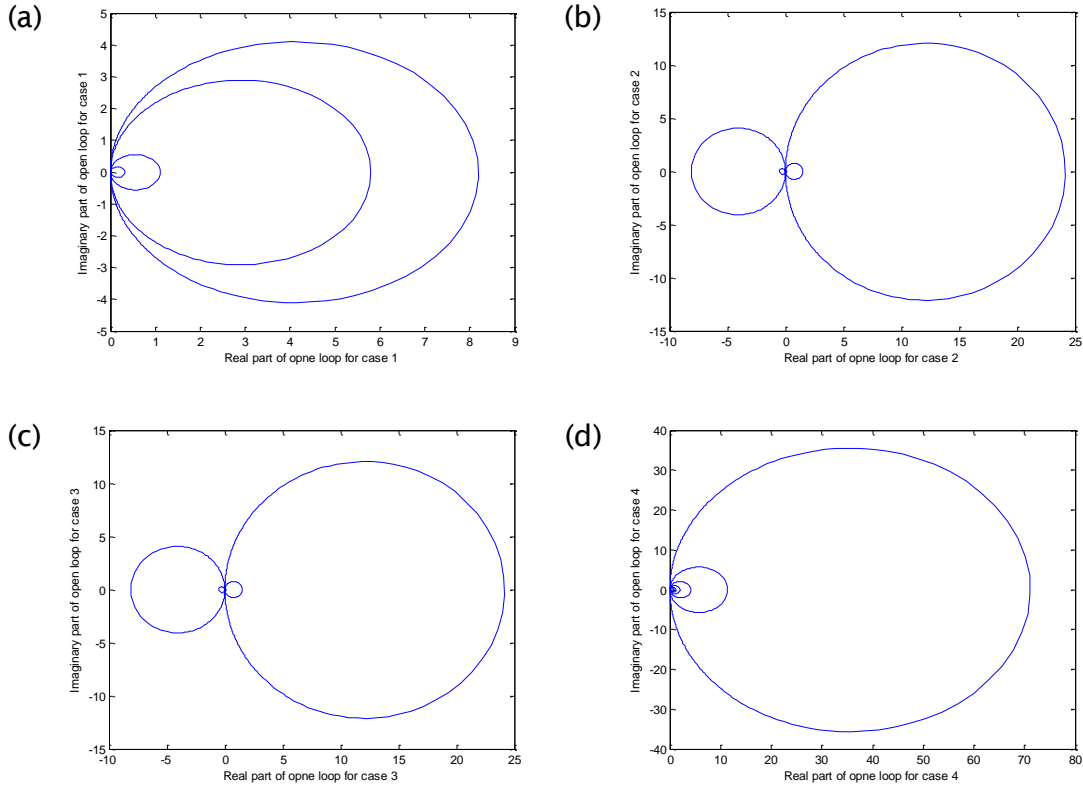


Figure C.12 Nyquist plots for an open loop for (a) Case 1, (b) Case 2, (c) Case 3 and (d) Case 4 with $\beta=1$ up to 1 kHz

From Figure C.12 (a) and (d), controls in Cases 1 and 4 are unconditionally stable in the frequency range considered. The stability for Cases 2 and 3 are, instead, conditionally guaranteed.

In order to avoid instability of control in the whole frequency range of interest for a 3 dB gain margin in Cases 2 and 3, control gain β should be limited to below 0.061. This can mean that in non-collocated control cases such as Cases 2 and 3, control is ineffective and limited to a low control gain because of stability issues. Control results for Cases 2 and 3 are obtained as shown in Figures C.13 and C.14.

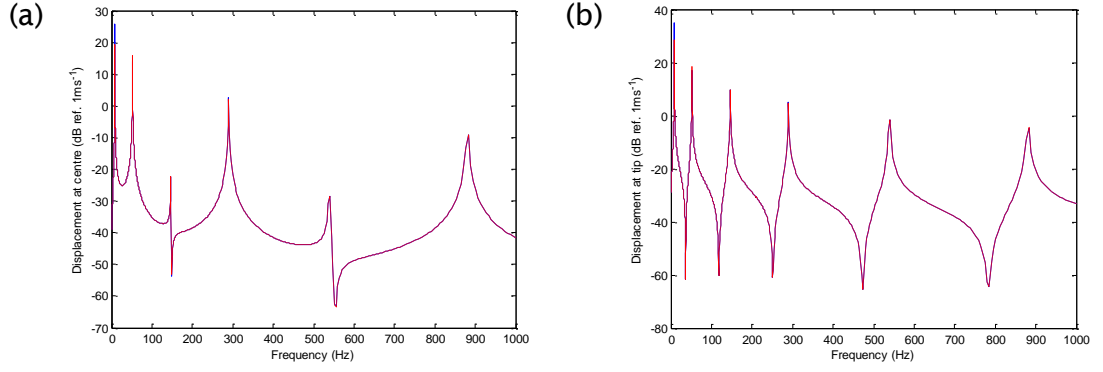


Figure C.13 (a) Displacement at the centre for Case 2 (b) Displacement at the tip for Case 2; — No control; — Control

$$\beta_{3dB} = 0.061$$

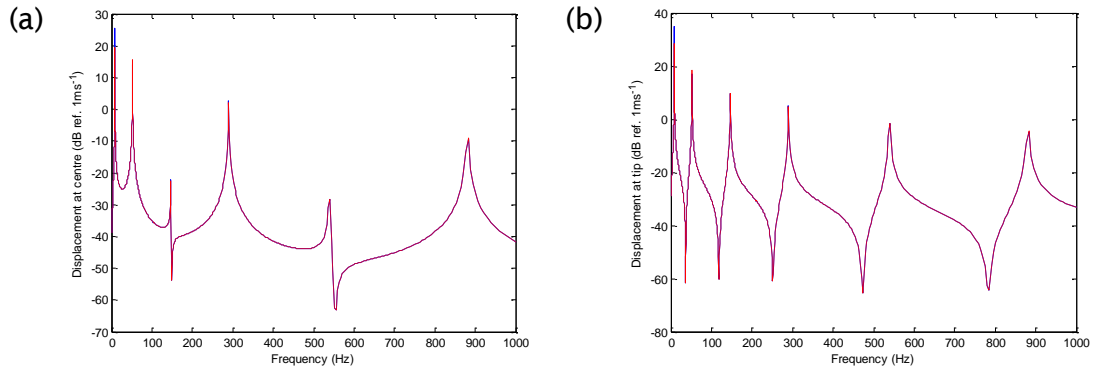


Figure C.14 (a) Displacement at the centre for Case 3 (b) Displacement at the tip for Case 3; — No control; — Control

$$\beta_{3dB} = 0.061$$

On the other hand, for collocated cases, stable control is guaranteed as shown by Figure C.12 (a) and (d), where circles of the open-loop of a controller are located only in the positive real domain, and an infinite control gain could be used. However, due to the pinning effect, it is actually better for the control gains to be limited. For this optimisation, the kinetic energy of the whole system or the absorbed power by an actuator could be considered as a cost function.

The power spectral density of kinetic energy using velocities at each node is calculated as

$$S_k(\omega) = \frac{M}{2R} \sum_{r=1}^R \left| \tilde{v}_r(\omega) \right|^2, \quad (C.7)$$

where M is the mass of the whole structure, R is the number of measuring points and $\left| \tilde{v}_r(\omega) \right|$ is the mean square value of the velocity measured by the r -th accelerometer.

The power spectral density of absorbed power by the control actuator is expressed as

APPENDIX C BASIC STUDY OF ACTIVE CONTROL

$$S_p(\omega) = \frac{1}{2} \beta \left| \tilde{v}_c(\omega) \right|^2, \quad (\text{C.8})$$

where β is the control gain and $\left| \tilde{v}_c(\omega) \right|$ denotes the mean square value of the control velocity.

Figure C.15 shows the variation of the power spectrum densities of kinetic energy and absorbed power for collocated control. These plots can be used to find control gains which can minimise the kinetic energy of a whole structure or maximise the absorbed power by an actuator. By using eqs. (C.7) and (5.8), the following figures and control gains are obtained for Cases 1 and 4 respectively as shown in Figure C.15 and Table C.1.

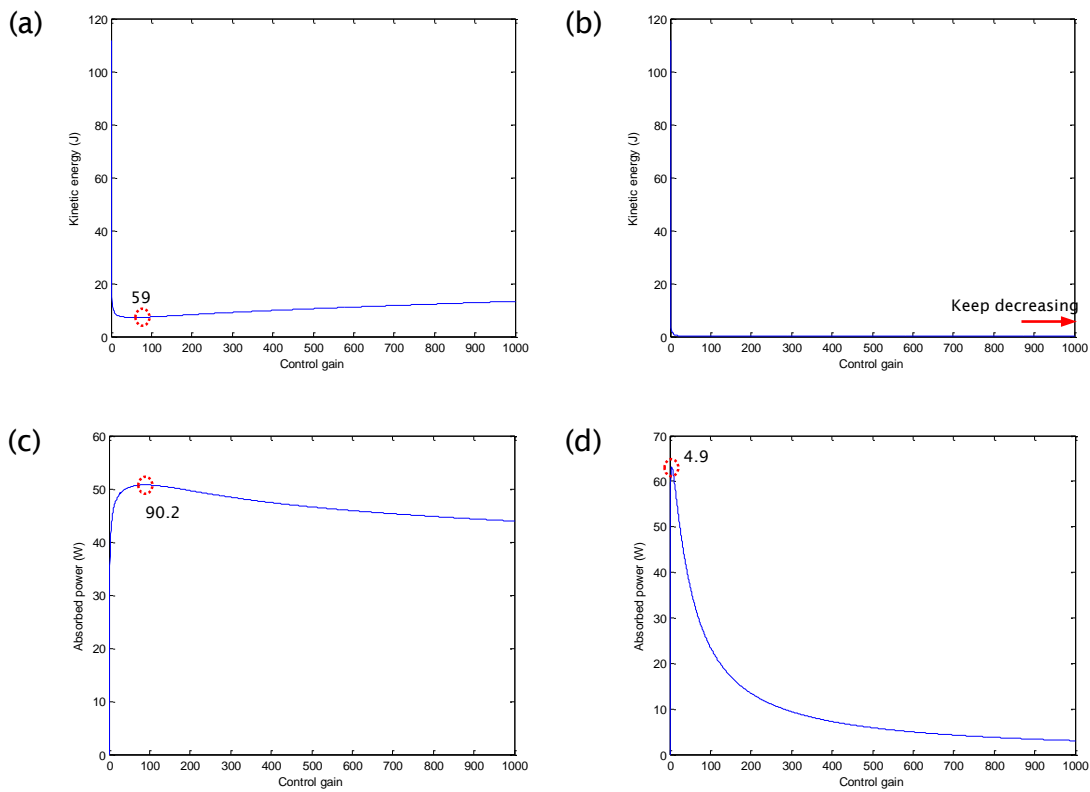


Figure C.15 Changes in kinetic energy of the whole structure for (a) Case 1 and (b) Case 4, and changes of absorbed power by an actuator for (c) Case 1 and (d) Case 4

Table C.1 Optimised control gains for collocated cases

	$b_{\min.\text{KE}}$	$b_{\max.\text{AP}}$
Case 1	59	90.2
Case 4	∞	4.9

From Figure C.15, the results were obtained as in Table C.1, where $b_{\min.\text{KE}}$ is the control gain to minimise the kinetic energy of a whole structure and $b_{\max.\text{AP}}$ denotes the control gain to maximise the absorbed power by an actuator.

For Case 4, the kinetic energy of a whole structure can be reduced to zero because of the pinning effect. Therefore, since $b_{\max.\text{AP}}$ can give the maximum power absorption of motion structure even with a small control gain, it would be efficient to use $b_{\max.\text{AP}}$ instead of $b_{\min.\text{KE}}$ which can give only approximately 85 % reduced power absorption with infinite control gain from the maximum power absorption of 63 W with $b_{\max.\text{AP}}$ as shown in Figure C.15.

For Case 1, while the difference in absorbed power between with $b_{\max.\text{AP}}$ and $b_{\min.\text{KE}}$ is only 0.25W, $b_{\min.\text{KE}}$ can minimise the motion of the whole structure with a smaller control gain than $b_{\max.\text{AP}}$, avoiding the pinning effect. This means that larger control gains than $b_{\min.\text{KE}}$ will cause the motions of other parts to increase due to the pinning effect. Therefore, $b_{\min.\text{KE}}$ could give a good enough and efficient enough control result compared with $b_{\max.\text{AP}}$.

Control results for Cases 1 and 4 are shown in Figures C.16 and C.17. When reductions at each peak are compared with each other case, the difference in the minimum kinetic energy shown in Figure C.15 (a) and (b) can be understood considering some peaks in Case 1 which remained uncontrolled. Therefore, when the stability and the efficiency of control are considered simultaneously, the collocation between an error signal, the control force and the disturbance is important for stable and efficient control in the broad band of frequency.

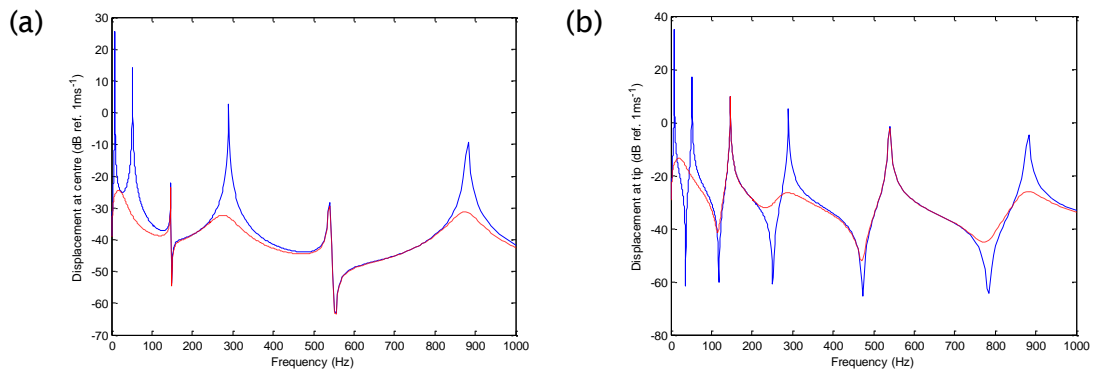


Figure C.16 (a) Displacement at the centre for Case 1 (b) Displacement at the tip for Case 1; — No control; — Control

$$\beta_{\max.\text{AP}} = 59$$

APPENDIX C BASIC STUDY OF ACTIVE CONTROL

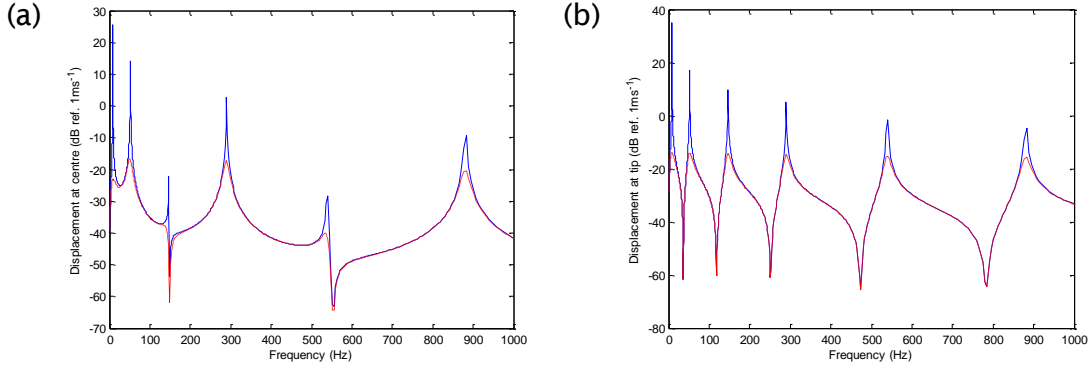


Figure C.17 (a) Displacement at the centre for Case 4 (b) Displacement at the tip for Case 4; — No control; - - with control

$$\beta_{\min. KE} = 4.9$$

In this section, the control gain determination process considering stability and efficiency with the Nyquist plot for an open loop, the kinetic energy of a whole structure and the absorbed power by an actuator is discussed. The collocation between an error signal and a control force is the most important for the stability of control. Moreover, for more efficient control results, it is recommended that an error signal and a primary exciting force are collocated.

C.2.4 Phase plots for Figure 5.13, 5.14, 5.15 and 5.16

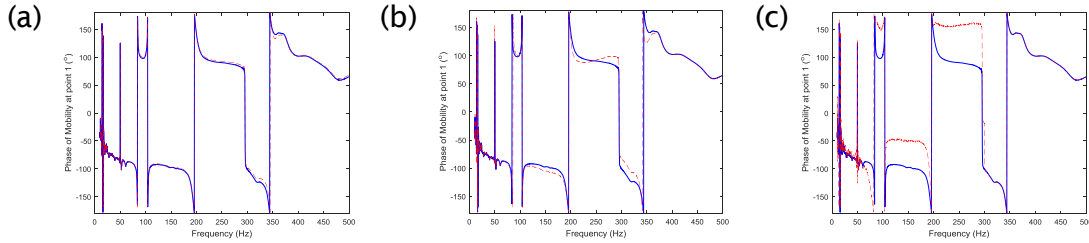


Figure C.18 Phases for APCLD treatment on a beam with (a) No filter ($G_{3dB} = 24.58$), (b) a KEMO low-pass filter ($G_{3dB} = 167.61$) and (c) a proposed ideal filter ($G_{3dB} = 1240$); — No control; - - with control

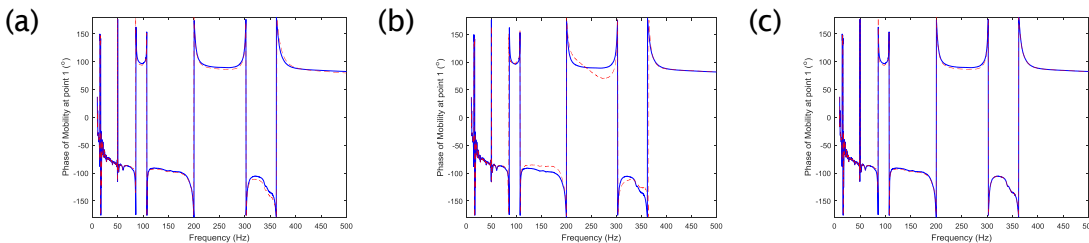


Figure C.19 Phases for AC/PCLD treatment on a beam with (a) No filter ($G_{3dB} = 8.42$), (b) a KEMO low-pass filter ($G_{3dB} = 61.79$) and (c) a proposed ideal filter ($G_{3dB} = 8.42$); — No control; - - with control

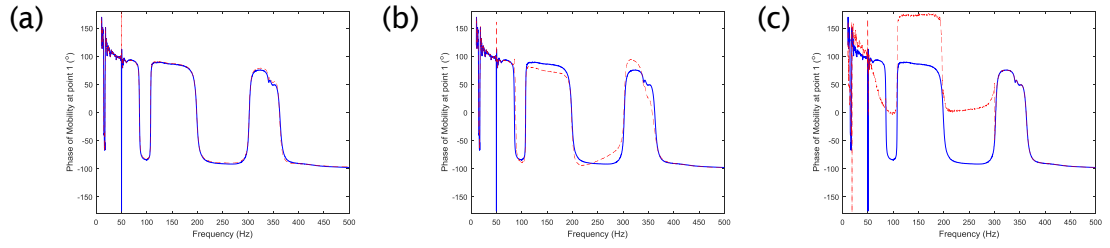


Figure C.20 Phases results for AC/PSOLD treatment on a beam with (a) No filter ($G_{3dB} = 4.79$), (b) a KEMO low-pass filter ($G_{3dB} = 69.77$) and (c) a proposed ideal filter ($G_{3dB} = 1302$); — No control; - - with control

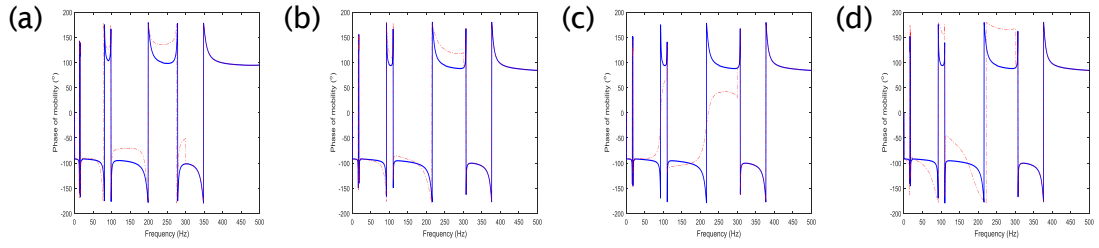


Figure C.21 Phase simulation results with a proposed ideal filter and G_{3dB} for (a) ACLD, (b) APCLD, (c) AC/PCLD and (d) AC/PSOLD treatments

APPENDIX D EQUATIONS OF MOTION FOR PLATES WITH HAPCLD TREATMENTS

In this appendix, equations for motion of plates with APCLD, AC/PCLD and AC/PSOLD treatments are presented. For equations for ACLD treatment, please refer to Section 6.5.

D.1 APCLD treatment

The configuration of a plate with APCLD treatment is shown in Figure D.1.

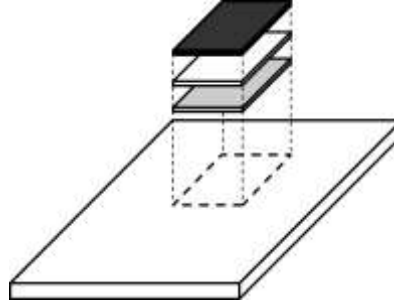





Figure D.1 Configuration of a plate with APCLD treatment;  : elastic plate,  : viscoelastic layer and  : piezoelectric patch

Equations for the piezoelectric plate are given by

$$\begin{bmatrix} \mathbf{m}_{in_p} & \mathbf{0} & \mathbf{0} & \mathbf{0} \\ \mathbf{0} & \mathbf{m}_{out_p} & \mathbf{0} & \mathbf{0} \\ \mathbf{0} & \mathbf{0} & \mathbf{0} & \mathbf{0} \\ \mathbf{0} & \mathbf{0} & \mathbf{0} & \mathbf{0} \end{bmatrix} \ddot{\mathbf{q}}_p + \begin{bmatrix} \mathbf{k}_{in_p} & \mathbf{0} & \mathbf{0} & \mathbf{k}_{u\phi} \\ \mathbf{0} & \mathbf{k}_{out_p} & \mathbf{0} & \mathbf{0} \\ \mathbf{0} & \mathbf{0} & \mathbf{0} & \mathbf{0} \\ \mathbf{k}_{\phi u} & \mathbf{0} & \mathbf{0} & -k_{\phi\phi} \end{bmatrix} \mathbf{q}_p = \mathbf{M}_p \ddot{\mathbf{q}}_p + \mathbf{K}_p \mathbf{q}_p = \mathbf{f}_p,$$

$$\text{where } \mathbf{q}_p = \left\{ \mathbf{u}_p \quad \mathbf{w}_p \quad \frac{\partial \mathbf{u}_p}{\partial z} \quad \phi_p \right\}^T, \quad \mathbf{u}_p = \left\{ u_{p_1} \quad v_{p_1} \quad \cdots \quad u_{p_{n+1}} \quad v_{p_{n+1}} \right\},$$

$$\mathbf{w}_p = \left\{ w_{p_1} \quad \theta_{xp_1} \quad \theta_{yp_1} \quad w_{xyp_1} \quad \cdots \quad w_{p_{n+1}} \quad \theta_{xp_{n+1}} \quad \theta_{yp_{n+1}} \quad w_{xyp_{n+1}} \right\},$$

$$\frac{\partial \mathbf{u}_p}{\partial z} = \left\{ \frac{\partial u_{p_1}}{\partial z} \quad \frac{\partial v_{p_1}}{\partial z} \quad \cdots \quad \frac{\partial u_{p_{n+1}}}{\partial z} \quad \frac{\partial v_{p_{n+1}}}{\partial z} \right\} \text{ and}$$

APPENDIX D EQUATIONS OF MOTION FOR PLATES WITH HYBRID ACTIVE-PASSIVE
CONSTRAINED LAYER DAMPING TREATMENTS

$$\mathbf{f}_p = \left\{ \mathbf{f}_{in_p} \quad \mathbf{f}_{out_p} \quad \mathbf{f}_{s_p} \quad Q_p \right\}^T, \quad \mathbf{f}_{in_p} = \left\{ f_{x_p 1} \quad f_{y_p 1} \quad \cdots \quad f_{x_p(n+1)} \quad f_{y_p(n+1)} \right\},$$

$$\mathbf{f}_{out_p} = \left\{ f_{z_p 1} \quad M_{x_p 1} \quad M_{y_p 1} \quad M_{xy_p 1} \quad \cdots \quad f_{z_p(n+1)} \quad M_{x_p(n+1)} \quad M_{y_p(n+1)} \quad M_{xy_p(n+1)} \right\},$$

$$\mathbf{f}_{s_p} = \left\{ f_{s_{xp} 1} \quad f_{s_{yp} 1} \quad \cdots \quad f_{s_{xp}(n+1)} \quad f_{s_{yp}(n+1)} \right\},$$

where each term is the same as those used in eq. (5.21).

Equations for the constraining layer (elastic plate) are given by

$$\begin{bmatrix} \mathbf{m}_{in_c} & \mathbf{0} & \mathbf{0} & \mathbf{0} \\ \mathbf{0} & \mathbf{m}_{out_c} & \mathbf{0} & \mathbf{0} \\ \mathbf{0} & \mathbf{0} & \mathbf{0} & \mathbf{0} \\ \mathbf{0} & \mathbf{0} & \mathbf{0} & \mathbf{0} \end{bmatrix} \ddot{\mathbf{q}}_c + \begin{bmatrix} \mathbf{k}_{in_c} & \mathbf{0} & \mathbf{0} & \mathbf{0} \\ \mathbf{0} & \mathbf{k}_{out_c} & \mathbf{0} & \mathbf{0} \\ \mathbf{0} & \mathbf{0} & \mathbf{0} & \mathbf{0} \\ \mathbf{0} & \mathbf{0} & \mathbf{0} & \mathbf{0} \end{bmatrix} \mathbf{q}_c = \mathbf{M}_c \ddot{\mathbf{q}}_c + \mathbf{K}_c \mathbf{q}_c = \mathbf{f}_c,$$

$$\text{where } \mathbf{q}_c = \left\{ \mathbf{u}_c \quad \mathbf{w}_c \quad \frac{\partial \mathbf{u}_c}{\partial z} \quad f_c \right\}^T, \quad \mathbf{u}_c = \left\{ u_{c_1} \quad v_{c_1} \quad \cdots \quad u_{c_{n+1}} \quad v_{c_{n+1}} \right\},$$

$$\mathbf{w}_c = \left\{ w_{c_1} \quad \theta_{xc_1} \quad \theta_{yc_1} \quad w_{xy_{c_1}} \quad \cdots \quad w_{c_{n+1}} \quad \theta_{xc_{n+1}} \quad \theta_{yc_{n+1}} \quad w_{xy_{c_{n+1}}} \right\},$$

$$\frac{\partial \mathbf{u}_c}{\partial z} = \left\{ \frac{\partial u_{c_1}}{\partial z} \quad \frac{\partial v_{c_1}}{\partial z} \quad \cdots \quad \frac{\partial u_{c_{n+1}}}{\partial z} \quad \frac{\partial v_{c_{n+1}}}{\partial z} \right\} \text{ and}$$

$$\mathbf{f}_c = \left\{ \mathbf{f}_{in_c} \quad \mathbf{f}_{out_c} \quad \mathbf{f}_{s_c} \quad Q_c \right\}^T, \quad \mathbf{f}_{in_c} = \left\{ f_{x_c 1} \quad f_{y_c 1} \quad \cdots \quad f_{x_c(n+1)} \quad f_{y_c(n+1)} \right\},$$

$$\mathbf{f}_{out_c} = \left\{ f_{z_c 1} \quad M_{x_c 1} \quad M_{y_c 1} \quad M_{xy_c 1} \quad \cdots \quad f_{z_c(n+1)} \quad M_{x_c(n+1)} \quad M_{y_c(n+1)} \quad M_{xy_c(n+1)} \right\},$$

$$\mathbf{f}_{s_c} = \left\{ f_{s_{xc} 1} \quad f_{s_{yc} 1} \quad \cdots \quad f_{s_{xc}(n+1)} \quad f_{s_{yc}(n+1)} \right\},$$

where each term is the same as those used in eqs. (A.16) and (A.18).

APPENDIX D EQUATIONS OF MOTION FOR PLATES WITH HYBRID ACTIVE-PASSIVE CONSTRAINED LAYER DAMPING TREATMENTS

Equations for the viscoelastic material are given by

$$\begin{bmatrix} \mathbf{m}_{\text{in}_v} & \mathbf{0} & \mathbf{0} & \mathbf{0} \\ \mathbf{0} & \mathbf{m}_{\text{out}_v} & \mathbf{0} & \mathbf{0} \\ \mathbf{0} & \mathbf{0} & \mathbf{0} & \mathbf{0} \\ \mathbf{0} & \mathbf{0} & \mathbf{0} & \mathbf{0} \end{bmatrix} \ddot{\mathbf{q}}_v + \begin{bmatrix} \mathbf{0} & \mathbf{0} & \mathbf{0} & \mathbf{0} \\ \mathbf{0} & \mathbf{0} & \mathbf{0} & \mathbf{0} \\ \mathbf{0} & \mathbf{0} & \mathbf{k}_{\text{Gu}} & \mathbf{0} \\ \mathbf{0} & \mathbf{0} & \mathbf{0} & \mathbf{0} \end{bmatrix} \mathbf{q}_v = \mathbf{M}_v \ddot{\mathbf{q}}_v + \mathbf{K}_v \mathbf{q}_v = \mathbf{f}_v,$$

$$\text{where } \mathbf{q}_v = \left\{ \mathbf{u}_v \quad \mathbf{w}_v \quad \frac{\partial \mathbf{u}_v}{\partial z} \quad f_v \right\}^T, \quad \mathbf{u}_v = \left\{ u_{v_1} \quad v_{v_1} \quad \cdots \quad u_{v_{n+1}} \quad v_{v_{n+1}} \right\},$$

$$\mathbf{w}_v = \left\{ w_{v_1} \quad \theta_{xv_1} \quad \theta_{yv_1} \quad w_{xyv_1} \quad \cdots \quad w_{v_{n+1}} \quad \theta_{xv_{n+1}} \quad \theta_{yv_{n+1}} \quad w_{xyv_{n+1}} \right\},$$

$$\frac{\partial \mathbf{u}_v}{\partial z} = \left\{ \frac{\partial u_{v_1}}{\partial z} \quad \frac{\partial v_{v_1}}{\partial z} \quad \cdots \quad \frac{\partial u_{v_{n+1}}}{\partial z} \quad \frac{\partial v_{v_{n+1}}}{\partial z} \right\} \text{ and}$$

$$\mathbf{f}_v = \left\{ \mathbf{f}_{\text{in}_v} \quad \mathbf{f}_{\text{out}_v} \quad \mathbf{f}_{s_v} \quad Q_v \right\}^T, \quad \mathbf{f}_{\text{in}_v} = \left\{ f_{x_v,1} \quad f_{y_v,1} \quad \cdots \quad f_{x_v,(n+1)} \quad f_{y_v,(n+1)} \right\},$$

$$\mathbf{f}_{\text{out}_v} = \left\{ f_{z_v,1} \quad M_{x_v,1} \quad M_{y_v,1} \quad M_{xy_v,1} \quad \cdots \quad f_{z_v,(n+1)} \quad M_{x_v,(n+1)} \quad M_{y_v,(n+1)} \quad M_{xy_v,(n+1)} \right\},$$

$$\mathbf{f}_{s_v} = \left\{ f_{s_{xv},1} \quad f_{s_{yv},1} \quad \cdots \quad f_{s_{xv},(n+1)} \quad f_{s_{yv},(n+1)} \right\},$$

where each term is the same as those used in eqs. (5.26) and (5.31).

Equations for the base layer (elastic plate) are given by

$$\begin{bmatrix} \mathbf{m}_{\text{in}_b} & \mathbf{0} & \mathbf{0} & \mathbf{0} \\ \mathbf{0} & \mathbf{m}_{\text{out}_b} & \mathbf{0} & \mathbf{0} \\ \mathbf{0} & \mathbf{0} & \mathbf{0} & \mathbf{0} \\ \mathbf{0} & \mathbf{0} & \mathbf{0} & \mathbf{0} \end{bmatrix} \ddot{\mathbf{q}}_b + \begin{bmatrix} \mathbf{k}_{\text{in}_b} & \mathbf{0} & \mathbf{0} & \mathbf{0} \\ \mathbf{0} & \mathbf{k}_{\text{out}_b} & \mathbf{0} & \mathbf{0} \\ \mathbf{0} & \mathbf{0} & \mathbf{0} & \mathbf{0} \\ \mathbf{0} & \mathbf{0} & \mathbf{0} & \mathbf{0} \end{bmatrix} \mathbf{q}_b = \mathbf{M}_b \ddot{\mathbf{q}}_b + \mathbf{K}_b \mathbf{q}_b = \mathbf{f}_b,$$

$$\text{where } \mathbf{q}_b = \left\{ \mathbf{u}_b \quad \mathbf{w}_b \quad \frac{\partial \mathbf{u}_b}{\partial z} \quad \phi_b \right\}^T, \quad \mathbf{u}_b = \left\{ u_{b_1} \quad v_{b_1} \quad \cdots \quad u_{b_{n+1}} \quad v_{b_{n+1}} \right\},$$

APPENDIX D EQUATIONS OF MOTION FOR PLATES WITH HYBRID ACTIVE-PASSIVE
CONSTRAINED LAYER DAMPING TREATMENTS

$$\mathbf{w}_b = \left\{ w_{b_1} \quad \theta_{xb_1} \quad \theta_{yb_1} \quad w_{xyb_1} \quad \cdots \quad w_{b_{n+1}} \quad \theta_{xb_{n+1}} \quad \theta_{yb_{n+1}} \quad w_{xyb_{n+1}} \right\},$$

$$\frac{\partial \mathbf{u}_b}{\partial z} = \left\{ \frac{\partial u_{b_1}}{\partial z} \quad \frac{\partial v_{b_1}}{\partial z} \quad \cdots \quad \frac{\partial u_{b_{n+1}}}{\partial z} \quad \frac{\partial v_{b_{n+1}}}{\partial z} \right\} \text{ and}$$

$$\mathbf{f}_b = \left\{ \mathbf{f}_{in_b} \quad \mathbf{f}_{out_b} \quad \mathbf{f}_{s_b} \quad \mathbf{Q}_b \right\}^T, \quad \mathbf{f}_{in_b} = \left\{ f_{x_b 1} \quad f_{y_b 1} \quad \cdots \quad f_{x_b(n+1)} \quad f_{y_b(n+1)} \right\},$$

$$\mathbf{f}_{out_b} = \left\{ f_{z_b 1} \quad M_{x_b 1} \quad M_{y_b 1} \quad M_{xy_b 1} \quad \cdots \quad f_{z_b(n+1)} \quad M_{x_b(n+1)} \quad M_{y_b(n+1)} \quad M_{xy_b(n+1)} \right\},$$

$$\mathbf{f}_{s_b} = \left\{ f_{s_{xb} 1} \quad f_{s_{yb} 1} \quad \cdots \quad f_{s_{xb}(n+1)} \quad f_{s_{yb}(n+1)} \right\},$$

where each term is the same as those used in eqs. (A.16) and (A.18).

Therefore, after stacking the mass and stiffness matrices for local coordinates into one matrix

according to the order of layer, the coupling matrix $\mathbf{C} = \begin{bmatrix} \mathbf{C}_p & \mathbf{C}_c & \mathbf{C}_p & \mathbf{C}_b \end{bmatrix}^T$ is given by

the four sub-matrices:

$$\mathbf{C}_p = \begin{bmatrix} 1 & 0 & 0 & 0 & \frac{h_p}{2} + h_c + \frac{h_b}{2} - d_3 & 0 & 0 & h_v & 0 \\ 0 & 1 & 0 & -\left(\frac{h_p}{2} + h_c + \frac{h_b}{2} - d_3\right) & 0 & 0 & -h_v & 0 & 0 \\ 0 & 0 & 1 & 0 & 0 & 0 & 0 & 0 & 0 \\ 0 & 0 & 0 & 1 & 0 & 0 & 0 & 0 & 0 \\ 0 & 0 & 0 & 0 & 1 & 0 & 0 & 0 & 0 \\ 0 & 0 & 0 & 0 & 0 & 1 & 0 & 0 & 0 \\ 0 & 0 & 0 & 0 & 0 & 0 & 1 & 0 & 0 \\ 0 & 0 & 0 & 0 & 0 & 0 & 0 & 1 & 0 \\ 0 & 0 & 0 & 0 & 0 & 0 & 0 & 0 & 1 \end{bmatrix},$$

APPENDIX D EQUATIONS OF MOTION FOR PLATES WITH HYBRID ACTIVE-PASSIVE
CONSTRAINED LAYER DAMPING TREATMENTS

$$\mathbf{C}_c = \begin{bmatrix} 1 & 0 & 0 & 0 & \frac{h_c}{2} + \frac{h_b}{2} - d_3 & 0 & 0 & h_v & 0 \\ 0 & 1 & 0 & -\left(\frac{h_c}{2} + \frac{h_b}{2} - d_3\right) & 0 & 0 & -h_v & 0 & 0 \\ 0 & 0 & 1 & 0 & 0 & 0 & 0 & 0 & 0 \\ 0 & 0 & 0 & 1 & 0 & 0 & 0 & 0 & 0 \\ 0 & 0 & 0 & 0 & 1 & 0 & 0 & 0 & 0 \\ 0 & 0 & 0 & 0 & 0 & 1 & 0 & 0 & 0 \\ 0 & 0 & 0 & 0 & 0 & 0 & 1 & 0 & 0 \\ 0 & 0 & 0 & 0 & 0 & 0 & 0 & 1 & 0 \\ 0 & 0 & 0 & 0 & 0 & 0 & 0 & 0 & 1 \end{bmatrix},$$

$$\mathbf{C}_v = \begin{bmatrix} 1 & 0 & 0 & 0 & \frac{h_b}{2} - d_3 & 0 & 0 & \frac{h_v}{2} & 0 \\ 0 & 1 & 0 & -\left(\frac{h_b}{2} - d_3\right) & 0 & 0 & -\frac{h_v}{2} & 0 & 0 \\ 0 & 0 & 1 & 0 & 0 & 0 & 0 & 0 & 0 \\ 0 & 0 & 0 & 0 & 0 & 0 & 0 & 0 & 0 \\ 0 & 0 & 0 & 0 & 0 & 0 & 0 & 0 & 0 \\ 0 & 0 & 0 & 0 & 0 & 0 & 0 & 0 & 0 \\ 0 & 0 & 0 & 0 & 0 & 0 & 1 & 0 & 0 \\ 0 & 0 & 0 & 0 & 0 & 0 & 0 & 1 & 0 \\ 0 & 0 & 0 & 0 & 0 & 0 & 0 & 0 & 1 \end{bmatrix},$$

$$\text{and } \mathbf{C}_b = \begin{bmatrix} 1 & 0 & 0 & 0 & -d_3 & 0 & 0 & 0 & 0 \\ 0 & 1 & 0 & d_3 & 0 & 0 & 0 & 0 & 0 \\ 0 & 0 & 1 & 0 & 0 & 0 & 0 & 0 & 0 \\ 0 & 0 & 0 & 1 & 0 & 0 & 0 & 0 & 0 \\ 0 & 0 & 0 & 0 & 1 & 0 & 0 & 0 & 0 \\ 0 & 0 & 0 & 0 & 0 & 1 & 0 & 0 & 0 \\ 0 & 0 & 0 & 0 & 0 & 0 & 1 & 0 & 0 \\ 0 & 0 & 0 & 0 & 0 & 0 & 0 & 1 & 0 \\ 0 & 0 & 0 & 0 & 0 & 0 & 0 & 0 & 1 \end{bmatrix},$$

where $d_3 = \frac{h_p + h_c + h_v + h_b}{2} - \frac{h_b}{2}$ for this configuration.

Finally, the global matrix equation of motion can be obtained as

APPENDIX D EQUATIONS OF MOTION FOR PLATES WITH HYBRID ACTIVE-PASSIVE CONSTRAINED LAYER DAMPING TREATMENTS

$$\mathbf{M}\ddot{\mathbf{q}} + \mathbf{K}\mathbf{q} = \mathbf{f},$$

$$\text{where } \mathbf{M} = \mathbf{C}^T \begin{bmatrix} \mathbf{M}_p & \mathbf{0} & \mathbf{0} & \mathbf{0} \\ \mathbf{0} & \mathbf{M}_c & \mathbf{0} & \mathbf{0} \\ \mathbf{0} & \mathbf{0} & \mathbf{M}_v & \mathbf{0} \\ \mathbf{0} & \mathbf{0} & \mathbf{0} & \mathbf{M}_b \end{bmatrix} \mathbf{C}, \mathbf{K} = \mathbf{C}^T \begin{bmatrix} \mathbf{K}_p & \mathbf{0} & \mathbf{0} & \mathbf{0} \\ \mathbf{0} & \mathbf{K}_c & \mathbf{0} & \mathbf{0} \\ \mathbf{0} & \mathbf{0} & \mathbf{K}_v & \mathbf{0} \\ \mathbf{0} & \mathbf{0} & \mathbf{0} & \mathbf{K}_b \end{bmatrix} \mathbf{C},$$

$$\mathbf{q} = \left\{ \mathbf{u} \quad \mathbf{w} \quad \frac{\partial \mathbf{u}}{\partial z} \quad \phi \right\}^T, \mathbf{u} = \left\{ u_1 \quad v_1 \quad \cdots \quad u_{n+1} \quad v_{n+1} \right\},$$

$$\mathbf{w} = \left\{ w_1 \quad \theta_{x_1} \quad \theta_{y_1} \quad w_{xy_1} \quad \cdots \quad w_{n+1} \quad \theta_{x_{n+1}} \quad \theta_{y_{n+1}} \quad w_{xy_{n+1}} \right\},$$

$$\frac{\partial \mathbf{u}}{\partial z} = \left\{ \frac{\partial u_1}{\partial z} \quad \frac{\partial v_1}{\partial z} \quad \cdots \quad \frac{\partial u_{n+1}}{\partial z} \quad \frac{\partial v_{n+1}}{\partial z} \right\} \text{ and}$$

$$\mathbf{f} = \{\mathbf{f}_{\text{in}} \quad \mathbf{f}_{\text{out}} \quad \mathbf{f}_s \quad Q\}^T, \mathbf{f}_{\text{in}} = \left\{ f_{x1} \quad f_{y1} \quad \cdots \quad f_{x(n+1)} \quad f_{y(n+1)} \right\},$$

$$\mathbf{f}_{\text{out}} = \left\{ f_{z1} \quad M_{x1} \quad M_{y1} \quad M_{xy1} \quad \cdots \quad f_{z(n+1)} \quad M_{x(n+1)} \quad M_{y(n+1)} \quad M_{xy(n+1)} \right\},$$

$$\mathbf{f}_s = \left\{ f_{s_x 1} \quad f_{s_y 1} \quad \cdots \quad f_{s_x(n+1)} \quad f_{s_y(n+1)} \right\}.$$

D.2 AC/PCLD treatment

The configuration for a plate with AC/PCLD treatment is shown in Figure D.2.

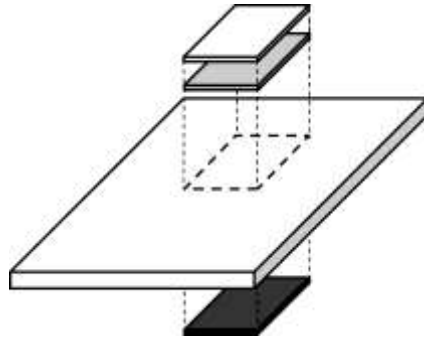





Figure D.2 Configuration of a plate with AC/PCLD treatment;  : elastic plate,  : viscoelastic layer and  : piezoelectric patch

APPENDIX D EQUATIONS OF MOTION FOR PLATES WITH HYBRID ACTIVE-PASSIVE CONSTRAINED LAYER DAMPING TREATMENTS

Equations for the constraining layer, the viscoelastic layer, the base layer and the piezoelectric layer are the same as those given for APCLD treatment.

After stacking the mass and stiffness matrices for local coordinates into one matrix according to the order of layer, the coupling matrix $\mathbf{C} = [\mathbf{C}_c \quad \mathbf{C}_v \quad \mathbf{C}_b \quad \mathbf{C}_p]^T$ is given by the four sub-matrices;

$$\mathbf{C}_c = \begin{bmatrix} 1 & 0 & 0 & 0 & \frac{h_c}{2} + \frac{h_b}{2} - d_3 & 0 & 0 & h_v & 0 \\ 0 & 1 & 0 & -\left(\frac{h_c}{2} + \frac{h_b}{2} - d_3\right) & 0 & 0 & -h_v & 0 & 0 \\ 0 & 0 & 1 & 0 & 0 & 0 & 0 & 0 & 0 \\ 0 & 0 & 0 & 1 & 0 & 0 & 0 & 0 & 0 \\ 0 & 0 & 0 & 0 & 1 & 0 & 0 & 0 & 0 \\ 0 & 0 & 0 & 0 & 0 & 1 & 0 & 0 & 0 \\ 0 & 0 & 0 & 0 & 0 & 0 & 1 & 0 & 0 \\ 0 & 0 & 0 & 0 & 0 & 0 & 0 & 1 & 0 \\ 0 & 0 & 0 & 0 & 0 & 0 & 0 & 0 & 1 \end{bmatrix},$$

$$\mathbf{C}_v = \begin{bmatrix} 1 & 0 & 0 & 0 & \frac{h_b}{2} - d_3 & 0 & 0 & \frac{h_v}{2} & 0 \\ 0 & 1 & 0 & -\left(\frac{h_b}{2} - d_3\right) & 0 & 0 & -\frac{h_v}{2} & 0 & 0 \\ 0 & 0 & 1 & 0 & 0 & 0 & 0 & 0 & 0 \\ 0 & 0 & 0 & 0 & 0 & 0 & 0 & 0 & 0 \\ 0 & 0 & 0 & 0 & 0 & 0 & 0 & 0 & 0 \\ 0 & 0 & 0 & 0 & 0 & 0 & 0 & 0 & 0 \\ 0 & 0 & 0 & 0 & 0 & 0 & 1 & 0 & 0 \\ 0 & 0 & 0 & 0 & 0 & 0 & 0 & 1 & 0 \\ 0 & 0 & 0 & 0 & 0 & 0 & 0 & 0 & 1 \end{bmatrix},$$

APPENDIX D EQUATIONS OF MOTION FOR PLATES WITH HYBRID ACTIVE-PASSIVE
CONSTRAINED LAYER DAMPING TREATMENTS

$$\mathbf{C}_b = \begin{bmatrix} 1 & 0 & 0 & 0 & -d_3 & 0 & 0 & 0 & 0 \\ 0 & 1 & 0 & d_3 & 0 & 0 & 0 & 0 & 0 \\ 0 & 0 & 1 & 0 & 0 & 0 & 0 & 0 & 0 \\ 0 & 0 & 0 & 1 & 0 & 0 & 0 & 0 & 0 \\ 0 & 0 & 0 & 0 & 1 & 0 & 0 & 0 & 0 \\ 0 & 0 & 0 & 0 & 0 & 1 & 0 & 0 & 0 \\ 0 & 0 & 0 & 0 & 0 & 0 & 1 & 0 & 0 \\ 0 & 0 & 0 & 0 & 0 & 0 & 0 & 1 & 0 \\ 0 & 0 & 0 & 0 & 0 & 0 & 0 & 0 & 1 \end{bmatrix}$$

$$\text{and } \mathbf{C}_p = \begin{bmatrix} 1 & 0 & 0 & 0 & -\frac{h_p}{2} - \frac{h_b}{2} - d_3 & 0 & 0 & 0 & 0 \\ 0 & 1 & 0 & -\left(-\frac{h_p}{2} - \frac{h_b}{2} - d_3\right) & 0 & 0 & 0 & 0 & 0 \\ 0 & 0 & 1 & 0 & 0 & 0 & 0 & 0 & 0 \\ 0 & 0 & 0 & 1 & 0 & 0 & 0 & 0 & 0 \\ 0 & 0 & 0 & 0 & 1 & 0 & 0 & 0 & 0 \\ 0 & 0 & 0 & 0 & 0 & 1 & 0 & 0 & 0 \\ 0 & 0 & 0 & 0 & 0 & 0 & 1 & 0 & 0 \\ 0 & 0 & 0 & 0 & 0 & 0 & 0 & 1 & 0 \\ 0 & 0 & 0 & 0 & 0 & 0 & 0 & 0 & 1 \end{bmatrix}.$$

where $d_3 = \frac{h_c + h_v + h_b + h_p}{2} - \left(\frac{h_b}{2} + h_v\right)$ for this configuration.

Finally, the global matrix equation of motion can be obtained as

$$\mathbf{M}\ddot{\mathbf{q}} + \mathbf{K}\mathbf{q} = \mathbf{f},$$

$$\text{where } \mathbf{M} = \mathbf{C}^T \begin{bmatrix} \mathbf{M}_p & \mathbf{0} & \mathbf{0} & \mathbf{0} \\ \mathbf{0} & \mathbf{M}_c & \mathbf{0} & \mathbf{0} \\ \mathbf{0} & \mathbf{0} & \mathbf{M}_v & \mathbf{0} \\ \mathbf{0} & \mathbf{0} & \mathbf{0} & \mathbf{M}_b \end{bmatrix} \mathbf{C}, \mathbf{K} = \mathbf{C}^T \begin{bmatrix} \mathbf{K}_p & \mathbf{0} & \mathbf{0} & \mathbf{0} \\ \mathbf{0} & \mathbf{K}_c & \mathbf{0} & \mathbf{0} \\ \mathbf{0} & \mathbf{0} & \mathbf{K}_v & \mathbf{0} \\ \mathbf{0} & \mathbf{0} & \mathbf{0} & \mathbf{K}_b \end{bmatrix} \mathbf{C},$$

$$\mathbf{q} = \left\{ \mathbf{u} \quad \mathbf{w} \quad \frac{\partial \mathbf{u}}{\partial z} \quad \phi \right\}^T, \mathbf{u} = \left\{ u_1 \quad v_1 \quad \cdots \quad u_{n+1} \quad v_{n+1} \right\},$$

$$\mathbf{w} = \left\{ w_1 \quad \theta_{x_1} \quad \theta_{y_1} \quad w_{xy_1} \quad \cdots \quad w_{n+1} \quad \theta_{x_{n+1}} \quad \theta_{y_{n+1}} \quad w_{xy_{n+1}} \right\},$$

APPENDIX D EQUATIONS OF MOTION FOR PLATES WITH HYBRID ACTIVE-PASSIVE CONSTRAINED LAYER DAMPING TREATMENTS

$$\frac{\partial \mathbf{u}}{\partial z} = \left\{ \frac{\partial u_1}{\partial z} \quad \frac{\partial v_1}{\partial z} \quad \dots \quad \frac{\partial u_{n+1}}{\partial z} \quad \frac{\partial v_{n+1}}{\partial z} \right\} \text{ and}$$

$$\mathbf{f} = \{\mathbf{f}_{\text{in}} \quad \mathbf{f}_{\text{out}} \quad \mathbf{f}_s \quad Q\}^T, \quad \mathbf{f}_{\text{in}} = \left\{ f_{x1} \quad f_{y1} \quad \dots \quad f_{x(n+1)} \quad f_{y(n+1)} \right\},$$

$$\mathbf{f}_{\text{out}} = \left\{ f_{z1} \quad M_{x1} \quad M_{y1} \quad M_{xy1} \quad \dots \quad f_{z(n+1)} \quad M_{x(n+1)} \quad M_{y(n+1)} \quad M_{xy(n+1)} \right\},$$

$$\mathbf{f}_s = \left\{ f_{s_x1} \quad f_{s_y1} \quad \dots \quad f_{s_x(n+1)} \quad f_{s_y(n+1)} \right\}.$$

D.3 AC/PSOLD treatment

The configuration of a plate with AC/PSOLD treatment is shown in Figure D.3.

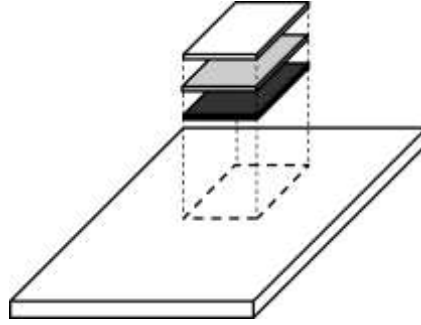


Figure D.3 Configuration of a plate with AC/PSOLD treatment; : elastic plate, : viscoelastic layer and : piezoelectric patch

Equations for the constraining layer, the viscoelastic layer, the base layer and the piezoelectric layer are the same as those given for APCLD treatment.

After stacking the mass and stiffness matrices for local coordinates into one matrix according to the order of layer, the coupling matrix $\mathbf{C} = [\mathbf{C}_e \quad \mathbf{C}_v \quad \mathbf{C}_p \quad \mathbf{C}_b]^T$ is given by the four sub-matrices;

APPENDIX D EQUATIONS OF MOTION FOR PLATES WITH HYBRID ACTIVE-PASSIVE
CONSTRAINED LAYER DAMPING TREATMENTS

$$\mathbf{C}_c = \begin{bmatrix} 1 & 0 & 0 & 0 & \frac{h_c}{2} + h_p + \frac{h_b}{2} - d_3 & 0 & 0 & h_v & 0 \\ 0 & 1 & 0 & -\left(\frac{h_c}{2} + h_p + \frac{h_b}{2} - d_3\right) & 0 & 0 & -h_v & 0 & 0 \\ 0 & 0 & 1 & 0 & 0 & 0 & 0 & 0 & 0 \\ 0 & 0 & 0 & 1 & 0 & 0 & 0 & 0 & 0 \\ 0 & 0 & 0 & 0 & 1 & 0 & 0 & 0 & 0 \\ 0 & 0 & 0 & 0 & 0 & 1 & 0 & 0 & 0 \\ 0 & 0 & 0 & 0 & 0 & 0 & 1 & 0 & 0 \\ 0 & 0 & 0 & 0 & 0 & 0 & 0 & 1 & 0 \\ 0 & 0 & 0 & 0 & 0 & 0 & 0 & 0 & 1 \end{bmatrix},$$

$$\mathbf{C}_v = \begin{bmatrix} 1 & 0 & 0 & 0 & \frac{h_p}{2} + \frac{h_b}{2} - d_3 & 0 & 0 & \frac{h_v}{2} & 0 \\ 0 & 1 & 0 & -\left(\frac{h_p}{2} + \frac{h_b}{2} - d_3\right) & 0 & 0 & -\frac{h_v}{2} & 0 & 0 \\ 0 & 0 & 1 & 0 & 0 & 0 & 0 & 0 & 0 \\ 0 & 0 & 0 & 0 & 0 & 0 & 0 & 0 & 0 \\ 0 & 0 & 0 & 0 & 0 & 0 & 0 & 0 & 0 \\ 0 & 0 & 0 & 0 & 0 & 0 & 0 & 0 & 0 \\ 0 & 0 & 0 & 0 & 0 & 0 & 1 & 0 & 0 \\ 0 & 0 & 0 & 0 & 0 & 0 & 0 & 1 & 0 \\ 0 & 0 & 0 & 0 & 0 & 0 & 0 & 0 & 1 \end{bmatrix},$$

$$\mathbf{C}_p = \begin{bmatrix} 1 & 0 & 0 & 0 & \frac{h_p}{2} + \frac{h_b}{2} - d_3 & 0 & 0 & 0 & 0 \\ 0 & 1 & 0 & -\left(\frac{h_p}{2} + \frac{h_b}{2} - d_3\right) & 0 & 0 & 0 & 0 & 0 \\ 0 & 0 & 1 & 0 & 0 & 0 & 0 & 0 & 0 \\ 0 & 0 & 0 & 1 & 0 & 0 & 0 & 0 & 0 \\ 0 & 0 & 0 & 0 & 1 & 0 & 0 & 0 & 0 \\ 0 & 0 & 0 & 0 & 0 & 1 & 0 & 0 & 0 \\ 0 & 0 & 0 & 0 & 0 & 0 & 1 & 0 & 0 \\ 0 & 0 & 0 & 0 & 0 & 0 & 0 & 1 & 0 \\ 0 & 0 & 0 & 0 & 0 & 0 & 0 & 0 & 1 \end{bmatrix}$$

APPENDIX D EQUATIONS OF MOTION FOR PLATES WITH HYBRID ACTIVE-PASSIVE
CONSTRAINED LAYER DAMPING TREATMENTS

$$\text{and } \mathbf{C}_b = \begin{bmatrix} 1 & 0 & 0 & 0 & -d_3 & 0 & 0 & 0 & 0 \\ 0 & 1 & 0 & d_3 & 0 & 0 & 0 & 0 & 0 \\ 0 & 0 & 1 & 0 & 0 & 0 & 0 & 0 & 0 \\ 0 & 0 & 0 & 1 & 0 & 0 & 0 & 0 & 0 \\ 0 & 0 & 0 & 0 & 1 & 0 & 0 & 0 & 0 \\ 0 & 0 & 0 & 0 & 0 & 1 & 0 & 0 & 0 \\ 0 & 0 & 0 & 0 & 0 & 0 & 1 & 0 & 0 \\ 0 & 0 & 0 & 0 & 0 & 0 & 0 & 1 & 0 \\ 0 & 0 & 0 & 0 & 0 & 0 & 0 & 0 & 1 \end{bmatrix}.$$

where $d_3 = \frac{h_c + h_v + h_p + h_b}{2} - \frac{h_b}{2}$ for this configuration.

Finally, the global matrix equation of motion can be obtained as

$$\mathbf{M}\ddot{\mathbf{q}} + \mathbf{K}\mathbf{q} = \mathbf{f},$$

$$\text{where } \mathbf{M} = \mathbf{C}^T \begin{bmatrix} \mathbf{M}_p & \mathbf{0} & \mathbf{0} & \mathbf{0} \\ \mathbf{0} & \mathbf{M}_c & \mathbf{0} & \mathbf{0} \\ \mathbf{0} & \mathbf{0} & \mathbf{M}_v & \mathbf{0} \\ \mathbf{0} & \mathbf{0} & \mathbf{0} & \mathbf{M}_b \end{bmatrix} \mathbf{C}, \quad \mathbf{K} = \mathbf{C}^T \begin{bmatrix} \mathbf{K}_p & \mathbf{0} & \mathbf{0} & \mathbf{0} \\ \mathbf{0} & \mathbf{K}_c & \mathbf{0} & \mathbf{0} \\ \mathbf{0} & \mathbf{0} & \mathbf{K}_v & \mathbf{0} \\ \mathbf{0} & \mathbf{0} & \mathbf{0} & \mathbf{K}_b \end{bmatrix} \mathbf{C},$$

$$\mathbf{q} = \left\{ \mathbf{u} \quad \mathbf{w} \quad \frac{\partial \mathbf{u}}{\partial z} \quad \phi \right\}^T, \quad \mathbf{u} = \left\{ u_1 \quad v_1 \quad \cdots \quad u_{n+1} \quad v_{n+1} \right\},$$

$$\mathbf{w} = \left\{ w_1 \quad \theta_{x_1} \quad \theta_{y_1} \quad w_{xy_1} \quad \cdots \quad w_{n+1} \quad \theta_{x_{n+1}} \quad \theta_{y_{n+1}} \quad w_{xy_{n+1}} \right\},$$

$$\frac{\partial \mathbf{u}}{\partial z} = \left\{ \frac{\partial u_1}{\partial z} \quad \frac{\partial v_1}{\partial z} \quad \cdots \quad \frac{\partial u_{n+1}}{\partial z} \quad \frac{\partial v_{n+1}}{\partial z} \right\} \text{ and}$$

$$\mathbf{f} = \{\mathbf{f}_{in} \quad \mathbf{f}_{out} \quad \mathbf{f}_s \quad Q\}^T, \quad \mathbf{f}_{in} = \left\{ f_{x1} \quad f_{y1} \quad \cdots \quad f_{x(n+1)} \quad f_{y(n+1)} \right\},$$

$$\mathbf{f}_{out} = \left\{ f_{z1} \quad M_{x1} \quad M_{y1} \quad M_{xy1} \quad \cdots \quad f_{z(n+1)} \quad M_{x(n+1)} \quad M_{y(n+1)} \quad M_{xy(n+1)} \right\},$$

$$\mathbf{f}_s = \left\{ f_{s_x 1} \quad f_{s_y 1} \quad \cdots \quad f_{s_x(n+1)} \quad f_{s_y(n+1)} \right\}.$$

APPENDIX E RESULTS OF SIMULATION AND MEASUREMENT FOR CHAPTER 8

In this appendix, various figures obtained during the numerical study and experiment, which are explained in Chapter 8, are gathered.

E.1 Simulation result for determination of optimal control gain and mobility reduction with flat plates

In this section, numerical study results to determine an optimal control gain and mobility reductions using the optimal control gain with APCLD, AC/PCLD and AC/PSOLD treatments attached on flat plates are presented.

E.1.1 APCLD treatment

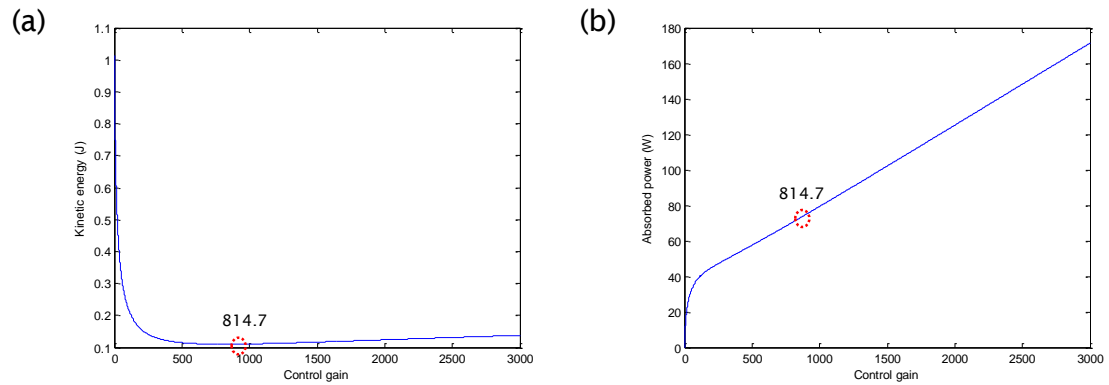


Figure E.1 The kinetic energy and absorbed power for a flat plate with APCLD treatment with control gains: (a) Change of the kinetic energy of a plate and (b) Change of absorbed power by an actuator

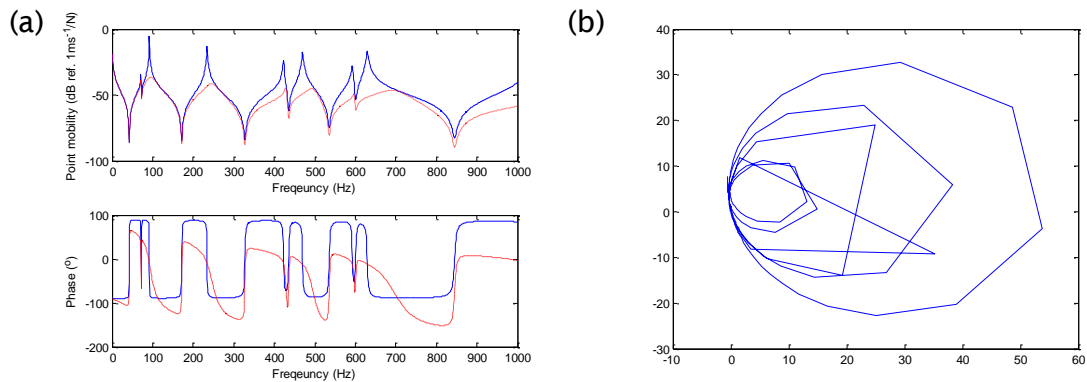


Figure E.2 Control result for a flat plate with APCLD treatment (a) Magnitude and phase of point mobility; — no control; - - - with control and (b) the Nyquist plot for a closed loop with the optimised control gain of 814.7

APPENDIX E RESULTS OF SIMULATION AND MEASUREMENT FOR CHAPTER 8

E.1.2 AC/PCLD treatment

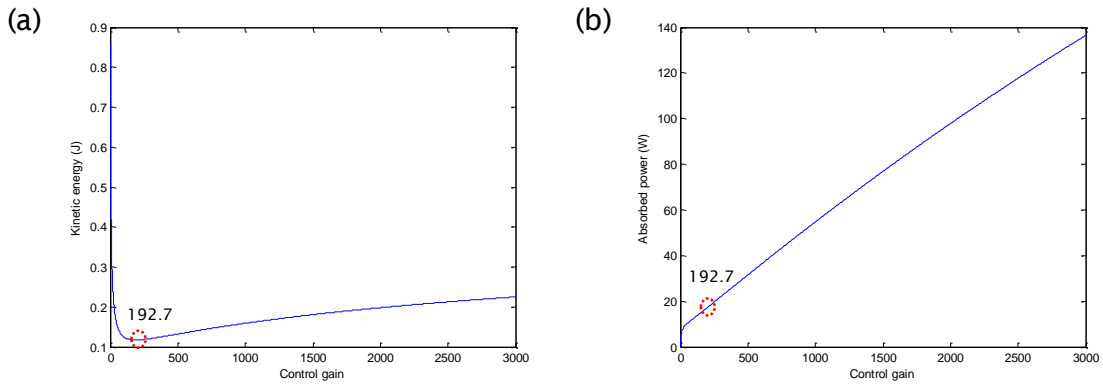


Figure E.3 The kinetic energy and absorbed power for a flat plate with AC/PCLD treatment with control gains: (a) Change in the kinetic energy of a plate and (b) Change of absorbed power by an actuator

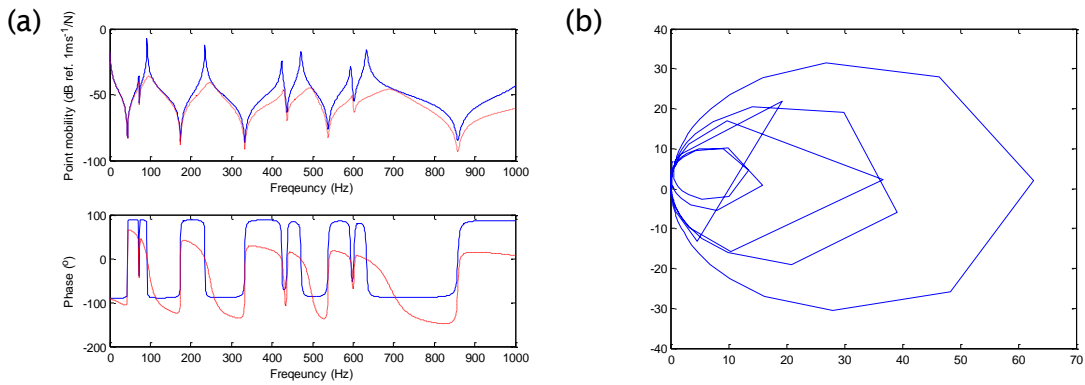


Figure E.4 Control result for a flat plate with AC/PCLD treatment (a) Magnitude and phase of point mobility; — no control; - - - with control and (b) the Nyquist plot for a closed loop with the optimised control gain of 192.7

E.1.3 AC/PSOLD treatment

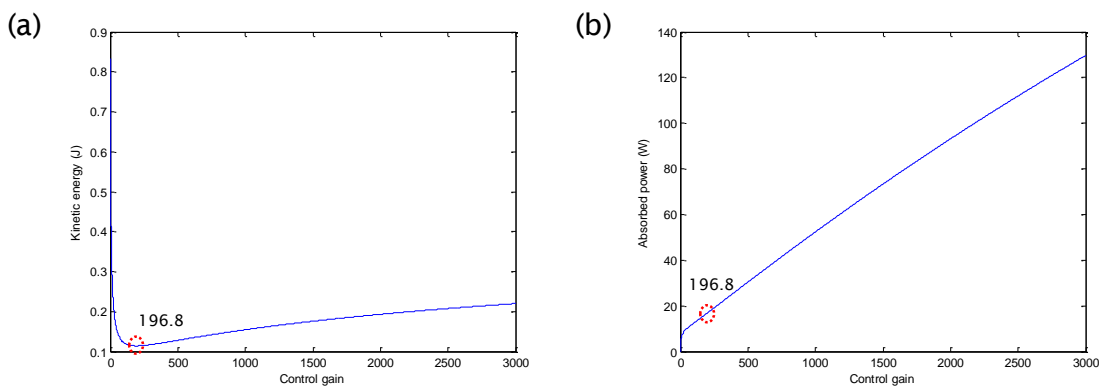


Figure E.5 The kinetic energy and absorbed power for a flat plate with AC/PSOLD treatment with control gains: (a) Change in the kinetic energy of a plate and (b) Change in the absorbed power by an actuator

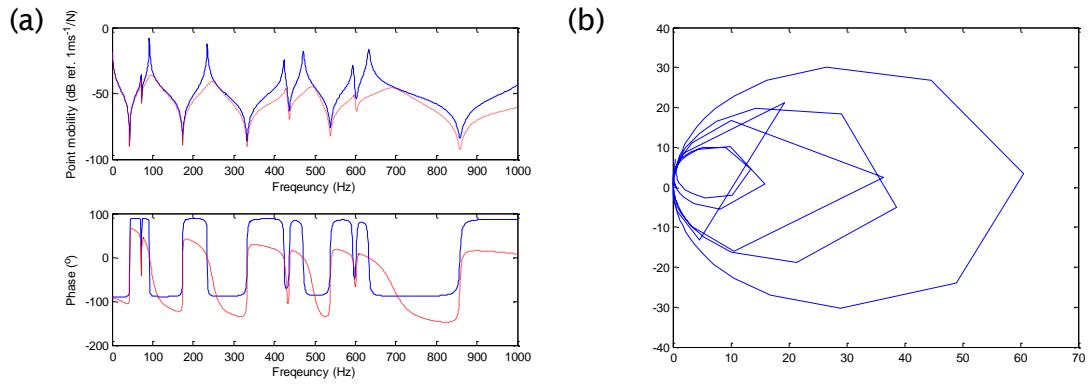


Figure E.6 Control result for a flat plate with AC/PSOLD treatment (a) Magnitude and phase of point mobility; — no control; - - - with control and (b) the Nyquist plot for a closed loop with the optimised control gain of 196.8

E.2 Simulation result for determination of optimal control gain and mobility reduction with curved plates

In this section, numerical study results to determine an optimal control gain and mobility reductions using the optimal control gain with APCLD, AC/PCLD and AC/PSOLD treatments attached on curved plates with maximum rises of 10 and 20 mm are presented.

E.1.1 APCLD treatment

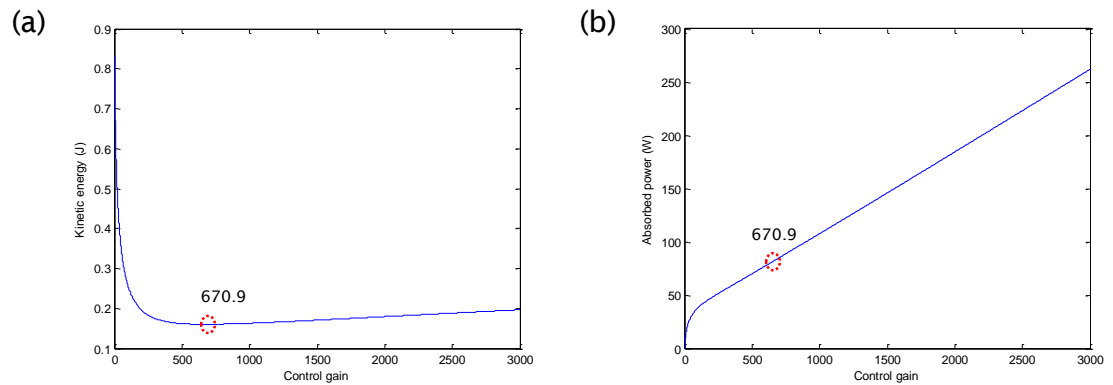


Figure E.7 The kinetic energy and absorbed power for a singly curved plate with a maximum rise of 10 mm with APCLD treatment with control gains: (a) Change of the kinetic energy of a plate and (b) Change of absorbed power by an actuator

APPENDIX E RESULTS OF SIMULATION AND MEASUREMENT FOR CHAPTER 8

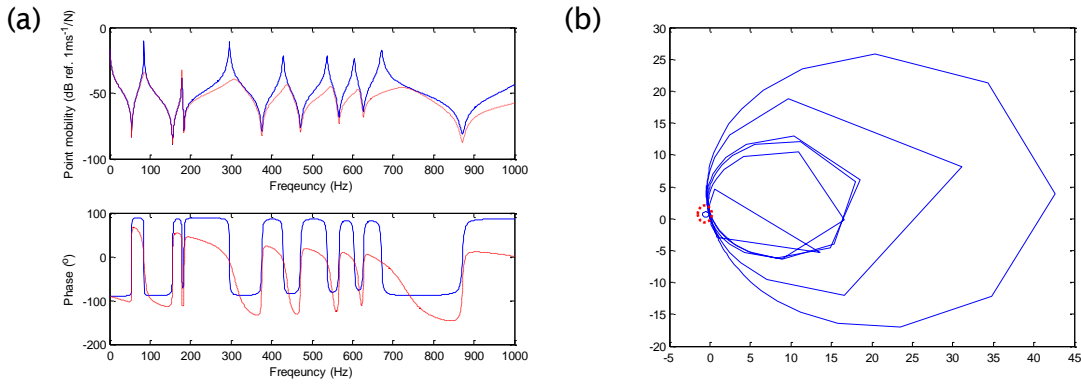


Figure E.8 Control result for a singly curved plate with a maximum rise of 10 mm with APCLD treatment (a) Magnitude and phase of point mobility; — no control; - - - with control and (b) the Nyquist plot for a closed loop with the optimised control gain of 670.9; \odot circle with negative effect on active control

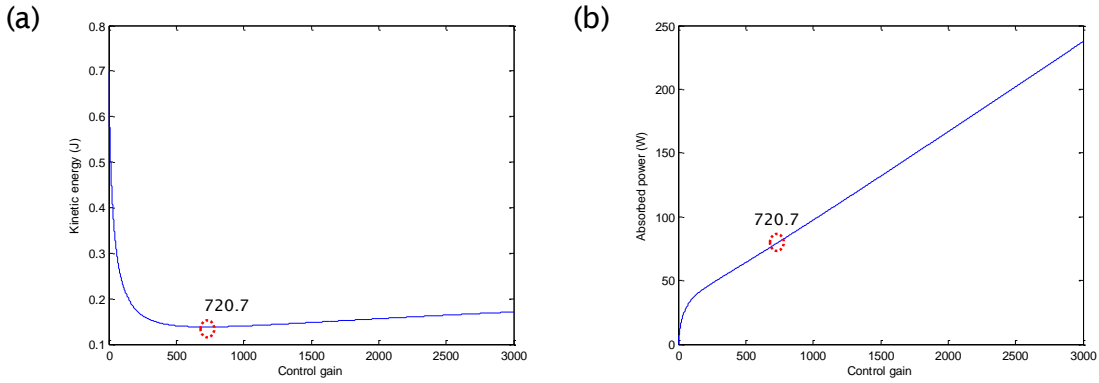


Figure E.9 The kinetic energy and absorbed power for a singly curved plate with a maximum rise of 20 mm with APCLD treatment with control gains: (a) Change of the kinetic energy of a plate and (b) Change of absorbed power by an actuator

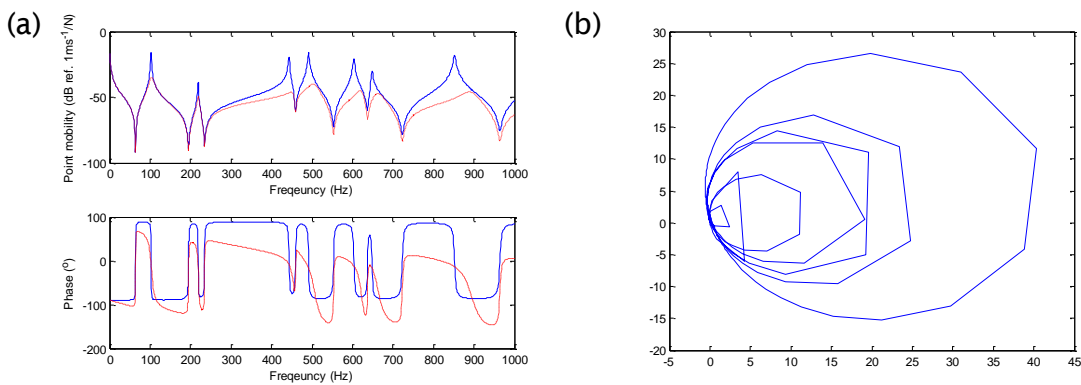


Figure E.10 Control result for a singly curved plate with a maximum rise of 20 mm with APCLD treatment (a) Magnitude and phase of point mobility; — no control; - - - with control and (b) the Nyquist plot for a closed loop with the optimised control gain of 720.7

E.1.2 AC/PCLD treatment

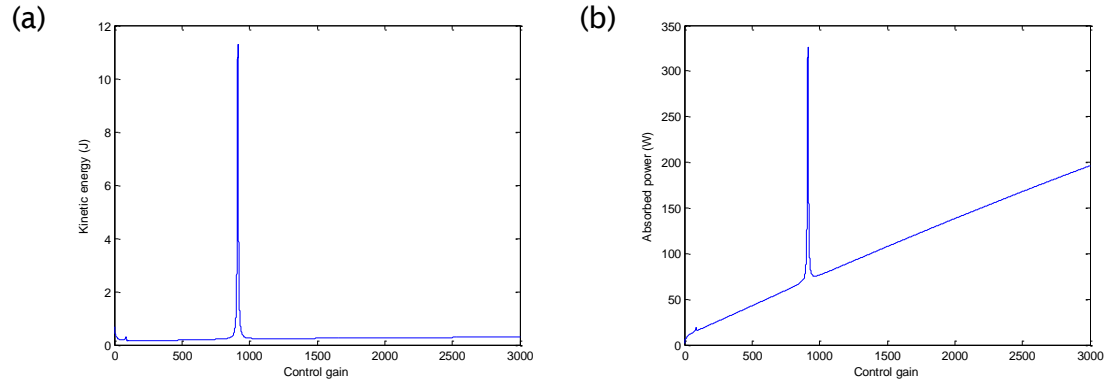


Figure E.11 The kinetic energy and absorbed power for a singly curved plate with a maximum rise of 10 mm with AC/PCLD treatment with control gains: (a) Change in the kinetic energy of a plate and (b) Change in absorbed power by an actuator

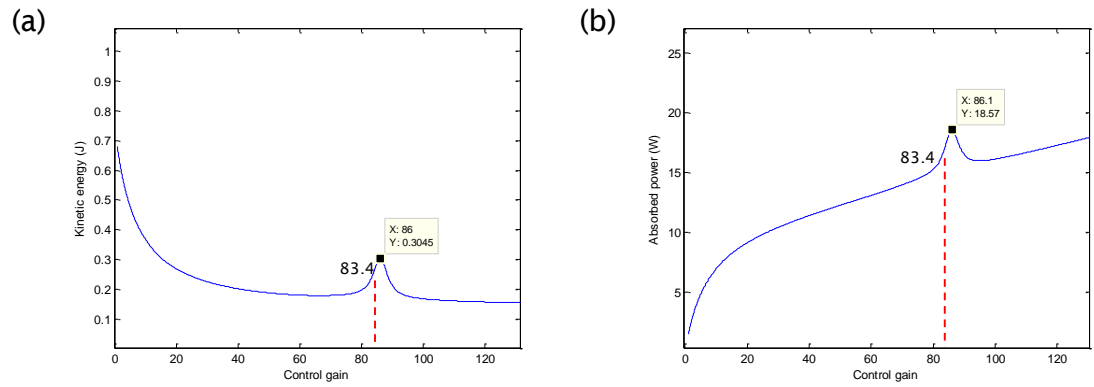


Figure E.12 Control gains for an unstable result obtained from kinetic energy and absorbed power for a singly curved plate with a maximum rise of 10 mm with AC/PCLD treatment with the change in control gain: (a) Change in the kinetic energy of a plate and (b) Change in absorbed power by an actuator

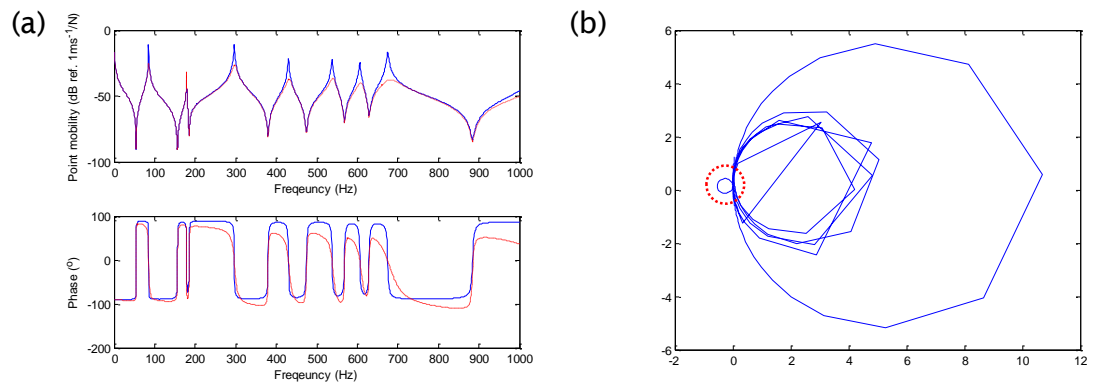


Figure E.13 Control result for a singly curved plate with a maximum rise of 10 mm with AC/PCLD treatment (a) Magnitude and phase of point mobility; — no control; - - - with control and (b) the Nyquist plot for a closed loop with the optimised control gain of 41.7; \odot circle with negative effect on active control

APPENDIX E RESULTS OF SIMULATION AND MEASUREMENT FOR CHAPTER 8

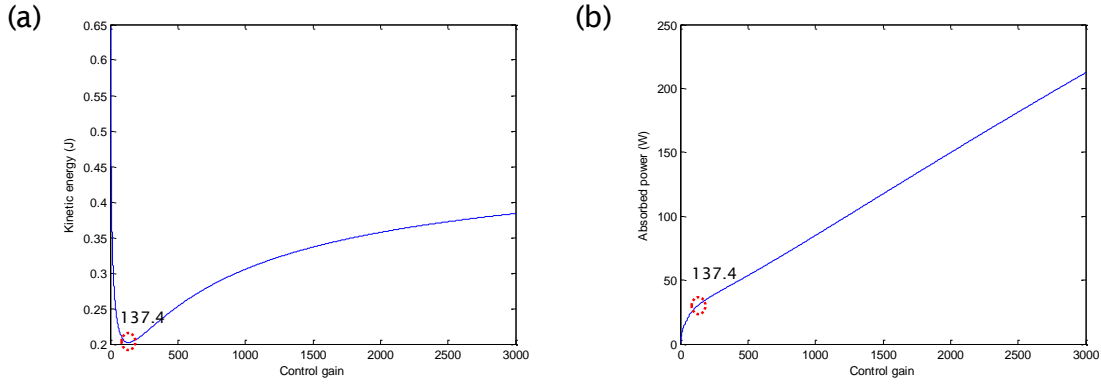


Figure E.14 The kinetic energy and absorbed power for a singly curved plate with a maximum rise of 20 mm with AC/PCLD treatment with control gains: (a) Change in the kinetic energy of a plate and (b) Change in absorbed power by an actuator

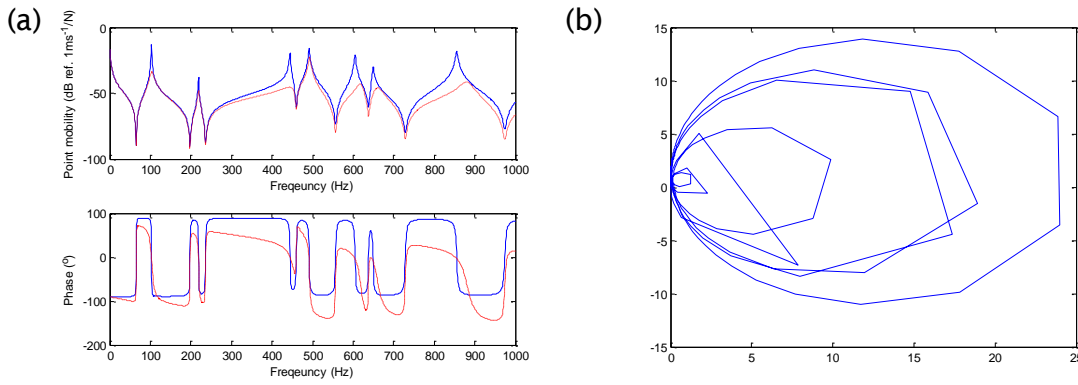


Figure E.15 Control result for a singly curved plate with a maximum rise of 20 mm with AC/PCLD treatment (a) Magnitude and phase of point mobility; — no control; - - - with control and (b) the Nyquist plot for a closed loop with the optimised control gain of 137.4

E.1.3 AC/PSOLD treatment

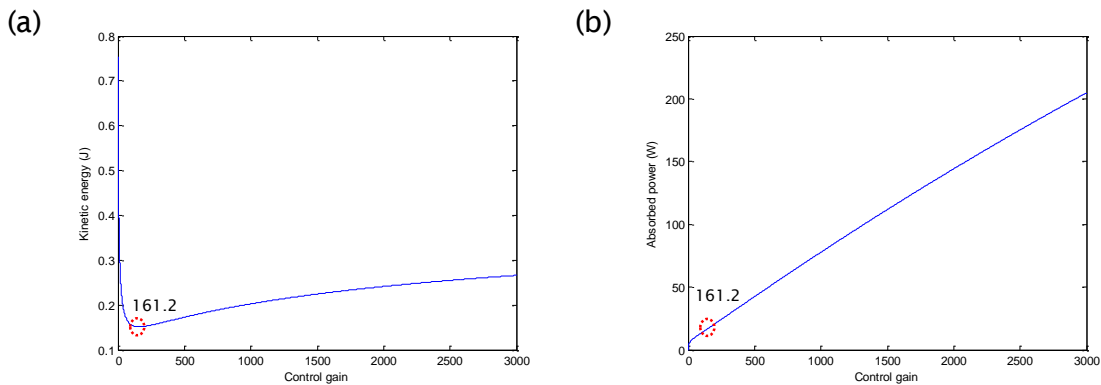


Figure E.16 The kinetic energy and absorbed power for a singly curved plate with a maximum rise of 10 mm with AC/PSOLD treatment with control gains: (a) Change in the kinetic energy of a plate and (b) Change in absorbed power by an actuator

APPENDIX E RESULTS OF SIMULATION AND MEASUREMENT FOR CHAPTER 8

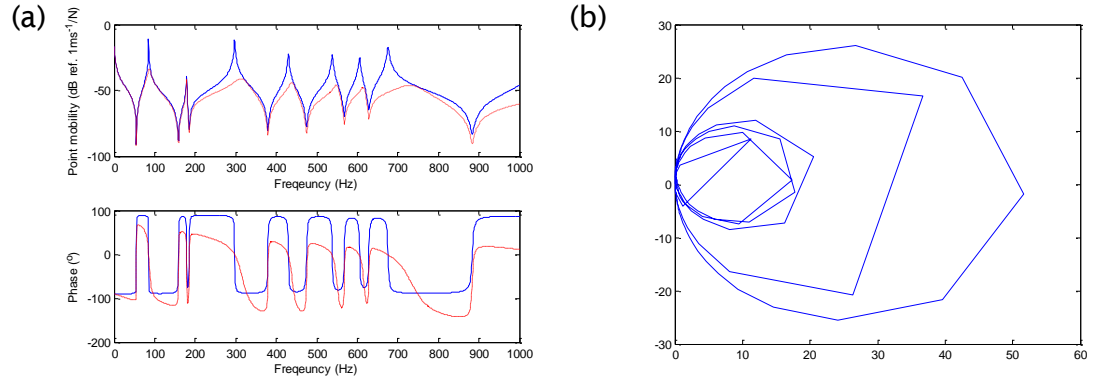


Figure E.17 Control result for a singly curved plate with a maximum rise of 10 mm with AC/PSOLD treatment (a) Magnitude and phase of point mobility; — no control; - - - with control and (b) the Nyquist plot for a closed loop with the optimised control gain of 161.2

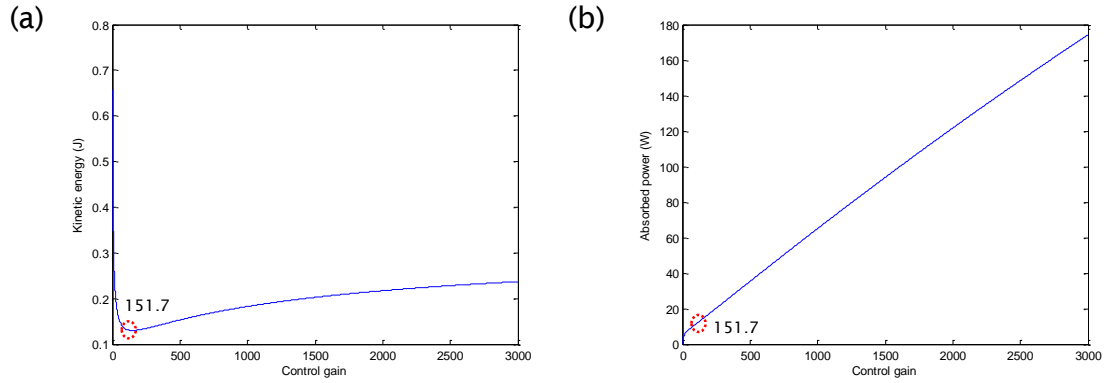


Figure E.18 The kinetic energy and absorbed power for a singly curved plate with a maximum rise of 20 mm with AC/PSOLD treatment with control gains: (a) Change in the kinetic energy of a plate and (b) Change in absorbed power by an actuator

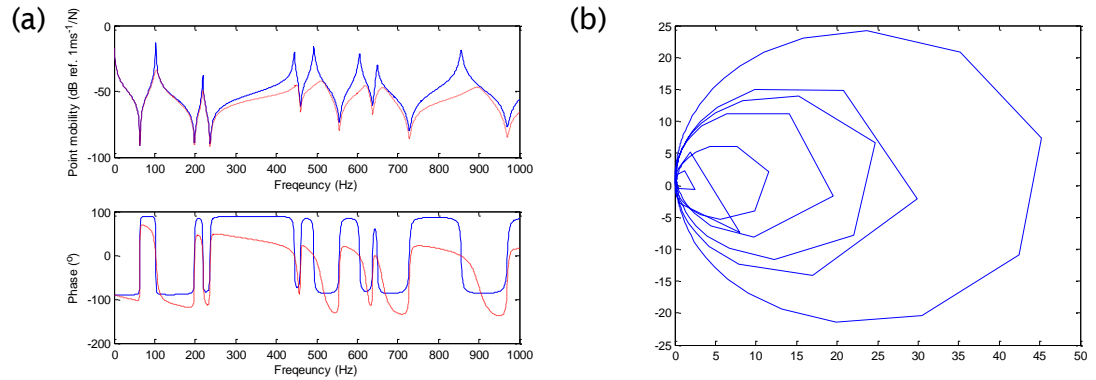


Figure E.19 Control result for a singly curved plate with a maximum rise of 20 mm with AC/PSOLD treatment (a) Magnitude and phase of point mobility; — no control; - - - with control and (b) the Nyquist plot for a closed loop with the optimised control gain of 151.7

E.3 FRFs of curved plated with HAPCLD treatments in impact hammer test

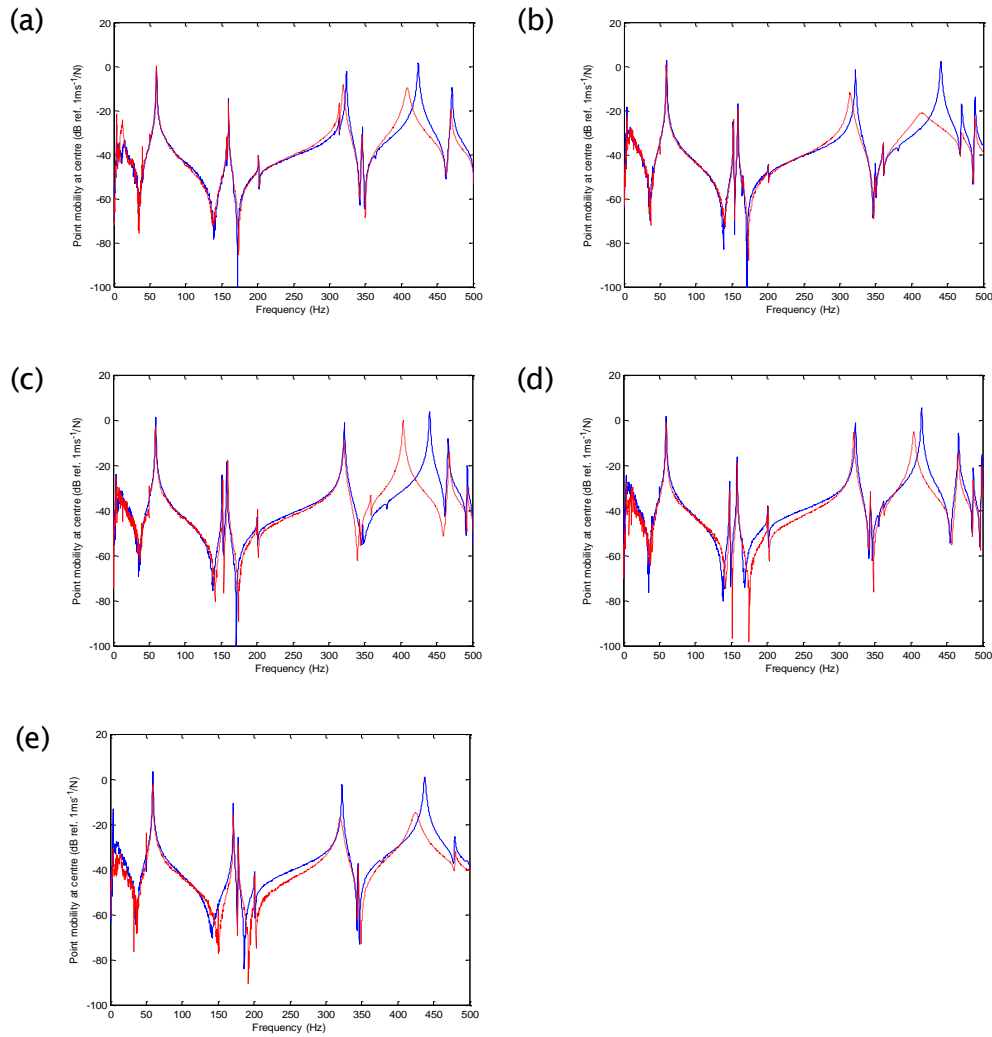


Figure E.20 FRFs of curved plated with HAPCLD treatments in impact hammer test; — without damping treatment; - - - with damping treatment (a) ACLD treatment, (b) APCLD treatment, (c) AC/PCLD treatment, (d) AC/PSOLD treatment and (e) inverse AC/PCLD treatment

E.4 Nyquist plot for a measured closed-loop and control simulation results for curved plates

In this section, Nyquist plots for a measured closed-loop and control simulation results using measured FRFs with a pseudo-random force and moment excitations for APCLD, AC/PCLD and AC/PSOLD treatments are presented. For results for ACLD treatment, please refer to Section 8.2.2.

E.4.1 APCLD treatment

From measured FRFs with pseudo-random moment excitation by a piezoelectric actuator and pseudo-random force excitation by a shaker with APCLD treatment, the following Nyquist plots and control simulation results are obtained according to applied filters.

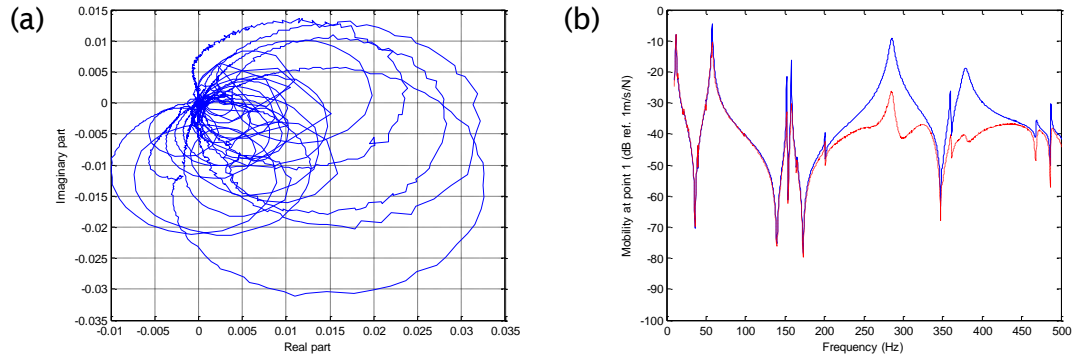


Figure E.21 (a) Nyquist plot for a closed loop without a filter and (b) controlled result without a filter (APCLD treatment, $G_{3dB} = 382.3789$)

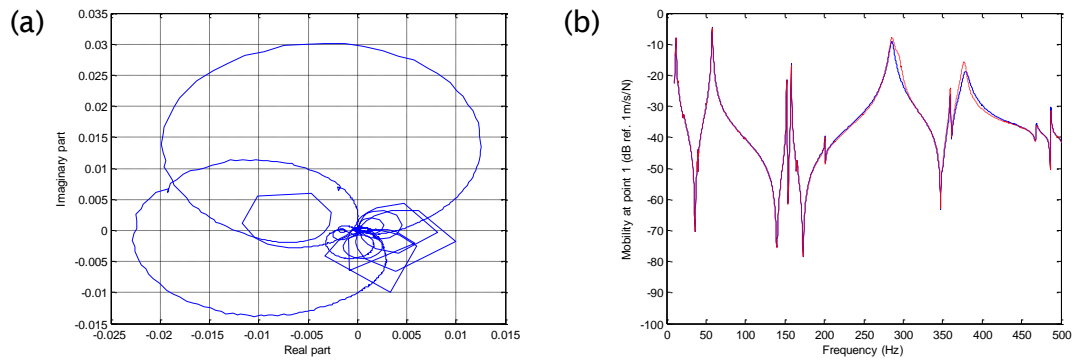


Figure E.22 (a) Nyquist plot for a closed loop with a low-pass filter with a cut-off frequency of 500 Hz and (b) controlled result with a low-pass filter with a cut-off frequency of 500 Hz (APCLD treatment, $G_{3dB} = 22.2564$)

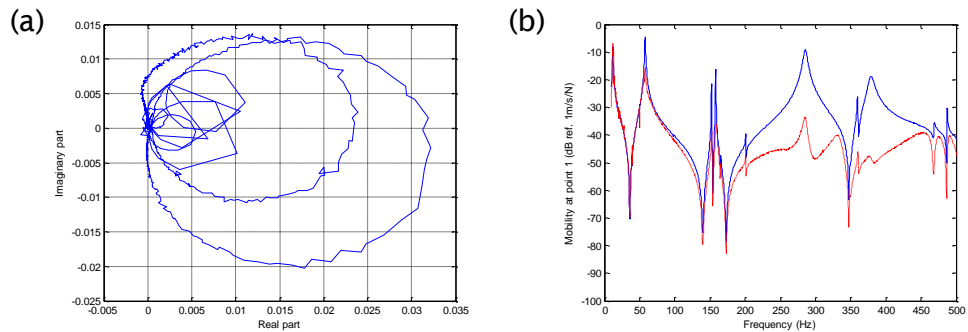


Figure E.23 (a) Nyquist plot for a closed loop with an ideal low-pass filter with a cut-off frequency of 500 Hz and (b) controlled result with an ideal low-pass filter with a cut-off frequency of 500 Hz (APCLD treatment, $G_{3dB} = 943.4783$)

APPENDIX E RESULTS OF SIMULATION AND MEASUREMENT FOR CHAPTER 8

E.4.2 AC/PCLD treatment

From measured FRFs with pseudo-random moment excitation by a piezoelectric actuator and pseudo-random force excitation by a shaker with AC/PCLD treatment, the following Nyquist plots and control simulation results are obtained according to applied filters.

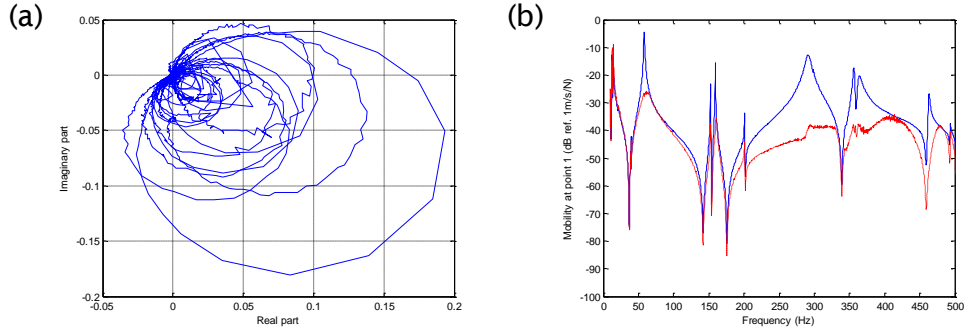


Figure E.24 (a) Nyquist plot for a closed loop without a filter and (b) controlled result without a filter (AC/PCLD treatment, $G_{3dB} = 218.8235$)

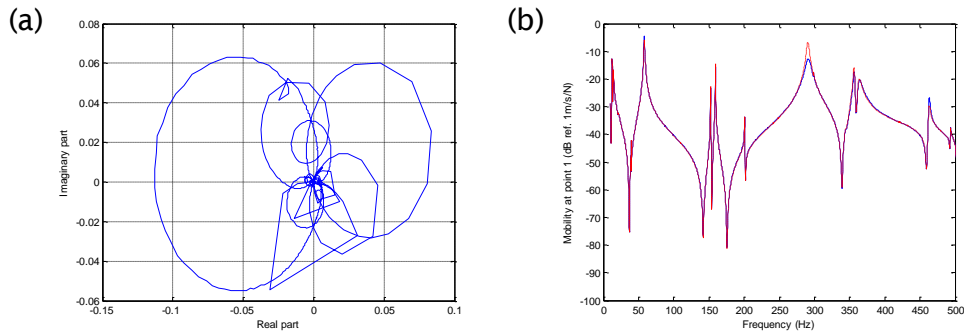


Figure E.25 (a) Nyquist plot for a closed loop with a low-pass filter with a cut-off frequency of 500 Hz and (b) controlled result with a low-pass filter with a cut-off frequency of 500 Hz (AC/PCLD treatment, $G_{3dB} = 4,4233$)

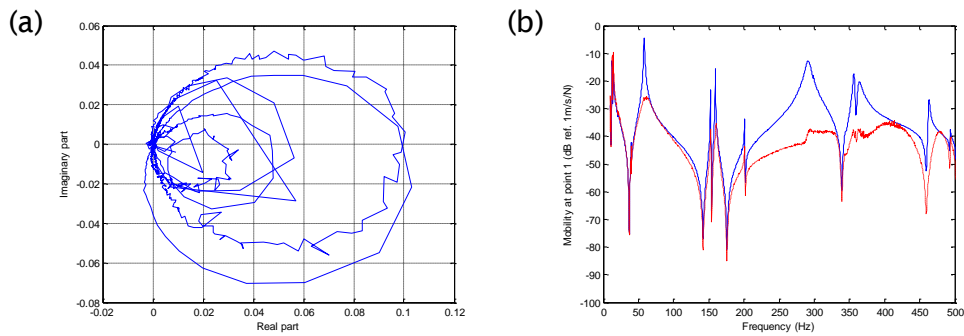


Figure E.26 (a) Nyquist plot for a closed loop with an ideal low-pass filter with a cut-off frequency of 500 Hz and (b) controlled result with an ideal low-pass filter with a cut-off frequency of 500 Hz (AC/PCLD treatment, $G_{3dB} = 206.6667$)

E.4.3 AC/PSOLD treatment

From measured FRFs with pseudo-random moment excitation by a piezoelectric actuator and pseudo-random force excitation by a shaker with AC/PSOLD treatment, the following Nyquist plots and control simulation results are obtained according to applied filters.

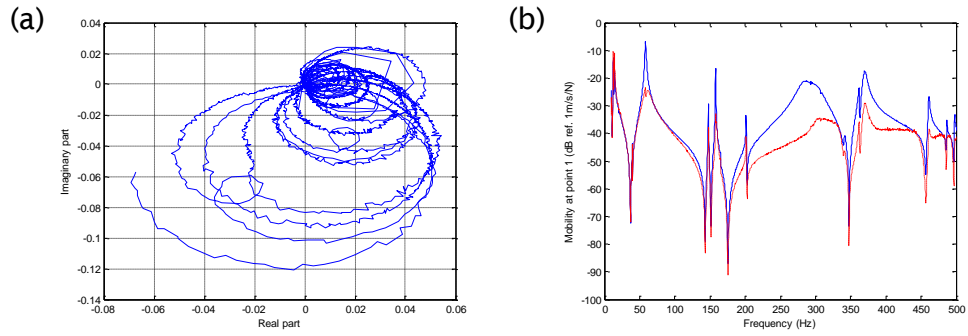


Figure E.27 (a) Nyquist plot for a closed loop without a filter and (b) controlled result without a filter (AC/PSOLD treatment, $G_{3dB} = 175.4717$)

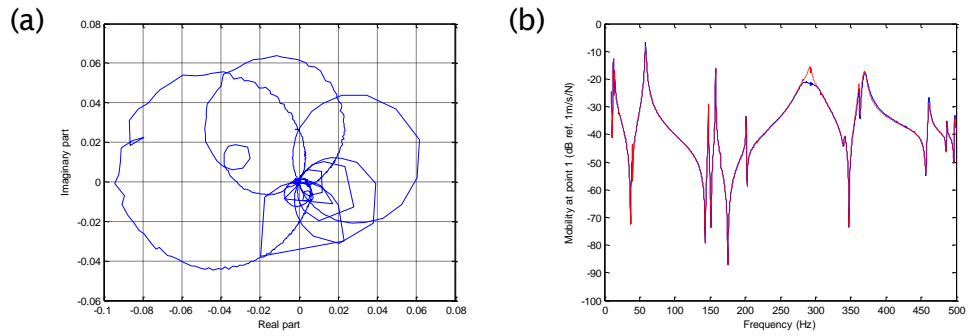


Figure E.28 (a) Nyquist plot for a closed loop with a low-pass filter with a cut-off frequency of 500 Hz and (b) controlled result with a low-pass filter with a cut-off frequency of 500 Hz (AC/PSOLD treatment, $G_{3dB} = 5.3278$)

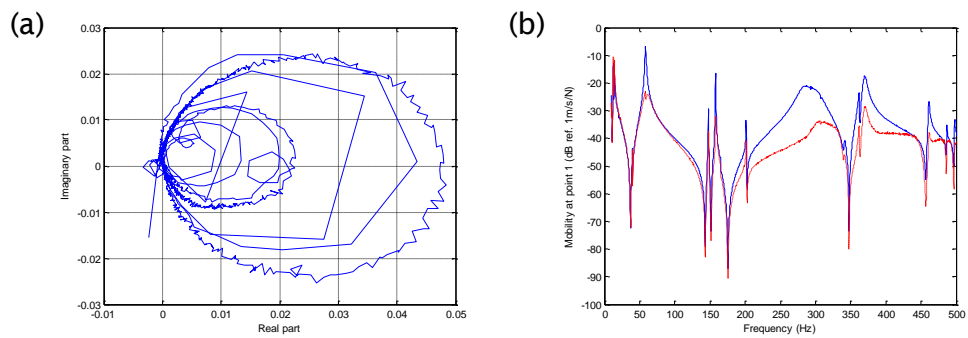


Figure E.29 (a) Nyquist plot for a closed loop with an ideal low-pass filter with a cut-off frequency of 500 Hz and (b) controlled result with an ideal low-pass filter with a cut-off frequency of 500 Hz (AC/PSOLD treatment, $G_{3dB} = 160.7407$)

List of References

- [1] D. J. Mead, *Passive Vibration Control*, John Wiley & Sons, Inc., 1998.
- [2] D. J. Mead and S. Markus, 'The Forced Vibration of a Three-Layer, Damped Sandwich Beam with Arbitrary Boundary Conditions', *Journal of Sound and Vibration*, Vol. 10(2), pp. 163-175, 1969.
- [3] M. A. Trindade and A. Benjeddou, 'Hybrid Active-Passive Damping Treatments using Viscoelastic and Piezoelectric Materials: Review and Assessment', *Journal of Vibration and Control*, Vol. 8 (6), pp. 699-745, 2002.
- [4] R. Stanway, J. A. Rongong and N. D. Sims, 'Active Constrained-Layer Damping: a State-of-the-art Review', *Proceedings of The Institution of Mechanical Engineers, Part I: Journal of Systems and Control Engineering* (Sep. 1. 2003), Vol. 217 (6), pp. 437-456, 2003.
- [5] E. M. Kerwin, 'Damping of flexural waves by a constrained viscoelastic layer', *Journal of the Acoustical Society of America*, Vol. 31 (7), pp. 952-962, 1959.
- [6] A. K. Jha, *Vibration Analysis and Control of an Inflatable Toroidal Satellite Component Using Piezoelectric Actuators and Sensors*, PhD Dissertation, Virginia Tech, Mechanical Engineering, 2002.
- [7] C. Chantalakhana and R. Stanway, 'Active Constrained Layer Damping of Clamped-Clamped Plate Vibrations', *Journal of Sound and Vibration*, Vol. 241 (5), pp. 755-777, 2001.
- [8] F. Fahy and J. Walker, *Advanced Applications in Acoustics, Noise and Vibration*, Chapter 11 High-frequency Structural Vibration by R. S. Langley and F. J. Fahy, Spon Press, 2004.
- [9] A. Baz and J. Ro, 'Optimum Design and Control of Active Constrained Layer Damping', *Journal of Vibration and Acoustics*, Vol. 117 (135), pp. 135-144, 1995.
- [10] D. L. G. Jones, *Viscoelastic Vibration Damping*, John Wiley & Sons, Ltd., 2001.
- [11] C. M. d. A. Vasques, *Vibration Control of Adaptive Structures: Modelling, Simulation and Implementation of Viscoelastic and Piezoelectric Damping Technologies*, PhD Thesis, University of Porto, Faculty of Engineering, 2008.
- [12] A. Baz, 'Boundary Control of Beams using Active Constrained Layer Damping', *Journal of Vibration and Acoustics*, Vol. 119 (167), pp. 166-172, 1997.
- [13] A. Baz, 'Dynamic Boundary Control of Beams using Active Constrained Layer Damping', *Mechanical Systems and Signal Proceeding*, Vol. 11 (6), pp. 811-825, 1997.

List of References

- [14] A. Baz and J. Ro, *Vibration Control of Rotating Beams with Active Constrained Layer Damping*, Smart Materials and Structures (2001), Vol. 10, pp. 112-120
- [15] A. Baz and J. Ro, 'Vibration Control of Plates with Active Constrained Layer Damping', *Smart Materials and Structures*, Vol. 5, pp. 272-280, 1996.
- [16] M. C. Ray, J. Oh and A. Baz, 'Active Constrained Layer Damping of Thin Cylindrical Shells', *Journal of Sound and Vibration*, Vol. 240 (5), pp. 921-935, 2001.
- [17] M. C. Ray and A. K. Pradhan, 'The Performance of Vertically Reinforced 1-3 Piezoelectric Composites in Active Damping of Smart Structures', *Smart Materials and Structures*, Vol. 15, pp. 631-641, 2006.
- [18] M. C. Ray and A. Faye, 'Active Structural-acoustic Control of Laminated Composite Plates using Vertically/Obliquely Reinforced 1-3 Piezoelectric Composite Patch', *International Journal of Mechanics and Materials in Design*, Vol. 5, pp. 123-141, 2009.
- [19] M. C. Ray and J. N. Reddy, 'Active Control of Laminated Cylindrical Shells using Piezoelectric Fiber Reinforced Composites', *Composite Science and Technology*, Vol. 65, pp. 1226-1236, 2005.
- [20] M. C. Ray and A. K. Pradhan, 'Performance of Vertically and Obliquely Reinforced 1-3 Piezoelectric Composites for Active Damping of Laminated Composite Shells', *Journal of Sound and Vibration*, Vol. 315, pp. 816-835, 2008.
- [21] M. C. Ray and A. K. Pradhan, 'Active Damping of Laminated Thin Cylindrical Composite Panels using Vertically/Obliquely Reinforced 1-3 Piezoelectric Composites', *Acta Mechanica*, Vol. 209, pp. 201-218, 2010.
- [22] S. K. Sarangi and M. C. Ray, 'Active Damping of Geometrically Nonlinear Vibrations of Laminated Composite Shallow Shells using Vertically/Obliquely Reinforced 1-3 Piezoelectric Composites', *International Journal of Mechanics and Materials in Design*, Vol. 7, pp. 29-44, 2011.
- [23] M. C. Ray and R. C. Batra, 'A Single-Walled Carbon Nanotube Reinforced 1-3 Piezoelectric Composite for Active Control of Smart Structures', *Smart Materials and Structures*, Vol. 16, pp. 1936-1947, 2007.
- [24] W. H. Liao and K. W. Wang, 'On the Active-Passive Hybrid Control of Structures with Active Constrained Layer Treatments', *Journal of Vibration and Acoustics*, Vol. 119 (4), pp. 563-572, 1997.

- [25] I. Y. Shen, 'Hybrid Damping through Intelligent Constrained Layer Treatments', *Journal of Vibration and Acoustics*, Vol. 116 (3), pp. 341-349, 1994.
- [26] I. Y. Shen, 'Stability and Controllability of Euler-Bernoulli Beams with Intelligent Constrained Layer Treatments', *Journal of Vibration and Acoustics*, Vol. 118 (1), pp. 70-77, 1996.
- [27] V. V. Varadan, Y.-H. Lim and V. K. Varadan, 'Closed Loop Finite-Element Modelling of Active/Passive Damping in Structural Vibration Control', *Smart Materials and Structures*, Vol. 5, pp. 685-694, 1996.
- [28] G. A. Lesieutre and U. Lee, 'A Finite Element for Beams having Segmented Active Constrained Layers with Frequency-Dependent Viscoelastics', *Smart Materials and Structures*, Vol. 5, pp. 615-627, 1996.
- [29] G. S. Agnes and K. Napolitano, *Active Constrained Layer Viscoelastic Damping*, 34th AIAA/ASME/ASCE/AHS/ASC Structures, Structural Dynamics, and Materials Conference, AIAA, Reston, VA, USA, pp. 3499-3506, 1993.
- [30] S. C. Huang, D. J. Inman and E. M. Austin, 'Some Design Considerations for Active and Passive Constrained Layer Damping Treatments', *Smart Materials and Structures*, Vol. 5 (3), pp. 301-313, 1996.
- [31] J. M. Yellin and I. Y. Shen, 'A Self-Sensing Active Constrained Layer Damping Treatment for a Euler-Bernoulli Beam', *Smart Materials and Structures*, Vol. 5 (5), pp. 628-637, 1996.
- [32] A. Baz, 'Robust Control of Active Constrained Layer Damping', *Journal of Sound and Vibrations*, Vol. 211 (3), pp. 467-480, 1998.
- [33] A. Baz and J. Ro, 'Partial Treatment of Flexible Beams with Active Constrained Layer Damping', *Recent Development in Stability, Vibration and Control of Structural Systems*, Vol. AMD-167, ASME, New York, pp. 61-80, 1993.
- [34] A. Baz and J. Ro, 'Optimum Design and Control of Active Constrained Layer Damping', *Journal of Vibration and Acoustics*, Vol. 117 (B), pp. 135-144, 1995.
- [35] D. E. Veley and S. S. Rao, 'A Comparison of Active, Passive and Hybrid Damping in Structural Design', *Smart Materials and Structures*, Vol. 5 (5), pp. 660-671, 1996.
- [36] R. K. Kapadia and G. Kawiecki, 'Experimental Evaluation of Segmented Active Constrained Layer Damping Treatments', *Journal of Intelligent Material Systems and Structures*, Vol. 8 (2), pp. 103-111, 1997.

List of References

- [37] B. Azvine, G. R. Tomlinson R. Wynne and O. Sensburg, *Vibration Suppression of Flexible Structures using Active Damping*, Proceedings of the 4th International Conference of Adaptive Structures and Technologies, Lancaster, PA, USA, pp. 340-356, 1993.
- [38] B. Azvine, G. R. Tomlinson and R. Wynne, 'Use of Active Constrained-Layer Damping for Controlling Resonant Vibration', *Smart Materials and Structures*, Vol. 4 (1), pp. 1-6, 1995.
- [39] J. A. Rongong, J. R. Wright, R. J. Wynne and G. R. Tomlinson, 'Modelling of a Hybrid Constrained Layer/Piezo-ceramic Approach to Active Damping', *Journal of Vibration and Acoustics*, Vol. 119 (1), pp. 120-130, 1997.
- [40] T. Chen and A. Baz, 'Performance Characteristics of Active Constrained Layer Damping Versus Passive Constrained Layer Damping with Active Control', *Smart Structures & Materials 1996: Mathematics and Control in Smart Structures*, Vol. 2715, SPIE, Bellingham, WA, USA, pp. 256-268, 1996.
- [41] J. Crassidis, A. Baz and N. Wereley, 'H ∞ Control of Active Constrained Layer Damping', *Journal of Vibration and Control*, Vol. 6 (1), pp. 113-136, 2000.
- [42] M. J. Lam, D. J. Inman and W. R. Saunders, 'Vibration Control through Passive Constrained Layer Damping and Active Control', *Journal of Intelligent Material Systems and Structures*, Vol. 8 (8), pp. 663-677, 1997.
- [43] M. I. Friswell and D. J. Inman, *Hybrid Damping Treatments in Thermal Environment*, *Smart Materials and Structures*, IOP Publishing, Bristol, UK, pp. 667-674, 1998.
- [44] M. J. Lam, D. J. Inman and W. R. Saunders, 'Variations of Hybrid Damping', *Smart Structures & Materials 1998: Passive Damping and Isolation*, Vol. 3327, SPIE, Bellingham, WA, USA, pp. 32-43, 1998.
- [45] J.S. Whittier, *The Effect of Configurational Additions using Viscoelastic Interfaces on the Damping of a Cantilever Beam*, WADC Technical Report, Wright Air Development Center, pp. 58-568, 1959.
- [46] F.-M. Li, K. Kishimoto, Y.-S. Wang, Z.-B. Chen and W.-H Huang, 'Vibration Control of Beams with Active Constrained Layer Damping', *Smart Materials and Structures*, Vol. 17, 065036 (9 pp.), 2008.
- [47] M. A. Trindade, 'Optimization of Active-Passive Damping Treatments using Piezoelectric and Viscoelastic Materials', *Smart Materials and Structures*, Vol. 16, pp. 2159-2168, 2007.

- [48] V. Balamurugan and S. Narayana, 'Finite Element Formulation and Active Vibration Control Study on Beams using Smart Constrained Layer Damping (SCLD) Treatment', *Journal of Sound and Vibration*, Vol. 249 (2), pp. 227-250, 2002.
- [49] M. A. Trindade, A. Benjeddou and R. Ohayon, 'Modelling of Frequency-Dependent Viscoelastic Materials for Active-Passive Vibration Damping', *Journal of Vibration and Acoustics*, Vol. 122, pp. 169-174, 2000.
- [50] W. H. Liao and K. W. Wang, 'A New Active Constrained Layer Configuration with Enhanced Boundary Actions', *Smart Materials and Structures*, Vol. 5, pp. 638-648, 1996.
- [51] A. Badre-Alam, K. W. Wang and F. Gandhi, 'Optimization of Enhanced Active Constrained Layer (EACL) Treatment on Helicopter Flexbeams for Aeromechanical Stability Augmentation', *Smart Materials and Structures*, Vol. 8, pp. 182-196, 1999.
- [52] D. Sun and L. Tong, 'Modelling and Vibration Control of Beams with Partially Debonded Active Constrained Layer Damping Patch', *Journal of Sound and Vibration*, Vol. 252 (3), pp. 493-507, 2002.
- [53] M. A. Trindade, A. Benjeddou and R. Ohayon, 'Piezoelectric Active Vibration Control of Damped Sandwich Beams', *Journal of Sound and Vibration*, Vol. 246 (4), pp. 653-677, 2001.
- [54] M. A. Trindade, 'Experimental Analysis of Active-Passive Vibration Control using Viscoelastic Materials and Extension and Shear Piezoelectric Actuators', *Journal of Vibration and Control*, Vol. 17 (6), pp. 917-929, 2011.
- [55] C. M. A. Vasques, B. R. Mace, P. Gardonio and J. Dias Rodrigues, 'Arbitrary Active Constrained Layer Damping Treatments on Beams: Finite Element Modelling and Experimental Validation', *Computers and Structures*, Vol. 84, pp. 1384-1401, 2006.
- [56] M. A. Trindade, A. Benjeddou and R. Ohayon, 'Finite Element Modelling of Hybrid Active-Passive Vibration Damping of Multilayer Piezoelectric Sandwich Beams – Part I: Formulation', *International Journal for Numerical Methods in Engineering*, Vol. 51, pp. 835-854, 2001.
- [57] Y. Shi, H. Hua and H. Sol, 'The Finite Element Analysis and Experimental Study of Beams with Active Constrained Layer Damping Treatments', *Journal of Sound and Vibration*, Vol. 278, pp. 342-363, 2004.
- [58] Y. M. Shi, Z. F. Li, H. X. Hua, Z. F. Fu and T. X. Liu, 'The Modelling and Vibration Control of Beams with Active Constrained Layer Damping', *Journal of Sound and Vibration*, Vol. 245 (5), pp. 785-800, 2001.

List of References

- [59] A. L. Araujo, C. M. Mota Soares and C. A. Mota Soares, 'A Viscoelastic Sandwich Finite Element Model for the Analysis of Passive, Active and Hybrid Structures', *Applied Composite Materials*, Vol. 17, pp. 529-542, 2010.
- [60] J. S. Moita, A. L. Araujo, P. G. Martins, C. M. Mota Soares and C. A. Mota Soares, *Analysis of Active-Passive Structures using a Simple and Efficient Finite Element Model*, Proceeding of 7th EUROMECH Solid Mechanics Conference (Sep. 7-11, 2009), Lisbon, Portugal, 2009.
- [61] C. Chantalakhana and R. Stanway, 'Active Constrained Layer Damping of Plate Vibrations: A Numerical and Experimental Study of Modal Controllers', *Smart Materials and Structures*, Vol. 9, pp. 940-952, 2000.
- [62] J. Kim, V. V. Varadan, V. K. Varadan and X.-Q. Bao, 'Finite-Element Modelling of a Smart Cantilever Plate and Comparison with Experiments', *Smart Materials and Structures*, Vol. 5, pp. 165-170, 1996.
- [63] H. Boudaoud, S. Belouettar, E. M. Daya and M. Potier-Ferry, 'A Shell Finite Element for Active-Passive Vibration Control of Composite Structures with Piezoelectric and Viscoelastic Layers', *Mechanics of Advanced Materials and Structures*, Vol. 15, pp. 208-219, 2008.
- [64] N. Kumar and S. P. Singh, 'Vibration Control of Curved Panel using Smart Damping', *Mechanical Systems and Signal Processing*, Vol. 30, pp. 232-247, 2012.
- [65] H. Illaire, W. Kropp and B. Mace, 'A Phenomenological Model of Active Constrained Layers', *Journal of Sound and Vibration*, Vol. 285, pp. 281-302, 2005.
- [66] E. H. K. Fung, J. Q. Zou and H. W. J. Lee, 'Lagrangian Formulation of Rotating Beam with Active Constrained Layer Damping Treatment in Time Domain Analysis', *Journal of Mechanical Design*, Vol. 126, pp. 359-364, 2004.
- [67] U. Lee and J. Kim, 'Spectral Element Modelling for the Beams Treated with Active Constrained Layer Damping', *International Journal of Solids and Structures*, Vol. 38, pp. 5679-5702, 2001.
- [68] A. Tessler, M. Di Sciuva and M. Gherlone, 'Refined Zigzag Theory for Homogeneous, Laminated Composite, and Sandwich Plates: A Homogeneous Limit Methodology for Zigzag Function Selection', *NASA/TP-2010-216214*, 2010.
- [69] P. Cerracchio, M. Gherlone, M. Di Sciuva and A. Tessler, 'A Novel Approach for Displacement and Stress Monitoring of Sandwich Structures Based on the Inverse Finite Element Method', *Composite Structures*, Vol. 127, pp. 68-76, 2015.

- [70] P. Vidal, L. Gallimard and O. Polit, 'Assessment of Variable Separation for Finite Element Medeling of Free Edge Effect for Composite Plates', *Composite Structures*, Vol. 123, pp. 19-29, 2015.
- [71] T. S. Plagianakos and E. G. Papadopoulos, 'Coupled Higher-order Layerwise Mechanics and Finite Element for Cylindrical Composite and Sandwich Shells with Piezoelectric Transducers', *European Journal of Mechanics/A Solids*, DOI: 10.1016/j.euromechsol. 2015.06.003, 2015.
- [72] D. Versino, H. M. Mourad, T. O. Williams and F. L. Addessio, 'A Global-Local Discontinuous Galerkin Finite Element for Finite-Deformation Analysis of Multilayered Shells', *Computer Methods in Applied Mechanics and Engineering*, Vol. 283, pp. 1401-1424, 2015.
- [73] Z.-S. Tian, Q.-P. Yang and A.-P. Wang, 'Three-dimensional Stress Analyses around Cut-outs in Laminated Composites by Special Hybrid Finite Elements', *Journal of Composite Materials*, DOI: 10.1177/0021998315570509/jcm.sagepub.com, 2015.
- [74] Y. Zhou, S. Li and H. Zhou, 'State Space Finite Element Analysis for Piezoelectric Precision Positioning Considering Secondary Converse Piezoelectric Effect', *Finite Elements in Analysis and Design*, Vol. 102-103, pp. 85-94, 2015.
- [75] Z. Yuan, G. A. Kardomateas and Y. Frostig, 'Finite Element Formulation based on the Extended High-order Sandwich Panel Theory', *AIAA Journal*, DOI: 10.2914/1.J053736, 2015.
- [76] S. Yazdani and P. Ribeiro, 'A Layerwise p-version Finite Element Formulation for Free Vibration Analysis of Thick Composite Laminates with Curvilinear Fibres', *Composite Structures*, Vol. 120, pp. 531-542, 2015.
- [77] P. Phung-Van, L. De Lorenzis, C. H. Thai, M. Abdel-Wahab and H. Nguyen-Xuan, 'Analysis of Laminated Composite Plates Integrated with Piezoelectric Sensors and Actuators using Higher-order Shear Deformation Theory and Isogeometric Finite Elements', *Computational Materials Science*, Vol. 96, pp. 495-505, 2015.
- [78] H. Zuo, Z. Tang, X. Chen, Y. Xie and H. Miao, 'Analysis of Laminated Composite Plates using Wavelet Finite Element Method and Higher-order Plate Theory', *Composite Structures*, Vol. 131, pp. 248-258, 2015.
- [79] C. H. Thai, H. Nguyen-Xuan, S. P. A. Bordas, N. Nguyen-Thanh and T. Rabczuk, 'Isogeometric Analysis of Laminated Composite Plates using the Higher-order Shear Deformation Theory', *Mechanics of Advanced Materials and Structures*, Vol. 22(6), pp. 451-469, 2015.

List of References

- [80] L. Xu, S. Lin and Y. Yang, 'Optimal Design of Viscoelastic Damping Structures using Layerwise Finite Element Analysis and Multi-objective Genetic Algorithm', *Computers and Structures*, Vol 157, pp. 1-8, 2015.
- [81] S. A. Thakur and C. Ray, 'An Accurate C^0 Finite Element Model of Moderately Thick and Deep Laminated Doubly Curved Considering Cross Sectional Warping', *Thin-Walled Structures*, Vol 94, pp. 384-393, 2015.
- [82] U. N. Band and Y. M. Desai, 'Coupled Higher Order and Mixed Layerwise Finite Element Based Static and Free Vibration Analyses of Laminated Plates', *Composite Structures*, Vol. 128, pp. 406-414, 2015.
- [83] G. Carpentieri, F. Tornabene, L. Ascione and F. Fraternali, 'An Accurate One-dimensional Theory for the Dynamics of Laminated Composite Curved Beams', *Journal of Sound and Vibration*, Vol. 336, pp. 96-105, 2015.
- [84] C. L. Dym and I. H. Shames, *Solid Mechanics: A Variational Approach*, McGraw-Hill, Inc., 1973.
- [85] L. L. Bucciarelli, *Engineering Mechanics for Structures*, Dover Publications, 2002.
- [86] F. Fahy and J. Walker, *Advanced Applications in Acoustics, Noise and Vibration*, Chapter 12 Noise Control by M.J. Brennan and N.S. Ferguson, Spon Press, 2004.
- [87] C. D. Marqui, A. Erturk, and D. J. Inman., 'An Electromechanical Finite Element Model for Piezoelectric Energy Harvester Plates', *Journal of Sound and Vibration*, Vol. 327, pp. 9-25, 2009.
- [88] C. M. A. Vasques, B. Mace, P. Gardonio and J. D. Rodrigues, 'Analytical Formulation and Finite Element Modelling of Beams with Arbitrary Active Constrained Layer Damping Treatments', *ISVR Technical Memorandum*, Vol. 934, University of Southampton, ISVR, 2004.
- [89] D. T. Detwiler, M.-H. H. Shen and V. B. Venkayya, 'Finite Element Analysis of Laminated Composite Structures containing Distributed Piezoelectric Actuators and Sensors', *Finite Elements in Analysis and Design*, Vol. 20, pp. 87-100, 1995.
- [90] W. Flügge, *Viscoelasticity*, Springer-Verlag, 1975.
- [91] D. J. McTavish and P. C. Hughes, 'Modelling of Linear Viscoelastic Space Structures', *Journal of Vibration and Acoustics*, Vol. 115, pp. 103-110, 1993.

- [92] M. Petyt, *Introduction to Finite Element Vibration Analysis*, Cambridge University Press, 1990.
- [93] A. J. M. Ferreira, 'Analysis of Composite Plates Using a Layerwise Theory and Multiquadrics Discretization', *Mechanics of Advanced Materials and Structures*, Vol. 12, pp. 99-112, 2005.
- [94] D. J. Ewins, *Modal Testing -theory, practice and application-*, Research Studies Press Ltd, 2000.
- [95] M. R. Ashory, *High Quality Modal Testing Methods*, PhD Thesis, University of London, Department of Mechanical Engineering, Imperial College of Science, Technology and Medicine, London, 1999.
- [96] M. Zilletti, *Self-Tuning Vibration Absorbers*, PhD Thesis, University of Southampton, ISVR, 2011.
- [97] W. M. Leach, Jr., 'The Differential Time-Delay Distortion and Differential Phase-Shift Distortion as Measures of Phase Linearity', *Journal of Audio Engineering Society*, Vol. 37 (9), pp. 709-715, 1989.
- [98] S. M. Kim and J. E. Oh, *A Modal Filter Approach to Non-collocated Vibration Control of Structures*, *Journal of Sound and Vibration* (2013), Vol. 332, pp. 2207-2221
- [99] G. Wang, S. Veermani and N. M. Wereley, 'Analysis of Sandwich Plates with Isotropic Face Plates and a Viscoelastic Core', *Journal of Vibration and Acoustics*, Vol. 122, pp. 305-312, 2000.
- [100] G. Wang, N. M. Wereley and D.-C. Chang, 'Analysis of Sandwich Plates with Viscoelastic Damping Using Two-Dimensional Plate Modes', *AIAA Journal*, Vol. 41 (5), pp. 924-932, 2003.
- [101] G.B. Warburton, *The Dynamical Behaviour of Structures*, Pergamon Press Ltd, 1976.
- [102] A.A. Khdeir and O.J. Aldraihem, 'Analysis of Smart Cross Ply Laminated Shells with Shear Piezoelectric Actuators', *Smart Materials and Structures*, Vol. 20, 105030 (11 pp.), 2011.
- [103] H. Kioua and S. Mirza, 'Free Vibration of Laminated Composite Shallow Shells Containing Piezoelectric Layers', *Mechanics of Composite Materials and Structures*, Vol. 8, pp. 181-197, 2001.
- [104] H. Kioua and S. Mirza, 'Piezoelectric Induced Bending and Twisting of Laminated Composite Shallow Shells', *Smart Materials and Structures*, Vol. 9, pp. 476-484, 2000.

List of References

- [105] D. S. Nourzad, *Active Vibration Control of Doubly-Curved Panels*, PhD Thesis, University of Southampton, ISVR, 2014.
- [106] M. D. Waller, 'Vibrations of Free Rectangular Plates', *The Proceedings of The Physical Society Section B*, Vol. 62, Part 5, pp. 277- 285, 1949.
- [107] C. R. Fuller, S. J. Elliot and P. A. Nelson, *Active Control of Vibration*, Elsevier Ltd, 1997.
- [108] J. K. Henry and R. L. Clark, 'A curved piezo-structure model: Implications on active structural acoustic control', *Journal of Acoustic Society of America*, Vol. 106, pp. 1400-1407, 1999.
- [109] S. J. Kim, J. S. Hwang and J. Mok, 'Sensor/Actuator Optimal Design for Active Vibration Control of Shell Structure', *Journal of Intelligent Material Systems and Structures*, Vol. 11, pp. 848-856, 2000.
- [110] E. B. Becker, G. F. Carey and J. T. Oden, *Finite Elements: An Introduction Volume 1*, Prentice-Hall, Inc., 1981.
- [111] W. T. Thomson, *Theory of Vibration with Application*, Chapman & Hall, 1993.
- [112] P. Y. H. Huang, P. G. Reinhall and I. Y. Shen, 'A Comment on Boundary Conditions in the Modelling of Beams with Constrained Layer Damping Treatments', *Journal of Vibration and Acoustics*, Vol. 123, pp. 280-284, 2001.
- [113] C. Hong, P. Gardonio and S. J. Elliott, 'Active Control of Resiliently-Mounted Beams using Triangular Actuators', *ISVR Technical Report*, No. 05/306, University of Southampton, ISVR, 2005.
- [114] Y. Zhang, X. Zhang and S. Xie, 'Adaptive Vibration Control of a Cylindrical Shell with Laminated PVDF Actuator', *Acta Mechanica*, Vol. 210, pp. 85-98, 2010.
- [115] I. Chopra, 'Review of State of Art of Smart Structures and Integrated Systems', *AIAA Journal*, Vol. 40 (11), pp. 2145-2187, 2002.
- [116] M. Dadfarnia, N. Jalili, B. Xian and D. B. Dawson, 'A Lyapunov-Based Piezoelectric Controller for Flexible Cartesian Robot Manipulators', *Journal of Dynamic Systems, Measurement and Control*, Vol. 126, pp. 347-358, 2004.
- [117] P. Gardonio and S. J. Elliot, 'Smart Panel with Velocity Feedback Control Systems Using Triangularly Shaped Strain Actuators', *Journal of Acoustic Society of America*, Vol. 117 (4), pp. 2046-2064, 2005.

- [118] F. E. Udwadi and R. Kumar, *Time-delayed Active Control of Structures*, The Proceedings of Eleventh World Conference on Earthquake Engineering, Paper No. 192, 1996.